UNIVERSITY OF SOUTHERN QUEENSLAND

NUMERICAL OPTIMISATION OF STRUCTURAL BEHAVIOUR OF HOLLOW BOX PULWOUND FIBRE COMPOSITE PROFILES

A Thesis submitted by

Mohammad Ahmad Abdel Rahman Alhawamdeh

MSc, BSc

For the award of

Doctor of Philosophy

2022

ABSTRACT

Hollow box Pultruded Fibre-reinforced Polymers (PFRP) profiles are increasingly used as structural elements in many civil infrastructure applications due to their cost-effective manufacturing process, excellent mechanical properties-to-weight ratios, and superior corrosion resistance. These structural composite elements manufactured by the pulwinding technology are governed by layup parameters (winding angle, axial-to-wound fibres ratio, and stacking sequence) and geometric parameters (wall slenderness, cross-sectional aspect ratio, and corner radius). However, there is still a lack of knowledge and guidelines in the design for manufacturing against local buckling, which deprives this novel construction material of a large market share compared to conventional construction materials. Investigating these design parameters and their interactions under structural loadings is going to enhance the current standards, provide reliable and economic design guidelines, and optimise the current designs for hollow box PFRP profiles. Therefore, this research investigated the local buckling behaviour of hollow box PFRP profiles under different load applications (compression and bending) and facilitated practical design guidelines for the manufacturing parameters of hollow box PFRP profiles to optimise their structural performance against local buckling.

First, experimental and numerical studies were undertaken under axial compression to characterise the local buckling of hollow box PFRP profiles and compare it to the compressive behaviour of hollow circular PFRP profiles. A numerical modelling approach was developed to simulate the local buckling, post-buckling, and progressive failure of hollow box PFRP profiles using the Finite Element Method (FEM). This approach used the Newton method along with the adaptive automatic stabilisation scheme and a controlled increment size in Abaqus 2019, to overcome the numerical difficulties in simulating local buckling. The numerical predictions were validated against the experimental data. The energy parameters and the constituent failure modes of the FEM models were used to explain the effect of dimension, layup, and slenderness ratio on the post-buckling behaviour and failure modes of hollow PFRP columns.

Secondly, the effect and contribution of the layup and geometric parameters were investigated under axial compression. The developed numerical approach based on FEM was used to perform an extensive parametric study of these parameters. Each geometric parameter was studied individually to obtain the failure map of hollow PFRP stub columns and to assess the applicable levels for each parameter in the interactive study. A full factorial design of experiment was applied to capture the critical parametric interactions with over 135 numerical models. The

corner (flange-web junction) geometry was the dominant design parameter in shaping the compressive strength of hollow box PFRP profiles. Supporting this critical zone obtained more reliable and economic designs. Guidelines and recommendations on the design for manufacturing were derived for the optimal compressive behaviour of hollow PFRP profiles to overcome local buckling and achieve material compressive failure.

Thirdly, a combined experimental and numerical methodology was used to investigate the failure modes of hollow box PFRP profiles under four-point bending. Two different profiles, each with 10 samples, were tested until failure and were used to validate the numerical model. The previous FEM approach was extended to suit flexural loading and reduce the computational cost. The validated model was used to study the failure sequence thoroughly and perform an extensive parametric study on the design parameters. Each geometric parameter was studied individually first to determine the relevant levels for each parameter in the full factorial study. A full factorial design of experiment was used to capture the critical parametric interactions with over 81 numerical models. The design rules and recommendations were established for the optimal flexural behaviour of hollow box PFRP profiles to withstand the local buckling of the top flange.

Finally, a fast-converging numerical approach combining the Finite Element Modelling (FEM) and the Genetic Algorithm (GA) was implemented to design the optimal configuration of the geometry and layup design parameters against local buckling under different structural loadings (compression and bending). The objective of the mixed-integer nonlinear-constrained optimisation problem was to minimise the manufacturing cost per metre of pultrusion while maintaining the same stiffness and strength properties of the control profile. The Kriging model, which is a geostatistical prediction tool capable of handling such design problems, was used to interpolate the design space based on the intermediate optimisation data output and produce a practical design chart linking the profile geometry to the local buckling capacity. An experimental case study on the design of a hollow rectangular PFRP girder demonstrated the proposed optimisation approach. The new design saved 10.6% of the cost per metre of pultrusion and enhanced the local buckling strength by 41%.

This research resulted in a comprehensive understanding regarding the design for manufacturing of hollow box PFRP profiles. The effect and significance of each design parameter on the structural behaviour of hollow box PFRP profiles were studied and analysed. This study outlines the importance of the interactions in obtaining optimised, economic, and reliable designs of these profiles and broadening their use in civil infrastructure applications.

CERTIFICATION OF THESIS

I ***Mohammad Ahmad Abdel Rahman Alhawamdeh*** declare that the PhD Thesis entitled ***NUMERICAL OPTIMISATION OF STRUCTURAL BEHAVIOUR OF HOLLOW BOX PULTRUDED FIBRE COMPOSITE PROFILES*** is not more than 100,000 words in length including quotes and exclusive of tables, figures, appendices, bibliography, references, and footnotes.

This Thesis is the work of ***Mohammad Ahmad Abdel Rahman Alhawamdeh*** except where otherwise acknowledged, with the majority of the contribution to the papers presented as a Thesis by Publication undertaken by the Student. The work is original and has not previously been submitted for any other award, except where acknowledged.

[redacted]

Signed: *Mohammad Alhawamdeh* Date: 07 March 2022

Endorsed by:

Associate professor Xuesen Zeng

Principal Supervisor

Professor Peter Schubel

Associate Supervisor

Professor Thiru Aravinthan

Associate Supervisor

Student and supervisors' signatures of endorsement are held at the University.

STATEMENTS OF CONTRIBUTIONS

The articles produced from this study were a joint contribution of the authors. The details of the scientific contribution of each author are provided below:

Manuscript 1: Mohammad Alhawamdeh, Omar Alajarmeh, Thiru Aravinthan, Tristan Shelley, Peter Schubel, Ali Mohammed, and Xuesen Zeng, (2021) “Review on Local Buckling of Hollow Box FRP Profiles in Civil Structural Applications” Polymers, 23, vol. 13, no. 23, p. 4159. (Impact factor: 4.329 and SNIP: 1.2)

DOI: https://doi.org/10.3390/polym13234159

The overall contribution of Mohammad Alhawamdeh was 70% related to the conceptualisation, methodology, data collection and curation, critical review of related literature, analysis and interpretation of data, writing the original draft and revising the final submission. Xuesen Zeng, Peter Schubel, Thiru Aravinthan, Omar Alajarmeh, Tristan Shelley, and Ali Mohammed contributed to the structuring of the manuscript, reviewing, editing, and providing important technical advice.

Manuscript 2: Mohammad Alhawamdeh, Omar Alajarmeh, Thiru Aravinthan, Tristan Shelley, Peter Schubel, Michael Kemp, and Xuesen Zeng, (2021) “Modelling hollow pultruded FRP profiles under axial compression: Local buckling and progressive failure” Composite Structures, vol. 262, p. 113650. (Impact factor: 5.407 and SNIP: 2.04)

DOI: https://doi.org/10.1016/j.compstruct.2021.113650

The overall contribution of Mohammad Alhawamdeh was 65% related to the conceptualisation, methodology, design of experiments, experimental works, data collection and curation, software, analysis and interpretation of data, writing the original draft and revising the final submission. Xuesen Zeng, Peter Schubel, Thiru Aravinthan, Omar Alajarmeh, Tristan Shelley, and Michael Kemp contributed to the concept development, design of experiments, reviewing, editing, and providing important technical advice.

Manuscript 3: Mohammad Alhawamdeh, Omar Alajarmeh, Thiru Aravinthan, Tristan Shelley, Peter Schubel, Michael Kemp, and Xuesen Zeng, “Effects of Layup and Geometry on Compressive Performance of Hollow Pultruded FRP Profiles" under review in Composite Structures (Impact factor: 5.407 and SNIP: 2.04).

The overall contribution of Mohammad Alhawamdeh was 65% related to the conceptualisation, methodology, design of experiments, data collection and curation, software, analysis and interpretation of data, writing the original draft and revising the final submission. Xuesen Zeng, Peter Schubel, Thiru Aravinthan, Omar Alajarmeh, Tristan Shelley, and Michael Kemp contributed to the reviewing, editing, and providing important technical advice.

Manuscript 4: Mohammad Alhawamdeh, Omar Alajarmeh, Thiru Aravinthan, Tristan Shelley, Peter Schubel, Ali Mohammed, and Xuesen Zeng, (2021) "Modelling flexural performance of hollow pultruded FRP profiles" Composite Structures, vol. 276, p. 114553. (Impact factor: 5.407 and SNIP: 2.04)

DOI: https://doi.org/10.1016/j.compstruct.2021.114553

The overall contribution of Mohammad Alhawamdeh was 70% related to the conceptualisation, methodology, design of experiments, experimental works, data collection and curation, software, analysis and interpretation of data, writing the original draft and revising the final submission. Xuesen Zeng, Peter Schubel, Thiru Aravinthan, Omar Alajarmeh, Tristan Shelley, and Ali Mohammed contributed to the design of experiments, reviewing, editing, and providing important technical advice.

Manuscript 5: Mohammad Alhawamdeh, Omar Alajarmeh, Thiru Aravinthan, Tristan Shelley, Peter Schubel, Ali Mohammed, and Xuesen Zeng "Design Optimisation of Hollow Box Pultruded FRP Profiles Using Mixed Integer Constrained Genetic Algorithm" under review in Engineering Structures (Impact factor: 4.471 and SNIP: 2.25).

The overall contribution of Mohammad Alhawamdeh was 70% related to the conceptualisation, methodology, design of experiments, experimental works, data collection and curation, software, analysis and interpretation of data, writing the original draft and revising the final submission. Xuesen Zeng, Peter Schubel, Thiru Aravinthan, Omar Alajarmeh, Tristan Shelley, and Ali Mohammed contributed to the reviewing, editing, and providing important technical advice.

ACKNOWLEDGEMENTS

First and foremost, all praise is due to ***ALLAH*** for giving me the patience, the knowledge, and the strength to complete this work.

I would like to express my sincere appreciation and thanks to my principal supervisor, associate professor ***Xuesen Zeng*** for his guidance, insight, helpful advice, and copious encouragement throughout the course of this research. I am so grateful for his friendship, support, ideas, and motivation. I was blessed to meet him and work under his supervision which enlightened within me the first glance of research. It is impossible to find words expressing my full gratefulness to him. His unique piece of mind and immense knowledge were my sources to build my research character and to think constructively.

Special thanks and gratitude to my associate supervisor Professor ***Peter Schubel*** for his prominent role in helping me to achieve one of the greatest accomplishments in my life. His incessant motivation, endless support, unique guidance, cooperative behaviour, and positive attitude added very worthy values to my life. My sincere gratitude and appreciation to my associate supervisor Professor ***Thiru Aravinthan***, for his immense support, encouragement, guidance, and motivation, which made me stronger and optimistic.

Special thanks to my dear friend ***Dr Omar Alajarmeh*** for his friendship, support, insightful comments, suggestions, and constructive ideas which were essential in improving the quality of this research and helping me to complete my work. Special thanks to ***Dr Tristan Shelley*** for his help and support.

I highly appreciate the financial support of the ***University of Southern Queensland*** who helped me to complete my PhD. Special thanks to ***Dr Ali Mohammed*** and ***Wagner CFT*** for the great support and help in the experimental testing. My sincere thanks to the ***Advanced Pultrusion CRC-P*** teams from USQ and Wagners CFT.

My wonderful colleagues at USQ, especially in the ***Centre of Future Materials***, many thanks for your friendship and technical supports.

My deepest love and appreciation go to my beloved ***parents, brothers, and sisters*** for their endless love, encouragement, patience, prayers, sacrifice, and believing in me.

Finally, to those whom I failed to mention, ***thank you All***.

TABLE OF CONTENTS

LIST OF TABLES

LIST OF FIGURES

ABBREVIATIONS

A: cross-sectional area of the profile

ANOVA: analysis of variance

b: cross-sectional width of a hollow box profile

CLPT: Classical Laminated Plate Theory

DOE: Design of Experiment

D: outer diameter of a hollow circular profile

D_{11}, D_{22}, D_{12}, and D_{66}: the flexural stiffness components of laminated plates

E: Elastic compressive modulus of the profile

FEM: Finite Element Method

FRP: Fibre-reinforced Polymers

GA: genetic algorithm

GFRP: Glass Fibre-Reinforced Polymer

h: cross-sectional height of a hollow box profile

I: the moment of inertia of the profile

L/D: length-to-width ratio of the profile

L: length of the profile

PFRP: Pultruded Fibre-reinforced Polymer

r: inner corner radius of a hollow box profile

R: outer corner radius of a hollow box profile

t: wall thickness of a hollow profile

θ: winding angle or the angle of the inclined fibres measured from the axial direction of the pultrusion.

V_f: fibre volume fraction of the lamina

CHAPTER 1: INTRODUCTION

1.1 Background

Fibre-reinforced Polymer (FRP) composites flourished as reliable manufacturing materials in the aerospace and automotive fields. Their early use in civil construction fields was as rehabilitation materials and semi-load bearing members (Barbero 2017; Daniel & Ishai 2006). In the last two decades, the demand for Pultruded Fibre-reinforced Polymer (PFRP) profiles for civil structural applications has increased as they became essential structural members in many applications (Bank 2006; Uddin 2013). This was due to the developments in the pultrusion manufacturing process, which became a reliable, fully-automated, low-cost, and high-quality control process (Boisse 2015; Hoa 2009; Starr 2000). Figure 1.1 presents the basic steps of the pultrusion process, at which unidirectional (UD) continuous glass fibre rovings and thermoset vinyl-ester or polyester resins are usually pulled out with constant cross-section and 50-65% fibre volume fraction (Bunsell & Renard 2005; Meyer 2012). Figure 1.2 shows PFRP profiles with different cross-sections.

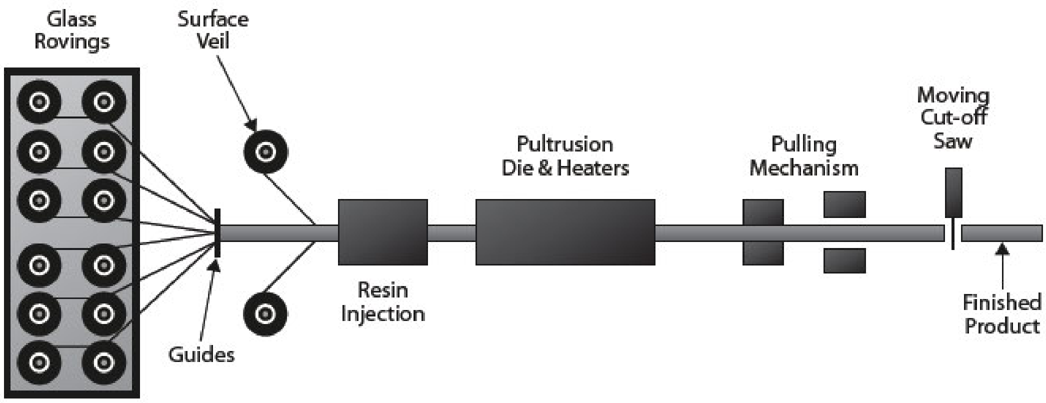

Figure 1.1. The basic steps of the pultrusion process *(Wagners CFT n.d.)*.

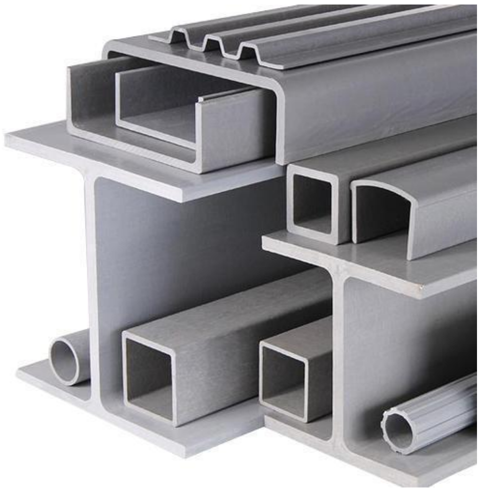

Figure 1.2. PFRP profiles with different cross-sections *(Unity Fibers n.d.)*.

Hollow PFRP profiles are featured by their lightweight, non-corrosive, excellent mechanical properties-to-weight, fast installation, lower emissions, and non-conductive properties compared to the conventional construction materials, such as concrete and steel (Ahn et al. 2014; Johnston et al. 2018). They are used as beams and columns (Friberg & Olsson 2014; Muttashar et al. 2019), decks and panels (Li, Hsu & Hsieh 2019; Satasivam & Bai 2014), and trusses (Hizam et al. 2019; Mottram & Henderson 2018) in buildings and bridges, frames in marine structures (Garrido et al. 2019; Vedernikov et al. 2020), lighting poles and cross-arms in infrastructure (Fangueiro 2011; Godat et al. 2013), pipes in the oil industry (Balasubramanian 2013; GAJJAR 2020), spar caps for wind turbines and cable trays and grating walkways in solar structures in the energy sector (Bakis et al. 2002; Kaw 2005), concrete-filled columns (Bunsell & Renard 2005; Van Den Einde, Zhao & Seible 2003), piles foundations (Bank 2006; Guades et al. 2012), and sleepers in railways (Sapuan 2017; Vinson & Sierakowski 2006). Figure 1.3 presents part of the applications of hollow PFRP profiles in civil infrastructure. The global market share of FRP profiles has increased rapidly in the last decade to reach 15.3 billion USD, which is 6.4% of the international construction market (Sellier 2019). Figure 1.4 shows the global market share of FRP profiles across different infrastructure sectors. Forecast made by European Pultrusion Technology Association (EPTA) predicts the growth of pultruded elements and structures market to be more than $100 billion in 2022 (Minchenkov et al. 2021).

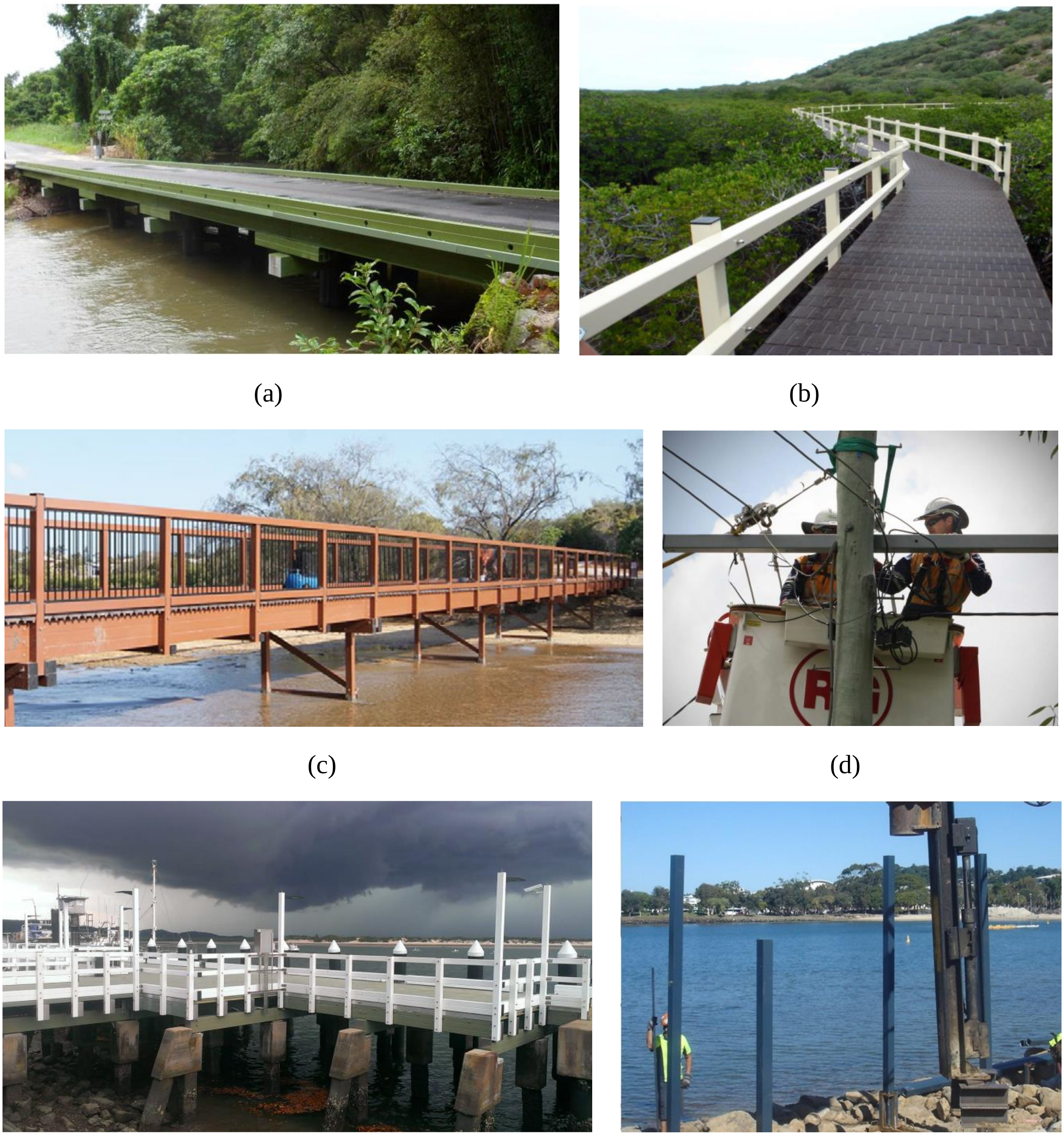

Figure 1.3. Various applications of hollow PFRP profiles (manufactured via pultrusion) in civil infrastructure *(Wagners CFT n.d.)*: (a) road bridge, (b) boardwalk, (c) pedestrian bridge, (d) crossarms, (e) jetties and wharfs, and (f) piles.

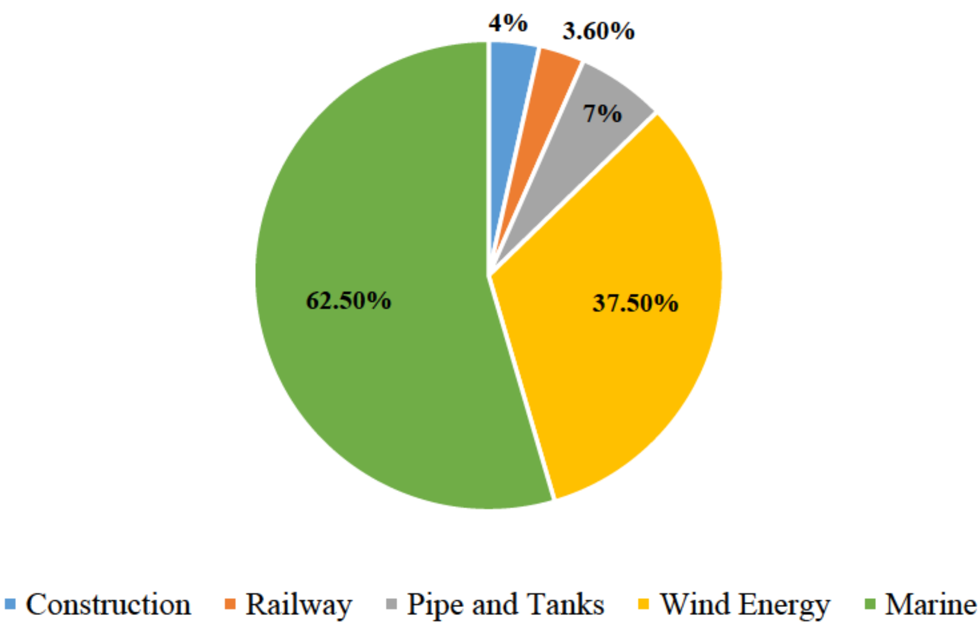

Figure 1.4. Global market share of FRP profiles across different infrastructure sectors (Sellier 2019).

The introduction of pulwinding technology has enriched the pultrusion industry by producing enhanced hollow box pulwound FRP profiles. Pulwinding is essentially a combination of pultrusion and filament winding allowing helical and hoop filaments to be incorporated in the pultruded section, which can increase design flexibility and enable tubular structure products with almost any combination of fibre alignment. In pulwinding, off-axis wound fibre rovings replace the continuous filament mats to be pulled along with the axial fibre rovings providing a higher fibre volume fraction, high-quality control, and low defects (resin-rich zones) content (Rangappa et al. 2020). The wound fibres improve the transverse properties, delamination resistance, and post-processing endurance, such as jointing and bolting (Al-saadi, Aravinthan & Lokuge 2019; Hizam et al. 2019). Moreover, the local buckling capacity is also higher in these profiles compared to normal pultruded profiles (Muttashar et al. 2016; Sayyad & Ghugal 2017). Unlike the design of isotropic materials, the design for manufacturing of hollow box pulwound FRP profiles demands the determination of more design parameters including layup parameters (winding angle, axial-to-wound fibres ratio, and stacking sequence) and geometric parameters (wall slenderness, cross-sectional aspect ratio, and corner radius). Studying these controlling parameters will lead to a comprehensive understanding of their effect on the structural behaviour of hollow box pulwound FRP profiles. Moreover, optimising these parameters and investigating the interactions between them will lead to economic and efficient designs of these profiles and widen their use in civil structural applications.

1.2 Problem statement

Local buckling is a dominant failure mode that controls the structural behaviour of hollow box PFRP profiles due to their anisotropic elasticity and the application-driven slenderness (Attaf 2011; Buragohain 2017). Local buckling can occur well below the ultimate load capacity of the profile and deprives it of being widely used as a primary compression member (Jones 1998; Singer, Arbocz & Weller 2002). Figure 1.5 shows the local buckling of hollow box PFRP profiles subjected to compression and bending loadings.

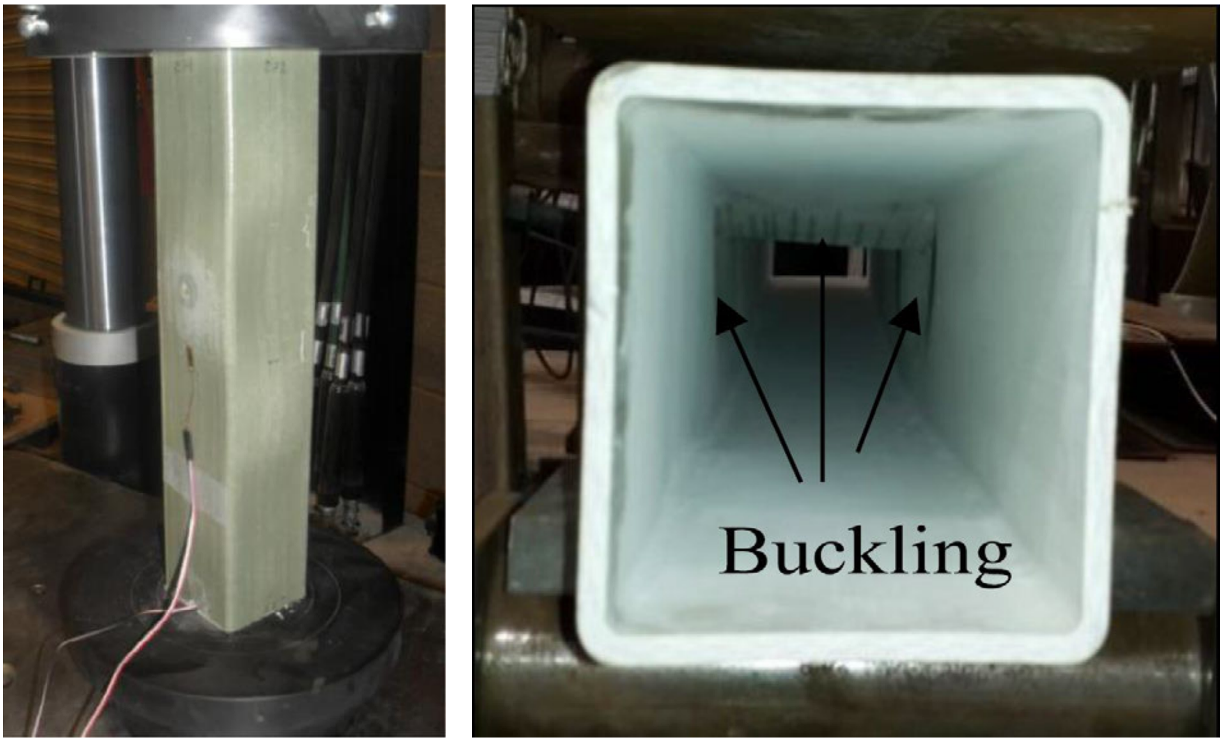

(a) (b)

Figure 1.5. Local buckling of hollow box PFRP (a) stub column (Cardoso, Harries & Batista 2014) and (b) beam (Muttashar 2017).

The local buckling behaviour of hollow box pulwound FRP profiles is controlled by two groups of manufacturing parameters: the layup parameters (winding angle, axial-to-wound fibres ratio, and stacking sequence) and geometric parameters (wall slenderness, cross-sectional aspect ratio, and corner radius) (Correia et al. 2011; Serhat & Basdogan 2019; Xu, Zhao & Qiao 2013). There is still a lack of knowledge and guidelines in the design for manufacturing against local buckling, which deprives this novel construction material of a large market share compared to the conventional construction materials, such as concrete and steel. This lack of knowledge discourages design engineers and contractors from heavily relying on these profiles in infrastructure applications due to the uncertainty and overdesign. The current design standards and manuals (American Society of Civil Engineers 2012; Ascione et al. 2016; Clarke 2005; National Research Council 2007) are still basic and contain only conservative uneconomic formulas for the design against local buckling with no considerations for the interactions between the design parameters. Investigating these design parameters and their interactions is going to provide the foundation for updating these current design standards and manuals and provide reliable and economic design guidelines for hollow box pulwound FRP profiles. Moreover, optimising these design parameters under structural loadings (compression and bending) is going to provide optimal designs of hollow box pulwound FRP profiles with competitive cost and superior structural performance, which will broaden the use of hollow box PFRP profiles in civil structural applications.

1.3 Research objectives

The use of hollow box PFRP profiles is still modest compared to the conventional construction materials due to the lack of design guidelines and recommendations against local buckling, which should account for all the design parameters and their interactions. This limitation presents an obstacle in designing these profiles and utilising their potentials. This research aims to investigate the local buckling behaviour of hollow box pulwound FRP profiles subjected to compressive and flexural loadings and facilitate practical design guidelines for the manufacturing parameters of hollow pulwound FRP profiles to optimise their structural performance against local buckling. The main objectives of this study are:

1- Develop a reliable Finite Element Method (FEM) modelling approach to simulate the local buckling, post-buckling, and progressive failure behaviours of hollow box pulwound FRP profiles under compression and bending loadings. This approach is going to be used to perform parametric studies on the design parameters with minimal cost and effort.

2- Characterise the local buckling behaviour of hollow box pulwound FRP profiles under compression and bending loadings using both experimental and numerical approaches.
3- Investigate the effect of the layup and geometric parameters on the local buckling of hollow box pulwound FRP profiles subjected to compression and bending loadings. In addition, quantify the contribution of each manufacturing parameter on the structural performance of hollow box pulwound FRP profiles subjected to compression and bending loadings to distinguish the significance and weight of each parameter.
4- Study the interactions between the manufacturing parameters of hollow box pulwound FRP profiles under compression and bending loadings to facilitate efficient and economic design guidelines and recommendations.
5- Conducting parametric studies to optimise the design configurations of the manufacturing parameters of hollow box pulwound FRP profiles subjected to compression and bending loadings against local buckling and report the optimised designs.

1.4 Scope and limitations

This study focused on optimising the structural performance of hollow box pulwound FRP profiles and providing design guidelines and recommended configurations of the design parameters against local buckling. Extensive experimental programs were conducted on full-scale specimens to characterise the compressive and flexural behaviours of the profiles and to assist in validating the numerical models. The developed modelling approach accurately captured the local buckling, post-buckling, and progressive failure of the profiles. The numerical models were used to perform parametric studies on the manufacturing parameters to investigate their effect on the local buckling behaviour of the profiles and their interactions. Finally, design guidelines and optimised designs against local buckling were reported. All the investigated profiles here were manufactured and sponsored (through the advanced pultrusion CRC-P) by Wagners CFT (Wagners CFT n.d.) using pulwinding technology and were made from E-glass fibres and Vinyl-ester resin. It should be highlighted that the manufacturing process conditions (curing rate and pulling speed) were the same for all profiles as provided by the manufacturer. The length of the stub columns and the test setup of the beams were chosen to prevent global buckling or lateral-torsional buckling and mitigate the shear effect on the hollow box PFRP beams. Consequently, the targeted failure modes were local buckling of walls and the ultimate strength of the material. Therefore, other failure modes such as shear failure were not considered in this study and are out of scope. The scope of this study can be summarised as follows:

1- Review the design parameters of hollow box pulwound FRP profiles and the latest studies on their effect and interactions on the local buckling of these profiles.
2- Investigate the structural performance of hollow box pulwound FRP profiles subjected to axial compression and bending loadings using both experimental and numerical approaches and characterise their local buckling behaviour.
3- Performing parametric studies to investigate the effect of the layup and geometric parameters on the structural performance of hollow box pulwound FRP profiles and study their interactions.
4- Reporting design guidelines for manufacturing against local buckling and obtaining optimised configurations of the manufacturing parameters of hollow box pulwound FRP profiles to broaden the use of these profiles in civil structural applications with facilitated and economic designs.

It is worth highlighting that geometric imperfections present in hollow box PFRP profiles. However, the effect of these imperfections is negligible when studying the local buckling behaviour of these profiles due to the small length of the specimens tested. This short length prevents the structure from failing in global buckling, which is highly dependent on these imperfections. Thus, the geometric imperfections were included in this study to speed up the numerical analysis only.

1.5 Thesis organisation

This research work is presented as a thesis by publication. This thesis consists of seven chapters including this introduction, which presents the research background, significance, objectives, and scope. Chapter 2 contains a literature review on hollow box PFRP profiles, their local buckling behaviour, and the methods used to analyse it. It also presents a review of the manufacturing parameters controlling the structural performance of these profiles and their effects and interactions. The numerical approach used to model the hollow box pulwound FRP profiles and their local buckling is developed and validated under axial compression in chapter 3. Chapter 4 presents the results of the parametric studies on the hollow box pulwound FRP profiles subjected to axial compression. It discusses the effect, contribution, and interactions of the design parameters on the compressive behaviour of the profiles. The numerical modelling approach was extended to simulate the local buckling of hollow box pulwound FRP profiles under bending in chapter 5. In addition, the effect, contribution, and interactions of the design parameters on the flexural behaviour of hollow box pulwound FRP profiles were reported. Chapter 6 presents the adopted numerical optimisation approach used to minimise the production cost of hollow box pulwound FRP profiles and enhance their structural performance. It also discusses the novel numerical approach used to generate interaction charts of the significant design parameters. Chapter 7 summarises the conclusions of this research and the suggested recommendations for future work. The flow chart of the thesis is presented in Figure 1.6. The supplementary data and optimisation codes available in Appendices A, B, and C represent a vital tool for the optimisation of future structural profiles.

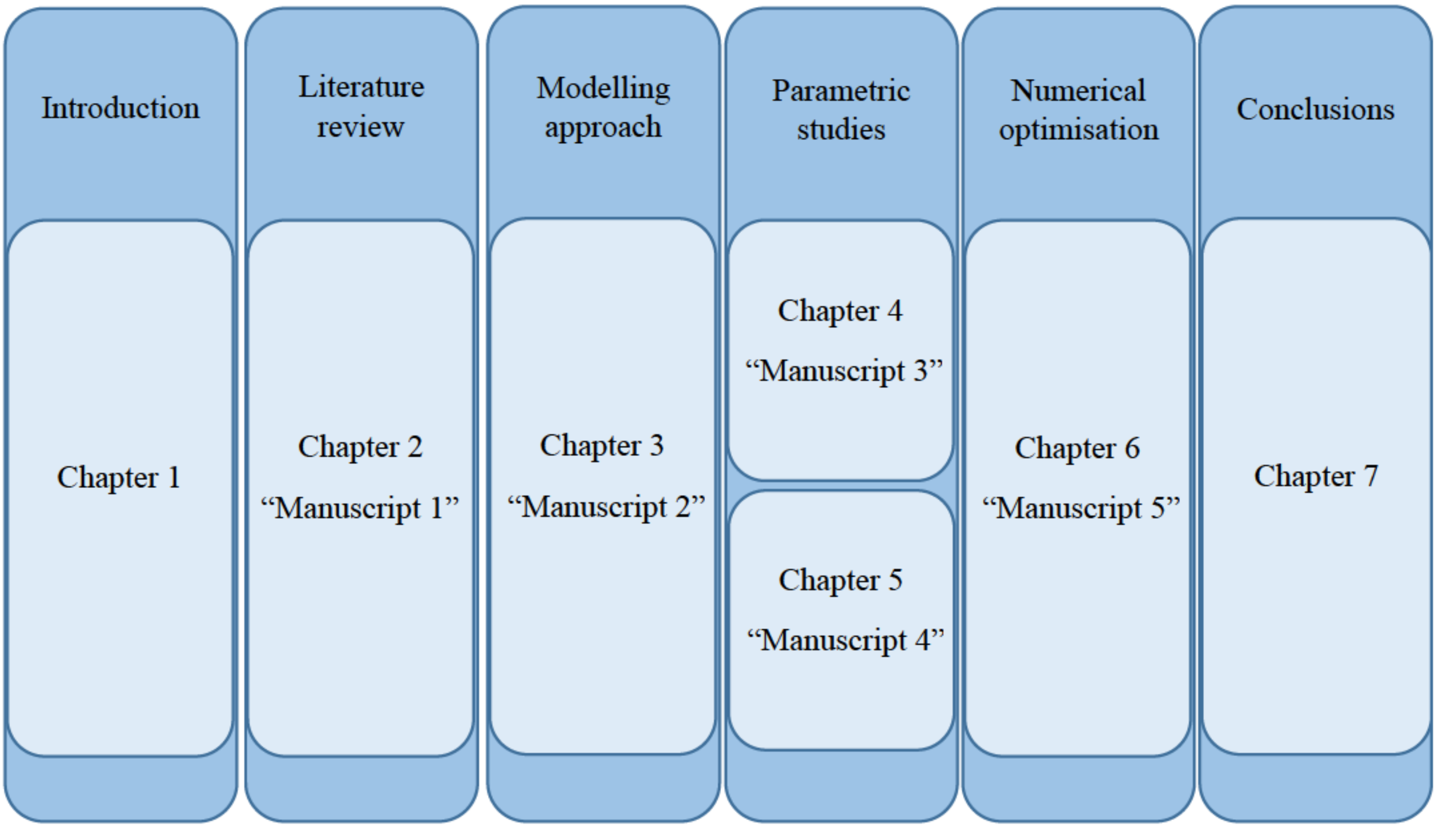

Figure 1.6. Thesis flow chart.

From this work, five journal articles were published or are currently under review in Q1 international journals. An overview of these publications is presented as follows:

Manuscript 1 (Published): Alhawamdeh, M, Alajarmeh, O, Aravinthan, T, Shelley, T, Schubel, P, Mohammed, A & Zeng, X 2021, 'Review on Local Buckling of Hollow Box FRP Profiles in Civil Structural Applications', Polymers, 23, vol. 13, no. 23, p. 4159. (Impact factor: 4.329 and SNIP: 1.2)

DOI: https://doi.org/10.3390/polym13234159

This article reviews the local buckling of hollow box FRP profiles and compares it to other open-section structural shapes. It also addresses the related design parameters to identify the research gaps in order to expand the current design standards and manuals of hollow box PFRP profiles and to broaden their applications in civil structures.

Manuscript 2 (Published): Alhawamdeh, M, Alajarmeh, O, Aravinthan, T, Shelley, T, Schubel, P, Kemp, M & Zeng, X 2021, 'Modelling hollow pultruded FRP profiles under axial compression: Local buckling and progressive failure', Composite Structures, vol. 262, p. 113650. (Impact factor: 5.407 and SNIP: 2.04)

DOI: https://doi.org/10.1016/j.compstruct.2021.113650

This article addresses the first and second objectives of this research where the numerical modelling approach was developed to characterise the local buckling and compressive failure of hollow box PFRP profiles under axial compression using Abaqus 2019. The numerical predictions were validated by experiments and the energy parameters and the constituent failure modes of the FEM models were used to explain the effect of dimensions, layup, and slenderness ratio on the failure mode. It is worth noting that further validation, apart from the visual comparison of contour plots and photographs of failed test specimens, was undertaken and published as part of this research project (Alajarmeh et al. 2021). In this study, the Digital Image Correlation (DIC) was used to map the strain contour experimentally and correlate the experimental test data to the numerical results.

Manuscript 3 (Under review): Alhawamdeh, M, Alajarmeh, O, Aravinthan, T, Shelley, T, Schubel, P, Kemp, M & Zeng, X, 'Effects of Layup and Geometry on Compressive Performance of Hollow Pultruded FRP Profiles', under review in Composite Structures (Impact factor: 5.407 and SNIP: 2.04).

This article discusses the third and fourth objectives of this research where extensive parametric studies were performed on the manufacturing parameters of hollow box PFRP profiles to determine their effect and interactions under axial compression. Each geometric parameter was studied individually to obtain the failure map of hollow PFRP stub columns and to assess the applicable levels for each parameter in the interactive study. A full factorial design of experiment was applied to capture the critical parametric interactions with over 135 numerical models. Guidelines and recommendations on the design for manufacturing were derived for the optimal compressive behaviour of hollow box PFRP profiles to overcome local buckling.

Manuscript 4 (Published): Alhawamdeh, M, Alajarmeh, O, Aravinthan, T, Shelley, T, Schubel, P, Mohammad, A & Zeng, X 2021, 'Modelling flexural performance of hollow pultruded FRP profiles', Composite Structures, vol. 276, p. 114553. (Impact factor: 5.407 and SNIP: 2.04)

DOI: https://doi.org/10.1016/j.compstruct.2021.114553

This article addresses the first, second, third, and fourth objectives of this research where the numerical modelling approach was extended to simulate the local buckling of hollow box PFRP profiles subjected to four-point bending. The validated models were used to study the failure sequence thoroughly and perform extensive parametric studies on the design parameters. Each geometric parameter was studied individually first to determine the relevant levels for each parameter in the full factorial study. A full factorial design of experiment was used to capture the critical parametric interactions with over 81 numerical models. Design guidelines and recommendations were established for the optimal flexural behaviour of hollow box PFRP profiles to withstand local buckling of the top flange.

Manuscript 5 (Under review): Alhawamdeh, M, Alajarmeh, O, Aravinthan, T, Shelley, T, Schubel, P, Mohammed, A & Zeng, X, 'Design Optimisation of Hollow Box Pultruded FRP Profiles Using Mixed Integer Constrained Genetic Algorithm', under review in Engineering Structures (Impact factor: 4.471 and SNIP: 2.25).

This research discusses the fifth objective of this research where a fast-converging numerical approach combining the FEM and the Genetic Algorithm (GA) was developed to design the optimal configuration of the geometry and layup design parameters against local buckling under compression and bending loadings. The "MI-LXPM" GA code was used to solve the mixed-integer constrained optimisation problem. The optimisation objective was to minimise the manufacturing cost per metre of pultrusion while maintaining the same stiffness and strength properties of the control profile. The Kriging model was used to interpolate the design space based on the intermediate optimisation data output and produce the practical interactions chart. An experimental case study on the design of a hollow rectangular pultruded FRP girder demonstrated the proposed optimisation approach. The new design saved 10.6% of the cost per metre of pultrusion.

CHAPTER 2: (PAPER 1) REVIEW ON LOCAL BUCKLING OF HOLLOW BOX FRP PROFILES IN CIVIL STRUCTURAL APPLICATIONS

This chapter presents a comprehensive literature review of the local buckling of Fibre-reinforced Polymers (FRP) profiles in civil infrastructure applications. It also compares the common cross-sectional shapes (open-section and box) and their local buckling behaviour. The theory of local buckling and the common methods used to analyse it were also reviewed. This article critically reviews the behaviour of hollow box FRP profiles under different loading conditions and the effect of different design parameters on the structural behaviour of the profiles. From this review, it was identified that local buckling is a critical failure mode that occurs well below the ultimate material strength of the profile depriving it of using its potentials. However, local buckling can be eliminated for hollow box FRP profiles if the geometric parameters are optimised.

The review article identifies the research gaps related to the critical design for manufacturing parameters of hollow box pultruded FRP profiles. It also presents a review of the interactions between the design parameters and their significance in enhancing the structural performance of the profiles and expanding the current design standards and manuals of hollow box pultruded FRP profiles. The effect of the critical design parameters on the local buckling behaviour of hollow box pultruded FRP profiles and their interactions identified in the review were systematically investigated and analysed in chapters 3 to 6, where significant results are presented.

polymers

MDPI

Review

Review on Local Buckling of Hollow Box FRP Profiles in Civil Structural Applications

Mohammad Alhawamdeh [1,*], Omar Alajarmeh [1], Thiru Aravinthan [1], Tristan Shelley [1], Peter Schubel [1], Ali Mohammed [2] and Xuesen Zeng [1]

[1] Centre for Future Materials, University of Southern Queensland, Toowoomba, QLD 4350, Australia; Omar.Alajarmeh@usq.edu.au (O.A.); Thiru.Aravinthan@usq.edu.au (T.A.); tristan.shelley@usq.edu.au (T.S.); Peter.Schubel@usq.edu.au (P.S.); Xuesen.Zeng@usq.edu.au (X.Z.)

[2] Wagners Composite Fibre Technologies, Wellcamp, QLD 4350, Australia; ali.mohammed@wagner.com.au

* Correspondence: Mohammad.Alhawamdeh@usq.edu.au; Tel.: +61-7-4631-5516

Abstract: Hollow box pultruded fibre-reinforced polymers (PFRP) profiles are increasingly used as structural elements in many structural applications due to their cost-effective manufacturing process, excellent mechanical properties-to-weight ratios, and superior corrosion resistance. Despite the extensive usage of PFRP profiles, there is still a lack of knowledge in the design for manufacturing against local buckling on the structural level. In this review, the local buckling of open-section (I, C, Z, L, T shapes) and closed-section (box) FRP structural shapes was systematically compared. The local buckling is influenced by the unique stresses distribution of each section of the profile shapes. This article reviews the related design parameters to identify the research gaps in order to expand the current design standards and manuals of hollow box PFRP profiles and to broaden their applications in civil structures. Unlike open-section profiles, it was found that local buckling can be avoided for box profiles if the geometric parameters are optimised. The identified research gaps include the effect of the corner (flange-web junction) radius on the local buckling of hollow box PFRP profiles and the interactions between the layup properties, the flange-web slenderness, and the corner geometry (inner and outer corner radii). More research is still needed to address the critical design parameters of layup and geometry controlling the local buckling of pulwound box FRP profiles and quantify their relative contribution and interactions. Considering these interactions can facilitate economic structural designs and guidelines for these profiles, eliminate any conservative assumptions, and update the current design charts and standards.

Keywords: pultruded FRP profiles; local buckling; wall slenderness; cross-sectional aspect ratio; corner geometry; layup properties

Citation: Alhawamdeh, M.; Alajarmeh, O.; Aravinthan, T.; Shelley, T.; Schubel, P.; Mohammed, A.; Zeng, X. Review on Local Buckling of Hollow Box FRP Profiles in Civil Structural Applications. *Polymers* **2021**, *13*, 4159. https://doi.org/10.3390/polym13234159

Academic Editors: Filippo Berto and Luciano Feo

Received: 1 November 2021
Accepted: 24 November 2021
Published: 28 November 2021

1. Introduction

1.1. Background

Pultruded fibre-reinforced polymer (PFRP) profiles have flourished in the last few decades and have become a reliable construction element, especially after the research and development efforts that made pultrusion a more robust and economic manufacturing process [1,2]. These profiles developed from being strengthening and rehabilitating elements to being essential structural members because of their excellent mechanical properties, light weight, and superior corrosion resistance [3,4]. They are currently used as beams [5], decks and panels [6–9], and trusses [10–12] in buildings and bridges, frames in marine structures [13–15], lighting poles and cross-arms in infrastructure [16,17], pipes in the oil industry [18,19], spar caps for wind turbines and cable trays and grating walkways in solar structures in the energy sector [20,21], reinforcements for concrete [22,23], piles foundations [24,25], and sleepers in railways [26–28].

The introduction of pulwinding technology was one of the most prominent developments in pultrusion. In this process, off-axis wound fibres replace continuous filament mats to be pulled along with the axial fibre rovings, which enables the laminate to reach a higher value of fibre volume fraction with high-quality control and low defects (resin-rich zones) content. The wound fibres improve the transverse properties and delamination resistance and enhance the post-processing endurance, such as jointing and bolting [10,29].

1.2. Research Significance

The market share of FRP profiles has increased rapidly in the last decade to reach USD 15.3 billion, which is 6.4% of the construction market [30]. Nevertheless, the current design standards and manuals are still basic and contain only conservative formulas for the design against local buckling with no considerations for the interactions between the design parameters [31]. This lack of knowledge discourages design engineers and contractors from heavily relying on these profiles in infrastructure applications due to uncertainty and overdesign. In addition, the structural design of FRP composites requires more specifications compared to isotropic materials since the layup and geometric parameters have to be assigned for composites while only the dimensions are to be determined for isotropic material [32,33]. Local buckling is a major failure mode controlling the behaviour of PFRP profiles because of their anisotropic and slender nature [34,35]. It can occur before the element reaches its ultimate strength [36–38]. The use of box PFRP profiles is still modest compared to the conventional construction materials due to the lack of local buckling design guidelines and manuals accounting for all the design parameters and their interactions [39]. This limitation presents an obstacle in designing these profiles and utilising their potentials.

This article presents a literature review on the local buckling design parameters controlling the structural behaviour of box PFRP profiles. First, the local buckling design of open-section (I, C, Z, L, T shapes) and closed-section (box) FRP structural shapes was reviewed and compared. Second, the critical design parameters were reviewed along with the available literature on each structural shape. Finally, each design parameter was discussed in terms of the interactions with the other parameters (the effect of one parameter on the influence of the other parameter). The article outlines the current state of knowledge and the further investigations to be conducted; thus, it provides a useful reference to design engineers and researchers. Although most of the parameters were studied on the open-section profiles, there is still a need to perform a comprehensive study to obtain the parametric contribution and interaction for box shape pulwound profiles due to their unique stresses' distribution. Considering these interactions will facilitate more economic and efficient structural designs and guidelines and will result in reliable design charts and recommendations on the design for manufacturing parameters for direct use. Consequently, it will broaden the use of PFRP in civil structural applications.

2. Local Buckling in Composites

Pultruded FRP profiles are prone to local buckling failure, well below their ultimate load capacity, due to their anisotropic elasticity and application-driven slenderness [24,40]. Unlike other failure modes, which depend on the material strength, local buckling depends on the stiffness, geometry, and boundary and loading conditions of the element and can occur before reaching the strength limit [37,41,42]. Contrary to ductile and isotropic metals, the local buckling behaviour of FRP composites is different as it is usually accompanied by a growth of cracks and delamination [43,44]. In this literature review, only the design for manufacturing parameters related to the stiffness and geometry of the box FRP profiles is discussed. The other parameters affecting the local buckling of these profiles, such as the boundary condition and geometric imperfection, are out of this review's scope.

The cross-sectional shape of the PFRP profiles controls their structural performance and their dominant failure mode [45–47]. Regarding local buckling behaviour, PFRP profiles are categorised into two groups of open-section and closed-section (box) shapes depending on the restraint provided for the flange, as shown in Figure 1. Figure 2 shows the percentage share of each cross-sectional shape in civil structural applications along with the studies characterising its local buckling behaviour. The circular tube shape was not considered here since local buckling is not critical in tubular PFRP profiles used in civil structural applications due to their relatively low slenderness ratio and uniformly distributed stresses [48–51]. The I-shape is most common in FRP profiles since it was inherited from the steel industry [52,53]. Nevertheless, box profiles are receiving more attention because of their higher structural stability and torsional stiffness with all walls being restrained [54]. Despite that, the majority of the local buckling studies were conducted on I-shape profiles, as shown in Figure 3, which compares the number of experimental studies undertaken on I-shape versus box shape in civil structural applications. The I-shape geometry was studied over three times more frequently than the box shape up to 2014. With the introduction of pulwinding technology for commercial production, the number of studies on box profiles was multiplied in 2014. Only three experimental studies on local buckling of pulwound FRP profiles were undertaken in 2014 [55], 2016 [56], and 2019 [29].

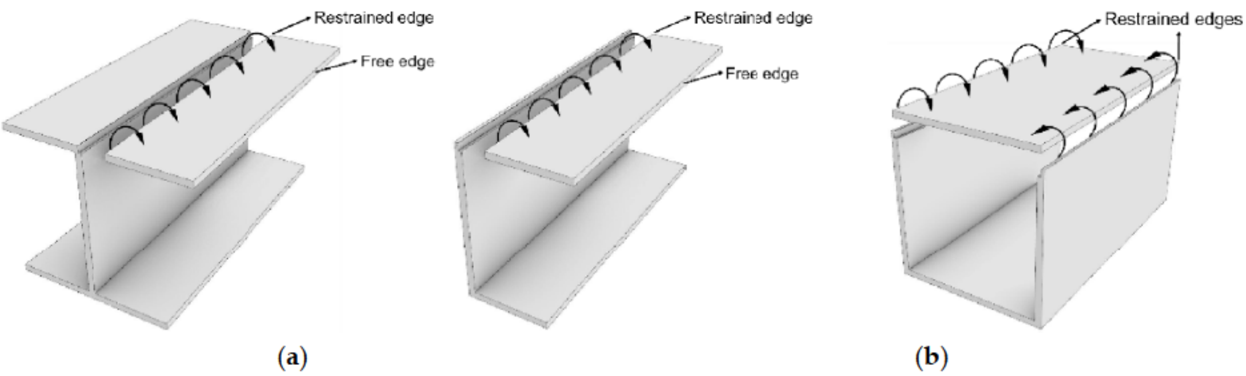

Figure 1. FRP composite profiles with (a) open-section and (b) closed-section (box) shapes (modified from [57]).

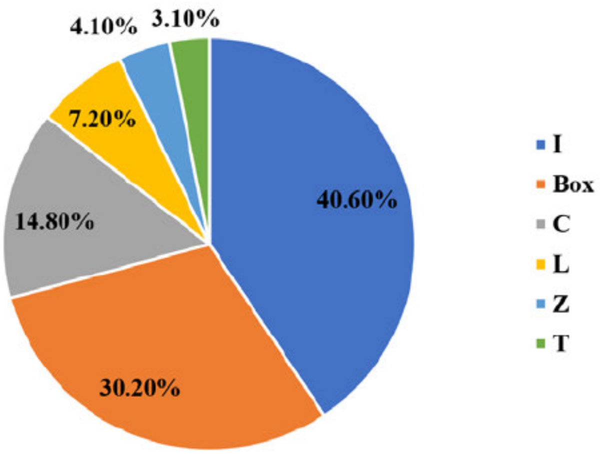

Figure 2. The percentage share of each cross-sectional shape in civil structural applications along with the studies (experimental and numerical) characterising its local buckling behaviour (I-shape: [17,52,53,57–92], Box-shape: [17,29,53–56,58,63,72,75,76,82,85,93–108], C-shape: [63,75,78,82,85–87,97,109–115], L-shape: [17,63,75,78,85–87], Z-shape: [78,85–87], and T-shape: [78,85,87]).

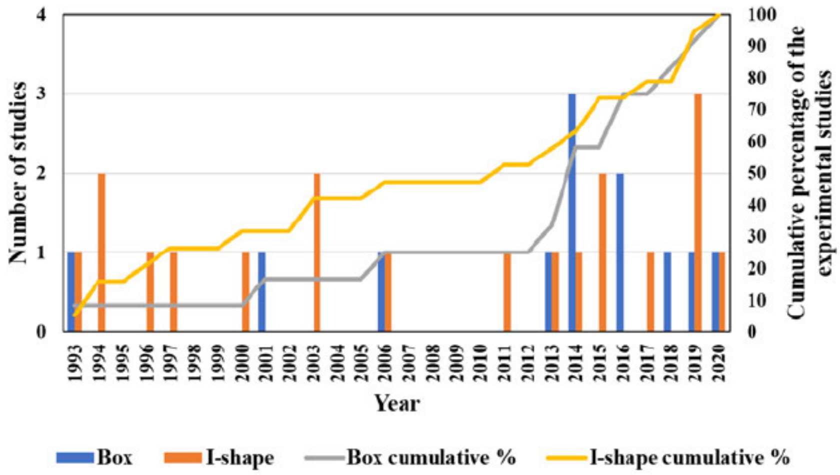

Figure 3. The number of experimental studies of local buckling undertaken on I-shape versus box shape for civil structural applications (Box-shape: [17,29,53,55,56,72,95,96,98,100,101,104] and I-shape: [17,53,61,62,64,66–72,77,79,81,89–92]).

Local buckling can be defined as a structural instability problem where the cross-sectional elements (e.g., flange or web) in a compressive loaded member will undergo an out-of-plane deformation and a stiffness reduction, which may lead to structural collapse [116–118]. It is a dominant failure mode for short-length FRP profiles and its capacity depends on the elastic properties of the laminate, the geometry, and the supporting and loading conditions of the cross-sectional elements [119–121]. Theoretically, local buckling of FRP profiles is analysed by considering each wall (e.g., flange or web) individually as an orthotropic plate and modelling the restraint of the flange-web junctions. Rayleigh–Ritz method is used to approximate the eigenvalue solution of the stability problem depending on the boundary and continuity conditions [85,122]. The theoretical approaches to simulate this restraint (boundary condition) are varying between three assumptions considering the flange-web junction to be clamped, simply supported, or elastically restrained, as shown in Figure 4 for box FRP profile. These three cases represent the upper, lower, and intermediate bounds of the buckling capacity (N_{cr}), respectively [123]. The explicit closed-form solutions for these cases are also presented in the same figure, where D_{11}, D_{22}, D_{12}, and D_{66} are the flexural rigidities (the equivalents of EI per unit width) of the orthotropic plate and the coefficients τ_1, τ_2, and τ_3 are functions of the rotational restraint (k) of the flange-web junction. It is worth mentioning that such closed-form equations are based on the classical laminated plate theory (CLPT) which does not count for shear deformations, and they consider only the geometry and layup of the plate [47,124]. They do not account for the flange-web junction (corner) geometry and cannot answer for the interactions with other failure modes. Thus, considering the local buckling of PFRP profiles as a plate instability problem results in inaccurate predictions due to the omission of stresses distribution from the adjacent walls. It is always preferable to consider the whole cross-sectional geometry when analysing buckling problems, and the finite element method (FEM), finite strip method (FSM), and generalised beam theory (GBT) are usually used for this purpose [125–127]. Nevertheless, the FEM surpasses the other numerical approaches due to its flexible and accurate simulation of geometry (e.g., tapering or thickening the corner radius). This is evident from the reviewed literature as shown in Figure 5, which shows the percentage of each research methodology used to study local buckling and its parameters. FEM is the best candidate to study the design parameters and perform parametric studies because of its flexibility in handling complex geometries, different loading and boundary conditions, and combined failure problems [128–130].

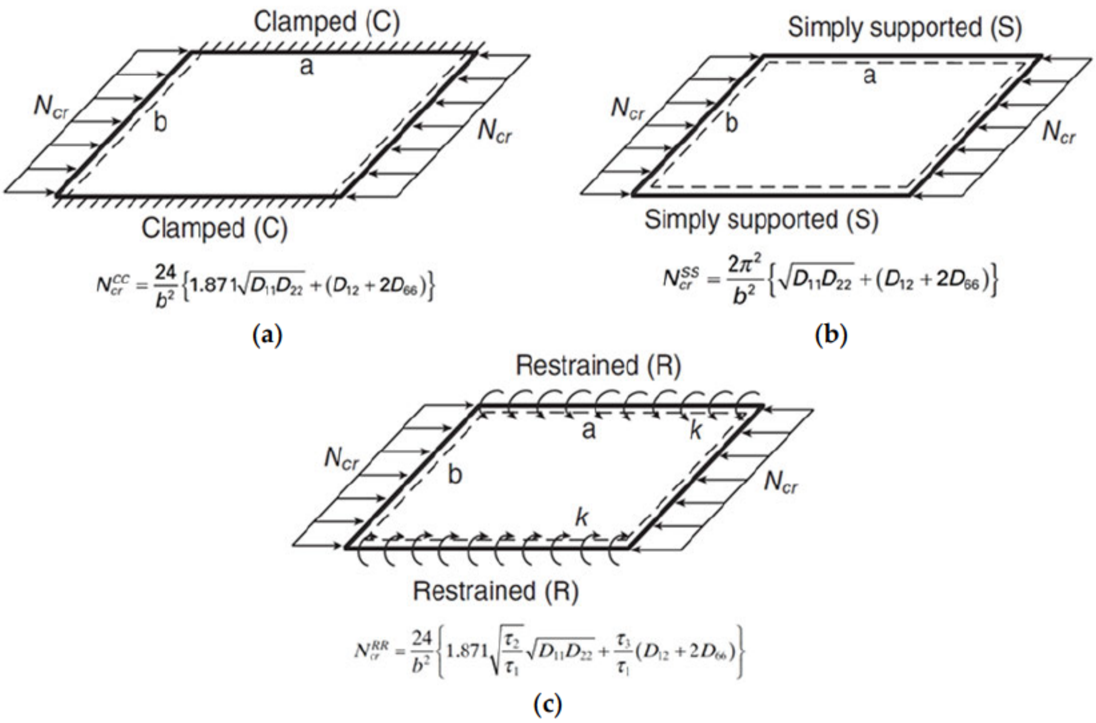

Figure 4. FRP plates of box profile with various unloaded edge conditions: (a) clamped, (b) simply supported, and (c) elastic restrain (modified from [121]).

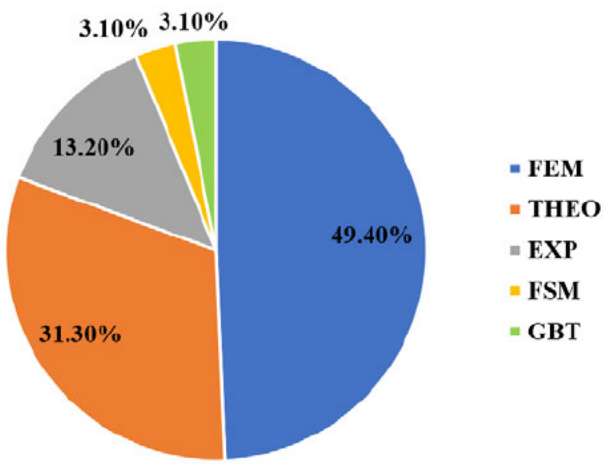

Figure 5. The percentage of each research methodology used to study local buckling and its parameters (FEM: finite element method [29,54,55,57,58,66,68,69,71,73,81,88,91,93–95,99,106,108–115,131–160], THEO: theoretical approaches [53,54,57,59,60,62–67,74–78,80,82–87,96,97,105,107,109,135,152,161–167], EXP: experimental investigations [17,52,56,61,70,72,79,89,90,92,98,100,101,103,104], FSM: finite strip method [63,64,168,169], and GBT: generalised beam theory [65,68,69,80,88]).

The local buckling behaviour of PFRP profiles varies depending on the loading condition as shown in Figure 6, which depicts the distribution of stress and strain in the hollow box profile subjected to compression versus bending. In profiles subjected to compression, all the walls buckle with a smaller buckle half-wavelength. Whereas in bending, only the walls under compressive stresses will buckle with a larger buckle half-wavelength [45,60,170]. Thus, local buckling is more critical in compression members than in flexural members due to the lower restraint provided by adjacent walls in compression members [24,171,172]. Consequently, investigating and optimising the local buckling behaviour should be undertaken under both loading conditions in which compression provides the upper limit case and bending provides the lower limit case.

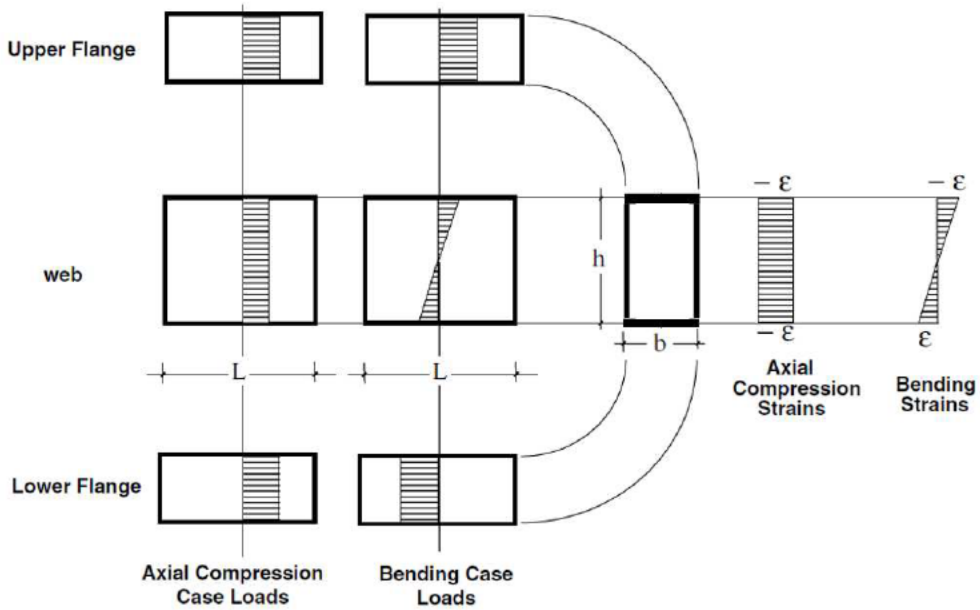

Figure 6. Distribution of strain and load per unit width in the flanges and the web of a box section subjected to axial compression or bending (modified from [86]).

The critical manufacturing design parameters controlling the local buckling behaviour of FRP composites can be categorised into two groups of geometric (wall slenderness, cross-sectional aspect ratio, and corner geometry) and layup parameters (axial-to-inclined fibre ratio, inclined fibre angle, and stacking sequence) [124,173–176]. After reviewing the available literature, it appears that these design parameters were not comprehensively studied for closed-section geometry (box profiles) when compared to other geometries, as shown in Figure 7, evident by the minimum number of publications for each manufacturing design parameter. Moreover, no study was found to investigate the corner radius effect on the local buckling capacity and failure mode of box profiles. Most of the publications on the layup parameters were undertaken for laminated plate geometry, not structural-level shapes. The effect of the layup parameters on the corners, which represent critical failure zones, was not considered in such studies. Table 1 summarises the local buckling design formulas of compression box and I-shape members in current standards and guides [177–180]. The effect of the cross-sectional aspect ratio is neglected in [177], which relies on the maximum slenderness ratio only. Reference [179] does not consider the effect of the rotational restraint between the flange and web. All the design standards neglect the corner radius in their local buckling design formulas. These design parameters should be studied in combination to obtain their contribution and interactions, allowing for a better understanding of the structural performance of box profile geometry and its unique stresses distribution. Consequently, this will enhance the current standards and make them more accurate by considering the corner geometry and its interactions with the other design parameters in the design formulas of these standards.

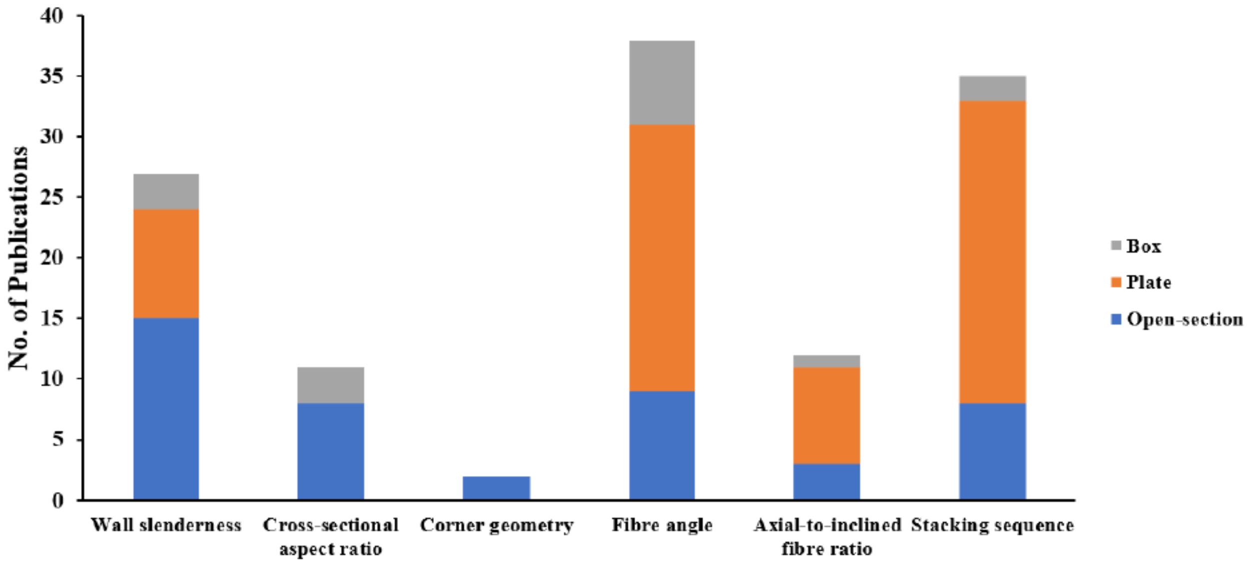

Figure 7. The number of publications on the manufacturing design parameters of local buckling for different FRP composite geometries (Wall slenderness: Open-section [17,66,67,72,75–77,81,83,84,87,90,108,109,111], Plate [133,137,143–146,152,153, 169], and Box [54,76,94], Cross-sectional aspect ratio: Open-section [63–65,68,69,74,86,111] and Box [63,106,108], Corner geometry: Open-section [61,89], Fibre angle: Open-section [53,58,74,78,80,87,97,113,114], Plate [131–134,136,139,141–143,145–149,151,153,155,156,163,165,166,168], and Box [29,53,54,58,94,95,97], Axial-to-inclined fibre ratio: Open-section [80,87,97], Plate [136,137,141,147,149,153,155,168], and Box [94], and Stacking sequence: Open-section [80,87,97,109,111,112,114,140], Plate [131,135–138,141,142,144–149,151,153,155,156,159,160,162–167], and Box [54,97]).

Table 1. Local buckling design formulas of compression box and I-shape members in current standards and guides.

Design Standard	Considered Geometry	Design Formula [1]
Pre-standard for load & resistance factor design (LRFD) of pultruded fibre-reinforced polymer (FRP) structures [177]	Hollow box	$(f) = \frac{\left(\frac{\pi^2}{6}\right)\left[\sqrt{E_L E_T} + v_{LT}E_T + 2G_{LT}\right]}{\left(\frac{b}{t}\right)^2}$
	I-shape	$(f)_{flange} = \frac{G_{LT}}{\left(\frac{b_f}{2t_f}\right)^2}$
Prospect for new guidance in the design of FRP [178]	Hollow box	$(f) = \frac{\pi^2}{b^2 t}\left[2\sqrt{(1+4.139\zeta)(D_{11}D_{22})} + (2+0.62\zeta^2)(D_{12}+2D_{66})\right]$ Where: $\zeta = \left(1 + \frac{5}{1-R}\frac{(D_{22})_f b_w}{(D_{22})_w b_f}\right)^{-1}$, $R = \frac{(f)_f^{ss}(E_L)_w}{(f)_w^{ss}(E_L)_f}$
	I-shape	Same as [180]
Structural Design of Polymer Composites EUROCOMP Design Code and Handbook [179]	Orthotropic plate	$(f) = 2\pi^2 \frac{\left(\sqrt{D_{11}D_{22}} + \mathrm{H_o}\right)}{tb^2}$ Where: $\mathrm{H_o} = 0.5(v_{LT}D_{22} + v_{TL}D_{11}) + \frac{G_{LT}t^3}{6}$
Guide for the Design and Construction of Structures made of FRP Pultruded Elements [180]	I-shape	$(f)_{flange} = \begin{cases} \frac{\sqrt{D_{11}D_{22}}}{t_f\left(\frac{b_f}{2}\right)^2}\left(K\left[15.1\eta\sqrt{1-\rho} + 6(1-\rho)(1-\eta)\right] + \frac{7(1-K)}{\sqrt{1+4.12\zeta}}\right), K \le 1 \\ \frac{\sqrt{D_{11}D_{22}}}{t_f\left(\frac{b_f}{2}\right)^2}\left[15.1\eta\sqrt{1-\rho} + 6(1-\rho)(K-\eta)\right], K > 1 \end{cases}$ Where: $\zeta = \frac{D_{22}}{\widetilde{k}\frac{b_f}{2}}$, $\rho = \frac{D_{12}}{2D_{66}+D_{12}}$, $\eta = \frac{1}{\sqrt{1+(7.22-3.55\rho)\zeta}}$, $K = \frac{2D_{66}+D_{12}}{\sqrt{D_{11}+D_{22}}}$

[1] D_{11}, D_{22}, D_{12}, and D_{66} are the flexural rigidities of the orthotropic plate. $\widetilde{k}$ is the torsional stiffness coefficient. t, b, and h are the section thickness, width, and height, respectively. The subscripts f and w refer to the flange and web, respectively. E_L, E_T, and G_{LT} are the longitudinal, transverse, and in-plane shear elastic moduli, respectively. v_{LT} and v_{TL} are the in-plane and out-of-plane Poisson's ratios, respectively. $(f)_f{}^{ss}$ and $(f)_w{}^{ss}$ are the buckling strengths of the flange and web, respectively, considering simply supported boundary conditions.

The boundary and interaction between local and global buckling modes were extensively investigated for both open-section and box profile geometries [73,92,100,181] and were incorporated in design standards [111,182]. However, the boundary and interactions between local buckling and compressive failure in terms of the design parameters have not been reported for hollow box PFRP profiles. Studying these interactions can lead to facilitated design guidelines and optimised configurations of the design parameters to fully utilise the profile potentials. In the following sections, these manufacturing design parameters are discussed and the available literature on their effect and interaction is summarised. Moreover, the lack of knowledge and the potential research gaps are highlighted in order to develop the current design for manufacturing manuals.

3. Geometric Parameters of Hollow Box PFRP Profiles

The geometric parameters control the PFRP profile stability and determine its load capacity and failure mode [67,183]. These parameters of local buckling are discussed in the following sections by summarising their effect, comparing them for different geometries, and highlighting the available literature on their interactions.

3.1. Wall Slenderness

The wall slenderness (width-to-thickness ratio) significantly contributes to the local buckling capacity of thin-walled PFRP profiles [77,184]. Reducing the wall slenderness increases the profile stability and buckling capacity exponentially [152,167], and shifts the failure mode from local buckling to material compressive failure due to the increase in the flexural stiffness of the laminated walls [170,185]. The effect of the wall slenderness was studied extensively for laminated plate geometry subjected to uniaxial compressive load [133,143,146,152] and the effect of the layup properties on the buckling load capacity of slender plates was found to be negligible compared to their dimensions [137,144,153]. This finding agrees with the results of parametric studies on open-section PFRP columns [67,81,114], shown in Figure 8. When the slenderness ratio is reduced (thicker walls), the effect of the layup properties becomes significant. On the contrary, the effect of the layup properties becomes negligible when the wall slenderness is increased (thinner walls). Consequently, the layup properties should be considered carefully in the ultimate strength design of thick open-section profiles, while they can be considered only in the serviceability limit (deflection) design of thin open-section profiles [115]. However, the interaction of the wall slenderness with the other geometric parameters and failure modes of box profile geometry was not studied in the available literature.

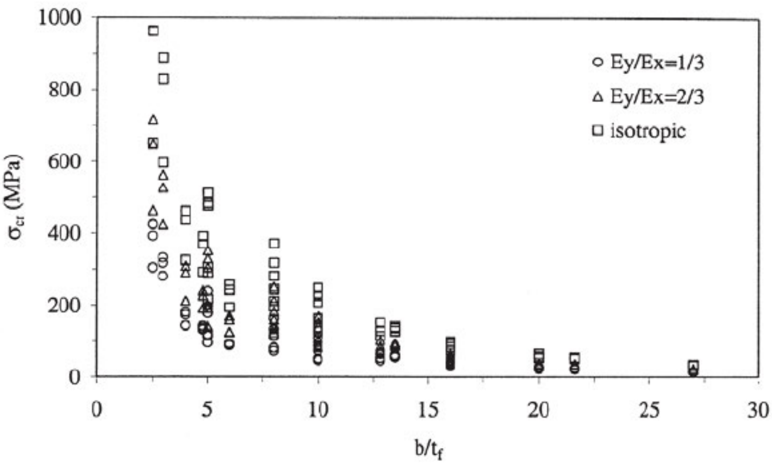

Figure 8. Critical buckling stresses versus the wall slenderness of I-shape PFRP profiles for different levels of orthotropy [81] (Ex and Ey are the longitudinal and transverse modulus, respectively).

When comparing the available data, the box profiles exhibited higher buckling capacity compared to the open-section profiles for the same wall slenderness range, as shown in Figure 9. This behaviour can be referred to the higher restraint and torsional rigidity provided on both sides of the wall of box profiles. It was noticed that the thick open-section profiles exhibited a low buckling-to-material strength ratio compared to their counterpart box profiles. Thus, local buckling can be counted as an inevitable failure mode for open-section profiles. On the contrary, local buckling can be avoided for the box profiles if the wall slenderness is slightly increased due to the higher buckling-to-material strength ratio and the available optimisation range. In other words, local buckling can be eliminated in the design for the manufacturing stage, allowing for the ultimate material strength to be used rather than considering the lower buckling strength in the structural design stage of box PFRP profiles. In addition, it was noticed that most of the open-section profiles were widely studied (larger number of references for the same wall slenderness) by experimental, theoretical, and numerical approaches to investigate the wall slenderness. On the contrary, the box profiles had fewer references for the same wall slenderness, which is a sign of few studies assessing the wall slenderness with various methodologies.

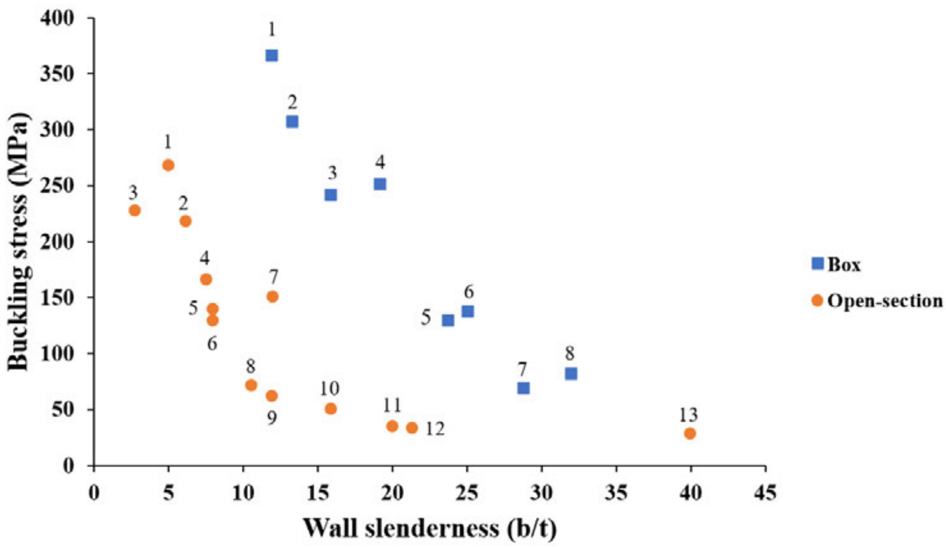

Figure 9. The studied range of wall slenderness for open-section versus box GFRP profiles (Box-shape: 1 [73,92,96], 2 [72], 3 [105], 4 [29,55,56,93,95,103], 5 [85,107], 6 [104], 7 [17], and 8 [75], Open-section: 1 [65,70], 2 [64,72], 3 [75], 4 [67], 5 [62,75,81,83,84,90], 6 [61,72,81,83,84,90,91], 7 [75,77,81,83,84], 8 [61,81,83,84,90], 9 [62,73,83–85,90,92], 10 [64,75], 11 [111], 12 [79], and 13 [109,110]).

Only one study was found to investigate the contribution of multiple design parameters on the local buckling behaviour of pulwound hollow square profiles [94]. The study was conducted on stub columns axially loaded using Taguchi (L9 array) design of experiment, as shown in Table 2 which shows the studied parameters and their levels.

Table 2. Parameters and levels investigated in Alsaadi 2019 [94] parametric study.

Profile Dimensions	Parameters	Level 1	Level 2	Level 3
Section (mm): 100 × 100	Wall thickness (mm)	5.2	6.4	7.8
Corner radius (mm): inner 4.8 and outer 10	Winding angle (degrees)	45	60	75
Height (mm): 500	Axial-to-wound fibre ratio (%)	80/20	70/30	60/40

The resulting compressive strength and stiffness were analysed statistically to rank the effect of these parameters using the signal-to-noise (SNR) ratio and to determine the contribution of each parameter using the analysis of variance (ANOVA). The wall thickness was the dominant parameter for load capacity with a contribution of 93.4%. The winding angle was the second parameter with 2.6% and the axial-to-wound fibre ratio was ranked third with 1.2%. Moreover, the effect of the wall slenderness on the boundary between local buckling and compressive failure of box profiles was reported in this study. The failure mode of the pulwound hollow square profile was estimated to change from local buckling to compressive failure at a wall thickness of 6.75 mm, as shown in Figure 10. However, the interactions between the studied parameters were not captured because of the Taguchi design of experiment limitation (using reduced not full factorial experiment matrix). No study was found to address the relative contributions and interactions of the wall slenderness and the other geometric parameters. Initiating such studies on the design parameters of pulwound box profiles can provide design guidelines and optimal design configurations with improved utilisation, weight, and cost characteristics.

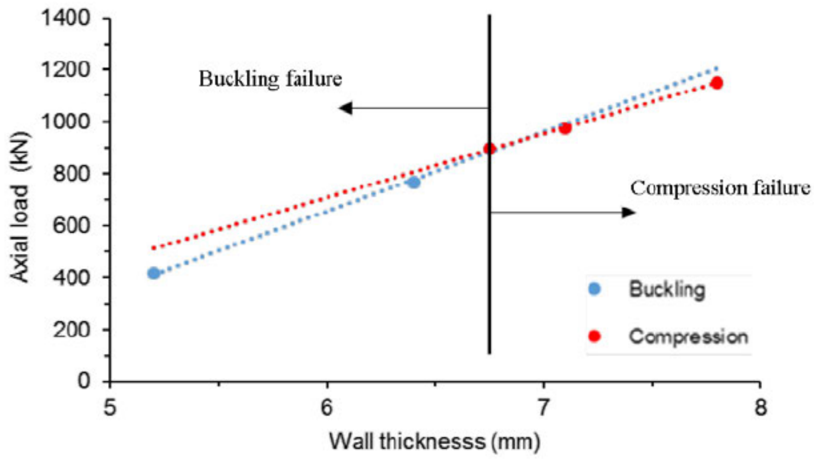

Figure 10. Effect of the wall thickness on the failure mode of pulwound box FRP profile [94].

3.2. Cross-Sectional Aspect Ratio

The cross-sectional aspect ratio (web height/flange width) defines the unsupported length of each wall and the major and minor axes of the cross-section. It affects the critical buckling load and stability of PFRP profiles [63] and alters their failure mode [186–188]. While maintaining a constant cross-sectional area, the flange and web buckling capacities were found to increase and decrease, respectively, when the cross-sectional aspect ratio is increased for both box [63] and open-section beams [172].

The significant effect of the cross-sectional aspect ratio was characterised under compression and bending for open-section profiles [59,86]. Increasing this ratio three times was found to decrease the buckling strength down to 42.8% under compression while it will increase the buckling strength up to 57.0% under bending. Moreover, the optimal cross-sectional aspect ratios of open-section PFRP profiles were investigated for column [65,109,111] and beam [65,82] applications. In addition, the interaction between the cross-sectional aspect ratio and the layup properties was studied for box [63] and I-shape [64] GFRP columns. The layup properties became insignificant when the flange width was increased and local buckling controlled it, as shown in Figure 11a,b, respectively.

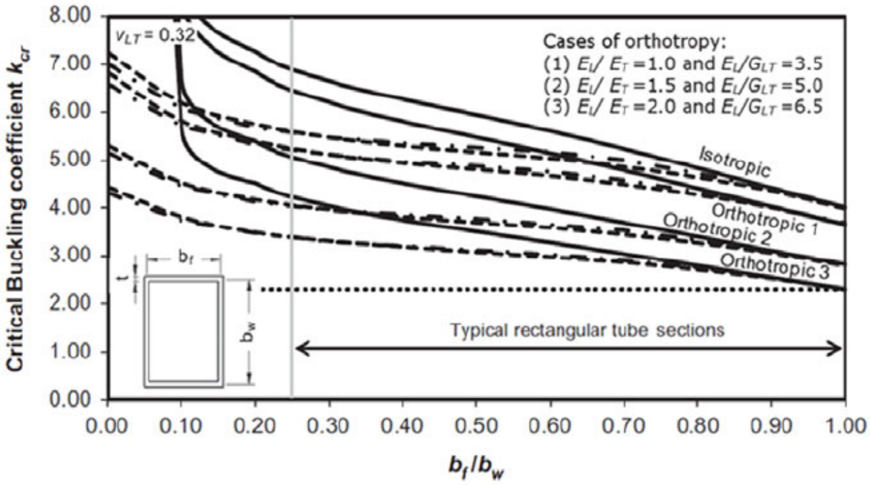

(a)

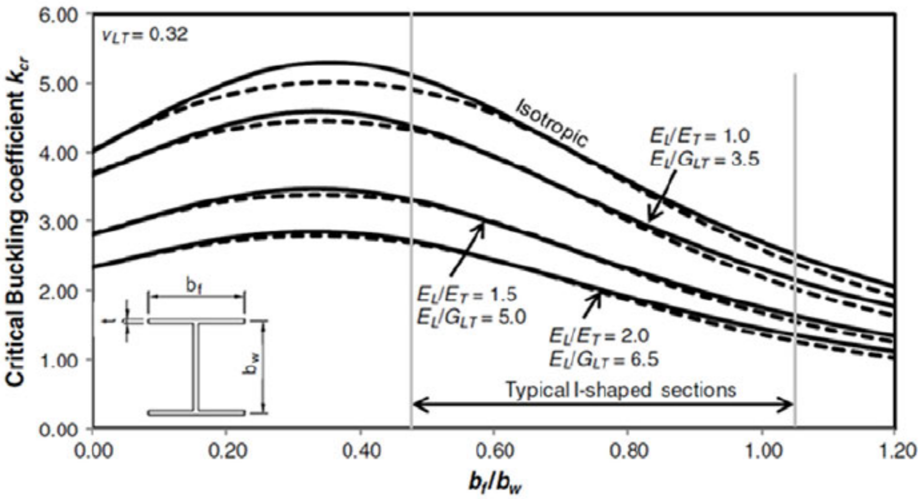

(b)

Figure 11. Buckling coefficient (k) versus b_f/b_w for different layup properties of (**a**) box [63] and (**b**) I-shape [64] GFRP columns.

Moreover, the interaction between compressive failure and local buckling failure modes was studied for box [96] and I-shape [69] GFRP columns. Figure 12 visualises this interaction for I-shape GFRP columns. The first stub column I_1 (narrow flange) showed an interactive failure mode between compressive crushing of fibres and local buckling of walls (buckling induced material crushing) since it has the lowest local slenderness. On the other hand, the second and third stub columns (I_2 and I_3, respectively) failed in local buckling with larger waviness in I_3 (wide flange). In addition, the boundaries between lateral buckling, web buckling, flange buckling, and interactive buckling failure modes of I-shape PFRP beams were investigated [74]. It was concluded that the interactive (local-lateral) distortional buckling is prominent over the other buckling types and should be considered in the design stage. The interaction of the failure modes influenced the layup properties as the optimal fibre angle was $\theta = \pm 45^{\circ}$ against local buckling and was $\theta = 60^{\circ} - 70^{\circ}$. against interactive buckling.

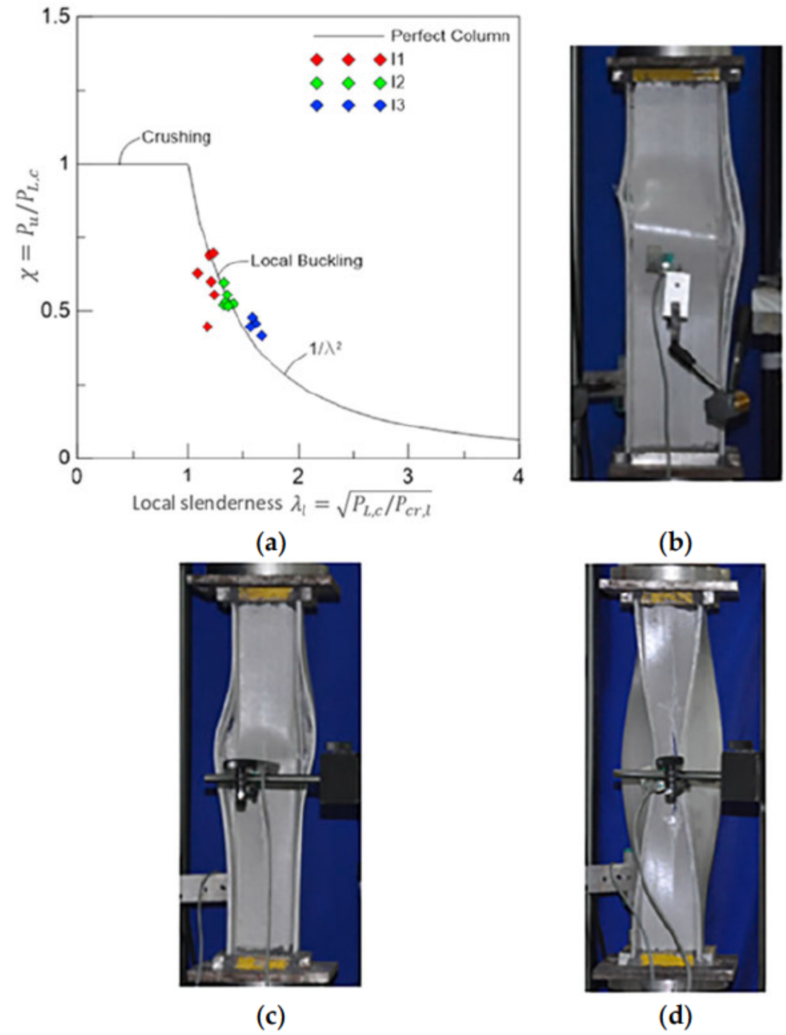

Figure 12. Interaction between local buckling and compressive failure of I-shape PFRP columns with different cross-sectional aspect ratios: (**a**) strength curve with experimental points (P_u: the ultimate compressive load, $P_{L,C}$: the experimental buckling load, and $P_{cr,l}$: the critical buckling load); (**b**) experimental failure mode of I_1 ($b_f/d = 0.5$); (**c**) experimental failure mode of I_2 ($b_f/d = 0.75$); and (**d**) experimental failure mode of I_3 ($b_f/d = 1.0$) [69].

Regarding the box profile geometry, the axial buckling capacity of walls in hollow square beams was reported to be higher than for hollow rectangular beams due to the higher buckling tendency at the weakest direction in the rectangular cross-section [58]. Nevertheless, the overall buckling moment of the beam under bending increases when the cross-sectional aspect ratio is increased since the wall slenderness of the top flange, which carries the majority of the compressive stresses, is decreased [106]. One study was found to examine the interaction between the walls of CFRP box beams [54]. It was reported that webs with a smaller slenderness ratio obtain a higher buckling capacity of the flange due to the higher rotational restraint provided by the thicker webs to the flange. Another study was found investigating the boundary of failure modes of box GFRP beam in terms of the cross-sectional aspect ratio [108]. The effect of the cross-sectional aspect ratio on the buckling of the top flange (spar cap) was significant compared to its effect on the shear web. This was referred to the higher compressive stresses acting on the top flange, which made its buckling load more sensitive to the change of dimensions. The optimal buckling capacity was obtained at the inflection point of the flange buckling and web buckling failure modes, which is denoted by the "○" symbol in Figure 13. This point represents the best cross-sectional aspect ratio for maximum buckling capacity and minimum material usage of the beam.

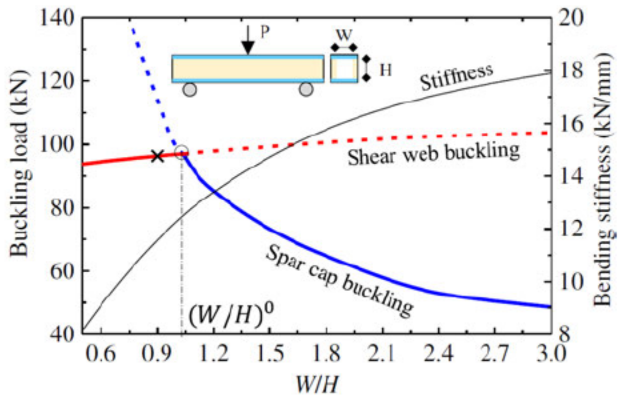

Figure 13. Buckling mode map of GFRP composite box beam with different cross-sectional aspect ratios, where the spar cap is the flange, ×is the baseline design, and O is the desired design [108].

Rectangular box profiles (with web height/flange width ≥ 1.5) were found to exhibit a post-buckling trend in their load-displacement curves under compression loading [17]. Figure 14 compares the load-displacement curves of hollow square and rectangular PFRP profiles subjected to axial compression. The hollow square profile exhibited linear elastic behaviour until the peak (buckling) point, then failed. On the other hand, the hollow rectangular profile showed a linear elastic behaviour until the buckling point of the wider walls then the structural stiffness was degraded due to the loss of stability of the wider walls and the load capacity increased under a new equilibrium path until failure occurred. Although the cross-sectional area of the rectangular profile is 26.9% higher than for the square profile, its buckling strength was 54.7% less than the square profile due to the higher wall slenderness of the wide walls, which caused earlier buckling and suppressed the profile potentials. However, no study was found to address the interactions between the cross-sectional aspect ratio and the other geometric parameters, or the effect of the interaction between the flange and webs on the stability and overall structural behaviour of pulwound box PFRP profiles. Such studies can provide optimal design configurations and better design guidelines as the current design formulas are conservative and consider only the wall with the maximum slenderness ratio for buckling capacity estimation and do not include the interaction between the flange and the webs and their corner radius.

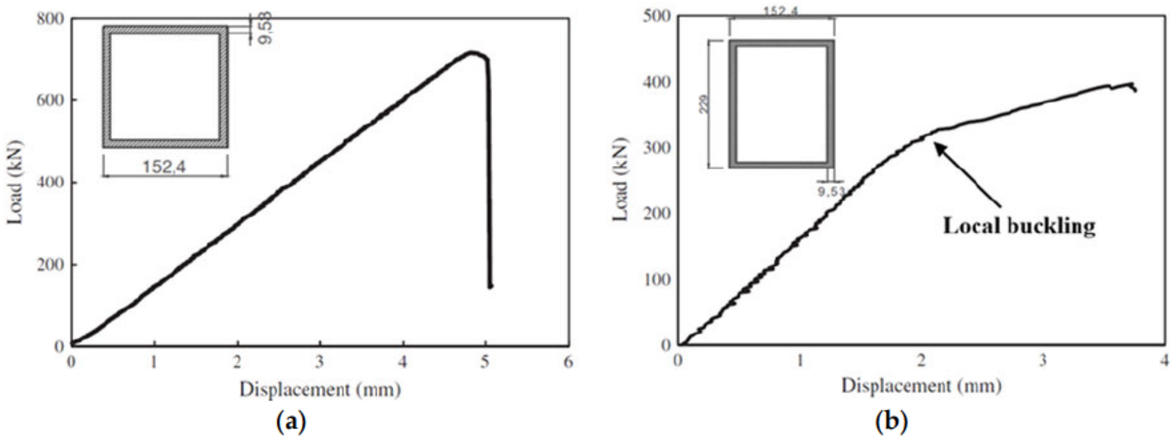

Figure 14. Load-displacement curves of hollow (a) square and (b) rectangular box PFRP profiles under axial compression [17].

3.3. Corner Geometry

The corner (flange-web junction) geometry of PFRP profiles is a critical manufacturing parameter affecting the production process, the pulling force, and the heated die settings. It is considered to be a weak point of premature failure due to stresses concentration at this critical zone [189–191]. It is recommended to increase the inner corner radius (fillet) to prevent cracking by uniformly distributing the stresses and preventing their concentration [192], as shown in Figure 15. Increasing the outer corner radius to be equal to the inner radius plus the wall thickness can also facilitate the production process and help to avoid thermal-induced cracks [192].

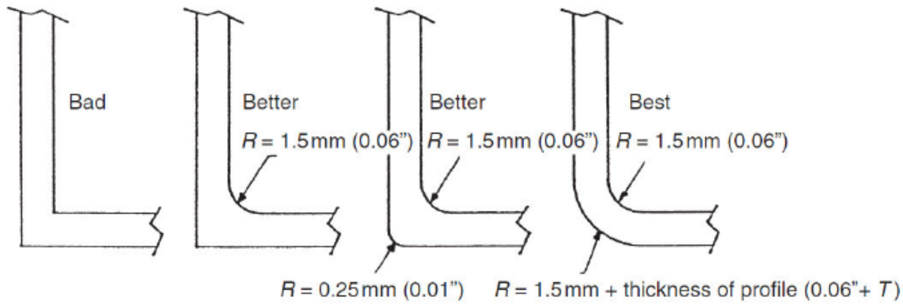

Figure 15. Recommended configurations of the corner of PFRP profiles [192].

One study was found to experimentally characterise the structural behaviour of the corner of commercial box GFRP beams with longitudinal glass rovings and continuous strand mat (CSM) layups [101]. Microscopic photos were taken to diagnose any resin-rich zones and fibre wrinkling, as shown in Figure 16a,b. Although these manufacturing defects were distributed along the walls, the failure of box GFRP beams initiated at the corners due to the discontinuity in fibres and stresses concentration was noticed, as shown in Figure 16c. It was recommended that the steep change in the inner corner geometry could be changed from right angle to fillet in order to uniformly distribute the stress between the walls.

Regarding the local buckling behaviour, the corners (initial radius 2.38 mm) of open-section (I-shape) PFRP beams were enhanced by bonding polyester pultruded equal leg angles (38 mm × 38 mm × 6.4 mm) or hand-layup fillets (38 mm) on the top corner [61], as shown in Figure 17. In both cases, the load capacity was significantly enhanced by 1.5 times due to the increased geometry, which enhanced the rotational stiffness and strength of the corners and allowed for uniform distribution of stresses. The failure mode was shifted from buckling of the top flange to compressive failure of fibres with the ultimate material strength fully utilised. In another study, CFRP layers and GFRP stiffening plates were used to strengthen the corners of I-shape beams to increase their buckling capacity [89]. This approach was proven to be very effective in preventing local buckling of the flange and enhancing the flange-web junction and the flexural strength of the beams. In these two studies, the fillet geometry exhibited a better effect than angles and plates due to the lower stresses concentration caused by their uniform change of geometry compared to the sudden change in the cross-section of the beam caused by the angles and plates.

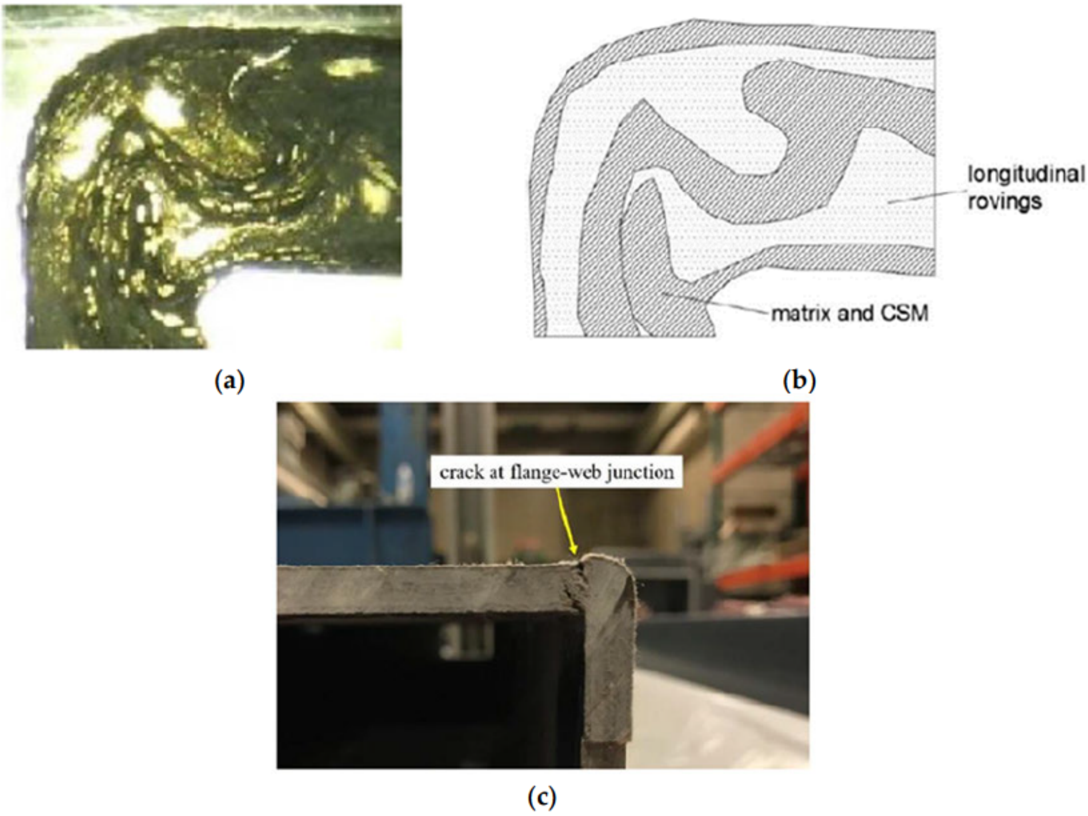

Figure 16. Flange-web junction of hollow box pultruded GFRP beam (102 mm × 152 mm × 6.4 mm): (**a**) image of fibre and matrix architecture, (**b**) schematic of fibre and matrix architecture, and (**c**) crack at the flange-web junction under bending [101].

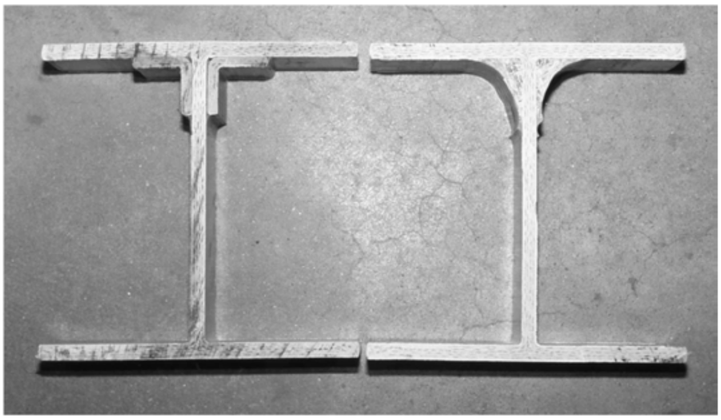

Figure 17. Corners of I-shape PFRP beam (203 mm × 203 mm × 9.5 mm, radius 2.38 mm) enhanced by (left side) polyester pultruded equal leg angles (38 mm × 38 mm × 6.4 mm) and (right side) hand-layup fillets (38 mm) on the top corners [61].

However, no study was found to address the inner and outer corner radii effect as manufacturing parameters on the local buckling capacity of PFRP profiles. In addition, no study was found to address the corner geometry effect on local buckling of box PFRP profiles. Moreover, the effect and interaction of the layup properties on the corner radii have not been studied for box profiles since most of the reported investigations on the layup parameters considered laminated plate geometry. In addition, the effect of continuous confinement provided by the wound fibres around the corners in pulwound box profiles has not been reported. Currently, standards and design manuals do not include the corner radius as a design parameter in their equations and structural designs. Moreover, the corner geometry (e.g., inner-to-outer radii ratio) needs to be investigated to reflect its contribution to the local buckling capacity in the related design equations. Consequently, understanding the corner geometry role as a design parameter for local buckling will lead to more stable designs of box PFRP profiles with enhanced load capacity and the avoidance of buckling failure.

4. Layup Parameters of Hollow Box PFRP Profiles

The layup properties define the anisotropy and mechanical properties of FRP profiles in the longitudinal and transverse directions and directly affect their local buckling behaviour [193]. These properties should be designed depending on the intended application since the design will address a specific geometry and loading condition and cannot be generalised for all composite structures [143,194]. The layup parameters of local buckling are discussed in the following sections by summarising their effects, comparing them for different geometries, and highlighting the available literature on their interactions.

4.1. Axial-to-Inclined Fibre Ratio

For civil structural applications, the layup of PFRP profiles consists of longitudinal fibre rovings to obtain the required axial and flexural stiffness and off-axis (inclined) fibres to enhance the shear and transverse properties [42,195]. The ratio of these axial-to-inclined fibres shapes the anisotropy and mechanical properties of the laminated walls to achieve the required axial and flexural stiffness and the desired shear and transverse properties. In general, it is recommended to add inclined fibres along with the axial plies to enhance the off-axis mechanical properties, damage tolerance, and stability of laminated plates [196,197]. These inclined fibres are also needed to fulfil the web stiffness and strength requirements of PFRP beams [198,199].

Regarding the geometry effect on this ratio, it was found that increasing the axial fibre percentage will increase axial buckling resistance of laminated plates [123]. On the contrary, increasing the inclined fibre percentage will increase the local buckling strength of open-section FRP columns due to the higher rotational rigidity between the orthogonal walls [200]. No study was found on the interaction between the axial-to-inclined fibre ratio and the other layup properties or on its effect on the geometric parameters of pulwound box FRP profiles.

4.2. Inclined Fibre Angle

In classical laminated plate theory (CLPT), FRP composite plates with angle-ply ($[\pm\theta]_S$) layup exhibit the maximum local buckling capacity at a fibre angle (θ) of $\pm 45^{\circ}$ since it obtains the highest bending-extension stiffness parameters (Dij) [153,201]. However, axial fibre rovings must be added to meet the axial and flexural stiffness requirements for civil structural applications. Moreover, it was proven that introducing new fibre angles apart from the traditional 0°, $\pm 45^{\circ}$, and 90° angles can also provide improved designs for local buckling of different geometries and loading conditions [147]. The contribution of the fibre angle on the buckling capacity was found to be significant for certain geometries. For instance, small fibre misalignments, such as $\pm 2^{\circ}$, were noticed to affect the buckling capacity of GFRP tubes up to 7.8% [161].

The optimal fibre angle to obtain the maximum buckling capacity is a function of the geometry, boundary condition, and loading condition [133,143,194]. Under flexural loading, it was found that increasing the web orthotropy exhibits the highest increase in the buckling capacity of the flange due to the increase in the rotational restraint at the flange-web junction. Moreover, the increase in the flange buckling capacity is higher when its orthotropy is low [54]. For open-section FRP beams, the buckling load was found to decrease when the fibre angle is increased [58].

Moreover, the interaction between the fibre angle and the stacking sequence was found to be significant and may shift the optimal fibre angle depending on the geometry and boundary and loading conditions [149,168]. For instance, antisymmetric laminated plates require a fibre angle of 25° to obtain the maximum buckling load unlike symmetric laminates [157]. Even for symmetric layups, the optimal fibre angle for maximum buckling of GFRP cylindrical shells changes depending on the introduction or removal of axial fibres [167], as shown in Figure 18. Stacking the inclined plies at the outer side to confine the axial fibres enhances the buckling capacity. Regarding the pulwound FRP profiles, no study was found to investigate the winding angle effect on the corner geometry or its interactions with the other layup parameters under compression or bending. Assessing the contribution of this parameter on the buckling resistance of pulwound box PFRP profiles will alleviate the lack of knowledge for this special shape.

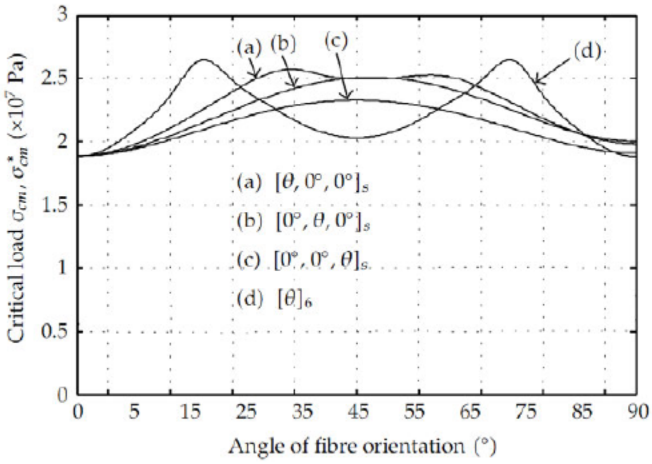

Figure 18. Critical buckling load versus varying inclined fibre orientation for different stacking sequences in GFRP cylindrical shells [167].

4.3. Stacking Sequence

The stacking sequence of laminated composites affects their stability, deflection response, interlaminar stresses, post-buckling behaviour, and progressive failure [202–204]. Its optimal configuration to resist local buckling depends on the geometry and boundary and loading conditions and has to be determined specifically for the intended application [138,205]. In general, stacking the inclined plies to the outer surface of a laminated plate enhances the local buckling resistance under axial compression due to the increase in confinement [162,206]. On the contrary, stacking the axial fibres to the outer surface increases the plate buckling resistance against transverse compression [207]. A compromise between the buckling capacity and other mechanical properties should be considered in the design since stacking axial fibres at the outer surface exhibits higher tensile and flexural moduli [208]. In general, stacking sequences with elastic coupling are not preferred for compressively loaded members as they are vulnerable to manufacturing imperfections, buckling, bending, and warping due to thermal effects [120,196,207]. Thus, symmetric and balanced layups are usually used to minimise the coupling effects. For simply supported laminated plates, the interaction between the stacking sequence and fibre angle was found to be significant at $\theta = 45^{\circ}$ [209], as shown in Figure 19. The minimum buckling load was obtained when the $-\theta$ plies were outmost from the mid-plane due to the maximum effect of bending-twisting coupling (maximum value of $D_{16} + D_{26}$). The reduction in the buckling load for this case reached its peak at $\theta = 45^{\circ}$ with a 25% drop in load from the optimal case ($[+\theta/-\theta/-\theta/+\theta]_S$).

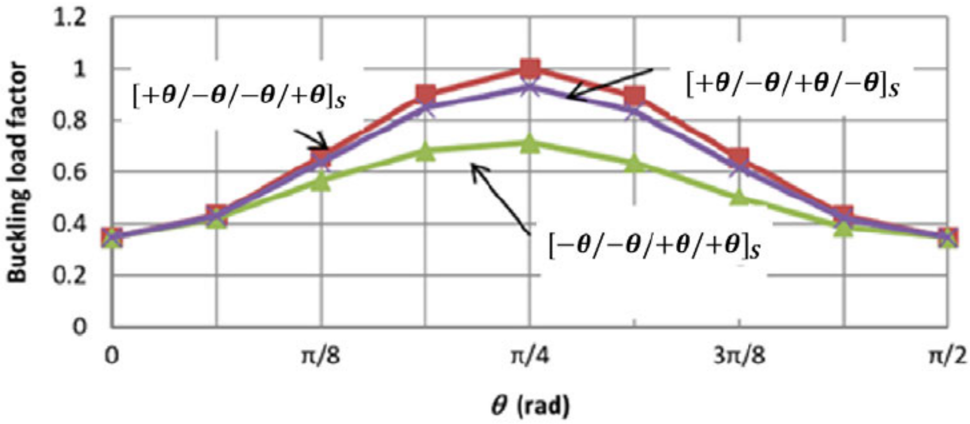

Figure 19. Effect of fibre angle on the buckling load of simply supported laminated plate with symmetric stacking sequences [209].

Regarding the geometry effect, the stacking sequence was found to affect the boundaries of different failure modes of CFRP composite cylindrical shells [160], as shown in Figure 20. Reducing the shape factor (radius/thickness) shifts the failure mode from local buckling towards compressive failure. The 0° laminate possesses the maximum axial compressive strength and the largest local buckling failure zone because of the axial direction of the fibres and the minimum circumferential confinement (maximum out-of-plane waviness), respectively. Conversely, the 90° laminate exhibits the minimum axial compressive strength and the smallest local buckling failure zone because of the transverse direction of the fibres and the maximum circumferential confinement (minimum out-of-plane waviness), respectively. The $[55/-55/0_6]_S$ laminate presents the optimal compromise against both local and global buckling. On the contrary, angle-ply laminates with $\pm$ 25° and $\pm$ 90° plies possess the highest local buckling strength for CFRP cylindrical shells with geometric imperfections [159]. When comparing cross-ply and angle-ply layups for laminated plates under uniaxial compression, cross-ply layups exhibited optimal buckling resistance [138,183] while for cylindrical shells angle-ply is better [155]. For open-section profiles, angle-ply laminates obtained a higher buckling load than quasi-isotropic laminates [113]. The buckling capacity of these profiles was decreasing when the fibre angle was increased and the cross-ply laminates were observed to sustain a larger buckling load than angle-ply when the fibre angle is larger than 30° [58,80]. It was found that the effect of the stacking sequence on the buckling capacity of laminated plates decreases as their dimensions are increased [128] but it becomes significant in open-section structural-level columns with slender walls [140]. No study was found on the effect of stacking continuous wound fibres with different sequences on the corner geometry of pulwound box PFRP profiles, or on the interaction between the stacking sequence and other layup parameters in such profiles.

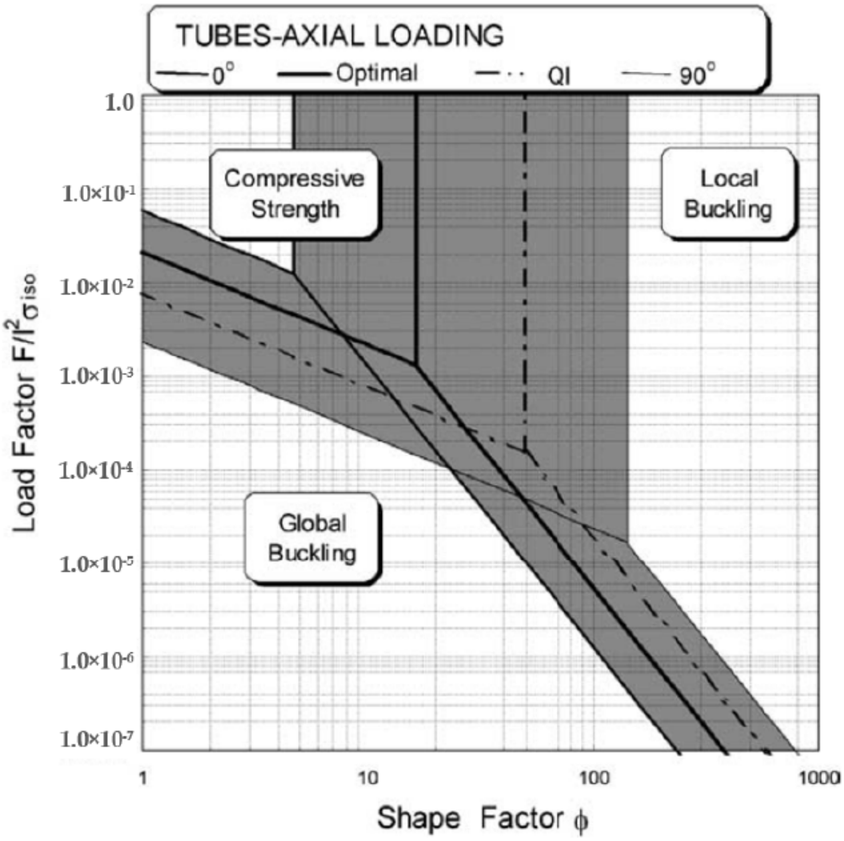

Figure 20. Failure chart of CFRP composite cylindrical shells as a function of the shape factor (wall slenderness = radius/thickness) and stacking sequence (0°: axial fibre layup, 90°: transverse fibre layup, QI: quasi-isotropic layup, and optimal: $[55/-55/0_6]_S$) [160].

5. Conclusions

Hollow box PFRP profiles are increasingly used as structural elements in civil structural applications. Although the studies and the standards were developed to facilitate the design process of PFRP profiles, there is still a lack of knowledge regarding the local buckling design parameters (layup and geometry) for box profile geometry. This presents an issue in designing these profiles and fully using their potentials, evident by the limited range of specifications in the available commercial profiles. This article presents a literature review on the local buckling design parameters controlling the structural behaviour of box PFRP profiles. Although most of these parameters were studied individually, there is still a need to perform a comprehensive study to obtain their contribution and interaction, which will provide practical design guidelines and recommended configurations of the design parameters. This review on the design parameters of PFRP profiles outlines the current state of knowledge and the investigations to be conducted. Thus, it provides a useful reference to researchers and design engineers. Furthermore, it presents a benchmark for the next generation of design guidelines, which will broaden the use of PFRP in construction by eliminating the current difficulties in PFRP profiles design. Based on this review, the current state of knowledge and future trends for optimising these profiles and their design parameters are summarised as follows:

- Hollow box PFRP profiles are featured with higher structural stability and torsional rigidity compared to the open-section profiles due to the restraint at both ends of the wall and its unique stresses distribution. However, their design parameters have not been studied comprehensively as for open-section and laminated plate geometries. While local buckling is inevitable for open-section profiles, it can be avoided for box profiles if the wall slenderness is optimised due to the high buckling-to-material strength ratio and the available optimisation range. This will allow the design to consider the ultimate material strength rather than considering the lower buckling strength.

- The flange-web junction (corner) radius and its effect on the local buckling of hollow box PFRP profiles have not been studied or quantified even though its effect was significant on the buckling behaviour and failure mode of open-section profiles. Moreover, the interaction between the layup properties or the flange-web slenderness and the corner geometry has not been studied for box profile geometry. In addition, the effect of continuous confinement provided by the wound fibres around the corners in pulwound box profiles has not been reported. The corner (fillet) radius is not included in the analysis and design equations of box PFRP profiles. No study was found to address the inner and outer corner radii effect on the local buckling capacity as manufacturing parameters of PFRP profiles.
- Pulwound box FRP profiles were recently introduced for infrastructure applications with better transverse and circumferential properties. However, studies are still needed to comprehensively address all the critical design parameters controlling the local buckling of these profiles and quantify their relative contributions and interactions. Considering these interactions can facilitate economic structural designs and guidelines for these profiles, eliminate any conservative assumptions, and update the current design standards and manuals. Understanding the contributions and interactions of these parameters will broaden the use of these profiles with competitive structural performance and cost versus the conventional construction materials.
- As with the other structural shapes, there is a need to construct design curves and failure maps for hollow box PFRP profiles, considering the interactions and showing the shift in the failure modes in terms of the critical design parameters. Investigating these review findings, especially the importance of the interactions, will enhance the current design guidelines, facilitate economic and competitive designs, and manufacture optimised profiles for civil structural applications.

Author Contributions: M.A.: Conceptualisation, methodology, software, data curation, writing—original draft preparation. O.A., T.A., T.S., P.S., A.M., and X.Z.: Supervision, writing—reviewing and editing. All authors have read and agreed to the published version of the manuscript.

Funding: The work was funded through a Cooperative Research Centres Projects (CRC-P) Grant (CRCPSIX000117).

Institutional Review Board Statement: Not applicable.

Informed Consent Statement: Not applicable.

Data Availability Statement: The data presented in this study are available on request from the corresponding author.

Acknowledgments: The authors wish to thank the support from the University of Southern Queensland and Wagners CFT.

Conflicts of Interest: The authors declare that there is no conflict of interest, and they have no known competing financial interests or personal relationships that could have appeared to influence the work reported in this paper.

References

1. Boisse, P. *Advances in Composites Manufacturing and Process Design*; Woodhead Publishing: Sawston, UK, 2015.
2. Hoa, S.V. *Principles of the Manufacturing of Composite Materials*; DEStech Publications, Inc.: Lancaster, PA, USA, 2009.
3. Ahn, N.; Lee, J.; Lee, K.; Jang, H.S. An experimental study on flexural behavior for a FRP composite girder. *Constr. Build. Mater.* **2014**, *50*, 13–21. [CrossRef]
4. Johnston, J.; Mirza, O.; Kemp, M.; Gates, T. Flexural behaviour of alternate transom using composite fibre pultruded sections. *Eng. Fail. Anal.* **2018**, *94*, 47–68. [CrossRef]
5. Muttashar, M.; Karunasena, W.; Manalo, A.; Lokuge, W. Behavior of pultruded multi-celled GFRP hollow beams with low-strength concrete infill. In *Mechanics of Structures and Materials XXIV: Proceedings of the 24th Australian Conference on the Mechanics of Structures and Materials, ACMSM24, Perth, Australia, 6–9 December 2016*; CRC Press: Boca Raton, FL, USA, 2019; p. 243.

6. Friberg, E.; Olsson, J. Application of Fibre Reinforced Polymer Materials in Road Bridges—General Requirements and Design Considerations. Master's Thesis, Chalmers University of Technology, Gothenburg, Sweden, 2014.
7. Li, Y.-F.; Hsu, T.-H.; Hsieh, F.-C. A Study on Improving the Mechanical Behaviors of the Pultruded GFRP Composite Material Members. *Sustainability* **2019**, *11*, 577. [CrossRef]
8. Satasivam, S.; Bai, Y. Mechanical performance of bolted modular GFRP composite sandwich structures using standard and blind bolts. *Compos. Struct.* **2014**, *117*, 59–70. [CrossRef]
9. Xin, H.; Mosallam, A.; Liu, Y.; Xiao, Y.; He, J.; Wang, C.; Jiang, Z. Experimental and numerical investigation on in-plane compression and shear performance of a pultruded GFRP composite bridge deck. *Compos. Struct.* **2017**, *180*, 914–932. [CrossRef]
10. Hizam, R.M.; Manalo, A.C.; Karunasena, W.; Bai, Y. Behaviour of pultruded GFRP truss system connected using through-bolt with mechanical insert. *Compos. Part B Eng.* **2019**, *168*, 44–57. [CrossRef]
11. Kumar, P.; Chandrashekhara, K.; Nanni, A. Testing and evaluation of components for a composite bridge deck. *J. Reinf. Plast. Compos.* **2003**, *22*, 441–461. [CrossRef]
12. Mottram, J.T.; Henderson, J. *Fibre-Reinforced Polymer Bridges—Guidance for Designers*; CIRIA: London, UK, 2018.
13. Cricrì, G.; Perrella, M. Investigation of mode III fracture behaviour in bonded pultruded GFRP composite joints. *Compos. Part B Eng.* **2017**, *112*, 176–184. [CrossRef]
14. Garrido, M.; Madeira, J.F.A.; Proença, M.; Correia, J.R. Multi-objective optimization of pultruded composite sandwich panels for building floor rehabilitation. *Constr. Build. Mater.* **2019**, *198*, 465–478. [CrossRef]
15. Vedernikov, A.; Safonov, A.; Tucci, F.; Carlone, P.; Akhatov, I. Pultruded materials and structures: A review. *J. Compos. Mater.* **2020**, *54*, 4081–4117. [CrossRef]
16. Fangueiro, R. *Fibrous and Composite Materials for Civil Engineering Applications*; Elsevier: Amsterdam, The Netherlands, 2011.
17. Godat, A.; Légeron, F.; Gagné, V.; Marmion, B. Use of FRP pultruded members for electricity transmission towers. *Compos. Struct.* **2013**, *105*, 408–421. [CrossRef]
18. Balasubramanian, M. *Composite Materials and Processing*; CRC Press: Boca Raton, FL, USA, 2013.
19. Gajjar, D. Development of applications and innovation of FRP Pultruded Profiles in India & Asia. In Proceedings of the Fifteenth World Pultrusion Conference, Antwerp, Belgium, 27–28 February 2020.
20. Bakis, C.E.; Bank, L.C.; Brown, V.; Cosenza, E.; Davalos, J.F.; Lesko, J.J.; Machida, A.; Rizkalla, S.H.; Triantafillou, T.C. Fiber-reinforced polymer composites for construction—State-of-the-art review. *J. Compos. Constr.* **2002**, *6*, 73–87. [CrossRef]
21. Kaw, A.K. *Mechanics of Composite Materials*; CRC Press: Boca Raton, FL, USA, 2005.
22. Bunsell, A.R.; Renard, J. *Fundamentals of Fibre Reinforced Composite Materials*; CRC Press: Boca Raton, FL, USA, 2005.
23. Van Den Einde, L.; Zhao, L.; Seible, F. Use of FRP composites in civil structural applications. *Constr. Build. Mater.* **2003**, *17*, 389–403. [CrossRef]
24. Bank, L.C. *Composites for Construction: Structural Design with FRP Materials*; John Wiley & Sons: Hoboken, NJ, USA, 2006.
25. Guades, E.; Aravinthan, T.; Islam, M.; Manalo, A. A review on the driving performance of FRP composite piles. *Compos. Struct.* **2012**, *94*, 1932–1942. [CrossRef]
26. Parke, G.A.; Hewson, N. *ICE Manual of Bridge Engineering*; Thomas Telford: London, UK, 2008.
27. Sapuan, S.M. *Composite Materials: Concurrent Engineering Approach*; Butterworth-Heinemann: Oxford, UK, 2017.
28. Vinson, J.R.; Sierakowski, R.L. *The Behavior of Structures Composed of Composite Materials*; Springer: Berlin/Heidelberg, Germany, 2006.
29. Al-saadi, A.U.; Aravinthan, T.; Lokuge, W. Effects of fibre orientation and layup on the mechanical properties of the pultruded glass fibre reinforced polymer tubes. *Eng. Struct.* **2019**, *198*, 109448. [CrossRef]
30. Daniel, I.M.; Ishai, O. *Engineering Mechanics of Composite Materials*; Oxford University Press: Oxford, UK, 2006.
31. Nikbakt, S.; Kamarian, S.; Shakeri, M. A review on optimization of composite structures Part I: Laminated composites. *Compos. Struct.* **2018**, *195*, 158–185. [CrossRef]
32. Najafi, A.; Rais-Rohani, M. Concurrent Process-Product Design Optimization Using Coupled Nonlinear Finite-Element Simulations. *Finite Elem. Anal. Appl. Mech. Eng.* **2012**, *10*, 47852. [CrossRef]
33. Rammerstorfer, F.G. *Engineering Mechanics of Fibre Reinforced Polymers and Composite Structures*; Springer: Berlin/Heidelberg, Germany, 1994.
34. Awad, Z.K.; Aravinthan, T.; Zhuge, Y.; Gonzalez, F. A review of optimization techniques used in the design of fibre composite structures for civil engineering applications. *Mater. Des.* **2012**, *33*, 534–544. [CrossRef]
35. Wang, Z.; Sobey, A. A comparative review between Genetic Algorithm use in composite optimisation and the state-of-the-art in evolutionary computation. *Compos. Struct.* **2020**, *233*, 111739. [CrossRef]
36. Chen, W.-F.; Duan, L. (Eds.) *Bridge Engineering Handbook: Fundamentals*, 2nd ed.; CRC Press: Boca Raton, FL, USA, 2014.
37. Jones, R.M. *Mechanics of Composite Materials*; CRC Press: Boca Raton, FL, USA, 1998.
38. Sadeghifar, M.; Bagheri, M.; Jafari, A.A. Multiobjective optimization of orthogonally stiffened cylindrical shells for minimum weight and maximum axial buckling load. *Thin-Walled Struct.* **2010**, *48*, 979–988. [CrossRef]
39. Gand, A.K.; Chan, T.-M.; Mottram, J.T. Civil and structural engineering applications, recent trends, research and developments on pultruded fiber reinforced polymer closed sections: A review. *Front. Struct. Civ. Eng.* **2013**, *7*, 227–244. [CrossRef]
40. Liu, D.; Bai, R.; Wang, R.; Lei, Z.; Yan, C. Experimental study on compressive buckling behavior of J-stiffened composite panels. *Opt. Lasers Eng.* **2019**, *120*, 31–39. [CrossRef]

41. Matthews, F.L.; Davies, G.A.O.; Hitchings, D.; Soutis, C. *Finite Element Modelling of Composite Materials and Structures*; Elsevier: Amsterdam, The Netherlands, 2000.
42. Wu, H. *Advanced Civil Infrastructure Materials: Science, Mechanics and Applications*; Woodhead Publishing: Sawston, UK, 2006.
43. Turvey, G.J.; Marshall, I.H. *Buckling and Postbuckling of Composite Plates*; Springer Science & Business Media: Berlin/Heidelberg, Germany, 1995.
44. Wang, X.; Lu, G. Local buckling of composite laminar plates with various delaminated shapes. *Thin-Walled Struct.* **2003**, *41*, 493–506. [CrossRef]
45. Attaf, B. *Advances in Composite Materials: Ecodesign and Analysis*; BoD—Books on Demand: Norderstedt, Germany, 2011.
46. Gay, D. *Composite Materials: Design and Applications*, 3rd ed.; CRC Press: Boca Raton, FL, USA, 2014. [CrossRef]
47. Vasiliev, V.V.; Morozov, E.V. *Advanced Mechanics of Composite Materials and Structures*; Elsevier: Amsterdam, The Netherlands, 2018.
48. Brigante, D. *New Composite Materials: Selection, Design, and Application*; Springer Science & Business Media: Berlin/Heidelberg, Germany, 2013.
49. Han, H.; Taheri, F.; Pegg, N.; Lu, Y. A numerical study on the axial crushing response of hybrid pultruded and ±45° braided tubes. *Compos. Struct.* **2007**, *80*, 253–264. [CrossRef]
50. Han, H.; Taheri, F.; Pegg, N. Crushing Behaviors and Energy Absorption Efficiency of Hybrid Pultruded and ±45° Braided Tubes. *Mech. Adv. Mater. Struct.* **2011**, *18*, 287–300. [CrossRef]
51. Wang, W.; Sheikh, M.N.; Hadi, M.N.S. Behaviour of perforated GFRP tubes under axial compression. *Thin-Walled Struct.* **2015**, *95*, 88–100. [CrossRef]
52. Bank, L.C.; Nadipelli, M.; Gentry, T.R. Local Buckling and Failure of Pultruded Fiber-Reinforced Plastic Beams. *J. Eng. Mater. Technol.* **1994**, *116*, 233–237. [CrossRef]
53. Barbero, E.J.; Raftoyiannis, I.G. Local Buckling of FRP Beams and Columns. *J. Mater. Civ. Eng.* **1993**, *5*, 339–355. [CrossRef]
54. Kasiviswanathan, M.; Upadhyay, A. Flange buckling behaviour of FRP box-beams: A parametric study. *J. Reinf. Plast. Compos.* **2018**, *37*, 105–117. [CrossRef]
55. Guades, E.; Aravinthan, T.; Islam, M.M. Characterisation of the mechanical properties of pultruded fibre-reinforced polymer tube. *Mater. Des.* **2014**, *63*, 305–315. [CrossRef]
56. Muttashar, M.; Karunasena, W.; Manalo, A.; Lokuge, W. Behaviour of hollow pultruded GFRP square beams with different shear span-to-depth ratios. *J. Compos. Mater.* **2016**, *50*, 2925–2940. [CrossRef]
57. Yang, J.-Q.; Liu, T.; Feng, P. Enhancing flange local buckling strength of pultruded GFRP open-section beams. *Compos. Struct.* **2020**, *244*, 112313. [CrossRef]
58. Asadi, A.; Sheikh, A.H.; Thomsen, O.T. Buckling behaviour of thin-walled laminated composite beams having open and closed sections subjected to axial and end moment loading. *Thin-Walled Struct.* **2019**, *141*, 85–96. [CrossRef]
59. Ascione, L.; Berardi, V.P.; Giordano, A.; Spadea, S. Local buckling behavior of FRP thin-walled beams: A mechanical model. *Compos. Struct.* **2013**, *98*, 111–120. [CrossRef]
60. Ascione, F.; Feo, L.; Lamberti, M.; Minghini, F.; Tullini, N. A closed-form equation for the local buckling moment of pultruded FRP I-beams in major-axis bending. *Compos. Part B Eng.* **2016**, *97*, 292–299. [CrossRef]
61. Bank, L.C.; Gentry, T.R.; Nadipelli, M. Local Buckling of Pultruded FRP Beams-Analysis and Design. *J. Reinf. Plast. Compos.* **1996**, *15*, 283–294. [CrossRef]
62. Barbero, E.; Tomblin, J. A phenomenological design equation for FRP columns with interaction between local and global buckling. *Thin-Walled Struct.* **1994**, *18*, 117–131. [CrossRef]
63. Cardoso, D.C.T.; Harries, K.A.; Batista, E.d.M. Closed-form equations for compressive local buckling of pultruded thin-walled sections. *Thin-Walled Struct.* **2014**, *79*, 16–22. [CrossRef]
64. Cardoso, D.C.T.; Harries, K.A.; Batista, E.d.M. Compressive Local Buckling of Pultruded GFRP I-Sections: Development and Numerical/Experimental Evaluation of an Explicit Equation. *J. Compos. Constr.* **2015**, *19*, 04014042. [CrossRef]
65. Cardoso, D.C.T.; Vieira, J.D. Comprehensive local buckling equations for FRP I-sections in pure bending or compression. *Compos. Struct.* **2017**, *182*, 301–310. [CrossRef]
66. Chawla, H.; Singh, S.B. Stability and failure characterization of fiber reinforced pultruded beams with different stiffening elements, part 2: Analytical and numerical studies. *Thin-Walled Struct.* **2019**, *141*, 606–626. [CrossRef]
67. Choi, J.-W.; Joo, H.-J.; Choi, W.-C.; Yoon, S.-J. Local buckling strength of pultruded FRP I-section with various mechanical properties compression members. *KSCE J. Civ. Eng.* **2015**, *19*, 710–718. [CrossRef]
68. Cintra, G.G.; Cardoso, D.C.T.; Vieira, J.D. On the Local Buckling of Pultruded GFRP I-Section Columns. In Proceedings of the XXXVIII Iberian Latin-American Congress on Computational Methods in Engineering, Florianopolis, Brazil, 5–8 November 2017. [CrossRef]
69. Cintra, G.G.; Cardoso, D.C.T.; Vieira, J.D. Parameters affecting local buckling response of pultruded GFRP I-columns: Experimental and numerical investigation. *Compos. Struct.* **2019**, *222*, 110897. [CrossRef]
70. Correia, J.R.; Branco, F.A.; Silva, N.M.F.; Camotim, D.; Silvestre, N. First-order, buckling and post-buckling behaviour of GFRP pultruded beams. Part 1: Experimental study. *Comput. Struct.* **2011**, *89*, 2052–2064. [CrossRef]
71. Di Tommaso, A.; Russo, S. Shape Influence in Buckling of GFRP Pultruded Columns. *Mech. Compos. Mater.* **2003**, *39*, 329–340. [CrossRef]

72. GangaRao, H.V.; Blandford, M.M. Critical buckling strength prediction of pultruded glass fiber reinforced polymeric composite columns. *J. Compos. Mater.* **2014**, *48*, 3685–3702. [CrossRef]
73. Hassan, N.K.; Mosallam, A.S. Buckling and ultimate failure of thin-walled pultruded composite columns. *Polym. Polym. Compos.* **2004**, *12*, 469–481. [CrossRef]
74. Kabir, M.Z.; Sherbourne, A.N. Lateral-Torsional Buckling of Post-Local Buckled Fibrous Composite Beams. *J. Eng. Mech.* **1998**, *124*, 754–764. [CrossRef]
75. Kollár, L.P. Local Buckling of Fiber Reinforced Plastic Composite Structural Members with Open and Closed Cross Sections. *J. Struct. Eng.* **2003**, *129*, 1503–1513. [CrossRef]
76. Kuehn, T.; Pasternak, H.; Mittelstedt, C. Local buckling of shear-deformable laminated composite beams with arbitrary cross-sections using discrete plate analysis. *Compos. Struct.* **2014**, *113*, 236–248. [CrossRef]
77. Liu, T.; Vieira, J.D.; Harries, K.A. Predicting Flange Local Buckling Capacity of Pultruded GFRP I-Sections Subject to Flexure. *J. Compos. Constr.* **2020**, *24*, 04020025. [CrossRef]
78. Mittelstedt, C. Local buckling of wide-flange thin-walled anisotropic composite beams. *Arch. Appl. Mech.* **2007**, *77*, 439–452. [CrossRef]
79. Mottram, J.T.; Brown, N.D.; Anderson, D. Physical testing for concentrically loaded columns of pultruded glass fibre reinforced plastic profile. *Proc. Inst. Civ. Eng.-Struct. Build.* **2003**, *156*, 205–219. [CrossRef]
80. Nguyen, N.-D.; Nguyen, T.-K.; Vo, T.P.; Nguyen, T.-N.; Lee, S. Vibration and buckling behaviours of thin-walled composite and functionally graded sandwich I-beams. *Compos. Part B Eng.* **2019**, *166*, 414–427. [CrossRef]
81. Pecce, M.; Cosenza, E. Local buckling curves for the design of FRP profiles. *Thin-Walled Struct.* **2000**, *37*, 207–222. [CrossRef]
82. Prachasaree, W.; Limkatanyu, S.; Kaewjuea, W.; GangaRao, H.V.S. Simplified Buckling-Strength Determination of Pultruded FRP Structural Beams. *Pract. Period Struct. Des. Constr.* **2019**, *24*, 04018036. [CrossRef]
83. Qiao, P.; Davalos, J.F.; Wang, J. Local Buckling of Composite FRP Shapes by Discrete Plate Analysis. *J. Struct. Eng.* **2001**, *127*, 245–255. [CrossRef]
84. Qiao Pizhong, Zou Guiping. Local Buckling of Composite Fiber-Reinforced Plastic Wide-Flange Sections. *J. Struct. Eng.* **2003**, *129*, 125–129. [CrossRef]
85. Qiao, P.; Shan, L. Explicit local buckling analysis and design of fiber–reinforced plastic composite structural shapes. *Compos. Struct.* **2005**, *70*, 468–483. [CrossRef]
86. Ragheb, W.F. Development of Closed-Form Equations for Estimating the Elastic Local Buckling Capacity of Pultruded FRP Structural Shapes. *J. Compos. Constr.* **2017**, *21*, 04017015. [CrossRef]
87. Schreiber, P.; Mittelstedt, C. A holistic approach for local buckling of composite laminated beams under compressive load. *Arch. Appl. Mech.* **2019**, *89*, 1243–1257. [CrossRef]
88. Silva, N.M.F.; Camotim, D.; Silvestre, N.; Correia, J.R.; Branco, F.A. First-order, buckling and post-buckling behaviour of GFRP pultruded beams. Part 2: Numerical simulation. *Comput. Struct.* **2011**, *89*, 2065–2078. [CrossRef]
89. Singh, S.B.; Chawla, H. Stability and failure characterization of fiber reinforced pultruded beams with different stiffening elements, Part I: Experimental investigation. *Thin-Walled Struct.* **2019**, *141*, 593–605. [CrossRef]
90. Tomblin, J.; Barbero, E. Local buckling experiments on FRP columns. *Thin-Walled Struct.* **1994**, *18*, 97–116. [CrossRef]
91. Turvey, G.J.; Zhang, Y. A computational and experimental analysis of the buckling, postbuckling and initial failure of pultruded GRP columns. *Comput. Struct.* **2006**, *84*, 1527–1537. [CrossRef]
92. Zureick, A.; Scott, D. Short-Term Behavior and Design of Fiber-Reinforced Polymeric Slender Members under Axial Compression. *J. Compos. Constr.* **1997**, *1*, 140–149. [CrossRef]
93. Alhawamdeh, M.; Alajarmeh, O.; Aravinthan, T.; Shelley, T.; Schubel, P.; Kemp, M.; Zeng, X. Modelling hollow pultruded FRP profiles under axial compression: Local buckling and progressive failure. *Compos. Struct.* **2021**, *262*, 113650. [CrossRef]
94. Alsaadi, A.U.K. Behaviour of Filled Pultruded Glass Fibre Reinforced Polymer Tubes under Axial Loading. PhD Thesis, University of Southern Queensland, Toowoomba, Australia, 2019.
95. Al-Saadi, A.; Aravinthan, T.; Lokuge, W. Numerical Investigation on Hollow Pultruded Fibre Reinforced Polymer Tube Columns. In *ACMSM25. Lecture Notes in Civil Engineering*; Springer: Singapore, 2020; pp. 455–465.
96. Cardoso, D.C.T.; Harries, K.A.; Batista, E.d.M. Compressive strength equation for GFRP square tube columns. *Compos. Part B Eng.* **2014**, *59*, 1–11. [CrossRef]
97. Esfahani, M.T.; Kabir, M.Z.; Heidari-Rarani, M. An analytical approach for local buckling analysis of initially delaminated composite thin-walled columns with open and closed sections. *Adv. Compos. Mater.* **2018**, *27*, 85–105. [CrossRef]
98. Estep, D.D.; GangaRao, H.V.S.; Dittenber, D.B.; Qureshi, M.A. Response of pultruded glass composite box beams under bending and shear. *Compos. Part B Eng.* **2016**, *88*, 150–161. [CrossRef]
99. Gan, L.-H.; Ye, L.; Mai, Y.-W. Optimum design of cross-sectional profiles of pultruded box beams with high ultimate strength. *Compos. Struct.* **1999**, *45*, 279–288. [CrossRef]
100. Hashem, Z.A.; Yuan, R.L. Short vs. long column behavior of pultruded glass-fiber reinforced polymer composites. *Constr. Build. Mater.* **2001**, *15*, 369–378. [CrossRef]
101. Liu, T.; Harries, K.A. Flange local buckling of pultruded GFRP box beams. *Compos. Struct.* **2018**, *189*, 463–472. [CrossRef]
102. Muttashar, M.D. Behaviour of multi-celled GFRP beam assembly with concrete infill: Experimental and theoretical evaluations. Ph.D. Thesis, University of Southern Queensland, Toowoomba, Australia, 2017.

103. Muttashar, M.; Manalo, A.; Karunasena, W.; Lokuge, W. Influence of infill concrete strength on the flexural behaviour of pultruded GFRP square beams. *Compos. Struct.* **2016**, *145*, 58–67. [CrossRef]
104. Puente, I.; Insausti, A.; Azkune, M. Buckling of GFRP Columns: An Empirical Approach to Design. *J. Compos. Constr.* **2006**, *10*, 529–537. [CrossRef]
105. Qiao, P.; Zou, G. Local Buckling of Elastically Restrained Fiber-Reinforced Plastic Plates and its Application to Box Sections. *J. Eng. Mech.* **2002**, *128*, 1324–1330. [CrossRef]
106. Regel, F. A Modelling Approach for 3D Braid Reinforced Composites under Non-Axial Loading. PhD Thesis, University of Minho, Braga, Portugal, 2014.
107. Shan, L.; Qiao, P. Explicit local buckling analysis of rotationally restrained composite plates under uniaxial compression. *Eng. Struct.* **2008**, *30*, 126–140. [CrossRef]
108. Tang, J.; Chen, X.; Yang, K. Evaluating Structural Failure of Load-Carrying Composite Box Beams with Different Geometries and Load Conditions. *Appl. Compos. Mater.* **2019**, *26*, 1151–1161. [CrossRef]
109. D'Aguiar, S.C.M.; Parente, E., Jr. Local buckling and post-critical behavior of thin-walled composite channel section columns. *Lat. Am. J. Solids Struct.* **2018**, 15. [CrossRef]
110. Debski, H.; Rozylo, P.; Gliszczynski, A.; Kubiak, T. Numerical models for buckling, postbuckling and failure analysis of pre-damaged thin-walled composite struts subjected to uniform compression. *Thin-Walled Struct.* **2019**, *139*, 53–65. [CrossRef]
111. Doan, Q.H.; Thai, D.-K.; Tran, N.L. A Numerical Study of the Effect of Component Dimensions on the Critical Buckling Load of a GFRP Composite Strut under Uniaxial Compression. *Materials* **2020**, *13*, 931. [CrossRef] [PubMed]
112. Kubiak, T.; Kolakowski, Z.; Swiniarski, J.; Urbaniak, M.; Gliszczynski, A. Local buckling and post-buckling of composite channel-section beams—Numerical and experimental investigations. *Compos. Part B Eng.* **2016**, *91*, 176–188. [CrossRef]
113. Lee, J.; Nguyen, H.T.; Kim, S.-E. Buckling and post buckling of thin-walled composite columns with intermediate-stiffened open cross-section under axial compression. *Int. J. Steel Struct.* **2009**, *9*, 175–184. [CrossRef]
114. Nguyen, H.X.; Lee, J.; Vo, T.P.; Lanc, D. Vibration and lateral buckling optimisation of thin-walled laminated composite channel-section beams. *Compos. Struct.* **2016**, *143*, 84–92. [CrossRef]
115. Szymczak, C.; Kujawa, M. Local buckling of composite channel columns. *Contin. Mech. Thermodyn.* **2018**, *32*, 555–567. [CrossRef]
116. Agarwal, B.D.; Broutman, L.J.; Chandrashekhara, K. *Analysis and Performance of Fiber Composites*; John Wiley & Sons: Hoboken, NJ, USA, 2006.
117. Oller, S. *Numerical Simulation of Mechanical Behavior of Composite Materials*, 1st ed.; Springer: Barcelona, Spain, 2014.
118. Tuttle, M.E. *Structural Analysis of Polymeric Composite Materials*, 2nd ed.; CRC Press: Boca Raton, FL, USA, 2012.
119. Eslami, M.R. *Buckling and Postbuckling of Beams, Plates, and Shells*; Springer: Berlin/Heidelberg, Germany, 2017.
120. Singer, J.; Arbocz, J.; Weller, T. *Buckling Experiments: Experimental Methods in Buckling of Thin-Walled Structures: Shells, Built-Up Structures, Composites and Additional Topics, Volume 2*; John Wiley & Sons, Inc.: Hoboken, NJ, USA, 2002.
121. Uddin, N. *Developments in Fiber-Reinforced Polymer (FRP) Composites for Civil Engineering*; Elsevier: Amsterdam, The Netherlands, 2013.
122. Qiao, P.; Chen, Q. Post-local-buckling of fiber-reinforced plastic composite structural shapes using discrete plate analysis. *Thin-Walled Struct.* **2014**, *84*, 68–77. [CrossRef]
123. Bank, L.C.; Yin, J. Buckling of orthotropic plates with free and rotationally restrained unloaded edges. *Thin-Walled Struct.* **1996**, *24*, 83–96. [CrossRef]
124. Xu, J.; Zhao, Q.; Qiao, P. A critical review on buckling and post-buckling analysis of composite structures. *Front. Aerosp. Eng.* **2013**, *2*, 157–168.
125. Aleksendric, D.; Carlone, P. *Soft Computing in the Design and Manufacturing of Composite Materials: Applications to Brake Friction and Thermoset Matrix Composites*; Woodhead Publishing: Sawston, UK, 2015.
126. Boscato, G.; Casalegno, C.; Russo, S. Performance of built-up columns made by pultruded FRP material. *Compos. Struct.* **2015**, *121*, 46–63. [CrossRef]
127. Kreja, I. A literature review on computational models for laminated composite and sandwich panels. *Cent. Eur. J. Eng.* **2011**, *1*, 59–80. [CrossRef]
128. Barbero, E.J. *Introduction to Composite Materials Design*; CRC Press: Boca Raton, FL, USA, 2017. [CrossRef]
129. Gibson, R.F. *Principles of Composite Material Mechanics*; CRC Press: Boca Raton, FL, USA, 2016.
130. Sadowski, T. *Multiscale Modelling of Damage and Fracture Processes in Composite Materials*; Springer Science & Business Media: Berlin/Heidelberg, Germany, 2007.
131. Abouhamze, M.; Shakeri, M. Multi-objective stacking sequence optimization of laminated cylindrical panels using a genetic algorithm and neural networks. *Compos. Struct.* **2007**, *81*, 253–263. [CrossRef]
132. Akbaş, Ş.D. Post-buckling analysis of a fiber reinforced composite beam with crack. *Eng. Fract. Mech.* **2019**, *212*, 70–80. [CrossRef]
133. Aktaş, M.; Balcıoğlu, H.E. Buckling behavior of pultruded composite beams with circular cutouts. *Steel Compos. Struct.* **2014**, *17*, 359–370. [CrossRef]
134. Allahbakhsh, H.; Dadrasi, D. Buckling Analysis of Laminated Composite Panel with Elliptical Cutout Subject to Axial Compression. *Model. Simul. Eng.* **2012**, *2012*, 10. [CrossRef]

135. Almeida, J.H.S.; Tonatto, M.L.P.; Ribeiro, M.L.; Tita, V.; Amico, S.C. Buckling and post-buckling of filament wound composite tubes under axial compression: Linear, nonlinear, damage and experimental analyses. *Compos. Part B Eng.* **2018**, *149*, 227–239. [CrossRef]
136. Aslan, Z.; Şahin, M. Buckling behavior and compressive failure of composite laminates containing multiple large delaminations. *Compos. Struct.* **2009**, *89*, 382–390. [CrossRef]
137. Bloomfield, M.W.; Herencia, J.E.; Weaver, P.M. Analysis and benchmarking of meta-heuristic techniques for lay-up optimization. *Comput. Struct.* **2010**, *88*, 272–282. [CrossRef]
138. Chikkol, S.V.; Wooday, P.K.P.; Yelaburgi, S.J. Buckling of laminated composite cylindrical skew panels. *J. Thermoplast. Compos. Mater.* **2017**, *30*, 1175–1199. [CrossRef]
139. Coburn, B.H.; Wu, Z.; Weaver, P. Buckling analysis and optimization of blade stiffened variable stiffness panels. In Proceedings of the 56th AIAA/ASCE/AHS/ASC Structures, Structural Dynamics, and Materials Conference, Kissimmee, FL, USA, 5–9 January 2015; American Institute of Aeronautics and Astronautics: Reston, VA, USA, 2015. [CrossRef]
140. Debski, H.; Teter, A.; Kubiak, T.; Samborski, S. Local buckling, post-buckling and collapse of thin-walled channel section composite columns subjected to quasi-static compression. *Compos. Struct.* **2016**, *136*, 593–601. [CrossRef]
141. Deveci, H.A.; Aydin, L.; Seçil Artem, H. Buckling optimization of composite laminates using a hybrid algorithm under Puck failure criterion constraint. *J. Reinf. Plast. Compos.* **2016**, *35*, 1233–1247. [CrossRef]
142. Ehsani, A.; Rezaeepazhand, J. Stacking sequence optimization of laminated composite grid plates for maximum buckling load using genetic algorithm. *Int. J. Mech. Sci.* **2016**, *119*, 97–106. [CrossRef]
143. Guo, M.-W.; Harik, I.E.; Ren, W.-X. Buckling behavior of stiffened laminated plates. *Int. J. Solids Struct.* **2002**, *39*, 3039–3055. [CrossRef]
144. Gupta, A.; Patel, B.; Nath, Y. Postbuckling response of composite laminated plates with evolving damage. *Int. J. Damage Mech.* **2014**, *23*, 222–244. [CrossRef]
145. Herencia, J.E.; Weaver, P.M.; Friswell, M.I. Optimization of Long Anisotropic Laminated Fiber Composite Panels with T-Shaped Stiffeners. *AIAA J.* **2007**, *45*, 2497–2509. [CrossRef]
146. Herencia, J.E.; Weaver, P.M.; Friswell, M.I. Initial sizing optimisation of anisotropic composite panels with T-shaped stiffeners. *Thin-Walled Struct.* **2008**, *46*, 399–412. [CrossRef]
147. Irisarri, F.-X.; Bassir, D.H.; Carrere, N.; Maire, J.-F. Multiobjective stacking sequence optimization for laminated composite structures. *Compos. Sci. Technol.* **2009**, *69*, 983–990. [CrossRef]
148. Karakaya, Ş.; Soykasap, Ö. Buckling optimization of laminated composite plates using genetic algorithm and generalized pattern search algorithm. *Struct. Multidiscip. Optim.* **2009**, *39*, 477. [CrossRef]
149. Karakaya, Ş.; Soykasap, Ö. Natural frequency and buckling optimization of laminated hybrid composite plates using genetic algorithm and simulated annealing. *Struct. Multidiscip. Optim.* **2011**, *43*, 61–72. [CrossRef]
150. Khakimova R, Castro SGP, Wilckens D, Rohwer K, Degenhardt R. Buckling of axially compressed CFRP cylinders with and without additional lateral load: Experimental and numerical investigation. *Thin-Walled Struct.* **2017**, *119*, 178–189. [CrossRef]
151. Kim, K.; Voyiadjis, G.Z. Buckling strength prediction of CFRP cylindrical panels using finite element method. *Compos. Part Appl. Sci. Manuf.* **1999**, *30*, 1093–1104. [CrossRef]
152. Pathirana, S.; Qiao, P. Local buckling analysis of periodic sinusoidal corrugated composite panels under uniaxial compression. *Compos. Struct.* **2019**, *220*, 148–157. [CrossRef]
153. Ravi Kumar, P.; Gupta, G.; Shamili, G.K.; Anitha, D. Linear Buckling Analysis and Comparative Study of Un-stiffened and Stiffened Composite Plate. *Mater. Today Proc.* **2018**, *5*, 6059–6071. [CrossRef]
154. Rouhi, M.; Ghayoor, H.; Hoa, S.V.; Hojjati, M. Multi-objective design optimization of variable stiffness composite cylinders. *Compos. Part B Eng.* **2015**, *69*, 249–255. [CrossRef]
155. Srinivasa, C.V.; Kumar, W.P.P.; Kumar, M.T.P.; Bangar, A.R.; Kumar, P.; Rudresh, M.S. Experimental and numerical studies on buckling of laminated composite skew plates with circular holes under uniaxial compression. *Mech. Adv. Mater. Struct.* **2017**, *24*, 304–317. [CrossRef]
156. Suleiman, O.M.E.; Osman, M.Y.; Hassan, T. Stability of thin laminated decks plates under plane compressive loading. *Int. Res. J. Eng. IT Sci. Res.* **2019**, *5*, 1–28. [CrossRef]
157. Vaziri, A. On the buckling of cracked composite cylindrical shells under axial compression. *Compos. Struct.* **2007**, *80*, 152–158. [CrossRef]
158. Vescovini, R.; Bisagni, C. Two-step procedure for fast post-buckling analysis of composite stiffened panels. *Comput. Struct.* **2013**, *128*, 38–47. [CrossRef]
159. Wagner, H.N.R.; Köke, H.; Dähne, S.; Niemann, S.; Hühne, C.; Khakimova, R. Decision tree-based machine learning to optimize the laminate stacking of composite cylinders for maximum buckling load and minimum imperfection sensitivity. *Compos. Struct.* **2019**, *220*, 45–63. [CrossRef]
160. Weaver, P.M.; Dickenson, R. Interactive local/Euler buckling of composite cylindrical shells. *Comput. Struct.* **2003**, *81*, 2767–2773. [CrossRef]
161. Betts, D.; Sadeghian, P.; Fam, A. Investigation of the stress-strain constitutive behavior of ±55° filament wound GFRP pipes in compression and tension. *Compos. Part B Eng.* **2019**, *172*, 243–252. [CrossRef]

162. Lakshmi, K.; Rama Mohan Rao, A. Multi-objective optimal design of laminated composite skirt using hybrid NSGA. *Meccanica* **2013**, *48*, 1431–1450. [CrossRef]
163. Nahas, M.N. Local buckling of composite corrugated compression panels. *Adv. Compos. Mater.* **1993**, *3*, 73–82. [CrossRef]
164. Rao, A.R.M.; Lakshmi, K. Optimal design of stiffened laminate composite cylinder using a hybrid SFL algorithm. *J. Compos. Mater.* **2012**, *46*, 3031–3055. [CrossRef]
165. Riche, R.L.; Haftka, R.T. Optimization of laminate stacking sequence for buckling load maximization by genetic algorithm. *AIAA J.* **1993**, *31*, 951–956. [CrossRef]
166. Setoodeh, A.R.; Shojaee, M. Critical buckling load optimization of functionally graded carbon nanotube-reinforced laminated composite quadrilateral plates. *Polym. Compos.* **2018**, *39*, E853–E868. [CrossRef]
167. Wang, H.; Croll, J.G. Design Optimisation of Lower-Bound Buckling Capacities for FRP-Laminated Cylindrical Shells. *ISRN Mech. Eng.* **2012**, *2012*, 636898. [CrossRef]
168. Chai, G.B.; Khong, P.W. The effect of varying the support conditions on the buckling of laminated composite plates. *Compos. Struct.* **1993**, *24*, 99–106. [CrossRef]
169. Shojaee, T.; Mohammadi, B.; Madoliat, R.; Salimi-Majd, D. Development of a finite strip method for efficient prediction of buckling and post-buckling in composite laminates containing a cutout with/without stiffener. *Compos. Struct.* **2019**, *210*, 538–552. [CrossRef]
170. Kollár, L.P.; Springer, G.S. *Mechanics of Composite Structures*; Cambridge University Press: Cambridge, UK, 2003.
171. McCarthy, M.J.; Bank, L.C. Sensitivity studies on local flange buckling equations for pultruded beams and columns. In *Advances in FRP Composites in Civil Engineering*; Springer: Beijing, China, 2010; pp. 115–118.
172. Ragheb, W.F. Local buckling analysis of pultruded FRP structural shapes subjected to eccentric compression. *Thin-Walled Struct.* **2010**, *48*, 709–717. [CrossRef]
173. Praveen, A.P.; Rajamohan, V.; Mathew, A.T. Recent developments in investigation on buckling and post buckling responses of laminated composite shells. *Polym. Compos.* **2018**, *39*, 4231–4242. [CrossRef]
174. Kollár, L.P. Buckling of Unidirectionally Loaded Composite Plates with One Free and One Rotationally Restrained Unloaded Edge. *J. Struct. Eng.* **2002**, *128*, 1202–1211. [CrossRef]
175. Sayyad, A.S.; Ghugal, Y.M. Bending, buckling and free vibration of laminated composite and sandwich beams: A critical review of literature. *Compos. Struct.* **2017**, *171*, 486–504. [CrossRef]
176. Zureick, A.; Shih, B. Local buckling of fiber-reinforced polymeric structural members under linearly-varying edge loading—Part 1. *Theoretical formulation. Compos. Struct.* **1998**, *41*, 79–86. [CrossRef]
177. American Society of Civil Engineers. *Pre-Standard for Load & Resistance Factor Design (LRFD) of Pultruded Fiber Reinforced Polymer (FRP) Structures*; ACMA: Arlington, VA, USA, 2012; p. 215.
178. Ascione, L.; Caron, J.F.; Godonou, P.; van IJselmuijden, K.; Knippers, J.; Mottram, T.; Oppe, M.; Gantriis Sorensen, M.; Taby, J.; Tromp, L. *Prospect for New Guidance in the Design of FRP: Support to the Implementation, Harmonization and Further Development of the Eurocodes*; Publications Office of the European Union: Luxembourg, 2016.
179. Clarke, J.L. *Structural Design of Polymer Composites EUROCOMP Design Code and Handbook*; CRC Press: Boca Raton, FL, USA, 2005.
180. National Research Council. Guide for the Design and Construction of Structures made of FRP Pultruded Elements. *CNR-DT* **2007**, *205*, 25–31.
181. Ascione, L.; Berardi, V.P.; Giordano, A.; Spadea, S. Buckling failure modes of FRP thin-walled beams. *Compos. Part B Eng.* **2013**, *47*, 357–364. [CrossRef]
182. Vanevenhoven, L.M.; Shield, C.K.; Bank, L.C. LRFD Factors for Pultruded Wide-Flange Columns. *J. Struct. Eng.* **2010**, *136*, 554–564. [CrossRef]
183. Reddy, J.N. *Mechanics of Laminated Composite Plates and Shells: Theory and Analysis*, 2nd ed.; CRC Press: Boca Raton, FL, USA, 2003.
184. Amoushahi, H.; Azhari, M. Buckling of composite FRP structural plates using the complex finite strip method. *Compos. Struct.* **2009**, *90*, 92–99. [CrossRef]
185. Al-saadi, A.U.; Aravinthan, T.; Lokuge, W. Structural applications of fibre reinforced polymer (FRP) composite tubes: A review of columns members. *Compos. Struct.* **2018**, *204*, 513–524. [CrossRef]
186. Ascione, L.; Berardi, V.P.; Giordano, A.; Spadea, S. Macro-scale analysis of local and global buckling behavior of T and C composite sections. *Mech. Res. Commun.* **2014**, *58*, 105–111. [CrossRef]
187. Campbell, F.C. *Structural Composite Materials*; ASM International: Materials Park, OH, USA, 2010.
188. Kim, H.-Y.; Hwang, Y.-K.; Park, K.-T.; Lee, Y.-H.; Kim, S.-M. Fiber reinforced plastic deck profile for I-girder bridges. *Compos. Struct.* **2005**, *67*, 411–416. [CrossRef]
189. Bai, Y.; Keller, T.; Wu, C. Pre-buckling and post-buckling failure at web-flange junction of pultruded GFRP beams. *Mater. Struct.* **2013**, *46*, 1143–1154. [CrossRef]
190. Meyer, R. *Handbook of Pultrusion Technology*; Springer Science & Business Media: Berlin/Heidelberg, Germany, 2012.
191. Mosallam, A.S.; Feo, L.; Elsadek, A.; Pul, S.; Penna, R. Structural evaluation of axial and rotational flexibility and strength of web–flange junctions of open-web pultruded composites. *Compos. Part B Eng.* **2014**, *66*, 311–327. [CrossRef]
192. Starr, T. *Pultrusion for Engineers*; Elsevier: Amsterdam, The Netherlands, 2000.
193. Soares, C.A.M.; Soares, C.M.M.; Freitas, M.J.M. *Mechanics of Composite Materials and Structures*; Springer Science & Business Media: Berlin/Heidelberg, Germany, 2013.

194. Di Sciuva, M.; Gherlone, M.; Lomario, D. Multiconstrained optimization of laminated and sandwich plates using evolutionary algorithms and higher-order plate theories. *Compos. Struct.* **2003**, *59*, 149–154. [CrossRef]
195. Quadrino, A.; Penna, R.; Feo, L.; Nisticò, N. Mechanical characterization of pultruded elements: Fiber orientation influence vs web-flange junction local problem. *Experimental and numerical tests. Compos. Part B Eng.* **2018**, *142*, 68–84. [CrossRef]
196. Buragohain, M.K. *Composite Structures: Design, Mechanics, Analysis, Manufacturing, and Testing*; CRC Press: Boca Raton, FL, USA, 2017.
197. Mustafa, A. An Introduction to Polymer-Matrix Composites. 2015. Available online: bookboom.com (accessed on 16 August 2021).
198. Abramovich, H. *Stability and Vibrations of Thin-Walled Composite Structures*; Woodhead Publishing: Sawston, UK, 2017.
199. Loughlan, J. The buckling of CFRP composite plates in compression and shear and thin-walled composite tubes in torsion—The effects of bend-twist coupling and the applied shear direction on buckling performance. *Thin-Walled Struct.* **2019**, *138*, 392–403. [CrossRef]
200. Naderian, H.R.; Ronagh, H.R.; Azhari, M. Torsional and flexural buckling of composite FRP columns with cruciform sections considering local instabilities. *Compos. Struct.* **2011**, *93*, 2575–2586. [CrossRef]
201. Silva, N.M.F.; Silvestre, N.; Camotim, D. GBT formulation to analyse the buckling behaviour of FRP composite open-section thin-walled columns. *Compos. Struct.* **2010**, *93*, 79–92. [CrossRef]
202. Chawla, K.K. *Composite Materials: Science and Engineering*; Springer Science & Business Media: Berlin/Heidelberg, Germany, 2012.
203. Ghiasi, H.; Pasini, D.; Lessard, L. Optimum stacking sequence design of composite materials Part I: Constant stiffness design. *Compos. Struct.* **2009**, *90*, 1–11. [CrossRef]
204. Tafreshi, A.; Oswald, T. Global buckling behaviour and local damage propagation in composite plates with embedded delaminations. *Int. J. Press. Vessel. Pip.* **2003**, *80*, 9–20. [CrossRef]
205. Almeida, J.H.S.; Bittrich, L.; Jansen, E.; Tita, V.; Spickenheuer, A. Buckling optimization of composite cylinders for axial compression: A design methodology considering a variable-axial fiber layout. *Compos. Struct.* **2019**, *222*, 110928. [CrossRef]
206. Department of Defense. *Composite Materials Handbook, Volume 3: Polymer Matrix Composites—Materials Usage, Design and Analysis*; SAE International: Warrendale, PA, USA, 2002.
207. Yi, X.-S.; Du, S.; Zhang, L. *Composite Materials Engineering, Volume 1: Fundamentals of Composite Materials*; Springer: Berlin/Heidelberg, Germany, 2017.
208. Mallick, P.K. *Fiber-Reinforced Composites: Materials, Manufacturing, and Design*; CRC Press: Boca Raton, FL, USA, 2007.
209. Butler, R.; Rhead, A.; Dodwell, T. Optimum Design and Damage Tolerance of Compressively Loaded Laminates. In *Comprehensive Composite Materials II*; Beaumont, P.W.R., Zweben, C.H., Eds.; Elsevier: Oxford, UK, 2018; pp. 118–135. [CrossRef]

CHAPTER 3: (PAPER 2) MODELLING HOLLOW PULTRUDED FRP PROFILES UNDER AXIAL COMPRESSION: LOCAL BUCKLING AND PROGRESSIVE FAILURE

In this chapter, a Finite Element Method (FEM) modelling approach was established to investigate the local buckling of hollow Pultruded Fibre-reinforced Polymers (PFRP) profiles subjected to axial compression. The FEM was selected to perform the parametric studies on the design parameters as recommended in the literature review (chapter 2, figure 5). The Newton method was used along with the adaptive automatic stabilisation scheme and a controlled increment size in Abaqus 2019, to overcome the numerical difficulties and termination errors in simulating local buckling due to the severe nonlinearity. An extensive experimental program consisting of hollow PFRP profiles with different cross-sections (square, rectangular, and circular) and slenderness ratios (length-to-width ratios L/D ranging from 2.0 to 5.0) was undertaken to validate the FEM results and assess the effect of different cross-sections and slenderness ratios on the sensitivity of the proposed modelling approach to the dimensional changes. The mesh sensitivity study, elements seeding, load-displacement curves, failure sequence, and the energy parameters for all specimens are presented in Appendix A.

The FEM approach was capable of capturing the experimental local buckling, post-buckling, and progressive failure of the hollow box PFRP profiles. It was also used to compare the failure mode of these profiles to the circular PFRP profiles, which were dominated by compressive and shear failure of the constituents. The relationship between the post-buckling behaviour and failure modes of the hollow box PFRP profiles and the energy parameters of the FEM models was established to explain the effect of dimension, layup, and slenderness ratio on the structural behaviour and failure modes of the tested profiles. The validated modelling approach was used to perform extensive parametric studies on the reviewed design parameters to investigate their effect on the local buckling of hollow box PFRP profiles subjected to axial compression along with their contributions and interactions, as discussed in the next chapter

CHAPTER 4: (PAPER 3) EFFECTS OF LAYUP AND GEOMETRY ON COMPRESSIVE PERFORMANCE OF HOLLOW PULTRUDED FRP PROFILES

The literature review in chapter 2 identified the most critical design parameters of hollow box Pultruded Fibre-reinforced Polymers (PFRP) profiles and the lack of knowledge in the design for manufacturing of these profiles as a novel construction material. These structural composite members by pulwinding manufacture process are governed by layup parameters (winding angle, axial-to-wound fibre ratio, and stacking sequence) and geometric parameters (wall slenderness, cross-sectional aspect ratio, and corner radius). Similarly, the findings from the experimental and numerical work in chapter 3 showed the significance of these parameters in shaping the structural performance and failure modes of hollow box PFRP profiles. This chapter investigated the effect of these design parameters on the structural behaviour of hollow PFRP profiles subjected to axial compression using the verified Finite Element Method (FEM) modelling approach developed in chapter 3.

Extensive parametric studies on 100×100×5.2 mm square and 89×6.0 mm circular hollow PFRP profiles with a slenderness ratio (length-to-width ratio L/D) of 5.0 were undertaken to investigate the effect of the design parameters on the structural behaviour of these two different profiles. A full factorial design of experiment was applied to capture the critical parametric interactions. The corner (flange-web junction) geometry was the dominant design parameter in shaping the compressive strength of hollow box PFRP profiles. Supporting this critical zone obtained more reliable and economic designs. Guidelines and recommendations on the design for manufacturing were derived for the optimal compressive behaviour of hollow PFRP profiles to overcome local buckling and enhance the compressive strength. The effect of these design parameters and their interactions under bending load was investigated in chapter 5.

Effects of Layup and Geometry on Compressive Performance of Hollow Pultruded FRP Profiles

Mohammad Alhawamdeh*[1], Omar Alajarmeh[1], Thiru Aravinthan[1], Tristan Shelley[1], Peter Schubel[1], Michael Kemp[2], Xuesen Zeng[1]

*Corresponding author: Mohammad.Alhawamdeh@usq.edu.au, University of Southern Queensland West Street Toowoomba Qld 4350 Australia

[1] University of Southern Queensland, Centre for Future Materials, Toowoomba Queensland Australia 4350

[2] Wagners Composite Fibre Technologies, Wellcamp Queensland Australia 4350

ABSTRACT

There is a lack of knowledge and guidelines in the design for manufacturing of hollow Pultruded Fibre-Reinforced Polymer (PFRP) profiles as a novel construction material. These structural composite members by pulwinding manufacture process are governed by layup and geometric parameters. The layup parameters consist of wound fibre angle, axial-to-wound fibre ratio, and stacking sequence, while the geometric parameters comprise wall thickness, cross-sectional aspect ratio, and corner radius. This paper presents an extensive parametric study of these parameters by the finite element modelling of progressive failure under axial compression. The numerical models were verified with the experimental data. Each geometric parameter was studied individually to obtain the failure map of hollow PFRP stub columns and to assess the applicable levels for each parameter in the interactive study. A full factorial design of experiment was applied to capture the critical parametric interactions with over 135 numerical models. Guidelines and recommendations on the design for manufacturing were

derived for the optimal compressive behaviour of hollow PFRP profiles to withstand local buckling and compressive failure.

Keywords: Hollow GFRP columns, Finite element analysis, Local buckling, Compressive failure.

1. INTRODUCTION

Hollow Pultruded Fibre-Reinforced Polymer (PFRP) profiles are widely used in civil infrastructure applications [1–3]. Pulwinding process, the filament winding technology integration with pultrusion, introduces off-axis wound fibres along with the axial fibres in PFRP profiles. Wound fibres enhance the transverse properties, resist delamination, and enhance post-processing activities, such as bolting and jointing [4–7]; it also increases the buckling load capacity of the profiles [8–10]. Hollow laminated composites manufactured by pulwinding possess tailorable design parameters including layup parameters (wound fibre angle, axial-to-wound fibres ratio, and stacking sequence) and geometric parameters (wall thickness, cross-sectional aspect ratio, and corner radius). Local buckling is a dominant failure mode in composite hollow profiles under compression due to their anisotropic and slender nature, and it is affected by these design parameters [11–18]. Studying the design parameters can help in simplifying the design for manufacturing of the hollow PFRP profiles and reach their optimal potentials with the recommended configurations of these parameters.

On the layup parameters, the effect of axial-to-wound fibre ratio of hollow box and circular Glass Fibre-Reinforced Polymer (GFRP) stub columns was studied numerically [19]. The axial fibre percentage increase from 60% to 80% increased the axial stiffness by 23% and 22.6% of the hollow box and circular profiles respectively, while the compressive strength was increased by 4% and 9% respectively. On the other hand, the reported increase in the compressive strength of the box profile, which was dominated by local buckling, raises a question that needs more investigation. It opposes the findings of the proportional relationship between the local buckling load capacity and the percentage of inclined fibres in laminated plates [20–22].

The effect of fibre orientation on the mechanical properties of laminated composites was widely studied under different loading conditions [23–25]. These studies addressed the relationship between the fibre orientation and the strength limits and did not cover the stability limits (e.g. local buckling). The fibre angle of hollow GFRP circular tubes with symmetric layups made from six unidirectional laminae was studied under axial compression [26,27] in order to optimise the buckling load capacity. It was found that the optimal fibre angle for the inclined fibres depends on the stacking sequence. For $[\theta]_6$ layup, the optimal fibre angles were reported to be 20^o and 70^o. Whereas the optimal fibre angle was 50^o and $45^o$for $[0/0/\theta]_S$ and $[90/0/\theta]_S$ layups, respectively. Nevertheless, these studies were performed using eigenvalue (linear) buckling analysis. Thus, the geometry nonlinearity and the post-buckling response were not included. The effect of fibre angle on the buckling load of unidirectional [28], angle-ply, and cross-ply [29,30] fibre-reinforced composite beams subjected to axial loading was studied numerically considering the shear deformations. It was concluded that the critical buckling load decreases when the fibre orientation increases. For the unidirectional composite beam, the critical buckling load decreased by 35% when the fibre angle increased from 10° to 30° [28]. When comparing the angle-ply vs cross-ply layups, the cross-ply laminate was found to sustain a larger buckling load than angle-ply laminate when the fibre angle is larger than 30^o[29,30]. Generally, symmetric and balanced layups are preferred to minimise the elastic coupling effect and limit manufacturing imperfection and warp [31–33]. However, the optimal location of the wound fibres within the layup and its effect on the confinement of hollow PFRP profiles is not quantified in the literature. In addition, the interaction between the wound fibre angle and the axial-to-wound fibres ratio was not studied in the literature.

Fewer studies were found on geometric parameters, especially the corner geometry of the hollow box PFRP profiles. The wall thickness effect on the compressive behaviour of hollow box and circular GFRP stub columns was investigated numerically [19]. Increasing the wall thickness from 5.2 mm to 6.75 mm changed the failure mode from local buckling at walls to compressive failure of fibres and doubled the load capacity of the box profile. The axial stiffness and load capacity were increased by 38% and 44%, respectively, for the hollow circular profile when the wall thickness was increased from 6 mm to 8.6 mm. The compressive behaviour of hollow circular PFRP profiles with two diameter-to-thickness ratios of 14.8 and 22.9 was investigated experimentally [25,34]. The first profile had 6 mm wall thickness and 89 mm outer diameter, while the dimensions of the second profile were 8 mm and 183 mm, respectively. Increasing the profile thickness and diameter enhanced its axial performance due to the increase in the cross-sectional area. This result was attributed to the failure mode of both profiles since they failed by compressive fibre failure and no instability was observed. In all these studies, the maximum allowed slenderness ratio to prevent local buckling was not reported. Moreover, the contribution and interactions of the wall thickness and other geometric parameters were not studied.

The cross-sectional dimensions (width and height of flange and web) of I-shape pultruded GFRP stub columns were studied [35,36]. Failure mode maps and design guidelines were reported for that shape. However, fewer studies were found on hollow box shape. The local buckling resistance of hollow square and rectangular PFRP profiles subjected to axial compression was studied [37]. The load-axial displacement curves of two cross-sectional aspect ratios of 1 (square section) and 1.5 (rectangular section) were compared. Unlike the square profile, the rectangular profile showed a five times larger post-buckling zone at which the axial stiffness was degraded. While the buckling load was the peak load for the square profile, the rectangular profile exhibited a 32% higher peak load than the buckling load. It was concluded that the wider walls buckled at a lower load due to their large slenderness ratio and caused the post-buckling behaviour. The higher peak load after buckling was attributed to the resistance provided by the narrower walls due to their higher buckling capacity because of their small slenderness ratio.

Regarding the corner geometry, the flange-web junction is considered to be a critical zone of stresses concentration that needs to be designed carefully [24]. This zone was studied experimentally for I-shape PFRP profiles [38]. Additional hand-layup fillets (38 mm) were added on the top flange-web junction of GFRP beams to strengthen the transition zone with the performance assessed. The load capacity significantly enhanced by 1.5 times when the corner area was increased due to the increase in rotational stiffness. The added fillets shifted the failure mode from buckling of the compression flange to compressive failure. However, no studies were found on the corner geometry of hollow box PFRP profiles. Also, the corner radius value that separates the two failure modes was not identified.

After reviewing the relevant literature, it is clear that most of the design parameters were studied individually. The contribution and interactions of these parameters were not systematically quantified. These two aspects are fundamental to build-up reliable design guidelines and to optimise the hollow pultruded profiles efficiently by targeting the most significant parameters. Most of the previous numerical studies did not investigate the relationship between the design parameters and the post-buckling behaviour of hollow PFRP profiles since they were undertaken using linear buckling analysis. The Finite Element Method (FEM) presents a suitable option to perform such parametric studies due to its flexibility in handling complex geometries and combined failure problems [11,13,15,39–46]. This paper develops a comprehensive numerical approach to study the effect, contribution, and interaction of the layup and geometric parameters under axial compression. The numerical models are validated by the experiments. The parameters have been analysed by a full factorial design of experiments. Each geometric parameter was studied individually to obtain the failure map of hollow PFRP stub columns and to assess the applicable levels for each parameter in the full factorial study. The current study is going to facilitate the design process of hollow wound PFRP profiles and maximise their utilisation by developing optimal configurations of these parameters for compression applications.

2. FINITE ELEMENT MODELLING

Abaqus/CAE 2019 was used to perform the parametric studies on two geometries of hollow PFRP profiles: square and circular. The two baseline profiles as shown in Fig. 1 were manufactured by Wagners CFT from E-glass/Vinyl-ester using the pulwinding process with the geometric and layup properties shown in Table 1. The inner corner radius of the box profile equals the profile outer radius minus the wall thickness. The profiles are assigned to a fixed-fixed boundary condition on both ends by restraining the movement along their translational and rotational degrees of freedom except the loading direction. The profiles are loaded under axial compression with a loading-rate of 1 mm/min. A length-to-width (L/D) ratio of 5 was used for these stub columns to remain in the compressive failure-local buckling failure zone and prevent failure by global buckling [47,48].

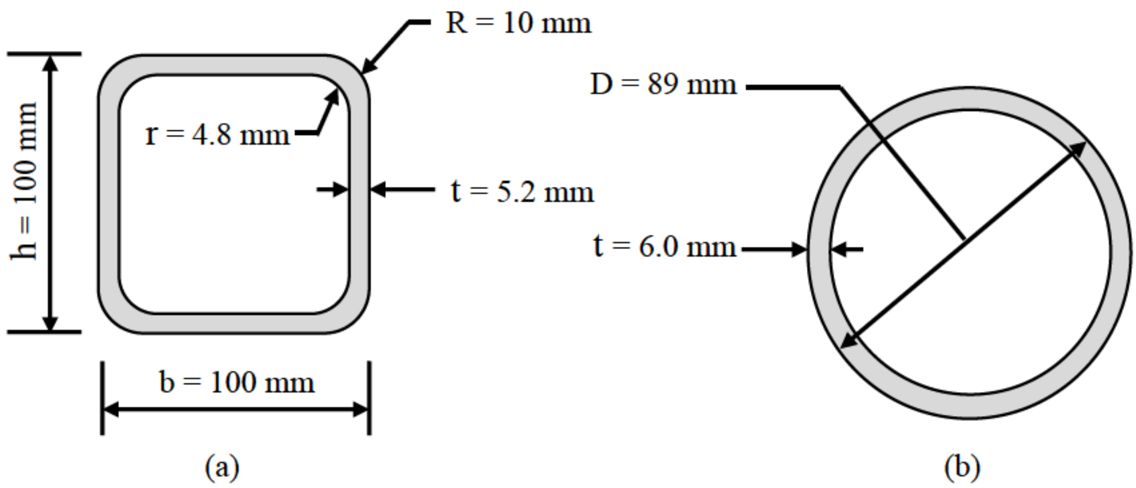

Fig. 1. Hollow PFRP profiles with (a) box and (b) circular geometries.

Table 1: Geometric and layup properties of hollow PFRP profiles.

Geometry	Geometric properties				Layup properties	
Square	Wall width (mm)	Wall thickness (mm)	Outer corner radius (mm)	Profile length (mm)	Stacking sequence	Fibre percentage (%)
	100	5.2	10	500	[0/+50/-50/0/-50/+50/0]	0^o: 82.2 50^o: 17.8
Circular	Outer diameter (mm)	Wall thickness (mm)		Profile length (mm)	Stacking sequence	Fibre percentage (%)
	89	6.0		445	[0/+56/-56/0/-56/+56/0]	0^o: 74.4 56^o: 25.6

The Newton method in Abaqus/Standard was used to perform a nonlinear geometric analysis by implementing the large displacement formulation to capture the deformations accompanying the post-buckling behaviour. The adaptive automatic stabilisation scheme was applied to damp the severe nonlinearities which accompany buckling and prevent termination errors. The dependency of the solution convergence on the increment size was eliminated by reducing the maximum increment size down to 0.35% of the total step time until convergence is achieved with a tolerance of 5% between the load capacities of the successive increment sizes. This novel modelling approach combining the local buckling, post-buckling, and progressive failure behaviours was addressed in details and verified in previous research [49].

The elastic behaviour of the hollow PFRP profiles was defined using the stiffness matrix components of a transversely isotropic lamina with fibre volume fraction (V_f) of 0.6 (as provided by the manufacturer) having the mechanical properties shown in Table 2. The elastic modulus in the fibre direction (E_1) was calculated using the rule of mixture. Whereas the transverse elastic modulus (E_2), the in-plane shear modulus (G_{12}), and the out-of-plane shear modulus (G_{23}) were calculated using empirical equations [50,51]. The value of (G_{13}) was set to equal the value of (G_{12}) since unidirectional plies are considered to be transversely isotropic materials [40].

Table 2: lamina mechanical properties of the hollow pultruded FRP profiles.

Elastic properties	E_1(MPa) 45700	E_2(MPa) 12100	v_{12} 0.28	$G_{12} = G_{13}$ (MPa) 4600	G_{23}(MPa) 4000	
Strength limits	X^T (MPa) 803	X^c (MPa) 548	Y^T (MPa) 43	Y^C (MPa) 187	S^L (MPa) 64	S^T (MPa) 50
Fracture energy	G_{LT} (N/mm) 92	G_{LC} (N/mm) 79	G_{TT} (N/mm) 5	G_{TC} (N/mm) 5		

Hashin damage model [52] was used to simulate the progressive failure in fibres and matrix at the lamina level. The model considers four different failure modes: fibre rupture in tension, fibre buckling and kinking in compression, matrix cracking under transverse tension and shearing, and matrix crushing under transverse compression and shearing. The model consists of three components that should be defined, including damage initiation criteria, damage evolution response, and damage stabilisation scheme. The damage evolution algorithm simulates the progressive damage after any damage initiation criterion for any failure mode is met within any element. The lamina strength limits of the damage initiation criteria used in this study are for unidirectional E-glass/Vinyl-Ester composites and were extracted for the same profiles [50]. These strength limits are shown in Table 2 with the notations X, Y, and S referring to the longitudinal, transverse, and shear strength values, and the superscripts T and C symbolising tension and compression. The damage evolution algorithm traces the damage progression based on energy dissipation. The fracture energy (the area under the equivalent stress-displacement diagram of the element) must be specified for each failure mode. Due to the lack of experimental data on the fracture energy of E-glass/Vinyl-ester lamina for each failure mode, fracture energy values of E-glass/Ly556 epoxy lamina were used [53]. These values are shown in Table 2 with double subscript notation consisting of L and T as first subscript referring to longitudinal and transverse directions and second subscript of T and C denoting tension and compression. To overcome severe convergence difficulties when modelling material softening (failure), a viscous stabilisation scheme is used to make the tangent stiffness matrix of the softening material positive for sufficiently time increments by introducing the viscosity coefficient for each failure mode. A sensitivity study was performed on the hollow PFRP profiles and a viscosity coefficient of 1×10^{-3} sec for each failure mode was found to be suitable.

The 8-node quadrilateral in-plane general-purpose continuum shell (SC8R) element was selected to model the hollow PFRP profiles due to its accuracy in capturing the through-thickness response and its flexibility in controlling the geometry by a three-dimensional representation of the element. The latter feature is very important for studying the geometry of the corner since this element provides the capability to taper or thicken the geometry. The suitable element size (allowing for results to converge) was assigned based on a mesh sensitivity study. The kinematic changes through the thickness were captured accurately and the hourglass modes were reduced greatly by refining the number of elements through the thickness. A mesh with a 5 mm element edge length and five elements through-thickness was selected for the hollow box profile. Five elements were locally assigned to each corner to refine the mesh since the corners form a critical zone for stress concentrations. A mesh with a 3 mm element edge length and five elements through-thickness was selected for the hollow circular profile.

3. EXPERIMENTAL VALIDATION

An experimental program was undertaken on five specimens of the hollow box profile, and data was collected from the literature [50,54] on two specimens of the hollow circular profile to validate the FEA models. These experimental tests were conducted on profiles manufactured by Wagners CFT with the same layup and geometric parameters shown in Table 1, and the same length-to-width (L/D) ratio of 5. The profiles were tested on SANS (SHT4206 – 2000 kN capacity) universal testing machine under the same supporting and loading conditions of the numerical models. Steel fixtures were used on the profiles ends to attain a fixed-fixed supporting condition. The specimens were subjected to axial compression load with a loading-rate of 1 mm/min. Table 3 compares the numerical and experimental results in terms of the axial stiffness (EA/L) and compressive strength. In general, a good agreement was found between the numerical and experimental results. Moreover, the post-buckling zone extent and the failure sequence were also matching, as shown in Fig. 2, for the hollow box profile. The matrix tensile damage was used to refer to the buckling waves propagation during the post-buckling zone. The fibres compressive damage was used to refer to fibres rupture at the profile's mid-height. For the hollow box profile, the failure was triggered by local buckling of the walls. Afterwards, a sudden drop in load capacity occurred due to the tensile and shear failure in the matrix, which was derived from the out-of-plane deformations in the walls. Subsequently, stability was restored under a new equilibrium path since the fracture energy of the laminate was not attained yet. The profile went through a post-buckling zone, which was featured by the propagation of localised waves. The final collapse happened at the mid-height because of the compressive failure of fibres. The hollow circular profile failed by shear in the matrix and compressive crushing of the fibres at the ends, as shown in Fig. 3.

Table 3. FEM vs experimental mechanical properties of hollow PFRP profiles.

Shape	FEM Stiffness [kN/mm]	EXP Stiffness [kN/mm]	EXP SD	Error (%)	FEM strength [MPa]	EXP strength [MPa]	EXP SD	Error (%)
Hollow box	154.6	158.9	5.1	2.7	243.0	252.1	6.7	3.6
Hollow circular	132.2	130.3	1.3	1.5	367.2	343.9	27.3	6.7

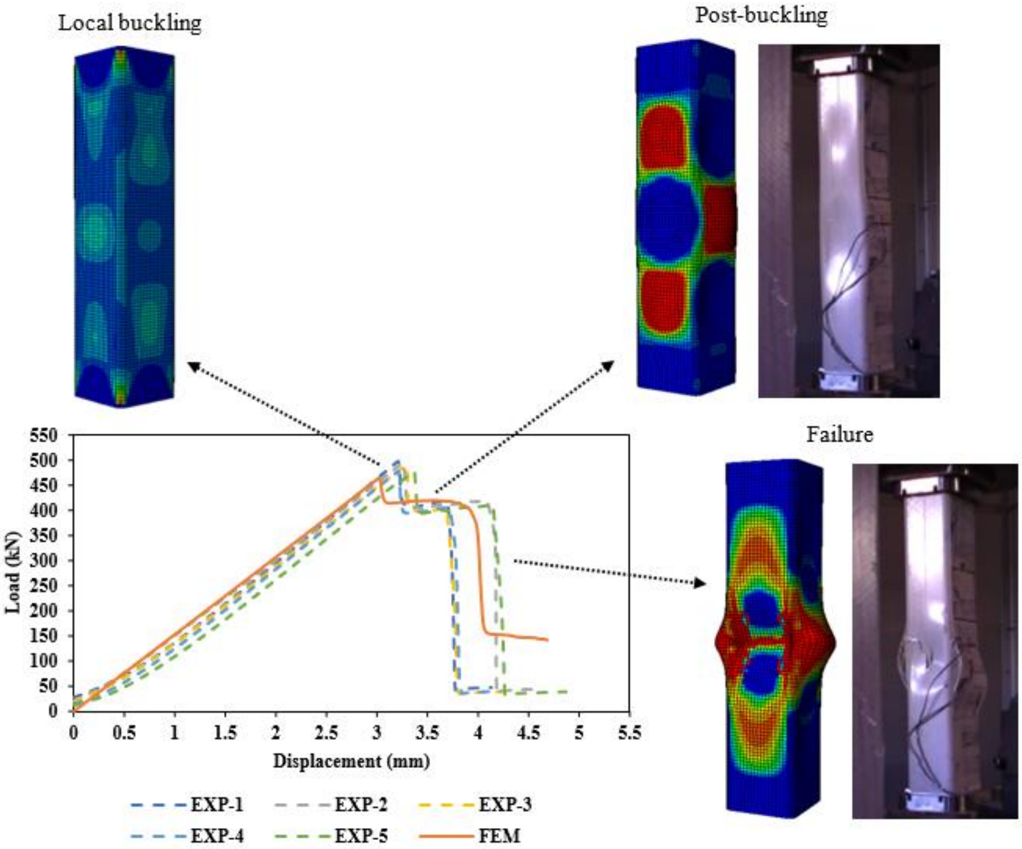

Fig. 2. Experimental vs FEM load-axial displacement curves and failure sequence of the hollow box profile (at same time increment).

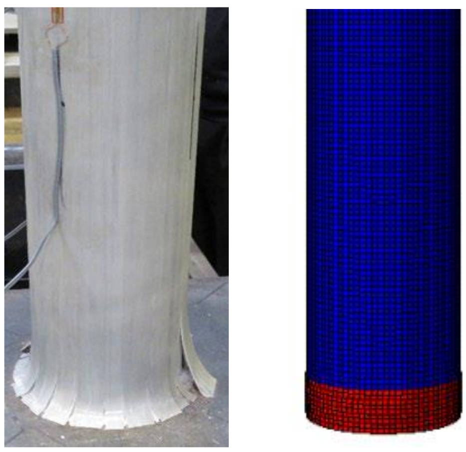

Fig. 3. Experimental [50] vs FEM failure mode of the hollow circular profile.

4. DESIGN OF EXPERIMENTS

Studying the six design parameters within one full factorial Design of Experiment (DOE) is not feasible due to the huge size of the experiment matrix and the enormous computational cost. Thus, the design parameters were studied in two phases. In the first phase, two separate full factorial DOEs were performed. One DOE was on the layup parameters of wound fibre angle, axial-to-wound fibres ratio and stacking sequence. The other DOE was on the geometric parameters of wall thickness, cross-sectional aspect ratio, and corner radius. In the second phase, the three most significant parameters were identified from the two DOEs in the first phase. They were grouped to perform the third full factorial DOE. With the pieces of evidence from the three DOEs, the design guidelines and recommendations for compressive applications were carefully made for pultruded FRP profiles.

Reduced design of experiments, such as the Taguchi method, face limitations in tracing unknown interactions since the intended interactions have to be selected in the design and before the analysis is performed. Thus, a full factorial design was selected for all the parametric studies to account for all the possible interactions [55]. Minitab 19 statistical analysis software was used to design the parametric studies and analyse the numerical results. In all the parametric studies of both the hollow box and circular profiles, the fibre volume fraction (V_f) was kept constant at 0.6 by using the same mechanical properties of an E-glass/Vinyl-ester lamina in all models.

4.1 Level settings of geometric parameters

It is evident that the geometric parameters play a significant role in the profile’s stability and its failure mode [22,40]. Thus, each geometric parameter was studied individually (when a parameter is studied, the others remain constant) to capture any inflection points in the structural behaviour and assess the practical levels range of each parameter to be implemented in the geometric factorial parametric study for the box profile. No geometric parametric study was performed on the hollow circular profile since it has only the wall thickness as a geometric parameter. The wall thickness of the hollow circular profile will be studied in this section individually to assign its range of levels. Then it will be introduced to the parametric study on the effective parameters, as will be shown in Section 5.3. The layup parameters (wound fibre angle, axial-to-wound fibres ratio, and stacking sequence) values currently used in production were maintained constant across all these individual parametric studies, as shown in Table 1.

The wall thickness studied values were 5.2, 6.4, 7.6, 8.8, and 10.0 mm for the box profile and 1.0, 1.2, 1.5, 2, and 6 mm for the circular profile. These values were successively chosen to circle the inflection point in the failure modes. The numerical results of the effect of the wall thickness on the hollow box and circular profiles are shown in Fig. 4 and Fig. 5, respectively. The wall thickness was normalised using the wall width (b/t) for the hollow box profile and the outer diameter (D/t) for the hollow circular profile to obtain the wall slenderness. For both profiles, the axial stiffness (EA/L) is increasing exponentially when the wall thickness is increased due to the increase in the cross-sectional area. The box profile benefited more from the increase in the wall thickness compared to the circular profile in terms of the axial stiffness due to its larger perimeter that obtains a higher cross-sectional area than a circular profile with the same wall thickness.

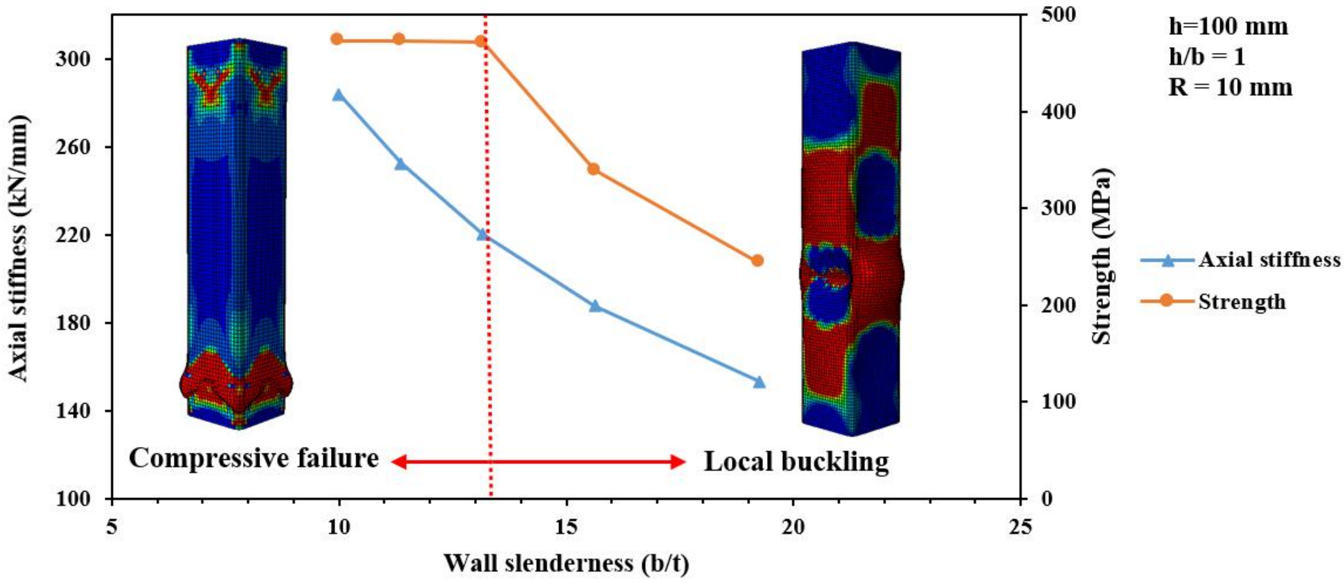

Fig. 4. Wall thickness effect on the compressive behaviour of hollow box PFRP profile.

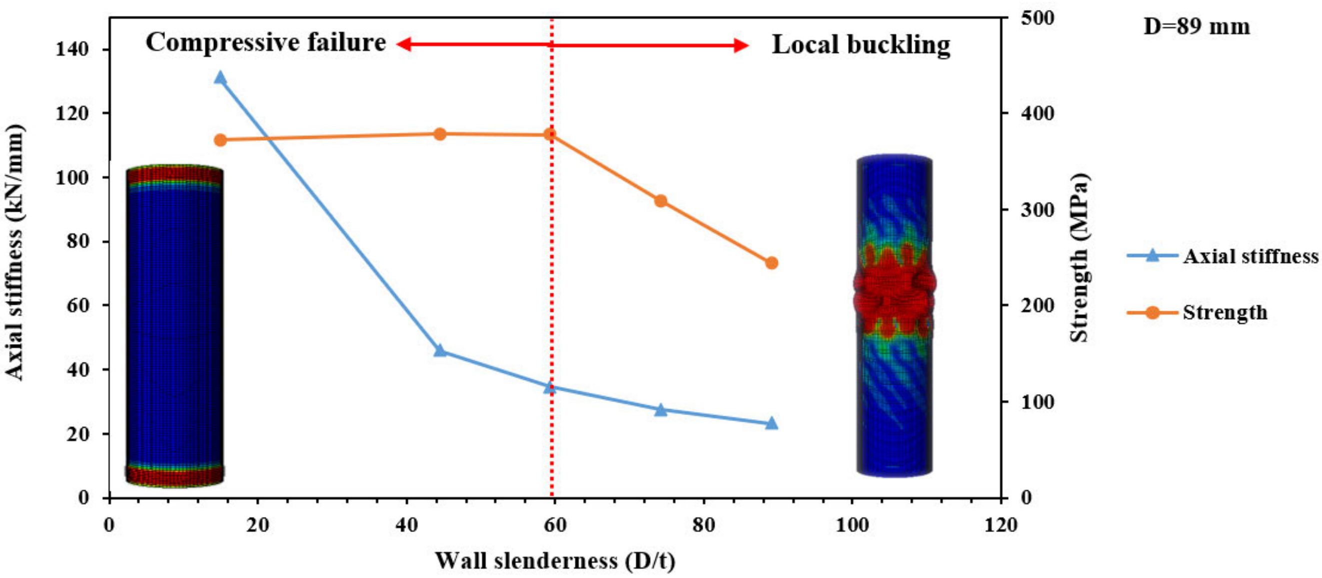

Fig. 5. Wall thickness effect on the compressive behaviour of hollow circular PFRP profile.

It is clear that local buckling greatly reduces the compressive strength and trigger the failure before the ultimate material strength is reached. For example, the numerical compressive strength of the box profile was 243 MPa, while its ultimate material strength from the coupons test was 485 MPa [56]. The compressive strength was reduced to half and failed due to instability, not a material failure. Numerically, increasing the wall thickness of the box profile increased the compressive strength up to 473 MPa and shifted the failure mode from local buckling to compressive failure of fibres. The inflection point between local buckling and compressive failure is larger in the hollow circular profiles (D/t = 59.3) compared to the hollow box profiles (b/t = 13.2) due to the higher circumferential confinement and uniform stress distribution in curved shells compared to plates, which provides a higher buckling resistance. When reviewing literature and manufacturing manuals, it appears that composite circular tubes with such a high wall slenderness ratio are usually produced by filament winding, not pultrusion [4,7,12,57–60]. Consequently, the chosen levels of the wall thickness of the circular profile were all taken within the compressive failure zone to represent typical pultruded tubes, as will be shown in Section 5.3. Regarding the hollow box profile, the levels of wall thickness were chosen to move gradually from local buckling to compressive failure so that different trends can be observed. For that purpose, wall thicknesses of 5.2, 6.4, and 7.6 mm were selected for the geometric parametric study, as shown in Table 4.

Table 4: Levels range for full factorial study on the geometric parameters of the hollow box profile.

Geometric parameter	Level 1	Level 2	Level 3
Wall thickness (mm)	5.2	6.4	7.6
Cross-sectional aspect ratio (h/b)	1 (100/100)	2 (133.5/66.5)	3 (150/50)
Corner radius (mm)	10	17.5	25

In addition to hollow square pultruded FRP profiles, rectangular profiles are also used for compression applications [37,61–63]. The cross-sectional aspect ratio was assigned as a design parameter to investigate the effect of changing the cross-sectional height and width while maintaining the same cross-sectional area. This parameter was defined as the height-to-width (h/b) ratio. The studied (h / b) ratios were 1.0, 1.5, 2.0, 2.5, and 3.0, and were chosen to follow up the change in the section from square to overstated rectangular. Fig. 6 shows the results of changing the aspect ratio on the load-displacement behaviour of the hollow PFRP section.

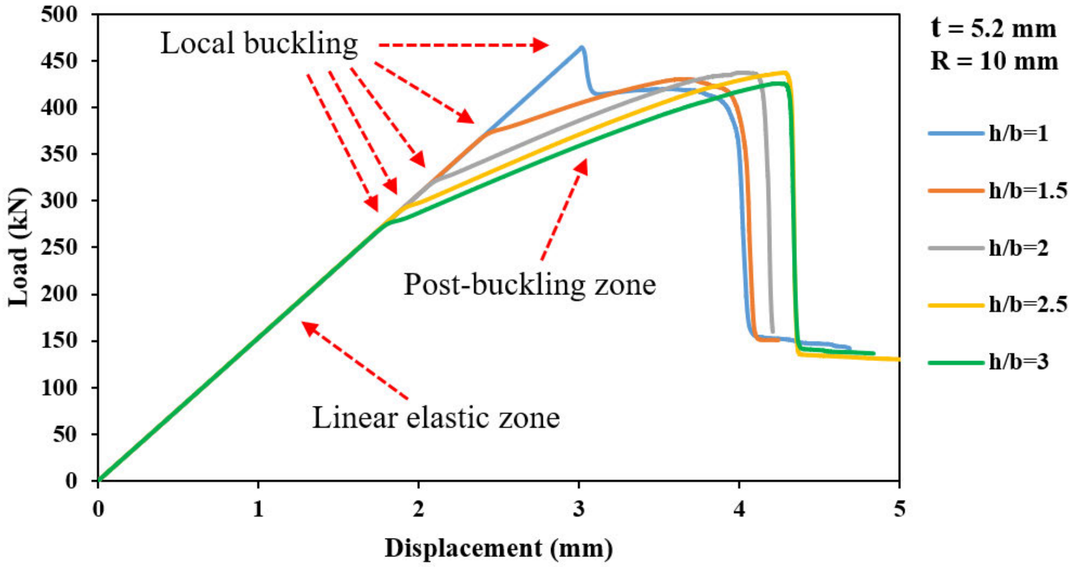

Fig. 6. Cross-sectional aspect ratio effect on the compressive behaviour of hollow box pultruded FRP profile.

It can be noticed that the buckling load decreases as the h/b ratio increases due to the increase in the unsupported length of the two opposite wide walls. This observation agrees with the findings of [29]. With the buckling load decrease, the post-buckling zone extends, limiting the linear elastic zone. Similar behaviour was observed experimentally by [37] for hollow rectangular glass FRP stub columns. After these walls are buckled, the load-axial displacement curves showed a reduction in the slope, in a sign of degradation in the axial stiffness (EA/L) during the post-buckling zone. The post-buckling zone became more stable in the rectangular sections as their degraded slopes were still positive and their load capacity was higher than the buckling load. Whereas the square profile exhibited an unstable post-buckling zone with a zero slope (the column undergoes axial displacement with no higher load resistance) and a load capacity equals to the buckling load. This observation was referred to the number of buckled walls at the post-buckling zone. In the rectangular profiles, the two wider walls are buckled but the two narrower walls are still sustaining load. Thus, providing a higher load capacity than the buckling load and a positive axial stiffness. On the other hand, all four walls buckle simultaneously in the square profile preventing any higher load resistance and causing a sharp drop in the load-axial displacement curve due to the sudden loss of stability. Local buckling triggers the matrix tensile failure due to the out-of-plane localised waves in the walls accompanying the buckling, as shown in Fig. 7. Nevertheless, the strength remains nearly constant across all h/b ratios. This can be referred to the increase in the buckling load capacity of the shorter walls when the h/b ratio is increased, which compromises the reduction in the buckling load capacity of the longer walls and allow larger axial displacement. No out-of-plane deformation was observed for the column axis, in a sign that global buckling did not occur.

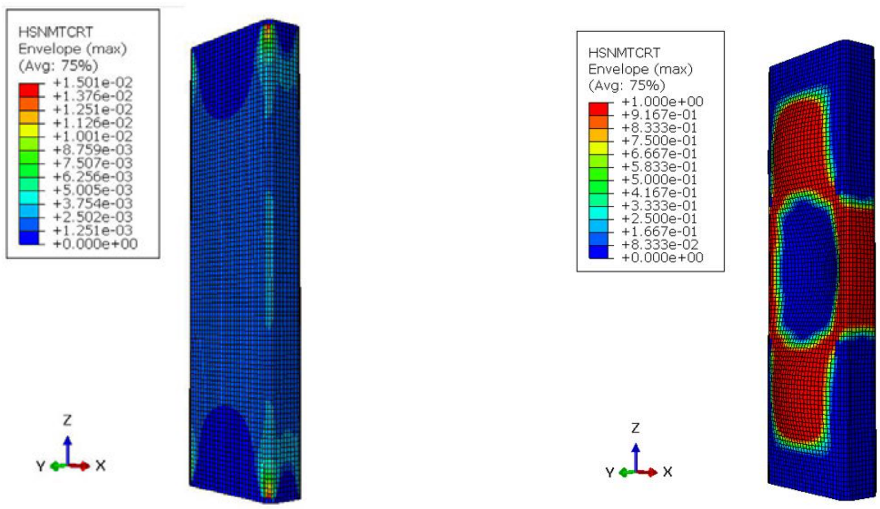

(a) (b)

Fig. 7. Matrix tensile failure of hollow box PFRP profile with h/b ratio equals 3 (a) linear elastic zone and (b) post-buckling zone.

The chosen h/b ratios for the geometric parametric study were 1, 2, and 3, which were selected to reflect square, moderate rectangular, and overstated rectangular shapes, respectively, as shown in Table 4.

Hollow box PFRP profiles are featured with fillet corners to facilitate the pulling process, avoid wound fibres fracture under high pulling force, reduce stress concentration, and minimise resin-rich zones at these corners [12,40,59,60,62]. The corner radius was studied here to assess its effect on the structural performance of these box profiles. In this research, the corner radius nomenclature is used to refer to the outer corner radius. The inner corner radius equals the outer corner radius minus the wall thickness. The studied values of the corner radius were 5, 10, 15, 20, 25, 30, 35, and 40 mm. These values were chosen to cover the entire range from square to circular section. Fig. 8 shows the numerical results of changing the outer corner radius of the hollow box PFRP profile. The corner radius was normalised with respect to the wall width (b/R) to trace the section change from box to circle shape. Increasing the corner radius enhanced the compressive strength since it increases the circumferential confinement and distributes the stresses uniformly. However, the axial stiffness (EA/L) slightly decreased since the cross-sectional area was reduced with a larger fillet. It was found that a large corner radius is needed to transfer the local buckling into compressive failure, which nearly transforms the box section into a circular profile. A transition zone was found between the local buckling and compressive failure zones, in which local buckling occurs at the walls but is restrained by the larger corners.

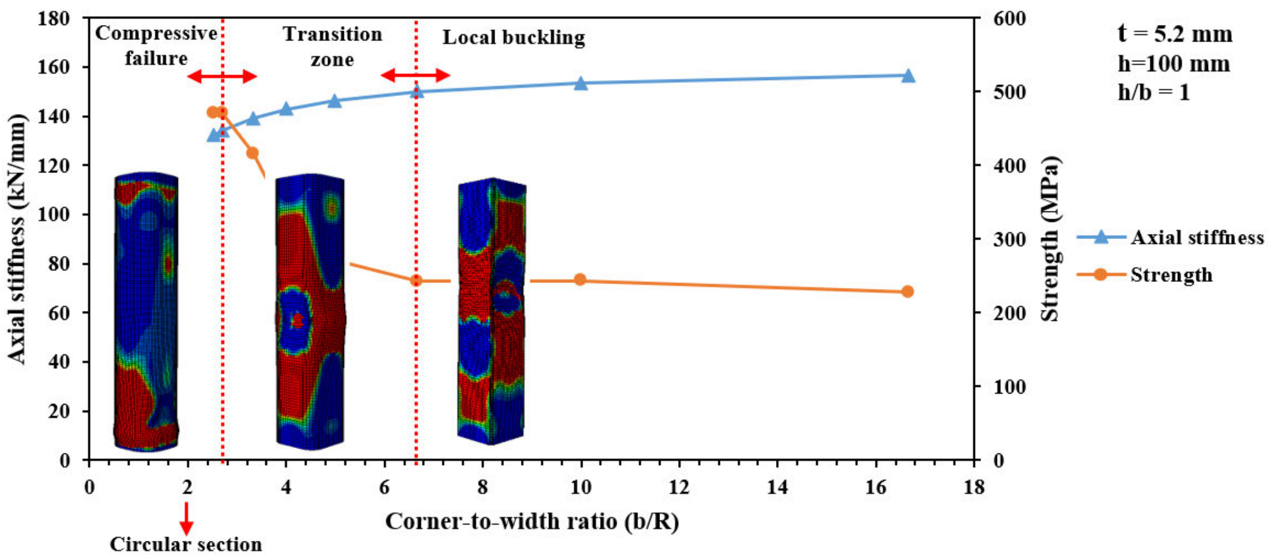

Fig. 8. Corner radius effect on the compressive behaviour of hollow box pultruded FRP profile.

The maximum selected corner radius for the parametric study was 25 mm (b/R = 4), as shown in Table 4, to maintain the box shape of the profile and to avoid any overlap between larger corner radii and cross-sectional aspect ratios.

The layup parameters (wound fibre angle, axial-to-wound fibres ratio, and stacking sequence) values currently used in production were maintained constant within this parametric study, as shown in Table 1.

4.2 Level settings of layup parameters

For both box and circular profiles, three levels were selected for each layup parameter, as shown in Table 5. Wound fibre angles of $20^{o}, 50^{o}$, and 80^{o}, measured from the axial direction of the pultrusion, were chosen to assess the variation of the winding angle of the wound fibres on the structural behaviour of the profile. The axial fibre percentage was assigned a larger value than the wound fibre percentage in all the levels of the study since the studied profiles are intended for axial compression applications. The chosen stacking sequences were representing three levels of confining the axial rovings by the wound rovings. Symmetric and balanced layups were used to minimise the elastic coupling effects since stacking sequences with coupling are not preferred for compressively loaded members as they can be vulnerable to buckling, bending, and warping due to thermal effects [13,16,40,64,65]. The geometric parameters (wall thickness, cross-sectional aspect ratio, and corner radius) values currently used in production were maintained constant within this parametric study, as shown in Table 1.

Table 5: Levels range for full factorial study on the layup parameters of the hollow box and circular profiles.

Layup parameter	Level 1	Level 2	Level 3
Wound fibre angle (Deg)	20	50	80
Axial-to-wound fibre percentage (%)	[60/40]	[75/25]	[90/10]
Stacking sequence	[0/+θ/-θ/0/-θ/+θ/0]	[+θ/0/-θ/0/-θ/0/+θ]	[+θ/-θ/0/-θ/+θ]

5. RESULTS AND DISCUSSION

The design parameters were assessed based on the two critical responses in structural design, namely, the axial stiffness (EA/L) and the compressive strength. Two-way ANOVA (analysis of variance) was performed to calculate the contribution (significance) of each design parameter statistically. Also, the main effect and interaction plots were used to obtain the effect and interaction of each design parameter, respectively. These plots display the averaged values for the levels of each parameter [66]. The full list of the design matrices and numerical results of the parametric studies are presented in Appendix A.

5.1 Effects of the geometric parameters of the box profile

The contributions of each geometric parameter on the compressive behaviour of the hollow box PFRP profile is shown in Table 6. The two-way ANOVA model results show that the wall thickness is the dominant parameter controlling the axial stiffness (EA/L) since its change will change the cross-sectional area of the profile. Whereas changing the h/b ratio will not change the area and the corner radius effect on the area is small compared to the wall thickness effect. It is worth noting that the h/b ratio does not affect the axial stiffness until local buckling occurs in the wide walls, after which, the stiffness is degraded, as shown in Fig. 6. The wall thickness and width control the compressive strength of hollow box profiles. Since these profiles are dominated by local buckling, the wall slenderness components play a significant role in profile stability. The contribution of the corner radius was modest due to the selected range of levels, as highlighted in section 4.1. Larger corner radii are needed to obtain a significant contribution, which nearly transforms the box section into circular. Increasing the corner radius from 10 mm to 25 mm reduced the cross-sectional area of the box profile by 7.0% and resulted in a reduction in the axial stiffness by 6.9%. Nevertheless, it enhanced the compressive strength exponentially up to 34.8% due to the uniform distribution of stresses at these critical zones.

Table 6: Percentile contribution of each geometric parameter on the compressive behaviour of the hollow box PFRP profile.

Geometric parameter	Axial stiffness (EA/L)	Strength
Wall thickness (%)	96.22	62.61
Cross-sectional aspect ratio (h/b) (%)	0.00	30.21
Corner radius (%)	3.77	5.52
Error (%)	0.01	1.66
ANOVA R^2 (%)	99.99	95.34

Increasing the wall thickness reduced its slenderness ratio and enhanced its stability, which provided more strength across all h/b values, as shown in Fig. 9 (a). When studying the h/b ratio separately, as in section 4.1, it was found that different h/b ratios obtained nearly the same strength. However, when the interaction between the h/b ratio and the wall thickness was considered in a full factorial design, it was found that the h/b ratio inversely affects the compressive strength of the hollow box profile, as shown in Fig. 9 (a). It was due to the increase in the width of the wide walls with the increasing h/b ratio. Since the wall slenderness of these walls was still higher compared to the hollow square profile, it resulted in a lower buckling capacity.

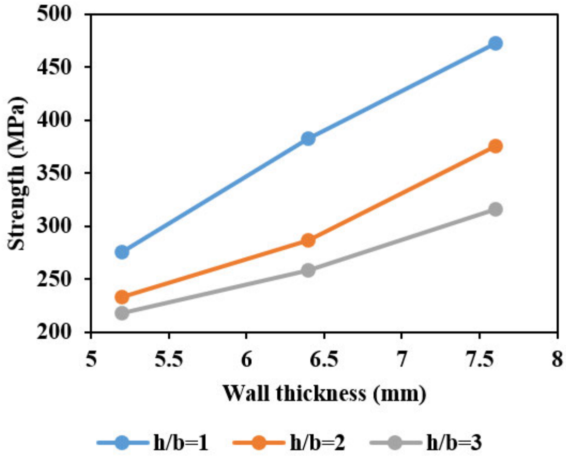

(a)

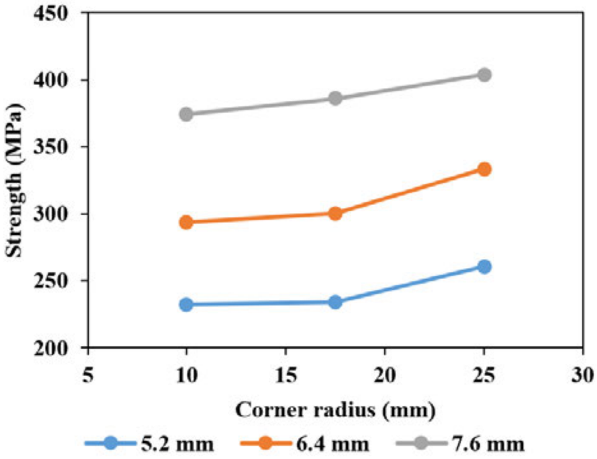

(b)

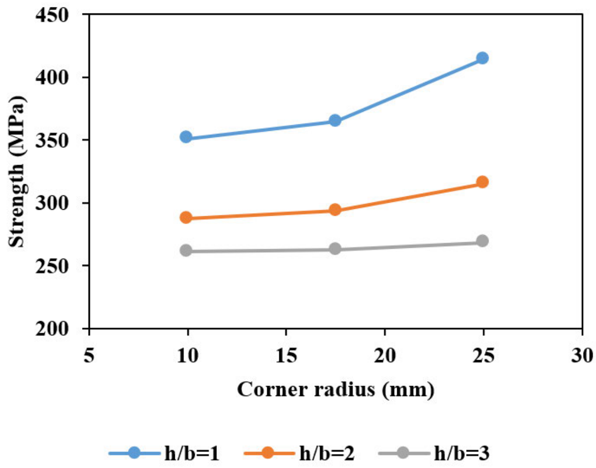

(c)

Fig. 9. Interaction plots of the geometric parameters affecting the compressive strength of hollow box PFRP profile (a) wall thickness and h/b ratio (b) wall thickness and corner radius and (c) h/b ratio and corner radius.

The interactions between the three geometric parameters were found to be significant. The first interaction is shown in Fig. 9 (a) between the wall thickness and h/b ratio. Although the increase in h/b ratio reduced the wall slenderness of the two narrow walls, it could not compensate for the high wall slenderness of the two wide walls. Only a wall thickness of 7.6 mm with h/b ratio of 1 obtained compressive failure with wall slenderness (b/t) equaling 13.2. The failure mode was local buckling for all the other cases since their maximum wall slenderness was higher than this critical value. Reducing the maximum wall slenderness obtains the most stable configuration. The optimal h/b value for hollow box profiles is to ensure all walls buckle simultaneously to achieve higher compressive strength. Also, the optimal enhancement from the increase in the wall thickness occurs when the h/b ratio equals 1, as shown in Fig. 9 (a).

The second interaction is observed in Fig. 9 (b) between the wall thickness and the corner radius. Increasing the corner radius is effective in increasing the compressive strength of slender walls. Nevertheless, when the wall slenderness is reduced, and the failure mode moves from local buckling to compressive failure, the corner radius enhancement of the strength diminishes, as shown in Fig. 9 (b). Thus, it is recommended to use a large corner radius in the design against local buckling for walls with b/t ≥ 13.2, while considering a small corner radius for the design against compressive failure (b/t ≤ 13.2) to enhance the axial stiffness (EA/L).

The third interaction is between the h/b ratio and the corner radius. From Fig. 9 (c), it appears that the increasing h/b ratio reduces the effect of the corner radius on improving the compressive strength. This was attributed to the increase in the wide walls slenderness. To obtain the optimal improvement in strength when increasing the corner radius, an h/b ratio of 1 should be used. This agrees with the recommended h/b ratio from the first interaction between the wall thickness and h/b ratio.

We introduce a new concept of "post-buckling zone extent" to assess the effect of the geometric parameters on the post-buckling behaviour of the hollow box profile. Understanding this effect can help in designing thin-wall members, at which, buckling will be a dominant failure mode and the post-buckling zone with degraded stiffness (EA/L) is a critical design criterion. It measures the horizontal extent of the post-buckling zone at the load-axial displacement curve (shown in Fig. 6) with respect to the ultimate axial displacement as a percentile:

$$Post\text{-}buckling\ zone\ extent\ (\%) = \frac{Axial\ displacement\ of\ the\ post\text{-}buckling\ zone}{Ultimate\ axial\ displacement} \times 100\% \qquad (1)$$

For example, a value of 20% means that the post-buckling zone forms 20% of the profile axial displacement and the linear elastic zone forms 80%. Increasing the wall thickness increases the wall stability and stiffness, and moves the failure mode from local buckling to compressive failure. Thus, the post-buckling zone will diminish as the wall thickness is increasing. In contrast, increasing the h/b ratio will increase the maximum wall slenderness and reduce the buckling load allowing for a larger post-buckling zone, as shown in Fig. 10 (a). Using h/b ratio of 1 obtained the minimum post-buckling zone extent and minimum degradation in stiffness, and provided the maximum linear elastic zone. Increasing the corner radius reduced the post-buckling zone as it increased the compressive strength and shifted the failure mode closer to compressive failure. When the profile was moved to the compressive failure zone (b/t ≤ 13.2), the post-buckling zone diminished across all corner radii, as shown in Fig. 10 (b). Thus, increasing the corner radius against local buckling failure while reducing it against compressive failure will obtain optimal design, in consistency with the previous analysis from the second interaction.

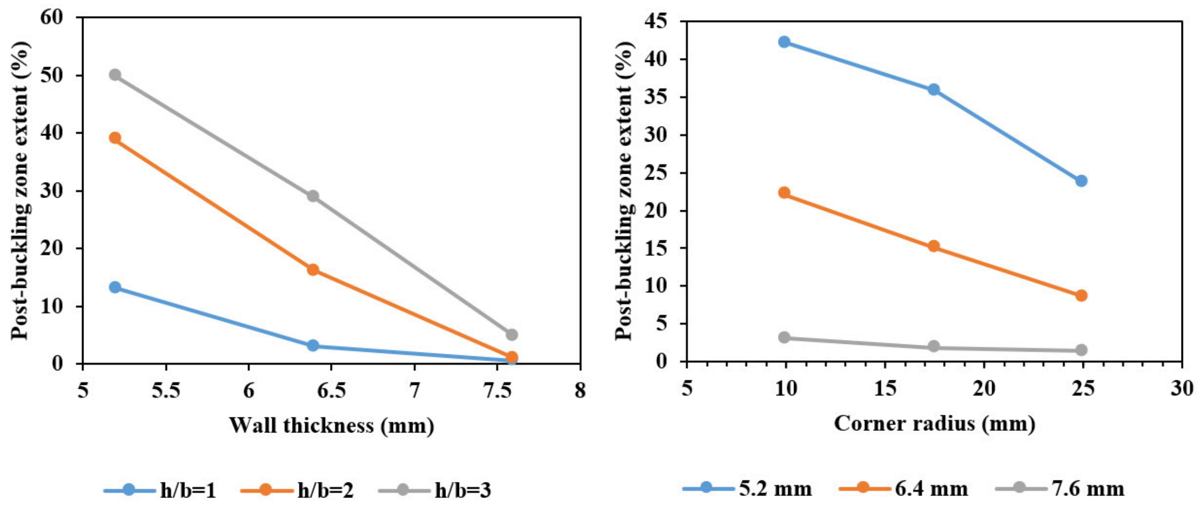

(a) (b)

Fig. 10. Interaction plots of the geometric parameters affecting the post-buckling zone extent of hollow box PFRP profile (a) wall thickness and h/b ratio and (b) wall thickness and corner radius.

From the discussion above, it is clear that the corner radius (outer radius) has a contradictive effect of reducing the axial stiffness while increasing the compressive strength. An alternative solution was proposed by keeping the outer radius (R) at its minimum applicable value from the manufacturing perspective and increasing the inner radius (r) of the corner with axial fibres. The box shape can be maintained, while both the axial stiffness and compressive strength can be increased with the reduction in the effective wall width and the increase in the corner restraint. Fig. 11 shows the numerical results of inner-to-outer radii (r/R) ratios of 0.5, 1.0, 1.5, 2,0 2.5, 3.0, and 3.5, with R being constant at 10 mm. It is recommended to use r/R > 1 to increase the area of the corners and strengthen the stresses concentration zones. It was found that increasing the r/R ratio is more beneficial than increasing the wall thickness, as shown in

Fig. 12. Local buckling can be eliminated, and the ultimate compressive strength of the section can be obtained with 12.6% less cross-sectional area.

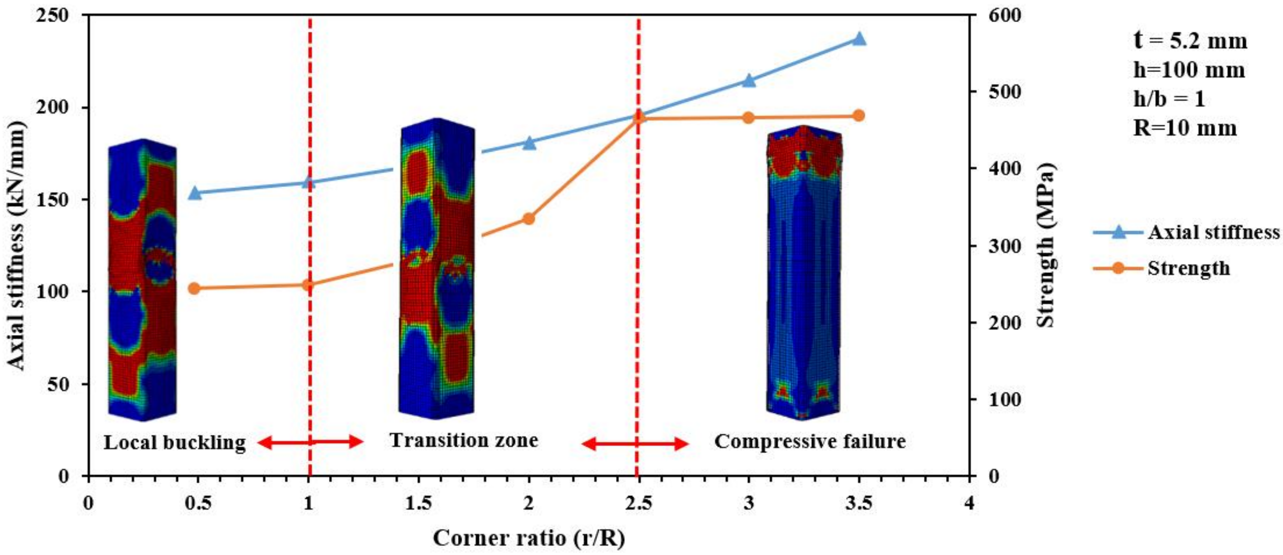

Fig. 11. Effect of the corner inner-to-outer radii ratio (r/R) on the compressive behaviour of hollow box PFRP profile, with R being constant at 10 mm.

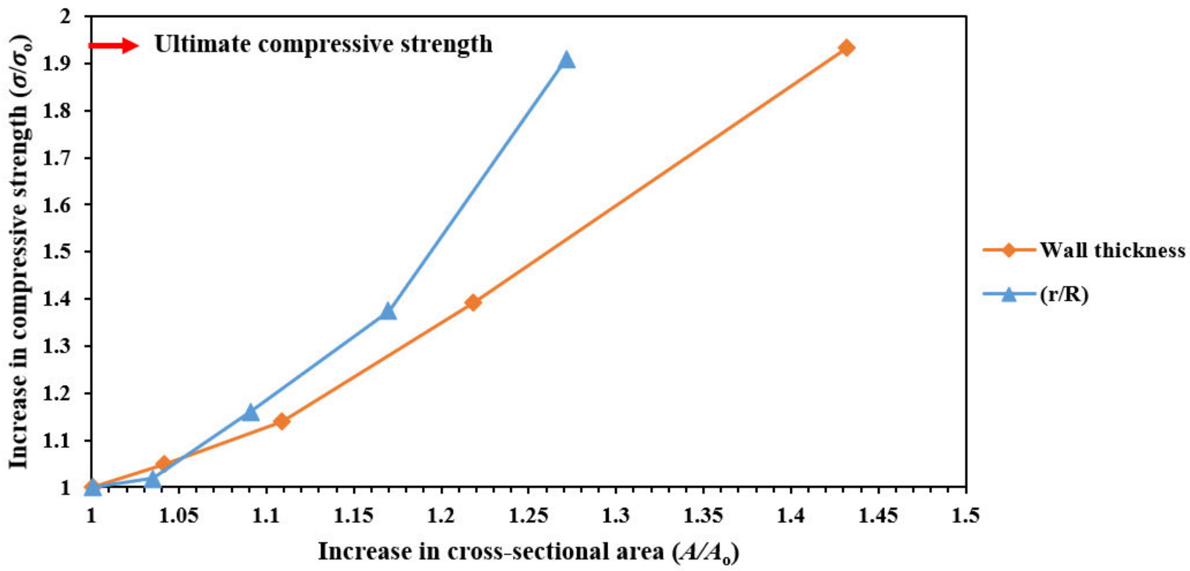

Fig. 12. Comparison of the wall thickness increase vs r/R ratio increase on the compressive strength of the hollow box PFRP profile.

5.2 Effects of the layup parameters

In this section, the results of the parametric studies on the layup parameters of the hollow box and circular profiles are discussed. The numerical models predicted that the box profile failed by local buckling while the circular profile was dominated by compressive failure due to the different stress formation and distribution. The contribution of each layup parameter is shown in Table 7. According to the Classical Laminated Plate Theory (CLPT), the stacking sequence does not affect the stiffness of the laminate. This agrees with the numerical results, as the contribution of the stacking sequence on the axial stiffness (EA/L) approaches to zero. Shifting the wound plies to the exterior side and the axial plies to the interior side of the profile provided higher confinement and compressive strength, especially for the hollow circular profile with a percentile of up to 4.7%, as shown in Fig. 13. Nevertheless, the stacking sequence effect on the compressive strength of the hollow box profile was insignificant with a percentile of 0.5%. The stacking sequence is essential in the design against delamination. However, delamination of plies was not dominant in determining the compressive strength of the studied hollow PFRP profiles due to the high confinement of the closed geometry and the continuous wound fibres across the section as reported by [54]. Also, all the tested stacking sequences presented the optimal choices against buckling since they were symmetric and balanced. Thus, aligning the wound fibres to the exterior side of the layup had a negligible effect on the compressive strength of the studied profile. This finding agrees with the reported results of [26] on using symmetric stacking sequences with different locations of axial and inclined fibres. The wound fibre angle contributes more to the compressive strength of the hollow box profile compared to the hollow circular profile. This was referred to the influence of the wound fibre angle on the flexural stiffness of the walls dominated by local buckling, as will be explained following.

Table 7: Percentile contribution of each layup parameter on the compressive behaviour of the hollow box and circular PFRP profile.

Layup parameter	Hollow box profile		Hollow circular profile	
	Axial stiffness	Strength	Axial stiffness	Strength
Wound fibre angle (%)	50.7	43.3	53.5	34.8
Axial-to-wound fibres ratio (%)	48.7	52.7	44.2	55.2
Stacking sequence (%)	0.00	1.39	0.04	8.17
Error (%)	0.6	2.7	2.2	1.9
ANOVA R^2 (%)	99.4	92.3	98.3	98.1

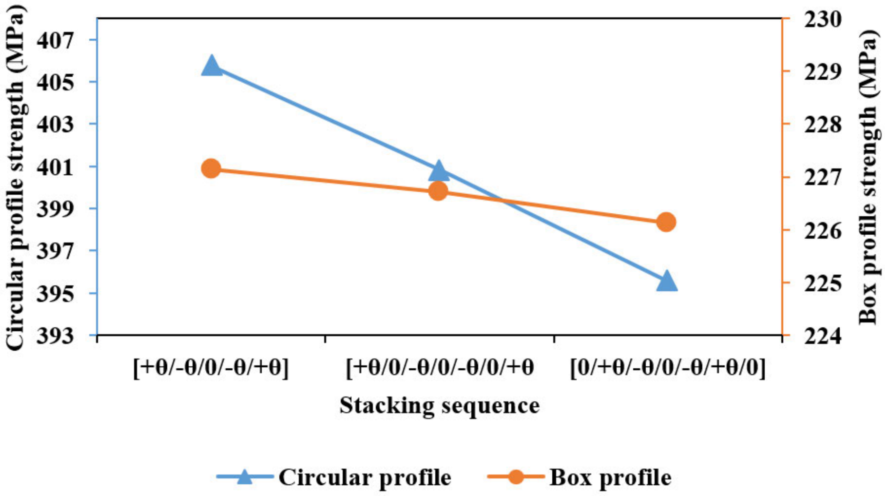

Fig. 13. The main effect of stacking sequence on the compressive strength of the hollow box and circular PFRP profiles.

The effect of the layup parameters on the axial stiffness (EA/L) was the same for both the hollow box and circular profiles, as shown in Fig. 14. The wound fibre angle affected the axial stiffness over two different zones. As the wound fibre angle increases till 50^o, the axial stiffness decrease is quite steep. Whereas, the reduction in the axial stiffness after 50^o is minor. Similar behaviour was reported by [67] for pultruded GFRP coupons. It can be explained by the inflection point between the axial and transverse components of the column stiffness at $\theta = 45^o$. When the angle of the wound fibres is below that angle, the wound fibres' contribution to the axial stiffness becomes significant, which increases the axial stiffness sensitivity. While their contribution to the axial stiffness becomes small when their angle exceeds the inflection angle, resulting in an insensitive axial stiffness zone. An interaction can be noticed between the wound fibre angle and axial-to-wound fibres ratio. Increasing the axial fibre percentage enhanced the axial stiffness of the profile as more fibres are directed against the axial compressive loading. As the axial fibre percentage is increasing, the effect of the wound fibre angle on the axial stiffness is decreased.

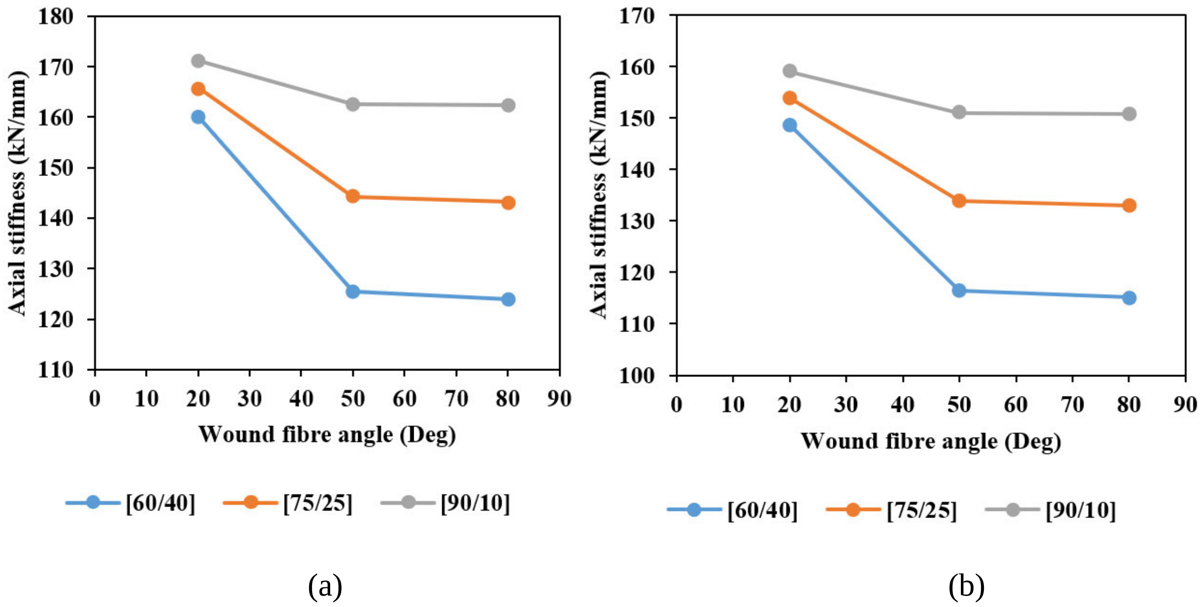

Fig. 14. Effect of the wound fibre angle on the axial stiffness of hollow (a) box and (b) circular PFRP profiles with different axial-to-wound fibres ratio.

The maximum compressive strength of the hollow box profile, which is dominated by local buckling, was obtained at 50^o, as shown in Fig. 15 (a). Also, the increase in the axial fibre percentage resulted in a reduction in the compressive strength of the hollow box profile. It was due to the effect of the axial-to-wound fibres ratio on the flexural stiffness components (D_{11}, D_{22}, D_{12}, and D_{66}) of the laminated walls. When the axial fibre percentage is decreasing, D_{11} is reduced, while D_{22}, D_{12}, and D_{66} are increased, resulting overall in higher resistance of the wall against out-of-plane deformations (buckling). The maximum buckling capacity can be obtained with the lowest possible axial fibre percentage and a medium wound fibre angle. On the other hand, the maximum compressive strength of the hollow circular profile occurs at the lowest wound fibre angle, as shown in Fig. 15 (b), since the contribution of the wound fibres to resist the axial compression will increase. As the wound fibre angle increases, the strength is reduced until 50^o. After that, the compressive strength increases gradually, which can be referred to the increase in the circumferential confinement. Contrary to the hollow box profile, the compressive strength in the hollow circular profile is directly proportional to the axial fibre percentage since more axial fibres will provide higher resistance against axial compressive failure. Consequently, the optimal compressive strength can be obtained with the highest axial fibre percentage and the lowest wound fibre angle. From Fig. 15, it appears that as the axial fibre percentage is increased, the effect of the wound fibre angle on the compressive strength is decreasing since the percentage of the wound fibres is decreasing too.

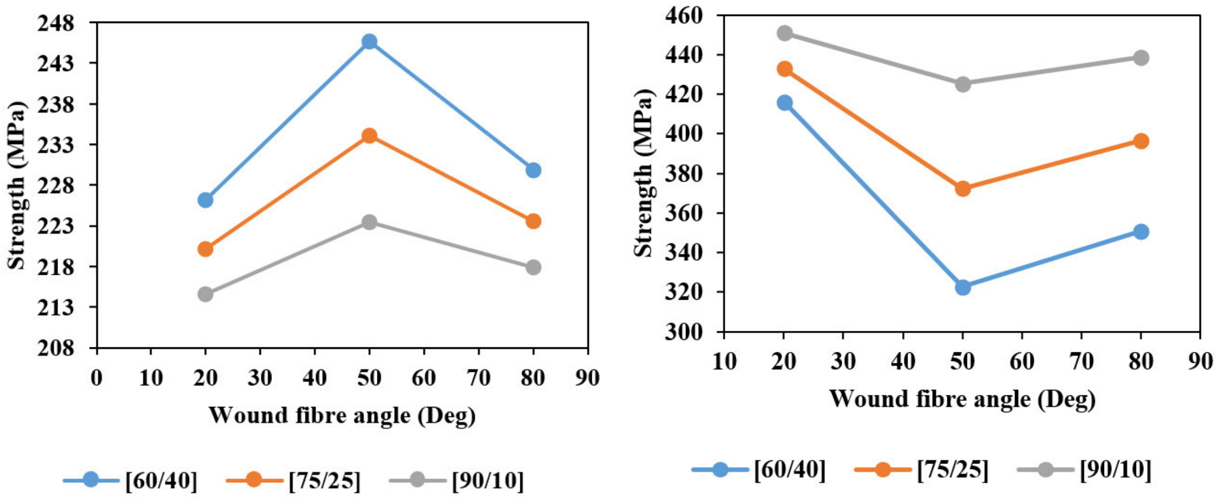

(a) (b)

Fig. 15. Effect of the wound fibre angle on the compressive strength of hollow (a) box and (b) circular PFRP profiles with different axial-to-wound fibres ratio.

It is evident that local buckling affects not only the design for compressive strength but also the design for axial stiffness. The maximum axial stiffness and compressive strength are not concurrent within the local buckling failure zone since each one requires different configurations of the layup parameters. However, the maximum stiffness and the maximum strength values are concurrent within the compressive failure zone with the optimal layup parameters. If the local buckling can be avoided by using the recommended geometries in section 5.1, the optimal axial stiffness and compressive strength can both be attained by the lowest wound fibre angle and the highest axial fibre percentage.

5.3 Combined effects of geometric and layup parameters

The parameters with the insignificant contributions presented in Section 5.1 and Section 5.2 were neglected in the combined parametric study since their contribution is still going to be statistically negligible [55]. These neglected parameters were the outer corner radius of the hollow box profile and the stacking sequence. The cross-sectional aspect ratio of the hollow box profile was also neglected since it was found to affect the buckling capacity inversely and causes a reduction in the axial stiffness (EA/L) due to local buckling in the wide walls. These parameters were kept constant within the parametric studies with the values shown in Table 1. The wall thickness, wound fibre angle, and axial-to-wound fibres ratio were shortlisted for the study of combined geometric and layup parameters. The same levels from the first phase studies were chosen for these parameters, as shown in Table 8.

Table 8: Levels range for full factorial study on the parameters of the hollow box and circular profiles.

Effective parameter	Wall thickness (mm)		Wound fibre angle (Deg)	Axial-to-wound fibres ratio (%)
	Box profile	Circular profile		
Level 1	5.2	6.0	20	[60/40]
Level 2	6.4	7.0	50	[75/25]
Level 3	7.6	8.0	80	[90/10]

The contribution of these parameters to the compressive behaviour of hollow PFRP profiles is shown in Table 9. The compressive strength of the hollow box profile is controlled by the wall thickness, in link with the local buckling failure mode. Local buckling is considered to be a stability problem, and the wall thickness is a primary factor affecting the stability, as documented by [68,69]. On the other hand, the compressive strength of the hollow circular profile is independent of wall thickness since this profile failed by compressive failure as the laminate reached its strength limit, which is a material property.

Table 9: Percentile contribution of the effective parameters on the compressive behaviour of the hollow box and circular PFRP profile.

Layup parameter	Hollow box profile		Hollow circular profile	
	Axial stiffness	Strength	Axial stiffness	Strength
Wall thickness (%)	63.05	96.94	48.16	0.57
Wound fibre angle (%)	14.26	1.22	21.23	32.08
Axial-to-wound fibres ratio (%)	20.68	1.25	28.04	65.33
Error (%)	2.01	0.59	2.57	2.02
ANOVA R^2 (%)	95.98	97.41	94.42	97.98

Contrary to the hollow circular profile, an interaction was found between the layup and geometric parameters of the hollow box profiles. Increasing the wall thickness up to 7.6 mm, which presents the inflection point of the failure mode (b/t =13.2), changed the optimal wound fibre angle and axial-to-wound fibres ratio, as shown in Fig. 16 (a) and (b). For b/t > 13.2, the maximum compressive strength was obtained by a wound fibre angle of 50^o and the highest wound fibre percentage to resist local buckling. For b/t ≤ 13.2, a wound fibre angle of 20^o and the highest axial fibre percentage exhibited the maximum compressive strength against compressive failure.

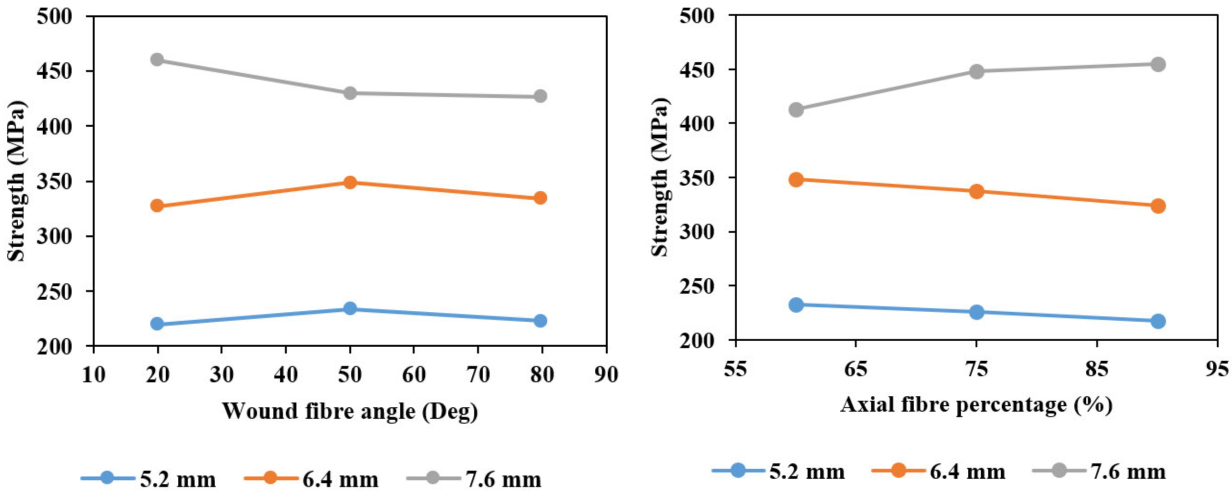

(a) (b)

Fig. 16. Compressive strength of hollow box profile versus (a) wound fibre angle and (b) axial fibre percentage with different wall thicknesses.

Moreover, It was found that the wound fibre percentage was inversely proportional to the post-buckling zone extent, as shown in Fig. 17. This was referred to the increase in the buckling load capacity when the wound fibre percentage is increased, which increased the linear elastic zone in the load-axial displacement curve and reduced the post-buckling zone. Nevertheless, the contribution of the wall thickness (geometric parameter) was more significant compared to the fibre percentage (layup parameter) since buckling and post-buckling behaviours are related to the wall stability as explained earlier in this section.

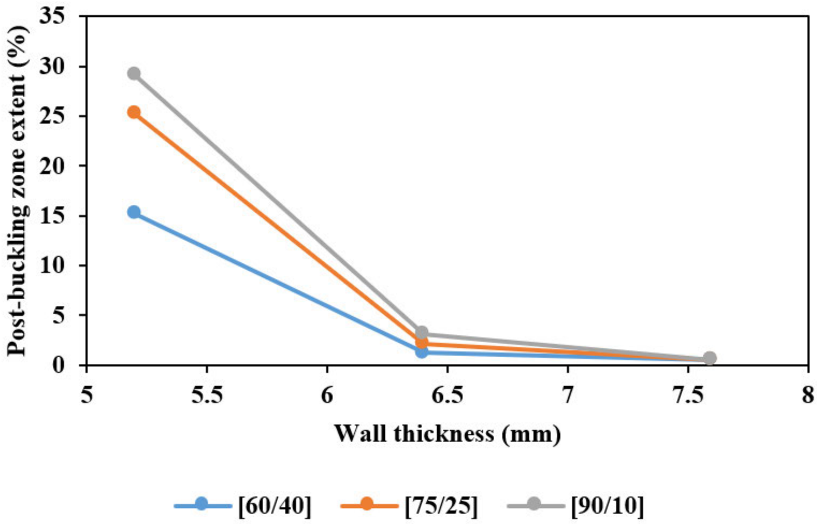

Fig. 17. Wall thickness effect on the post-buckling zone extent with different axial-to-wound fibres ratio.

6. CONCLUSIONS

In this numerical investigation, five full factorial parametric studies were undertaken to examine the effect, contribution, and interaction of the design parameters controlling the compressive behaviour of hollow box and circular PFRP profiles. The numerical models were verified against experimental data. The manufacturing parameters were divided into two groups, according to their nature, to reduce the computational cost. The first group consisted of the wall thickness, cross-sectional aspect ratio (h/b), and the corner radius as the geometric parameters. The wound fibre angle, axial-to-wound fibres ratio, and stacking sequence formed the layup parameters group. Afterwards, the effective parameters from the two groups were studied. Useful guidelines on the design for manufacturing were concluded and recommended configurations of the design parameters were provided. This work reached the following conclusions:

- Hollow circular PFRP profiles fail by a compressive failure of fibres under axial compression due to the higher circumferential confinement and uniform distribution of stresses. Very slender laminated tubes with an approximate wall slenderness ratio (D/t) of 60 would experience local buckling. However, such tubes are not usually manufactured by pultrusion.
- The geometric parameters dominate the structural behaviour of hollow PFRP profiles controlled by stability. In contrast, the layup parameters dictate the behaviour of PFRP profiles controlled by the strength limits. The most significant parameter in controlling the compressive behaviour and failure mode of hollow box PFRP profiles was the wall thickness. It was found that a wall slenderness of b/t ≤ 13.2 is needed to shift the failure mode from local buckling to compressive failure and fully utilise the profile strength. This parameter contributes to nearly half of the axial stiffness (EA/L) of the hollow PFRP profiles.
- For compression applications, h/b = 1 presents the optimal design for hollow box PFRP profiles. For local buckling, It was found that a section with equal height and width will allow a simultaneous buckling of all the walls with a higher compressive strength since it represents the lowest case of the maximum wall slenderness. In addition, it was inferred that the wall with the maximum slenderness ratio controls the failure mode. Consequently, increasing the h/b ratio above the recommended value (h/b = 1) may shift the failure mode from compressive failure to local buckling in the slender walls and greatly reduce the compressive strength of the profile.
- The outer corner radius has a contradictory effect on axial stiffness and compressive strength. It is recommended to increase it to enhance the compressive strength of hollow box profiles dominated by local buckling. In contrast, reducing it will be the optimal choice to provide

higher axial stiffness for profiles dominated by compressive failure. Alternatively, the inner-to-outer radii ratio (r/R) is recommended to be increased to a value larger than one to enhance both the compressive strength and the axial stiffness of hollow box profiles controlled by local buckling.

- Hollow box profile with $(b/t)_{max} \leq 13.2$, $(h/b) = 1$, $(b/R) \geq 10$, and $(r/R) > 1$ presents a recommended configuration of the geometric parameters to avoid local buckling and will provide the optimal case for compression applications with maximum axial stiffness and strength under compressive failure.
- As long as symmetric and balanced layups are used, the effect of the stacking sequence on the compressive behaviour of hollow box PFRP profiles is negligible. Thus, the manufacturing process limitations can control any preferable stacking configuration of the axial and wound fibres provided that an axial ply will form the profile core.
- The wound fibre angle affects the compressive strength of the hollow PFRP profile depending on the failure mode. A medium angle is recommended to resist local buckling, while small or large angles should be used against compressive failure. The optimal axial-to-wound fibres ratio also depends on the failure mode. A higher axial fibre percentage is recommended to endure compressive failure, whereas a higher wound fibre percentage is preferred to sustain local buckling.
- The optimal axial stiffness and compressive strength are not concurrent within the local buckling failure zone since each one requires different configurations of the layup parameters. However, the optimal stiffness and strength values are concurrent within the compressive failure zone as the same layup parameters configurations can achieve them both. Thus, the potential stiffness of the profile cannot be fully allocated at local buckling without inversely affecting the compressive strength. It is recommended to avoid the local buckling failure by using the recommendations provided for the geometric parameters to eliminate it and shift the

failure mode to the compressive failure zone. Consequently, the optimal axial stiffness and compressive strength can be attained by the lowest wound fibre angle and the highest axial fibre percentage.

ACKNOWLEDGEMENTS

This work was supported through a Cooperative Research Centres Projects (CRC-P) Grant (CRCPSIX000117). The authors wish to thank all the supporters for their finance and providing the required computational resources and testing specimens.

APPENDIX A.

Table A. 1 shows the design of experiment of the full factorial study on the geometric parameters of the hollow box pultruded FRP profile along with its results.

Table A. 1: Design matrix and results of the full factorial study on the geometric parameters of the hollow box profile (Wound fibre angle (Deg)=50, Axial and wound fibre percentage (%)=[82.2/17.8], Stacking sequence=[0/+θ/-θ/0/-θ/+θ/0]).

Series	Wall thickness (mm)	Cross-sectional aspect ratio (h/b)	Corner radius (mm)	Axial Stiffness (kN/mm)	Strength (MPa)	Failure mode
S-1	5.2	1	10	154.6	243.7	Local buckling
S-2	5.2	1	17.5	147.8	254.4	Local buckling
S-3	5.2	1	25	142.4	327.6	Local buckling
S-4	5.2	2	10	153.1	229.4	Local buckling
S-5	5.2	2	17.5	147.8	229.8	Local buckling
S-6	5.2	2	25	142.4	240.5	Local buckling
S-7	5.2	3	10	153.2	223.5	Local buckling
S-8	5.2	3	17.5	147.9	217.6	Local buckling
S-9	5.2	3	25	143.3	212.9	Local buckling
S-10	6.4	1	10	186.6	339.3	Local buckling
S-11	6.4	1	17.5	180.0	365.7	Local buckling
S-12	6.4	1	25	173.4	441.4	Local buckling
S-13	6.4	2	10	186.6	280.4	Local buckling
S-14	6.4	2	17.5	180.1	278.6	Local buckling
S-15	6.4	2	25	173.5	300.1	Local buckling
S-16	6.4	3	10	186.6	260.3	Local buckling
S-17	6.4	3	17.5	180.2	256.8	Local buckling
S-18	6.4	3	25	174.4	257.6	Local buckling
S-19	7.6	1	10	219.2	470.3	Compressive failure
S-20	7.6	1	17.5	211.5	472.9	Compressive failure
S-21	7.6	1	25	203.6	472.8	Compressive failure
S-22	7.6	2	10	219.3	352.2	Local buckling
S-23	7.6	2	17.5	211.6	371.1	Local buckling
S-24	7.6	2	25	203.8	404.2	Local buckling
S-25	7.6	3	10	219.4	299.7	Local buckling
S-26	7.6	3	17.5	211.7	313.1	Local buckling
S-27	7.6	3	25	204.9	333.5	Local buckling

Table A. 2 shows the design of experiment of the full factorial study on the layup parameters of the hollow box pultruded FRP profile along with its results. The observed failure mode was local buckling at all the series.

Table A. 2: Design matrix and results of the full factorial study on the layup parameters of the hollow box profile (Wall thickness (mm)=5.2, (h/b)=1, Corner radius (mm)=10).

Series	Wound fibre angle (Deg)	Axial-to-wound fibre ratio (%)	Stacking sequence	Axial Stiffness (kN/mm)	Strength (MPa)
S-1	20	[60/40]	[0/+θ/-θ/0/-θ/+θ/0]	160.1	225.9
S-2	20	[60/40]	[+θ/0/-θ/0/-θ/0/+θ]	160.1	226.1
S-3	20	[60/40]	[+θ/-θ/0/-θ/+θ]	160.1	226.3
S-4	20	[75/25]	[0/+θ/-θ/0/-θ/+θ/0]	165.7	219.2
S-5	20	[75/25]	[+θ/0/-θ/0/-θ/0/+θ]	165.7	219.2
S-6	20	[75/25]	[+θ/-θ/0/-θ/+θ]	165.7	221.7
S-7	20	[90/10]	[0/+θ/-θ/0/-θ/+θ/0]	171.2	214.4
S-8	20	[90/10]	[+θ/0/-θ/0/-θ/0/+θ]	171.2	214.5
S-9	20	[90/10]	[+θ/-θ/0/-θ/+θ]	171.2	214.6
S-10	50	[60/40]	[0/+θ/-θ/0/-θ/+θ/0]	125.5	244.9
S-11	50	[60/40]	[+θ/0/-θ/0/-θ/0/+θ]	125.5	245.6
S-12	50	[60/40]	[+θ/-θ/0/-θ/+θ]	125.5	246.4
S-13	50	[75/25]	[0/+θ/-θ/0/-θ/+θ/0]	144.2	252.7
S-14	50	[75/25]	[+θ/0/-θ/0/-θ/0/+θ]	144.1	234.1
S-15	50	[75/25]	[+θ/-θ/0/-θ/+θ]	144.1	234.4
S-16	50	[90/10]	[0/+θ/-θ/0/-θ/+θ/0]	162.6	222.7
S-17	50	[90/10]	[+θ/0/-θ/0/-θ/0/+θ]	162.6	223.5
S-18	50	[90/10]	[+θ/-θ/0/-θ/+θ]	162.6	223.9
S-19	80	[60/40]	[0/+θ/-θ/0/-θ/+θ/0]	123.9	229.7
S-20	80	[60/40]	[+θ/0/-θ/0/-θ/0/+θ]	123.9	229.9
S-21	80	[60/40]	[+θ/-θ/0/-θ/+θ]	123.9	229.9
S-22	80	[75/25]	[0/+θ/-θ/0/-θ/+θ/0]	143.1	223.1
S-23	80	[75/25]	[+θ/0/-θ/0/-θ/0/+θ]	143.1	223.6
S-24	80	[75/25]	[+θ/-θ/0/-θ/+θ]	143.1	223.8
S-25	80	[90/10]	[0/+θ/-θ/0/-θ/+θ/0]	162.2	217.6
S-26	80	[90/10]	[+θ/0/-θ/0/-θ/0/+θ]	162.2	217.8
S-27	80	[90/10]	[+θ/-θ/0/-θ/+θ]	162.2	217.9

Table A. 3 shows the design of experiment of the full factorial study on the layup parameters of the hollow circular pultruded FRP profile along with its results. The observed failure mode was a compressive failure of fibres at all the series.

Table A. 3: Design matrix and results of the full factorial study on the layup parameters of the hollow circular profile (Wall thickness (mm)=6.0).

Series	Wound fibre angle (Deg)	Axial-to-wound fibre ratio (%)	Stacking sequence	Axial Stiffness (kN/mm)	Strength (MPa)
S-1	20	[60/40]	[0/+θ/-θ/0/-θ/+θ/0]	148.6	406.3
S-2	20	[60/40]	[+θ/0/-θ/0/-θ/0/+θ]	148.6	416.3
S-3	20	[60/40]	[+θ/-θ/0/-θ/+θ]	148.6	425.7
S-4	20	[75/25]	[0/+θ/-θ/0/-θ/+θ/0]	153.7	426.3
S-5	20	[75/25]	[+θ/0/-θ/0/-θ/0/+θ]	153.8	433.2
S-6	20	[75/25]	[+θ/-θ/0/-θ/+θ]	153.9	438.8
S-7	20	[90/10]	[0/+θ/-θ/0/-θ/+θ/0]	159.0	448.6
S-8	20	[90/10]	[+θ/0/-θ/0/-θ/0/+θ]	159.0	451.0
S-9	20	[90/10]	[+θ/-θ/0/-θ/+θ]	159.0	453.1
S-10	50	[60/40]	[0/+θ/-θ/0/-θ/+θ/0]	116.5	314.5
S-11	50	[60/40]	[+θ/0/-θ/0/-θ/0/+θ]	116.5	322.6
S-12	50	[60/40]	[+θ/-θ/0/-θ/+θ]	116.5	330.6
S-13	50	[75/25]	[0/+θ/-θ/0/-θ/+θ/0]	133.8	367.1
S-14	50	[75/25]	[+θ/0/-θ/0/-θ/0/+θ]	133.8	372.3
S-15	50	[75/25]	[+θ/-θ/0/-θ/+θ]	133.8	377.4
S-16	50	[90/10]	[0/+θ/-θ/0/-θ/+θ/0]	151.0	423.1
S-17	50	[90/10]	[+θ/0/-θ/0/-θ/0/+θ]	151.0	425.2
S-18	50	[90/10]	[+θ/-θ/0/-θ/+θ]	151.0	427.3
S-19	80	[60/40]	[0/+θ/-θ/0/-θ/+θ/0]	115.1	344.4
S-20	80	[60/40]	[+θ/0/-θ/0/-θ/0/+θ]	115.0	350.9
S-21	80	[60/40]	[+θ/-θ/0/-θ/+θ]	115.0	357.1
S-22	80	[75/25]	[0/+θ/-θ/0/-θ/+θ/0]	133.0	392.4
S-23	80	[75/25]	[+θ/0/-θ/0/-θ/0/+θ]	133.0	396.8
S-24	80	[75/25]	[+θ/-θ/0/-θ/+θ]	133.0	401.1
S-25	80	[90/10]	[0/+θ/-θ/0/-θ/+θ/0]	150.7	437.1
S-26	80	[90/10]	[+θ/0/-θ/0/-θ/0/+θ]	150.7	438.6
S-27	80	[90/10]	[+θ/-θ/0/-θ/+θ]	150.7	440.6

Table A. 4 shows the design of experiment of the full factorial study on the effective parameters of the hollow box pultruded FRP profile along with its results.

Table A. 4: Design matrix and results of the full factorial study on the effective parameters of the hollow box profile ((h/b)=1, Corner radius (mm)=10, Stacking sequence=[0/+θ/-θ/0/-θ/+θ/0]).

Series	Wall thickness (mm)	Wound fibre angle (Deg)	Axial-to-wound fibre ratio (%)	Axial Stiffness (kN/mm)	Strength (MPa)	Failure mode
S-1	5.2	20	[60/40]	160.1	223.7	Local buckling
S-2	5.2	20	[75/25]	165.7	219.2	Local buckling
S-3	5.2	20	[90/10]	171.2	214.5	Local buckling
S-4	5.2	50	[60/40]	125.5	246.1	Local buckling
S-5	5.2	50	[75/25]	144.2	233.7	Local buckling
S-6	5.2	50	[90/10]	162.6	220.5	Local buckling
S-7	5.2	80	[60/40]	123.9	227.3	Local buckling
S-8	5.2	80	[75/25]	143.2	224.1	Local buckling
S-9	5.2	80	[90/10]	162.3	217.5	Local buckling
S-10	6.4	20	[60/40]	195.1	334.1	Local buckling
S-11	6.4	20	[75/25]	202.0	325.5	Local buckling
S-12	6.4	20	[90/10]	208.6	320.7	Local buckling
S-13	6.4	50	[60/40]	153.0	368.8	Local buckling
S-14	6.4	50	[75/25]	175.7	349.8	Local buckling
S-15	6.4	50	[90/10]	198.2	327.6	Local buckling
S-16	6.4	80	[60/40]	151.0	342.1	Local buckling
S-17	6.4	80	[75/25]	174.5	336.4	Local buckling
S-18	6.4	80	[90/10]	197.7	324.1	Local buckling
S-19	7.6	20	[60/40]	229.4	470.1	Local buckling
S-20	7.6	20	[75/25]	237.4	460.5	Local buckling
S-21	7.6	20	[90/10]	245.3	448.6	Local buckling
S-22	7.6	50	[60/40]	179.9	383.2	Compressive failure
S-23	7.6	50	[75/25]	206.5	443.5	Compressive failure
S-24	7.6	50	[90/10]	233.0	463.1	Local buckling
S-25	7.6	80	[60/40]	177.5	385.0	Compressive failure
S-26	7.6	80	[75/25]	205.1	441.5	Compressive failure
S-27	7.6	80	[90/10]	232.5	454.1	Local buckling

Table A. 5 shows the design of experiment of the full factorial study on the effective parameters of the hollow circular pultruded FRP profile along with its results. The observed failure mode was a compressive failure of fibres at all the series.

Table A. 5: Design matrix and results of the full factorial study on the effective parameters of the hollow circular profile (Stacking sequence=[0/+θ/-θ/0/-θ/+θ/0]).

Series	Wall thickness (mm)	Wound fibre angle (Deg)	Axial-to-wound fibre ratio (%)	Axial Stiffness (kN/mm)	Strength (Mpa)
S-1	6	20	[60/40]	148.6	406.4
S-2	6	20	[75/25]	153.9	427.2
S-3	6	20	[90/10]	159.0	448.6
S-4	6	50	[60/40]	116.5	314.5
S-5	6	50	[75/25]	133.8	367.0
S-6	6	50	[90/10]	151.0	423.1
S-7	6	80	[60/40]	115.0	344.4
S-8	6	80	[75/25]	133.0	392.4
S-9	6	80	[90/10]	150.7	437.1
S-10	7	20	[60/40]	171.3	399.7
S-11	7	20	[75/25]	177.4	420.3
S-12	7	20	[90/10]	183.3	441.3
S-13	7	50	[60/40]	134.3	308.7
S-14	7	50	[75/25]	154.3	360.8
S-15	7	50	[90/10]	174.1	416.2
S-16	7	80	[60/40]	132.7	337.8
S-17	7	80	[75/25]	153.3	385.2
S-18	7	80	[90/10]	173.7	429.4
S-19	8	20	[60/40]	193.5	391.1
S-20	8	20	[75/25]	200.3	413.9
S-21	8	20	[90/10]	206.9	434.5
S-22	8	50	[60/40]	151.7	303.9
S-23	8	50	[75/25]	174.2	355.3
S-24	8	50	[90/10]	196.5	409.7
S-25	8	80	[60/40]	149.8	331.6
S-26	8	80	[75/25]	173.1	378.7
S-27	8	80	[90/10]	196.2	422.7

REFERENCES

[1] Van Den Einde L, Zhao L, Seible F. Use of FRP composites in civil structural applications. Constr Build Mater 2003;17:389–403. https://doi.org/10.1016/S0950-0618(03)00040-0.

[2] Awad ZK, Aravinthan T, Zhuge Y, Gonzalez F. A review of optimization techniques used in the design of fibre composite structures for civil engineering applications. Mater Des 2012;33:534–44. https://doi.org/10.1016/j.matdes.2011.04.061.

[3] Bakis CE, Bank LC, Brown Vl, Cosenza E, Davalos JF, Lesko JJ, et al. Fiber-reinforced polymer composites for construction—State-of-the-art review. J Compos Constr 2002;6:73–87.

[4] Al-saadi AU, Aravinthan T, Lokuge W. Structural applications of fibre reinforced polymer (FRP) composite tubes: A review of columns members. Compos Struct 2018;204:513–24. https://doi.org/10.1016/j.compstruct.2018.07.109.

[5] Hizam RM, Manalo AC, Karunasena W, Bai Y. Behaviour of pultruded GFRP truss system connected using through-bolt with mechanical insert. Compos Part B Eng 2019;168:44–57. https://doi.org/10.1016/j.compositesb.2018.12.052.

[6] Scalici T, Fiore V, Orlando G, Valenza A. A DIC-based study of flexural behaviour of roving/mat/roving pultruded composites. Compos Struct 2015;131:82–9. https://doi.org/10.1016/j.compstruct.2015.04.058.

[7] Gand AK, Chan T-M, Mottram JT. Civil and structural engineering applications, recent trends, research and developments on pultruded fiber reinforced polymer closed sections: a review. Front Struct Civ Eng 2013;7:227–44. https://doi.org/10.1007/s11709-013-0216-8.

[8] Kim K, Voyiadjis GZ. Buckling strength prediction of CFRP cylindrical panels using finite element method. Compos Part Appl Sci Manuf 1999;30:1093–104. https://doi.org/10.1016/S1359-835X(99)00015-9.

[9] Nikbakt S, Kamarian S, Shakeri M. A review on optimization of composite structures Part I: Laminated composites. Compos Struct 2018;195:158–85. https://doi.org/10.1016/j.compstruct.2018.03.063.

[10] Sayyad AS, Ghugal YM. Bending, buckling and free vibration of laminated composite and sandwich beams: A critical review of literature. Compos Struct 2017;171:486–504. https://doi.org/10.1016/j.compstruct.2017.03.053.

[11] Attaf B. Advances in Composite Materials: Ecodesign and Analysis. BoD – Books on Demand; 2011.

[12] Bank LC. Composites for Construction: Structural Design with FRP Materials. John Wiley & Sons; 2006.

[13] Buragohain MK. Composite Structures: Design, Mechanics, Analysis, Manufacturing, and Testing. CRC Press; 2017.

[14] Department of Defense. Composite materials handbook, volume 3: polymer matrix composites—materials usage, design and analysis. SAE International; 2002.

[15] Matthews FL, Davies GAO, Hitchings D, Soutis C. Finite Element Modelling of Composite Materials and Structures. Elsevier; 2000.

[16] Singer J, Arbocz J, Weller T. Buckling Experiments: Experimental Methods in Buckling of Thin-Walled Structures Shells, Built-up Structures, Composites and Additional Topics. vol. 2. 2002.

[17] Uddin N. Developments in Fiber-Reinforced Polymer (FRP) Composites for Civil Engineering. Elsevier; 2013.

[18] Xu J, Zhao Q, Qiao P. A critical review on buckling and post-buckling analysis of composite structures. Front Aerosp Eng 2013;2:157–68.

[19] Alsaadi AUK. BEHAVIOUR OF FILLED PULTRUDED GLASS FIBRE REINFORCED POLYMER TUBES UNDER AXIAL LOADING. PhD Thesis. University of Southern Queensland, 2019.

[20] Abramovich H. Stability and Vibrations of Thin-Walled Composite Structures. Woodhead Publishing; 2017.

[21] Jones RM. Mechanics Of Composite Materials. CRC Press; 1998.

[22] Reddy JN. Mechanics of Laminated Composite Plates and Shells: Theory and Analysis, Second Edition. CRC Press; 2003.

[23] Zhang S, Caprani C, Heidarpour A. Influence of fibre orientation on pultruded GFRP material properties. Compos Struct 2018;204:368–77. https://doi.org/10.1016/j.compstruct.2018.07.104.

[24] Quadrino A, Penna R, Feo L, Nisticò N. Mechanical characterization of pultruded elements: Fiber orientation influence vs web-flange junction local problem. Experimental and numerical tests. Compos Part B Eng 2018;142:68–84. https://doi.org/10.1016/j.compositesb.2018.01.001.

[25] Wang Y, Feng J, Wu J, Hu D. Effects of fiber orientation and wall thickness on energy absorption characteristics of carbon-reinforced composite tubes under different loading conditions. Compos Struct 2016;153:356–68. https://doi.org/10.1016/j.compstruct.2016.06.033.

[26] Wang H, Croll JG. Design Optimisation of Lower-Bound Buckling Capacities for FRP-Laminated Cylindrical Shells. ISRN Mech Eng 2012;2012.

[27] Vaziri A. On the buckling of cracked composite cylindrical shells under axial compression. Compos Struct 2007;80:152–8. https://doi.org/10.1016/j.compstruct.2006.05.007.

[28] Akbaş ŞD. Post-buckling analysis of a fiber reinforced composite beam with crack. Eng Fract Mech 2019;212:70–80. https://doi.org/10.1016/j.engfracmech.2019.03.007.

[29] Asadi A, Sheikh AH, Thomsen OT. Buckling behaviour of thin-walled laminated composite beams having open and closed sections subjected to axial and end moment loading. Thin-Walled Struct 2019;141:85–96. https://doi.org/10.1016/j.tws.2019.04.005.

[30] Nguyen N-D, Nguyen T-K, Vo TP, Nguyen T-N, Lee S. Vibration and buckling behaviours of thin-walled composite and functionally graded sandwich I-beams. Compos Part B Eng 2019;166:414–27. https://doi.org/10.1016/j.compositesb.2019.02.033.

[31] Garrido M, Madeira JFA, Proença M, Correia JR. Multi-objective optimization of pultruded composite sandwich panels for building floor rehabilitation. Constr Build Mater 2019;198:465–78.

[32] Srinivasa CV, Kumar WPP, Kumar MTP, Bangar AR, Kumar P, Rudresh MS. Experimental and numerical studies on buckling of laminated composite skew plates with circular holes under uniaxial compression. Mech Adv Mater Struct 2017;24:304–17. https://doi.org/10.1080/15376494.2016.1142023.

[33] Wagner HNR, Köke H, Dähne S, Niemann S, Hühne C, Khakimova R. Decision tree-based machine learning to optimize the laminate stacking of composite cylinders for maximum buckling load and minimum imperfection sensitivity. Compos Struct 2019;220:45–63. https://doi.org/10.1016/j.compstruct.2019.02.103.

[34] Wang W, Sheikh MN, Hadi MNS. Behaviour of perforated GFRP tubes under axial compression. Thin-Walled Struct 2015;95:88–100. https://doi.org/10.1016/j.tws.2015.06.019.

[35] Cardoso DCT, Harries KA, Batista E de M. Compressive Local Buckling of Pultruded GFRP I-Sections: Development and Numerical/Experimental Evaluation of an Explicit Equation. J Compos Constr 2015;19:04014042. https://doi.org/10.1061/(ASCE)CC.1943-5614.0000501.

[36] Cintra GG, Cardoso DCT, Vieira JD. Parameters affecting local buckling response of pultruded GFRP I-columns: Experimental and numerical investigation. Compos Struct 2019;222:110897. https://doi.org/10.1016/j.compstruct.2019.110897.

[37] Godat A, Légeron F, Gagné V, Marmion B. Use of FRP pultruded members for electricity transmission towers. Compos Struct 2013;105:408–21. https://doi.org/10.1016/j.compstruct.2013.05.025.

[38] Bank LC, Gentry TR, Nadipelli M. Local Buckling of Pultruded FRP Beams-Analysis and Design. J Reinf Plast Compos 1996;15:283–94. https://doi.org/10.1177/073168449601500304.

[39] Aleksendric D, Carlone P. Soft Computing in the Design and Manufacturing of Composite Materials: Applications to Brake Friction and Thermoset Matrix Composites. Woodhead Publishing; 2015.

[40] Barbero EJ. Introduction to Composite Materials Design. CRC Press; 2017. https://doi.org/10.1201/9781315296494.

[41] Gibson RF. Principles of Composite Material Mechanics. CRC Press; 2016.

[42] Mallick PK. Fiber-reinforced composites: materials, manufacturing, and design. CRC press; 2007.

[43] Najafi A, Rais-Rohani M. Concurrent Process-Product Design Optimization Using Coupled Nonlinear Finite-Element Simulations. Finite Elem Anal - Appl Mech Eng 2012. https://doi.org/10.5772/47852.

[44] Rammerstorfer FG. ENGINEERING MECHANICS OF FIBRE REINFORCED POLYMERSAND COMPOSITE STRUCTURES. Springer; 1994.

[45] Soares CAM, Soares CMM, Freitas MJM. Mechanics of Composite Materials and Structures. Springer Science & Business Media; 2013.

[46] Vasiliev VV, Morozov EV. Advanced Mechanics of Composite Materials and Structures. Elsevier; 2018.

[47] Hashem ZA, Yuan RL. Short vs. long column behavior of pultruded glass-fiber reinforced polymer composites. Constr Build Mater 2001;15:369–78. https://doi.org/10.1016/S0950-0618(01)00018-6.

[48] Hassan NK, Mosallam AS. Buckling and ultimate failure of thin-walled pultruded composite columns. Polym Polym Compos 2004;12:469–81.

[49] Alhawamdeh M, Alajarmeh O, Aravinthan T, Shelley T, Schubel P, Kemp M, et al. Modelling hollow pultruded FRP profiles under axial compression: Local buckling and progressive failure. Compos Struct 2021;262:113650. https://doi.org/10.1016/j.compstruct.2021.113650.

[50] Al-Saadi A, Aravinthan T, Lokuge W. Numerical Investigation on Hollow Pultruded Fibre Reinforced Polymer Tube Columns. ACMSM25, Springer; 2020, p. 455–65.

[51] Daniel IM, Ishai O. Engineering Mechanics of Composite Materials. Oxford University Press; 2006.

[52] Simulia DS. Abaqus 6.13 Analysis User's Guide. Dassault Syst Provid RI 2013.

[53] Sharma AP, Khan SH, Parameswaran V. Experimental and numerical investigation on the uni-axial tensile response and failure of fiber metal laminates. Compos Part B Eng 2017;125:259–74. https://doi.org/10.1016/j.compositesb.2017.05.072.

[54] Al-saadi AU, Aravinthan T, Lokuge W. Effects of fibre orientation and layup on the mechanical properties of the pultruded glass fibre reinforced polymer tubes. Eng Struct 2019;198:109448. https://doi.org/10.1016/j.engstruct.2019.109448.

[55] Antony J. Design of Experiments for Engineers and Scientists. 2nd Edition. Elsevier; 2014.

[56] Wagners CFT. Wagners-Composite Fibre Technologies (CFT). Wagner n.d. https://www.wagner.com.au/main/what-we-do/composite-fibre-technologies/cft-home/ (accessed March 8, 2020).

[57] Boisse P. Advances in Composites Manufacturing and Process Design. Woodhead Publishing; 2015.

[58] Fam AZ, Rizkalla SH. Flexural Behavior of Concrete-Filled Fiber-Reinforced Polymer Circular Tubes. J Compos Constr 2002;6:123–32. https://doi.org/10.1061/(ASCE)1090-0268(2002)6:2(123).

[59] Meyer R. Handbook of Pultrusion Technology. Springer Science & Business Media; 2012.

[60] Starr T. Pultrusion for Engineers. Elsevier; 2000.

[61] American Society of Civil Engineers. Pre-standard for load & resistance factor design (LRFD) of pultruded fiber reinforced polymer (FRP) structures. Arlingt VA ACMA 2012:215.

[62] Clarke JL. Structural Design of Polymer Composites EUROCOMP Design Code and Handbook. CRC Press; 2005.

[63] Kollár LP, Springer GS. Mechanics of Composite Structures. Cambridge University Press; 2003.

[64] Butler R, Rhead A, Dodwell T. 8.7 Optimum Design and Damage Tolerance of Compressively Loaded Laminates. In: Beaumont PWR, Zweben CH, editors. Compr. Compos. Mater. II, Oxford: Elsevier; 2018, p. 118–35. https://doi.org/10.1016/B978-0-12-803581-8.10060-8.

[65] Gay D. Composite Materials : Design and Applications, Third Edition. CRC Press; 2014. https://doi.org/10.1201/b17106.

[66] Minitab-18. Minitab Reference Manual: statistical software. Minitab Inc. State College, PA; 2017.

[67] Zhang S, Caprani CC, Heidarpour A. Strain rate studies of pultruded glass fibre reinforced polymer material properties: A literature review. Constr Build Mater 2018;171:984–1004. https://doi.org/10.1016/j.conbuildmat.2018.03.113.

[68] Eslami MR. Buckling and Postbuckling of Beams, Plates, and Shells. Springer; 2017.

[69] Turvey GJ, Marshall IH. Buckling and Postbuckling of Composite Plates. Springer Science & Business Media; 1995.

CHAPTER 5: (PAPER 4) EFFECTS OF LAYUP AND GEOMETRY ON FLEXURAL PERFORMANCE OF HOLLOW PULTRUDED FRP PROFILES

After studying the effect and interactions of the design parameters on the compressive behaviour of hollow box Pultruded Fibre-reinforced Polymers (PFRP) profiles in chapter 4, this chapter investigated these parameters under flexural loading. From the literature review (chapter 2), it was found that the local buckling behaviour of hollow box PFRP profiles varies depending on the loading condition (compression or bending). Therefore, it was important to investigate the local buckling behaviour and the design parameters under bending to obtain a comprehensive understanding and recommendations for this loading condition.

The Finite Element Method (FEM) modelling approach developed in chapter 3 was extended here to suit flexural loading and reduce the computational cost. A large experimental program was performed on 100×100×5.2 mm and 125×125×6.4 mm hollow square PFRP profiles subjected to four-point bending to investigate the failure modes and verify the numerical models. The influence of the corner geometry (flange-web junction) on the failure sequence of these profiles was characterised. A full factorial design of experiment was used to capture the critical parametric interactions with over 81 numerical models. In the first part of this chapter, the effect of the geometric parameters on the flexural performance and failure modes of hollow box PFRP profiles was reported. While in the second part, the layup parameters and their interactions were investigated. Guidelines and recommendations on the design for manufacturing were established for the optimal flexural behaviour of hollow box PFRP profiles to overcome local buckling of the top flange. After the design parameters and their interactions were studied in chapters 4 and 5, a fast-converging numerical approach was introduced in chapter 6 to design the optimal configuration of the geometry and layup design parameters against local buckling under compression and bending loadings.

5.1 (PAPER 4) Modelling flexural performance of hollow pultruded FRP profiles

Manuscript 4 (Published): Alhawamdeh, M, Alajarmeh, O, Aravinthan, T, Shelley, T, Schubel, P, Mohammad, A & Zeng, X 2021, ‘Modelling flexural performance of hollow pultruded FRP profiles’, Composite Structures, vol. 276, p. 114553. (Impact factor: 5.407 and SNIP: 2.04)

DOI: https://doi.org/10.1016/j.compstruct.2021.114553

5.2 Effect of layup parameters on flexural performance of hollow box pultruded FRP profiles

The S-100×100×5.2 hollow square PFRP profile introduced in section 5.1 was used in this section to study the effect and interactions of the layup parameters on the flexural behaviour of hollow box PFRP profiles subjected to four-point bending. The same FEM modelling approach and test setup validated in section 5.1 were used in this section.

5.2.1 Level settings of layup parameters

Three levels were assigned for each layup parameter of the hollow box PFRP beam, as shown in Table 5.1. The winding angle was changed from 20^{o}, 50^{o}, to 80^{o} (measured from the pulling direction) to assess the effect of placing the wound fibres in longitudinal, intermediate, and circumferential directions, respectively, on the structural behaviour of the beam. The axial-to-wound fibre ratio was introduced to investigate the relationship between the percentages of axial and wound fibres on the flexural behaviour of the profile. Since the flexural design of PFRP beams is stiffness-controlled (American Society of Civil Engineers 2012; Bank 2006; Barbero 2017), the axial fibre percentage was larger than the wound fibre percentage in all levels to suit flexural applications. The stacking sequence was assigned to three levels of confinement, at which the location of the axial and wound rovings through the section is changed. To minimise the elastic coupling effects, symmetric and balanced layups were used for best performance against buckling, bending, and warping due to thermal effects (Buragohain 2017; Butler, Rhead & Dodwell 2018).

Table 5.1: Levels range for full factorial study on the layup parameters of the hollow box PFRP profile.

Layup Parameter	Level 1	Level 2	Level 3
Wound fibre angle (Deg)	20	50	80
Axial-to-wound fibre ratio (%)	[60/40]	[75/25]	[90/10]
Stacking sequence	[0/+θ/-θ/0/-θ/+θ/0]	[+θ/0/-θ/0/-θ/0/+θ]	[+θ/-θ/0/-θ/+θ]

The geometric parameters (wall thickness, cross-sectional aspect ratio, and corner radius) were maintained constant in the layup parametric study with the same values currently used in production.

5.2.2 Effects of the layup parameters

The dominant failure mode in all models of the layup parametric study was local buckling of the top flange. This finding emphasises the aforementioned domination of the geometric parameters on the failure mode of hollow box PFRP profiles. The design configurations of the layup parametric study along with the numerical results are presented in Appendix B. The contribution of each layup parameter on the flexural behaviour of the hollow box PFRP profile is shown in Table 5.2, which shows the two-way ANOVA model results. The numerical results showed that the flexural stiffness (EI/L^3) is independent of the stacking sequence, which agrees with the Classical Laminated Plate Theory (CLPT). However, the stacking sequence contributed by the tenth of the flange buckling capacity due to the effect of confinement on the out-of-plane deformation and corners restraint, as will be explained later in this section. The wound fibre angle was the dominant parameter in controlling the flexural stiffness and strength. This dominance was attributed to the major role of the fibre angle in shaping the stiffness, stresses distribution, and failure cracks of the laminate. The axial-to-wound fibre ratio was the second parameter affecting the flexural stiffness and strength of the hollow box beam due to its dependency on the wound fibre angle, as will be demonstrated next.

Table 5.2: Percentile contribution of each layup parameter on the flexural behaviour of hollow box PFRP beams.

Layup Parameter	Flexural stiffness (EI/L^3)	Flexural strength
Wound fibre angle (%)	68.5	49.6
Axial-to-wound fibre ratio (%)	29.5	37.4
Stacking sequence (%)	0.0	9.5
Error (%)	2.0	3.5
ANOVA R^2 (%)	98.0	92.5

The flexural stiffness of the hollow box profile decreased steeply when the wound fibre angle was below 50^o, while the reduction of the flexural stiffness above 50^o was gradual, as shown in Fig. 5.1. A similar response for pultruded GFRP coupons was found in the literature (Zhang, Caprani & Heidarpour 2018). This behaviour was attributed to the variation of the axial and transverse components of the beam stiffness around $\theta = 45^o$. The contribution of the wound fibres to the longitudinal stiffness becomes significant when the winding angle is below 45^o, which increases the sensitivity of the flexural stiffness. Whereas the flexural stiffness becomes insensitive when the winding angle exceeds 45^o because of the lower contribution of the wound fibres towards the longitudinal direction. Furthermore, the relationship between the wound fibre angle and axial-to-wound fibres ratio was found to be interactive. The flexural stiffness of the profile was enhanced when the axial fibre percentage was increased since more fibres contributed to the longitudinal direction of the beam. The two zones with different slopes (Fig. 5.1) were transformed into one as the axial fibre percentage was increased since the effect of the wound fibre angle on the flexural stiffness was decreased.

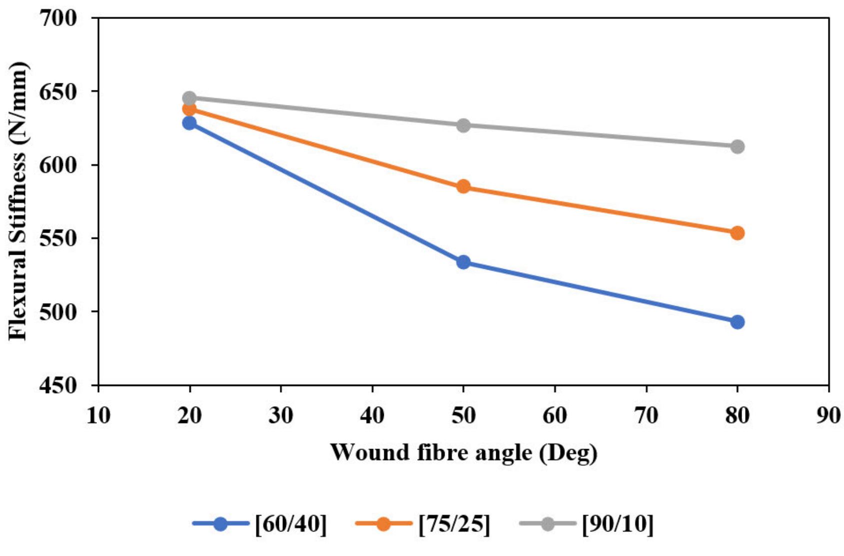

Fig. 5.1. Effect of the wound fibre angle on the flexural stiffness of hollow box PFRP beams with different axial-to-wound fibres ratios.

The layup parameters were also found to be interactive when studying their effect on flexural strength. Firstly, the axial-to-wound fibre ratio affected the response of the flexural strength to the wound fibre angle, as shown in Fig. 5.2 (a). The maximum strength for a higher percentage of wound fibres ([60/40] and [75/25]) was attained at a winding angle of 50^o while it was obtained at 80^o for lower percentage of wound fibres ([90/10]). This shift in the winding angle, that produces the maximum buckling resistance, from 50^o to 80^o was attributed to the flexural stiffness components (D_{22}, D_{12}, and D_{66}) of the top flange and the corners restraint, and to their response to different wound fibre percentages. The maximum value of these flexural stiffness components occurs at 45^o (Abramovich 2017), while the maximum corners restraint is obtained at a circumferential angle (80^o in this case) due to the maximum confinement (Bank 2006). When the percentage of the wound fibres is reduced, the flexural stiffness components of the top flange are decreased until they become smaller than the corner restraint provided from the high transverse properties at 80^o. Consequently, the maximum buckling resistance will be at a winding angle of 80^o and will rely on the optimal corner restraint supporting the top flange at 80^o, which is higher than the optimal flexural stiffness components at 50^o for wound fibre percentage of 10%. Contrarily, when the wound fibre percentage is increased to 25% or higher, the flexural stiffness components will be increased and exceed the maximum corner restraint at 80^o, providing the maximum resistance of the top flange against out-of-plane deformations (buckling) at 50^o. Nevertheless, this behaviour is limited to the stacking sequence currently used in production ([0/+θ/-θ/0/-θ/+θ/0]). Stacking the wound rovings around the axial fibres increased the confinement, especially at the corners, which shifted the maximum flexural strength from 50^o to 80^o, as shown in Fig. 5.2 (b). It was inferred that when the confinement is increased, the corner restraint (maximum value at 80^o) becomes higher than the flexural stiffness components (maximum values at 45^o) of the top flange. This is evident by the rotational displacement ($\Delta\theta$) which greatly decreased when the winding angle and confinement were increased, as shown in Fig. 5.3. Thus, at 80^o more rigidity was provided from the confined corners to the top flange in the transverse direction, which resulted in a higher buckling resistance in the top flange. The variation of the rotational displacement was higher when the stacking sequence was changed from [0/+θ/-θ/0/-θ/+θ/0] to [+θ/0/-θ/0/-θ/0/+θ] than when it was changed from [+θ/0/-θ/0/-θ/0/+θ] to [+θ/-θ/0/-θ/+θ], as shown in Fig. 5.2 (b) and Fig. 5.3. This observation was referred to the fact that the former change moved from one confined axial ply to three confined axial plies while the latter change only gathered the confined plies at the middle. Thus, more confinement was acquired from the former change. Moreover, the stacking sequences [+θ/0/-θ/0/-θ/0/+θ] and [+θ/-θ/0/-θ/+θ] showed a higher reduction in the rotational displacement at winding angles above 50^o, which highlights the interaction between large winding angles and confining the corners.

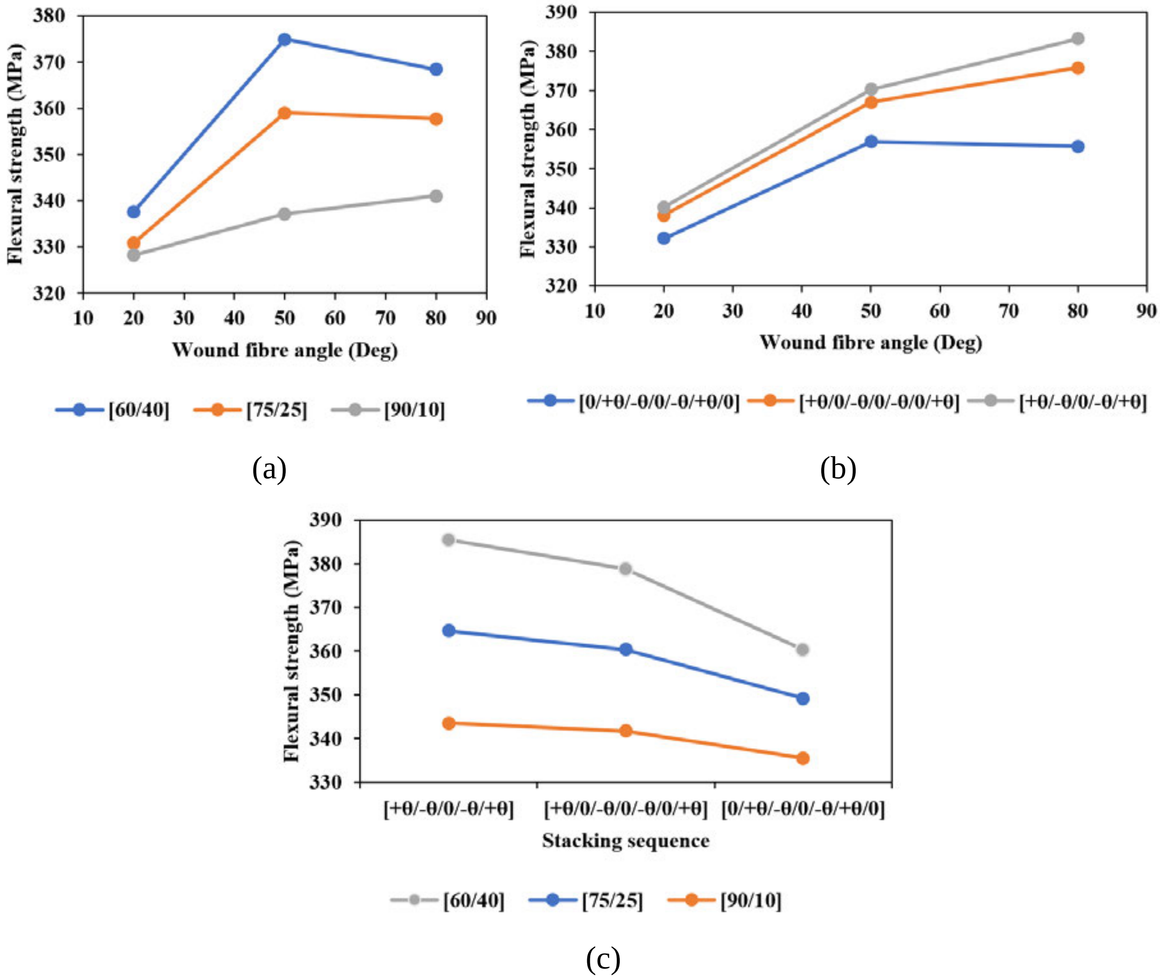

Fig. 5.2. Interaction plots of the layup parameters affecting the flexural strength of hollow box PFRP beam (a) wound fibre angle and axial-to-wound fibre ratio (b) wound fibre angle and stacking sequence (c) stacking sequence and axial-to-wound fibre ratio.

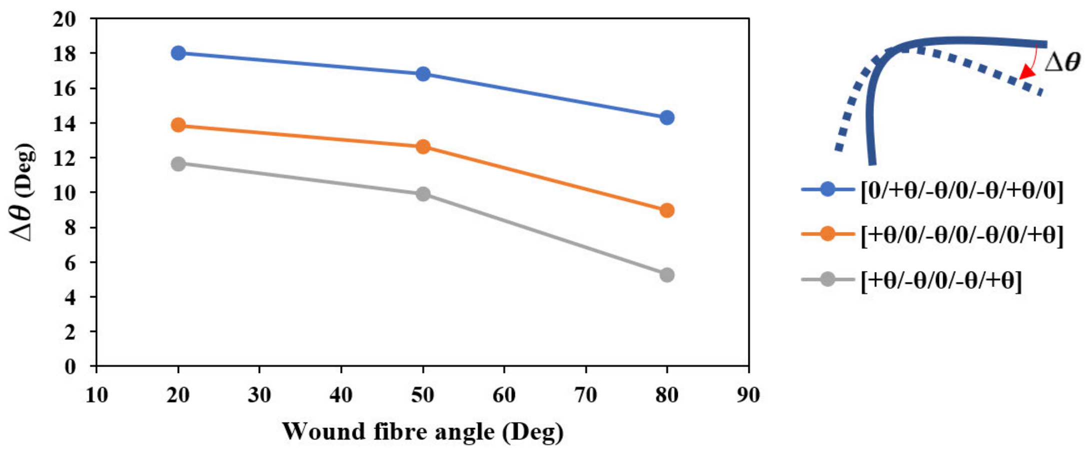

Fig. 5.3. The effect of the stacking sequence of hollow box PFRP beams on the rotational displacement (Δθ) of the corners along the wound fibre angle.

Finally, the axial-to-wound fibre ratio influenced the response of the flexural strength to the stacking sequence, as shown in Fig. 5.2 (c). Stacking the wound fibres around the axial rovings enhanced the flexural strength of the hollow box beam. Moreover, increasing the wound fibres percentage improved the buckling resistance of the top flange due to the increase in the flexural stiffness components and the corner restraint. The confined stacking sequences ([+θ/0/-θ/0/-θ/0/+θ] and [+θ/-θ/0/-θ/+θ]) showed a higher response to the increase in the wound fibres percentage compared to the default stacking sequence ([0/+θ/-θ/0/-θ/+θ/0]). This was attributed to the boost of confinement in the confined stacking sequences when more wound rovings are used, which multiplied the increase of the buckling resistance.

5.2.3 Level settings of layup properties under different failure modes

The effect of the wound fibre angle and axial-to-wound fibres ratio on the flexural strength of hollow box PFRP profiles was significant compared to the negligible effect from the stacking sequence, as shown previously in Table 5.2. Thus, these two parameters were selected to study the effect and interactions of layup properties on the failure modes of hollow box PFRP profiles under bending. The wall thickness was also selected to determine different failure modes when changed (local buckling or compressive failure of the top flange). The selected levels of the wound fibre angle and the axial-to-wound fibre ratio were the same as in the layup parametric study (section 5.2.1). The wall thickness values were chosen to represent both failure modes of local buckling at 5.2 mm wall thickness and compressive failure at 6.4 mm wall thickness, as shown in Table 5.3. A full factorial design of experiment was used to investigate the effect and interactions of the wound fibre angle and axial-to-wound fibre ratio at different failure modes.

Table 5.3: Levels range for full factorial study on the chosen parameters of the hollow box profile.

Parameter	Level 1	Level 2	Level 3
Wall thickness (mm)	5.2	5.8	6.4
Wound fibre angle (Deg)	20	50	80
Axial-to-wound fibre ratio (%)	[60/40]	[75/25]	[90/10]

The other parameters (cross-sectional aspect ratio, corner radius, and stacking sequence) were maintained constant in this parametric study with the same values currently used in production.

5.2.4 Effect of layup properties under different failure modes

The two-way ANOVA model results showing the contribution of the wound fibre angle and axial-to-wound fibres ratio compared to the wall thickness are presented in Table 5.4. The design configurations of the parametric study along with the numerical results are presented in Appendix B. The wall thickness was the major parameter affecting the flexural stiffness (EI/L^3) of the hollow box profile by 50%. This was attributed to the exponential contribution of the wall thickness to the moment of inertia of the section, which was higher than the unfactored effect of the layup parameters on the elastic modulus of the laminate. Moreover, the wall thickness controlled the flexural strength of the hollow box PFRP beam by approximately 90%. It was inferred that the failure mode was the reason. Local buckling as a stability problem is highly affected by the profile dimensions, especially the wall thickness (Almeida et al. 2018; Eslami 2017; Turvey & Marshall 1995).

Table 5.4: Percentile contribution of each chosen parameter on the flexural behaviour of the hollow box PFRP beam.

Parameter	Flexural stiffness (EI/L^3)	Flexural Strength
Wall thickness (%)	50.5	87.6
Wound fibre angle (%)	25.8	6.4
Axial-to-wound fibre ratio (%)	21.0	3.1
Error (%)	2.7	2.9
ANOVA R^2 (%)	93.3	91.1

The wound fibre angle and axial-to-wound fibre ratio exhibited two different effects on the flexural behaviour of hollow box PFRP profiles depending on the wall thickness (the dominant failure mode). The maximum flexural strength was obtained by the highest wound fibre percentage and winding angle of 50^o when the dominant failure mode was local buckling, as shown in Fig. 5.4 (a). When the wall thickness was increased up to 6.4 mm, the failure mode shifted to compressive failure of the top flange and the maximum strength peak was changed, as shown in Fig. 5.4 (b). The maximum strength was obtained at the lowest wound fibre percentage and a winding angle of 20^o since this configuration align the fibres in the longitudinal direction to resist the compressive stresses on the top flange. This shift in the optimal configuration to produce the maximum flexural strength was because of the transform from stability limit to strength limit failure. From Fig. 5.4 (a), it appears that the variation of the strength when changing the layup parameters was not significant since the maximum enhancement was obtained by increasing the strength from 328.2 up to 374.9 (14.2%) when the profile was under local buckling of the top flange. Whereas the maximum improvement was from 326.3 up to 454.2 (40.2%) when the layup parameters were changed for the profile dominated by a compressive failure of the top flange. This finding agrees with the aforementioned conclusion stating that the geometric parameters govern the flexural behaviour under local buckling (stability limit). However, the layup parameters possess a significant effect on the flexural behaviour of hollow box PFRP profiles governed by the material ultimate strength (strength limit).

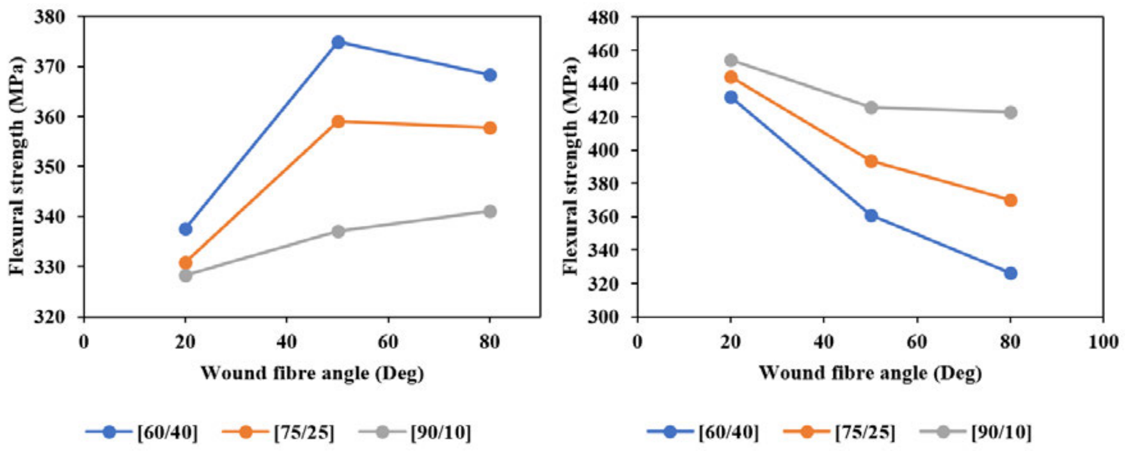

(a) (b)

Fig. 5.4. Effect of wound fibre angle and axial-to-wound fibre ratio on the flexural strength of the hollow box beam dominated by (a) local buckling of the top flange (5.2 mm wall thickness) and (b) compressive failure of the top flange (6.4 mm wall thickness).

Because of local buckling, the maximum flexural stiffness (EI/L^3) and strength cannot be achieved by using one design configuration of the layup parameters since each one of them require a different configuration. The maximum flexural stiffness requires a small winding angle and a low percentage of wound fibres, while the maximum flexural strength requires a large winding angle and a high percentage of wound fibres. Using the recommended configurations of the geometric parameters (mentioned in section 5.1) will eliminate local buckling and shift the failure mode to compressive failure of the top flange. Thus, allowing for both maximum flexural stiffness and strength to be attained by the smallest wound fibre angle and the highest axial fibre percentage.

5.3 Summary

This chapter studied the design for manufacturing parameters of hollow box PFRP profiles under flexural loading. A combined experimental and numerical approach was used to investigate the failure modes. The validated model helped in characterising the failure mechanism of hollow box PFRP profiles and their sequence. The failure sequence started by local buckling of the top flange. Tensile damage of matrix occurred at the top corners as they were resisting the buckling. This damage extended to the webs until the beam's collapse. Nevertheless, the flange-web junction maintained its rotational stiffness to resist the buckling of the top flange and the webs. Finally, the buckling waves subsided when the collapse occurred at the top flange due to compressive failure of fibres, in addition to localised tensile failure in the matrix evident by the spalling and delamination of fibres at the top flange and webs.

The most contributing parameter to the flexural stiffness (EI/L^3) was the cross-sectional aspect ratio (h/b) due to its higher influence on the moment of inertia of the section. Whereas, the most significant parameter on the flexural strength was the corner radii ratio (r/R) because of the increase in the corners restraint when the r/R ratio is increased due to the higher rigidity transferred from the web to the flange and to the effect of large r/R ratio on reducing the effective buckling width of the flange. Moreover, investing in the flange thickness provides more enhancement to the flexural strength than reducing the unsupported width of the top flange due to the exponential effect of the wall thickness on the buckling capacity of the flange.

The wound fibre angle was the most significant layup parameter affecting the flexural stiffness and strength. This was attributed to the major role of the fibre angle in shaping the stiffness, stresses distribution, and failure cracks of the laminate. The effect of the axial-to-wound fibre ratio on the flexural stiffness and strength of the hollow box beam was dependent on the wound fibre angle. The stacking sequence contributed by the tenth (compared to the other layup parameters) of the flange buckling capacity due to the effect of confinement on the out-of-plane deformation and corners restraint. The maximum flexural stiffness and strength cannot be achieved by using one design configuration of the layup parameters since each one of them require a different configuration under local buckling. Using the recommended configurations of the geometric parameters will eliminate local buckling and shift the failure mode to compressive failure of the top flange. Thus, obtaining the maximum flexural stiffness and strength by the smallest wound fibre angle and the highest axial fibre percentage.

After the design parameters and their interactions were studied in chapters 4 and 5, a fast-converging numerical approach to design the optimal configuration of the geometry and layup design parameters against local buckling under compression and bending loadings is introduced in chapter 6.

CHAPTER 6: (PAPER 5) DESIGN OPTIMISATION OF HOLLOW BOX PULTRUDED FRP PROFILES USING MIXED INTEGER CONSTRAINED GENETIC ALGORITHM

After studying the effect of the design parameters and their relative interactions on the compressive and flexural behaviours of hollow box Pultruded Fibre-reinforced Polymers (PFRP) profiles in chapters 4 and 5, this chapter presents a numerical optimisation approach to minimise the production cost of hollow box PFRP profiles, enhance their structural performance, and generate design charts considering the interactions of the design parameters for design engineers to use. The fast-converging numerical approach combined the Finite Element Modelling (FEM) and the Genetic Algorithm (GA) to design the optimal configuration of the geometry and layup design parameters against local buckling under compression and bending loadings. The FEM code was parametrised using Python 3.9.1, and Abaqus 2019 was used to evaluate the nonlinear buckling strength constraint. The mixed-integer constrained optimisation GA code (MI-LXPM) was used to solve the problem using MATLAB 2020b. The MATLAB and Python codes used in this numerical study are presented in Appendix C. These codes will be compiled to develop a design App for the analysis and design optimisation of hollow box PFRP profiles manufactured by any pultrusion technology and subjected to a wider range of loading applications and failure modes.

The adjusted FEM approach incorporated geometric imperfections and controlled increment size to increase the computational efficiency and achieve the required number of models. The optimised designs were estimated to save up to 11.5% and 26.4% of the materials cost per metre of pultrusion for axial and flexural applications, respectively. An experimental case study on the design of a hollow rectangular pultruded FRP girder demonstrated the proposed optimisation approach. The new design saved 10.6% of the material cost and enhanced the local buckling strength by 41%. The significant conclusions of this research are highlighted in the next chapter. Moreover, recommendations for future research were proposed to facilitate the design for manufacturing of hollow box PFRP profiles and broaden their use in civil structural applications.

Design Optimisation of Hollow Box Pultruded FRP Profiles Using Mixed Integer Constrained Genetic Algorithm

Mohammad Alhawamdeh*[1], Omar Alajarmeh[1], Thiru Aravinthan[1], Tristan Shelley[1], Peter Schubel[1], Ali Mohammed[2], Xuesen Zeng[1]

*Corresponding author: Mohammad.Alhawamdeh@usq.edu.au, University of Southern Queensland, West Street Toowoomba Qld 4350 Australia

[1] University of Southern Queensland, Centre for Future Materials, Toowoomba Queensland 4350 Australia

[2] Wagners Composite Fibre Technologies, Wellcamp Queensland 4350 Australia

ABSTRACT

Hollow Pultruded Fibre-Reinforced Polymer (FRP) profiles are increasingly used as structural members in many infrastructure applications. However, there is still a lack of coherent design methodology considering local buckling. This research presents a fast-converging numerical approach combining the Finite Element Modelling (FEM) and the Genetic Algorithm (GA) to design the optimal configuration of the geometry and layup design parameters against local buckling under two separate loading conditions of axial compression and four-point bending. The FEM model was validated experimentally. The mixed-integer constrained optimisation GA code (MI-LXPM) was used to solve the problem. The optimisation objective was to minimise the manufacturing cost per metre of pultrusion while maintaining the same stiffness and strength properties of the control profile. The Kriging model was used to interpolate the design space based on the intermediate optimisation data output and produce a practical design chart linking the profile geometry to the local buckling capacity. An experimental case study on the design of a hollow rectangular pultruded FRP girder demonstrated the proposed optimisation approach. The new design saved 10.6% of the material cost and enhanced the local buckling strength by 41%.

Keywords: Hollow box FRP profile, Finite element analysis, Genetic algorithm, Local buckling, geometry and layup optimization, structural design.

1. INTRODUCTION

Hollow Pultruded Fibre-Reinforced Polymer (PFRP) profiles are increasingly used as beams and columns in the civil infrastructure sector due to their excellent corrosion resistance and the high mechanical properties-to-weight ratio [1–3]. The pulwinding technology improves the pultrusion capability by providing continuous off-axis wound fibres to be pulled along with the axial fibres, which improves the transverse properties, optimise the delamination resistance, and enhance the post-processing durability [4–6]. Moreover, the local buckling capacity is also higher in these profiles compared to normal pultruded profiles [7,8]. The design parameters of hollow box pulwound FRP profiles include layup parameters (winding angle and axial-to-wound fibres ratio) and geometric parameters (wall slenderness, cross-sectional aspect ratio, and corner radii ratio). Local buckling is a dominant failure mode of the anisotropic and slender PFRP profiles and is controlled by these design parameters [9–11]. There is still a lack of knowledge and guidelines in the design for manufacturing against local buckling, which hinders this novel construction material from a larger market share compared to conventional construction materials. Current standards [12–15] do not provide comprehensive design charts or formulas of these design parameters and their interactions, but only conservative uneconomic formulas. Optimising these design parameters under structural loadings (compression and bending) is going to provide optimal configurations of hollow box pulwound FRP profiles with competitive cost, material saving, and superior local buckling strength.

In this research, the Finite Element Method (FEM) was selected as a numerical prediction tool to determine the nonlinear buckling capacity of different design configurations to minimise the manufacturing cost per linear metre while maintaining the same stiffness and strength properties of the control profile. FEM is capable of handling complex geometries and combined failure problems [16–18]. Among the wide variety of optimisation techniques, the Genetic Algorithm (GA) was selected to solve the optimisation problem. This optimisation technique has rarely been used in civil structural applications as compared to the aerospace and automotive disciplines [19] with no study found on hollow box pulwound FRP profiles. GA is the most common global meta-heuristic optimisation algorithm with an extensive capability to locate the global minima, unlike the gradient-based optimisation methods which can be deviated to local minima [20–22]. It can handle many optimisation problems, such as nondifferentiable, discontinuous, nonlinear constrained, and stochastic problems with real and integer design variables [23–25].

In this study, two optimisation problems were undertaken on the control profile under two separate loading conditions of axial compression and four-point bending to obtain the optimal configuration of the design parameters for different load applications. Afterwards, the results of the GA codes were interpolated using the Kriging model, which is a geostatistical prediction tool capable of handling such design problems, to generate design curves of the compressive and flexural buckling strengths in terms of the critical geometric parameters including their interactions. The controlled increment size approach introduced by the authors in previous studies [26,27] was adjusted to increase the computational efficiency and achieve the required number of models. The derived design guidelines and design charts will facilitate the design for manufacturing of hollow box PFRP profiles and broaden their use in civil structural applications. It is worth highlighting that this research addresses the structural design of hollow box PFRP profiles under a single loading condition (axial compression or four-point bending).

Thus, the structural design of beam-column members subjected to combined compression and bending is out of this research scope.

2. PROBLEM FORMULATION

2.1 Background

The hollow square PFRP profile as the baseline control design in this research was manufactured from E-glass fibre & Vinyl-Ester polymer resin, by Wagners Composite Fibre Technologies (CFT), using pulwinding technology. The layup and geometric properties of this profile are shown in Table 1 and Fig. 1, respectively.

Table 1: Layup properties of hollow square PFRP profile.

Layup property	Detail
Stacking sequence	[0°/+θ/-θ/0°/-θ/+θ/0°]
Wound fibre angle θ (Deg)	50°
Axial fibre percentage (%)	82.2
Wound fibre percentage (%)	17.8
Elastic compressive modulus (MPa)	40,100

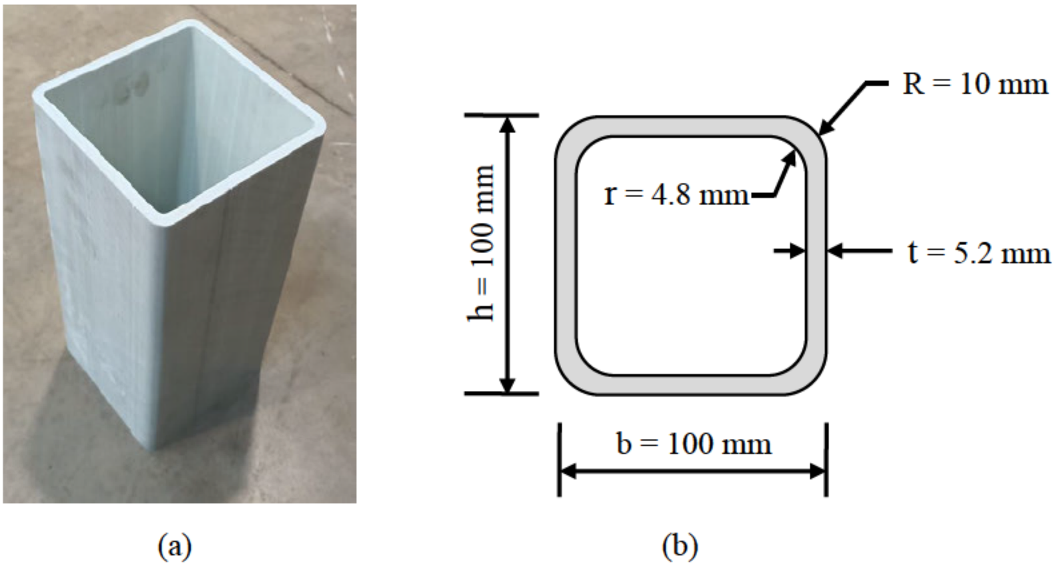

Fig. 1. Cross-sectional (a) geometry and (b) dimensions of the hollow square PFRP profile.

One of the main motivations of this research was to optimise this control profile (cross-sectional area = 1910 mm^2) to achieve a lighter weight (lower cost per metre of pultrusion) by seeking the optimal configuration of the design parameters (layup and geometry) of the profile while maintaining its structural performance. The structural performance of the profile was characterised by the authors in previous works under axial compression [26] and bending [27] using experimental and numerical approaches, as summarised in Table 2. The triggering failure mode was local buckling of the walls under compression and local buckling of top flange under bending. The loading condition controls the local buckling behaviour of the profile as it shapes the distribution of stress and strain along the cross-section [28,29] and results in the buckling of four walls (with a smaller buckle half-wavelength) under compression versus the buckling of the top flange (with a larger buckle half-wavelength) under bending [30–32]. Thus, the optimisation of the design parameters of the profile against local buckling must be performed under each loading condition separately. In this research, two optimisation problems were considered to optimise the profile under two separate loading conditions of axial compression and four-point bending in order to reach the optimal configuration of the design parameters for compression and bending applications, respectively, for different production lines. Afterwards, interaction curves of the compressive and flexural buckling strengths in terms of the critical design parameters were generated to obtain a design chart including the effect and interactions of these design parameters on the compressive and flexural strength of hollow box PFRP profiles.

Table 2: Structural performance of the square PFRP profile under axial compression and four-point bending.

Property	Compression [26]	Bending [27]
Test setup	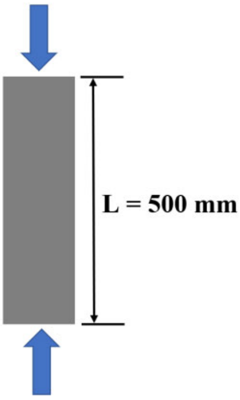	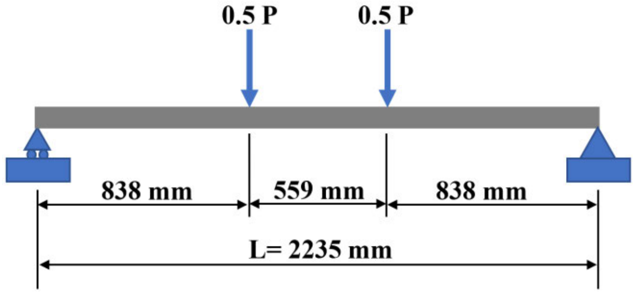
Stiffness	EA/L=151.8 kN/mm	EI/L^3= 605.8 N/mm
Local buckling strength (MPa)	243.1	324.2

The manufacturing design parameters in this study were divided into two groups: geometric parameters (the wall slenderness h/t, the cross-sectional aspect ratio h/b, and the corner radii ratio r/R) and layup parameters (the winding angle θ and the axial-to-wound fibre ratio). The stacking sequence was excluded from the design variables to reduce the computational cost since there are limited designs of stacking sequences in pulwound FRP profiles (due to the limited number of plies). Moreover, the contribution of stacking sequence towards the structural behaviour of hollow PFRP profiles was found to be negligible compared to the other design parameters [27]. The GA method, which is the most common global meta-heuristic algorithm [20], was used as an optimisation method for this problem because of its ability to reach the global solution (minima) where the gradient-based optimisation methods can deviate to local solutions. It can handle discontinuous, nondifferentiable, stochastic, and nonlinear constrained optimisation problems containing both real and integer design variables [23,33,34], such as this problem. It is worth mentioning here that the targeted failure modes are local buckling of walls under compression and local buckling of top flange and webs under bending. Shear failure and web crippling were excluded using pure flexural test setup (Span-to-depth ratio L/D = 22.35 and shear span-to-depth ratio a/D = 8.38) for the profile under bending in compliance with ASTM D7249/D7249M specifications [35–38]. The type of the GA code implemented in this research along with its objective function, variables, and constraints are discussed in the following section.

2.2 Genetic algorithm

The genetic algorithm effectively searches for the optimal solution in the design space by sieving through a constant number of diverse candidates (population) and transferring the fittest candidate(s) to the next generation. At each iteration, high-quality solutions are generated and evolve towards the optimal solution using biologically inspired operators such as selection (passing the fittest individuals of the current population to the next generation), crossover (generating a new offspring by combining the genes of different parents), and mutation (generating a new offspring by randomly changing the genes of a single parent) [39]. The optimisation scheme applied in this research is shown in Fig. 2. Abaqus 2019 was selected to perform the FEM analysis because its kernel uses Python scripting language to interpret the FE code [40], which makes it compatible with parametrised codes written using Python. The FE modelling approach will be discussed in detail in the next section.

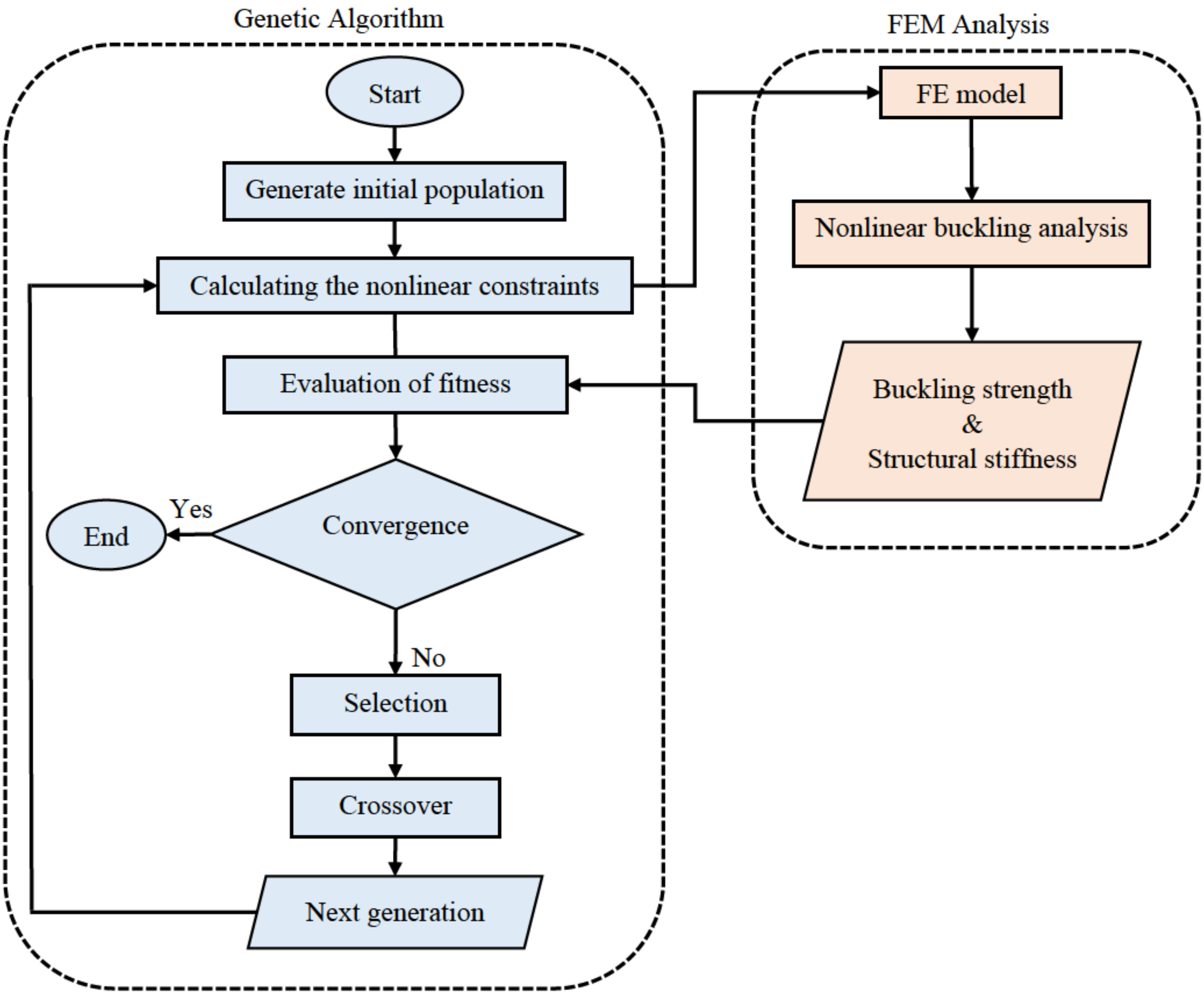

Fig. 2. The optimisation scheme used in this research incorporating GA and FEM.

As described in the previous section, the manufacturing design parameters of hollow box PFRP profiles are a mixture of real values (wall slenderness, cross-sectional aspect ratio, corner radii ratio, and axial-to-wound fibre ratio) and one integer value (winding angle). Moreover, the corresponding constraints (stiffness and buckling strength) properties in the optimisation problem are nonlinear [27]. Based on these two considerations, the mixed-integer constrained optimisation GA code (MI-LXPM) proposed by Deep et al. [41] was chosen. This algorithm is appropriate for mixed-integer nonlinear-constrained optimisation problems and requires minimum experience in the numerical operators for selection, crossover, and handling constraints compared to other existing schemes [39]. The MI-LXPM algorithm is briefly introduced here by expressing a general optimisation problem [41]:

$$
\begin{aligned}
&\text{minimise} \quad && f(X,Y), \\
&\text{subject to} \quad && g_j(X,Y) \leq 0, \;\; j = 1,..J, \\
& && h_k(X,Y) = 0, \;\; k = 1,..K, \\
& && X^L \leq X \leq X^U: real, \\
& && Y^L \leq Y \leq Y^U: integer.
\end{aligned}
\tag{1}
$$

Where X and Y are the vectors of real and integer value parameters in the range of $[X^L,X^U]$ and $[Y^L,Y^U]$, respectively. $f(X,Y)$ is the objective function. $g_j(X,Y)$ and $h_k(X,Y)$ are the jth inequality and the kth equality constraints, respectively. A parameter-free, penalty function [42] is used to handle the constraints $g_j(X,Y)$ and $h_k(X,Y)$. The penalty function is implemented as [41]:

$$
penalty(X,Y) = \begin{cases} f(X,Y) \quad if\ (X,Y)\ is\ feasible; \\ f_{worst} + \sum_{j=1}^{m} \left|\phi_j(X,Y)\right| \quad otherwise; \end{cases} \tag{2}
$$

Where $\phi_j(X,Y)$ is a tolerance function used to convert the equality constraints $h_k(X,Y)$ to inequality constraints. f_{worst} refers to the worst value of the objective function in the feasible solutions of the same population.

The genetic operators of the MI-LXPM GA code do not require the user to input any numerical parameters. The selection operator selects the fittest solution (elite) to enter the next iteration and uses binary tournament technique to randomly choose two solutions and nominate them for the Laplace crossover operation. The Laplace crossover operator generates two new solutions ($y^1(X,Y)$,$y^2(X,Y)$) for the next iteration using two selected solutions ($x^1(X,Y)$,$x^2(X,Y)$) from the current iteration [39]. A random number following the Laplace distribution is used in the crossover operator [41]:

$$\beta_i = \begin{cases} a - b \log^{u_i} & r_i \leq 0.5 \\ a + b \log^{u_i} & r_i > 0.5 \end{cases} \tag{3}$$

Where β_i, u_i, and r_i are random numbers. a is the location parameter and b (>0) is the scaling parameter with either integer or real value depending on the value of the decision variable. The new two solutions resulting from crossover are:

$$y_i{}^1 = x_i{}^1 + \beta_i |x_i{}^1 - x_i{}^2|$$
$$y_i{}^2 = x_i{}^2 + \beta_i |x_i{}^1 - x_i{}^2| \tag{4}$$

The new solutions y_i are truncated to $\overline{y}_i$ in order to ensure the integer condition for the Y parameters [39]:

$$\overline{y}_i = y_i, if\ y_i\ is\ integer;\ otherwise,$$
$$\overline{y}_i = \begin{cases} [y_i] \\ [y_i] + 1 \end{cases}, either\ value\ with\ a\ 50-50\ chance, where\ [y_i]\ is\ the\ integer\ part\ of\ y_i \tag{5}$$

The mutation operator was not applied in this study due to the diverse population introduced by the crossover operator of MI-LXPM GA [39]. The elite count (i.e. the number of the fittest solutions moved to the next generation) was maintained at 1 to ensure population diversity. The population size and stall count (i.e. the maximum number of iterations allowed with the same fittest solution) were assigned to values of 20 and 15, respectively, to achieve the best converging performance of the MI-LXPM GA [39]. In this study, the MI-LXPM GA code was implemented to solve the two mixed-integer nonlinear-constrained optimisation problems (one for each loading condition) using MATLAB 2020b [43]. The optimisation workflow, shown in Fig. 2, was automated using Python 3.9.1 since it is compatible with both MATLAB and Abaqus. These two optimisation problems are discussed in the following section.

2.3 Optimisation of hollow box pultruded FRP profile

Two optimisation problems (one for each loading condition) on minimising the weight (lower cost per metre of pultrusion) while maintaining the same structural performance (structural stiffness and local buckling strength) of the hollow box PFRP control profile were undertaken in this research. These two optimisation problems are listed as follow:

minimise $f(\boldsymbol{X},\boldsymbol{Y}) = 2ht + 2bt - 4t^2 - (4-\pi)(R^2 - r^2)$

Subject to

$$\left.\begin{aligned} g_1(X,Y) &= \sigma_{control} - \sigma_{BL}(X,Y) \le 0 \\ g_2(X,Y) &= (\frac{EA}{L})_{control} - \frac{EA}{L}(X,Y) \le 0 \end{aligned}\right\} \text{Compression}$$

$$\left.\begin{aligned} g_1(X,Y) &= \sigma_{control} - \sigma_{BL}(X,Y) \le 0 \\ g_2(X,Y) &= (\frac{EI}{L^3})_{control} - \frac{EI}{L^3}(X,Y) \le 0 \end{aligned}\right\} \text{Bending}$$

and (6)

$$\left.\begin{aligned} & 3 > \frac{h}{b} \ge 1 \\ & \frac{t}{b} \le \frac{1}{4} \\ & r < \frac{b-2t}{2} \end{aligned}\right\} \text{Geometry limitations}$$

$$\left.\begin{aligned} & 0.5 < \frac{r}{R} \le 2.5 \\ & 1.5 \le \frac{Axial\ fibres\ \%}{Wound\ fibres\ \%} < 9 \\ & \theta \in [20^o, 80^o] \end{aligned}\right\} \text{Manufacturing limitations}$$

Where $f(\boldsymbol{X},\boldsymbol{Y})$ is the cross-sectional area of the hollow box PFRP profile in terms of the geometric parameters shown in Fig. 1(b). The cross-sectional area of the profile was assigned as the objective function (penalty function) since it is directly proportional to the weight per metre of pultrusion. $\sigma_{control}$, $(\frac{EA}{L})_{control}$, and $(\frac{EI}{L^3})_{control}$ are the local buckling strength, the axial stiffness, and the flexural stiffness of the control profile, respectively, as listed in Table

2. These constraints were imposed to obtain an optimised profile with minimum weight (cost) and equivalent (or better) local buckling strength (σ_{BL}) and structural stiffness ($\frac{EA}{L}$ under compression and $\frac{EI}{L^3}$ under bending) of the hollow square PFRP control profile. The values of σ_{BL}, $\frac{EA}{L}$, and $\frac{EI}{L^3}$ are calculated by the FEM analysis for each configuration of the design parameters. The structural stiffness constraints were introduced to maintain the same serviceability (deflection) limits of the control profile in the design standards. Geometry limitations were imposed to avoid overlapping geometry in the FEA models. The maximum allowed value of h/b was assigned as 3.0 to avoid the local buckling and crippling of webs [27]. Manufacturing limitations on the corner radii ratio and the winding angle from the manufacturer [44] were considered. A higher percentage of axial rovings than wound fibres was enforced to fulfil the compressive and flexural stiffness requirements for civil applications. It should be noted that only the geometric parameters are represented in the objective function (cross-sectional area of the profile) while all the manufacturing parameters (layup and geometry) are represented in the constraints inequalities. The winding angle and axial-to-wound fibre ratio contribute towards the structural stiffness and buckling strength inequalities as they determine the modulus of elasticity (E) and affect σ_{BL}, respectively. The wall slenderness h/t, cross-sectional aspect ratio h/b, corner radii ratio r/R, and axial-to-wound fibre ratio were defined as real values (X) while the winding angle θ was assigned to an integer value (Y).

3. NUMERICAL APPROACH

The FEM approach implemented in this study was previously validated against experimental and theoretical results under compression [26] and bending [27] for the hollow square PFRP control profile. In this study, this approach was adjusted to reduce the computational cost and speed up the convergence in order to simulate the large number of models needed. The details of this numerical approach are discussed in the following sections.

3.1 Background

Abaqus 2019 was used to simulate the structural behaviour of the hollow box PFRP profile under two separate loading conditions of axial compression and four-point bending to evaluate the nonlinear buckling strength constraint. The FEM code was parametrised using Python 3.9.1 by scripting the geometry and layup of the profile as functions of the design parameters. The "Mask" command was replaced by the "findAt" command in the generated script to write the dimensional coordinates instead of the process mask ID. These coordinates were written as a function of the geometric parameters. The winding angle and the axial-to-wound fibre ratio were parametrised by changing the fibre angle of the inclined laminas (plies) and the thickness of each lamina, respectively, in the composite layup part of the generated script. Lamina material definition of the composite layup was used to model the elastic behaviour of the profile with a two-dimensional plane stress formulation for laminated shells [45]. The fibre volume fraction (V_f) of the lamina is 0.6 (as provided by the manufacturer) and its mechanical properties are shown in Table 3. The in-plane (G_{12}) and out-of-plane (G_{13}) shear moduli were assumed to be equivalent since the material is transversely isotropic [46]. The fibre volume fraction of the lamina was kept constant for all the models in the optimisation problems.

Table 3: Mechanical properties of unidirectional E-glass/Vinyl-Ester lamina used to model the pultruded FRP profile [26].

Elastic properties[a]	E_1(MPa)	E_2(MPa)	v_{12}	$G_{12} = G_{13}$ (MPa)	G_{23}(MPa)	
	45700	12100	0.28	4600	4000	
Strength limits[b]	X^T (MPa)	X^c (MPa)	Y^T (MPa)	Y^C (MPa)	S^L (MPa)	S^T (MPa)
	803	548	43	187	64	50
Fracture energy[c]	G_{LT} (N/mm)	G_{LC} (N/mm)	G_{TT} (N/mm)	G_{TC} (N/mm)		
	92	79	5	5		

[a] E_1 and E_2 are the axial and transverse elastic moduli, respectively. G_{12}, G_{13}, and G_{23} are the in-plane and out-of-plane shear moduli, respectively. v_{12} is the in-plane Poisson's ratio.[b] X^T and X^c are the longitudinal tensile and

compressive strengths, respectively. Y^T and Y^C are the transverse tensile and compressive strengths, respectively. S^L and S^T are the longitudinal and transverse shear strengths, respectively.[c] G_{LT} and G_{LC} are the longitudinal tensile and compressive fracture energies, respectively. G_{TT} and G_{TC} are the transverse tensile and compressive fracture energies, respectively.

The progressive failure of the fibres and matrix in the lamina was simulated using the Hashin damage model [45]. The model considered four different failure modes: fibre rupture in tension, fibre buckling and kinking in compression, matrix cracking under transverse tension and shearing, and matrix crushing under transverse compression and shearing. The failure starts at any element when its damage initiation criterion (strength limit) is met. Afterwards, the damage evolution algorithm, of the met failure mode, simulate the energy release, which is equivalent to the area of the stress-displacement curve of the element [45]. Consequently, the fracture energy of the element has to be assigned for each failure mode. The damage stabilisation scheme was implemented to eliminate the convergence problems accompanying the material failure by obtaining a positive tangent stiffness of the element for sufficient time increments during the failure. A viscosity coefficient of 1×10^{-3} sec was assigned for the stabilisation scheme of each failure mode based on a sensitivity study on the energy balance of the models [27].

The hollow box PFRP profile was modelled using the quadrilateral three-dimensional in-plane general-purpose continuum shell (SC8R) element because of its flexibility in simulating tapered or thickened geometries at the corners and capturing the through-thickness response accurately [45]. Based on mesh sensitivity studies [26,27], the element size was kept constant at all models with 5 mm in the longitudinal and transverse directions,1 mm through the thickness, and 1 mm locally seeded at the corner radii to obtain convergence in the numerical results. The same test setups shown in Table 2 were simulated in the FEM models with discrete rigid loading plates using tie constraint definition and displacement-control loading.

3.2 Nonlinear geometric incremental approach for local buckling

The Newton method in Abaqus/Standard was used to perform a nonlinear geometric analysis based on incremental time steps. The nonlinear deformations from geometry, material failure, and boundary conditions were captured by the implemented large displacement formulation. These severe nonlinearities accompanying buckling were damped using the adaptive automatic stabilisation scheme, which is used to prevent such termination errors. The reliance of the incremental approach on the number of increments was subsided by controlling the maximum increment size to reach convergence with 5% tolerance in the solution. This novel modelling approach to simulate the local buckling, post-buckling, and progressive failure of hollow box PFRP profiles was introduced and discussed in detail under compression [26] and bending [27] loadings. In this study, this approach was adjusted by introducing geometric imperfections to reduce the computational cost (speed up the convergence) and make it feasible to simulate the large number of models needed (1800 model) under each loading condition. Generally, geometric imperfections are introduced to assist in locating the buckling point in finite element analysis [47,48]. This feature is introduced here to speed up the analysis. The first three local buckling modes from linear eigenvalue buckling analysis were introduced as geometric imperfections in the nonlinear buckling incremental analysis to assist in locating the buckling point and speed up the solution convergence. It is worth highlighting that these geometric imperfections were used in this study for numerical purposes (speed up the solution convergence) only and do not reflect any physical out-of-straightness in the studied profile. A sensitivity study was performed to assign the proper amplitude (scale factor) of these imperfections for maximum increase in the analysis speed without compromising the accuracy of the results. Fig. 3 depicts the results of this study on the hollow square PFRP control profile under axial compression and four-point bending. The figure compares the models with geometric imperfections versus the validated modelling approach established for compression

[26] and bending [27] loadings. It also highlights the effect of the scale factor of these imperfections on the convergence and validity of the results. Introducing geometric imperfections assisted in capturing the local buckling with a lower number of increments needed to reach convergence, thus it increased the analysis speed. This FEM approach incorporating geometric imperfections and controlled increment size represents an efficient and fast-converging tool that reduced the computational cost up to three times (under compression) compared to the models with controlled increment size only.

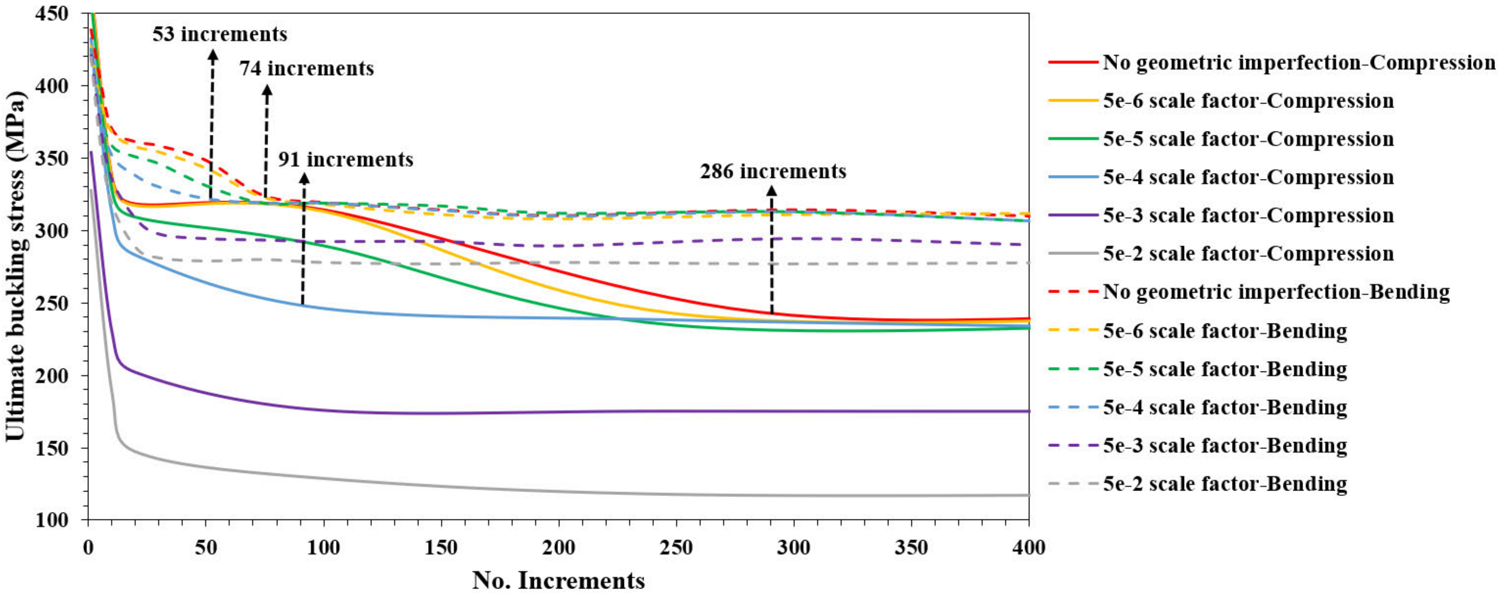

Fig. 3. The ultimate buckling stress versus the number of increments for different scale factors of the first three buckling modes of the hollow box PFRP profile under axial compression and four-point bending.

A scale factor of 5×10^{-4} (solid blue line for compression and dashed blue line for bending in Fig. 3) for the geometric imperfections presented the optimal amplitude with the fastest convergence and the unaffected accuracy of the results. This amplitude increased the analysis speed 3.1 and 1.4 times under compression and bending, respectively, compared to the models with no geometric imperfections (solid red line for compression and dashed red line for bending in Fig. 3). The increase in the analysis speed due to the addition of geometric imperfections was found to be higher under compression compared to bending. This was referred to the buckling behaviour under each loading condition since local buckling is more severe under compression compared to bending [49–51]. The geometric imperfections affect the four walls of the profile under compression while they influence only the top flange under bending. Consequently, the geometric imperfections covering a larger area under compression greatly reduced the number of increments needed to capture the instability. This is the same reason for the faster convergence of the solution under bending (four times the increment size) compared to compression despite the larger number of elements in the bending model. A smaller number of increments (larger increment size) was sufficient to capture the local buckling of the top flange and converge the solution under bending, while a larger number of increments (smaller increment size) was needed for the buckling of four walls under compression. The sensitivity study was extended to cover different configurations of layup and geometric parameters to ensure the validity of the selected scale factor, and the same results were obtained compared to the validated models [26,27].

4. NUMERICAL RESULTS AND DISCUSSION

In this section, the results of the two optimisation problems under axial compression and four-point bending loadings are discussed separately for each loading condition. The design interactions are then presented by harmonising the results under both loading conditions. For each loading condition, the GA optimisation results were presented in terms of the solution convergence and the design guidelines for the optimal parameters and their structural performance. The data generated from the GA codes were interpolated using the Kriging model to fully explore the design space for the interactive compressive and flexural buckling strengths of the hollow box PFRP profile.

4.1 GA optimisation under single load condition

The optimisation problem for each loading condition was executed three times to assess the convergence of the optimisation results and to check how close the solution reached global minima. The numerical results of the optimisation under compression along with the convergence curves are shown in Fig. 4. Due to the presence of one integer variable (winding angle), the objective function was renamed to be the penalty function, as discussed in section 2.2. For each optimisation run, there are two representative points. The mean penalty value is the value of the average penalty of the entire population in the iteration (i.e. the average cross-sectional area over the entire population of 20 models) and the best penalty is the value of the fittest solution within the current generation (i.e. the minimum cross-sectional area over the entire population of 20 models). The red dashed line in Fig. 4 shows the penalty (cross-sectional area) value of the control profile. The solution of all runs started to converge at the 19th generation (after 18 iterations). The optimal configuration of the design parameters of hollow box PFRP profile under compression was h/t = 31.2, h/b = 1.0, r/R = 2.5, fibre angle of the wound fibres = 22°, and axial fibre ratio = 87%, after rounding. The optimised profile obtained a buckling strength ratio of $\sigma/\sigma_o = 1.03$ and axial stiffness ratio of 1.001 compared to the control profile with buckling strength and axial stiffness of 251.5 MPa and 151.9 kN/mm, respectively. The cross-sectional area of the optimised profile was 1689.7 mm^2 with a reduction in the weight (cost) per metre by 11.53%. The optimal configuration consisted of a low inclined (wound) fibres ratio (13%) even though increasing this ratio can enhance the buckling capacity of laminated walls [52,53]. Moreover, the winding angle of the optimal configuration was 22° instead of 45°, which provides the maximum buckling capacity for laminated walls [54,55]. These shifts in the layup parameters were caused by the axial stiffness constraint (inequality), which dedicated these parameters to serve the axial stiffness with a low winding angle and a high axial fibre ratio required to fulfil this design condition. This observation highlights the importance of including such serviceability limits in these optimisation runs in order to obtain applicable and reliable configurations matching the design requirements of standards ([12,14]).

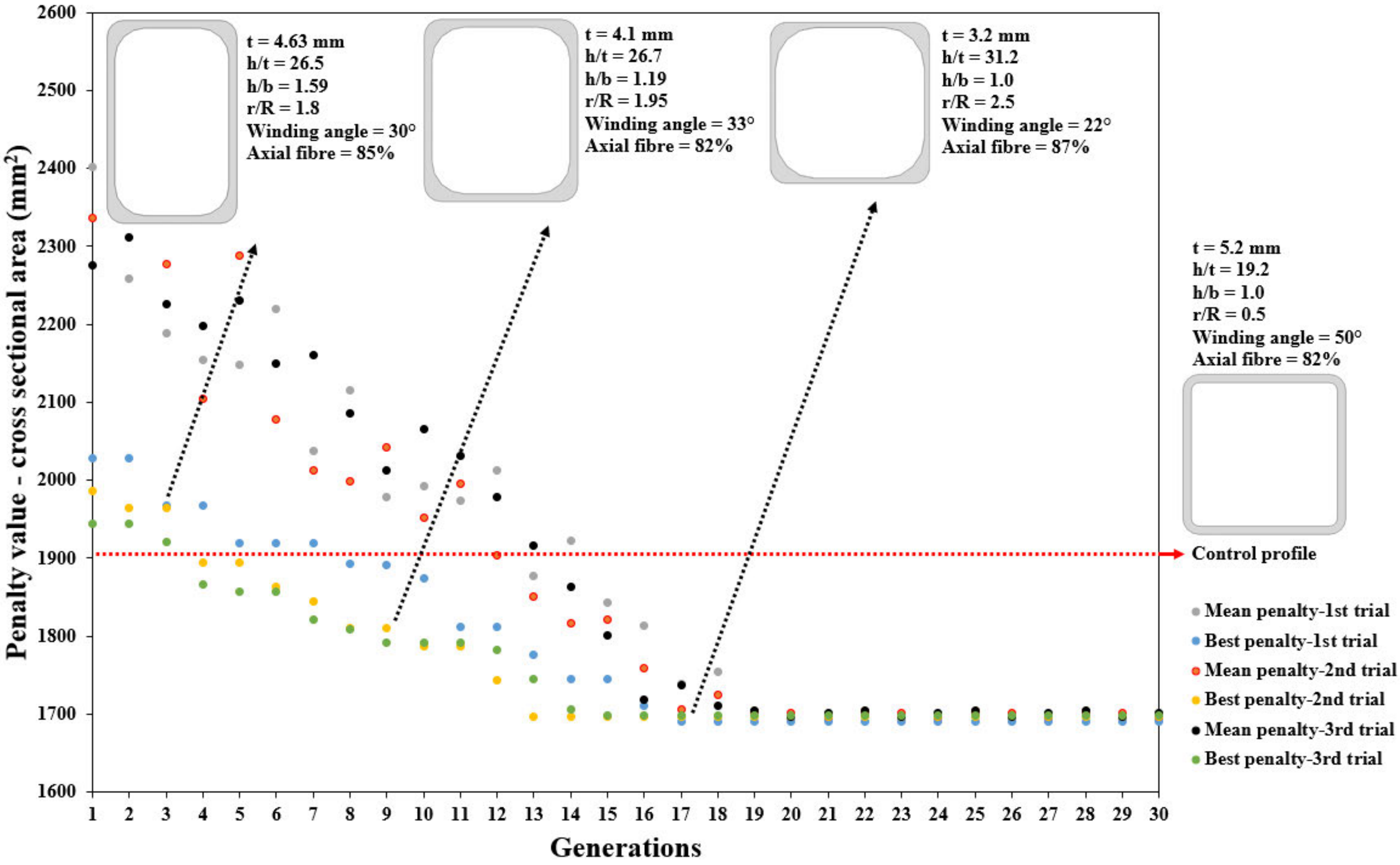

Fig. 4. Convergence of the objective function (cross-sectional area) and the change in the configurations of the design parameters versus the number of generations for the hollow box PFRP profile under axial compression (wound fibre percentage = 100% - axial fibre percentage).

Two observations were noted regarding the change of the geometry as the solution converges. The first one was related to the change in the cross-sectional aspect ratio (h/b) from rectangular to square section and the second one was on the decrease of the wall thickness (t) and the increase in the corner radii ratio (r/R). A cross-sectional aspect ratio of h/b = 1 obtained the optimal local buckling resistance, which agrees with Asadi et al. [56] findings on the local buckling behaviour of laminated composite box columns. The local buckling strength is increased as the maximum wall slenderness is reduced since the unsupported length of the wider walls is decreasing and preventing local buckling at lower loads. The square cross-section obtains the lowest value of the maximum wall slenderness (the shortest unsupported length of the wider walls), which drives local buckling to occur simultaneously at all walls instead of occurring earlier in the wider walls for rectangular sections.

The wall thickness decreased and the profile mass started concentrating at the corners as the solution converges. This finding confirms that increasing the corner radii ratio (r/R) enhances the local buckling capacity of the section higher than increasing the wall thickness (reducing the wall slenderness). It was inferred that the critical role of a larger r/R ratio in uniformly distributing the concentrated stresses at the corners was the reason, as shown in Fig. 5. The larger area at the corners of the optimal profile eliminated any concentration of stresses while maintaining the same stress distribution at the thinner walls. Thus, making the entire cross-section (walls and corners) works at the same level of stress instead of stressing the corners more than the walls as in the control profile. Moreover, thicker corners exhibit higher rotational restraint and reduce the effective unsupported wall width. Investing in larger r/R can result in optimised profiles with lower weight (cost) and equivalent local buckling capacity (or higher) to the control profile. It is worth to mention that the increased area at the corners (from a larger r/R ratio) was modelled with the same axial-to-wound fibre ratio of the walls, at which the axial fibres represent 87% and the wound fibres are 13%. This assumption is ideal and might be hard to be implemented in manufacturing as wound fibres might face wrinkling at a large r/R ratio. Thus, unidirectional (axial fibres) fillets can be proposed as a practical alternative solution to fill the increased area at the corners. Simulating this alternative option obtained 2.1% lower buckling strength and 0.9% higher axial stiffness compared to the optimal profile results, which is a negligible difference that does not affect the two constraints of the optimisation problem.

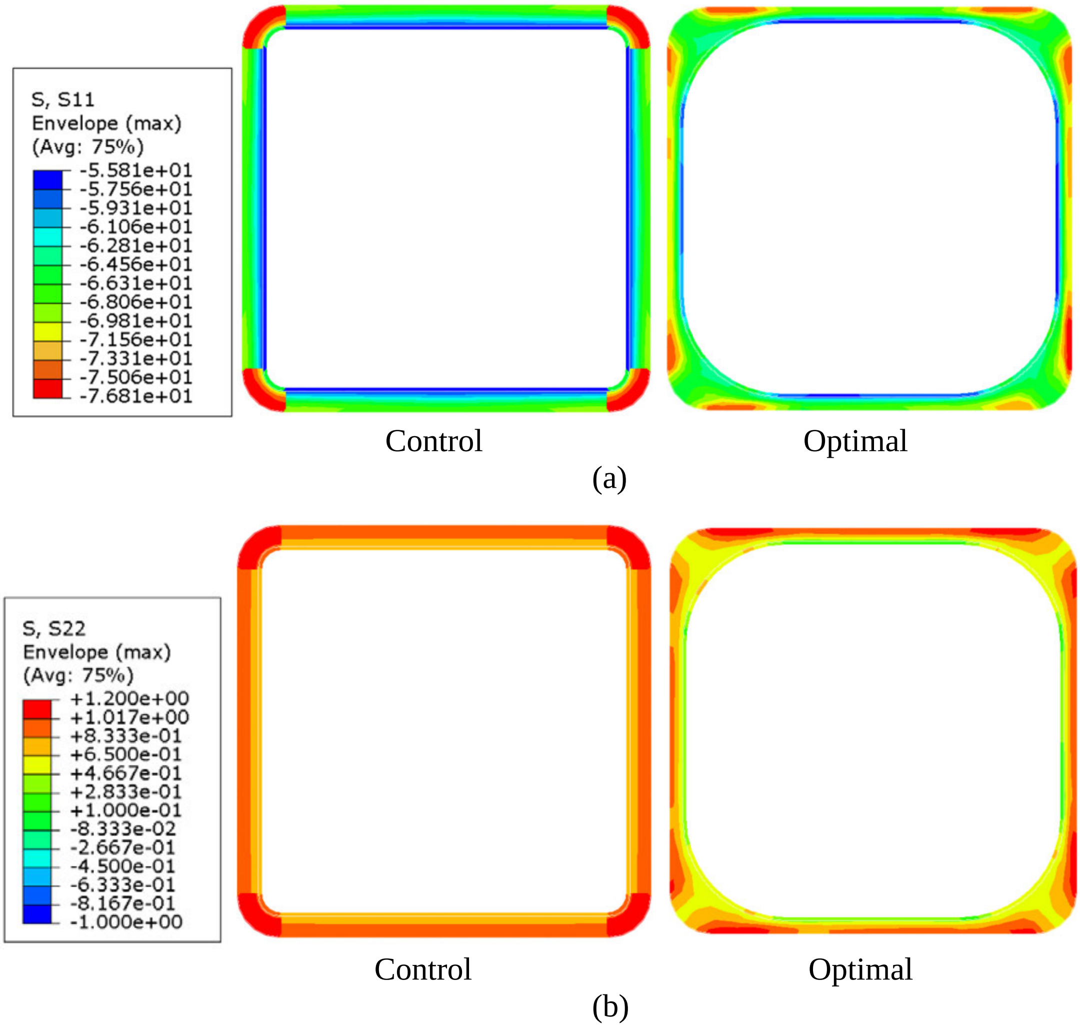

Fig. 5. The stresses distribution along cross-section of the control profile versus the optimal profile under compression (a) axial stress and (b) transverse stress.

Regarding the optimisation runs under bending, the numerical results along with the convergence curves are shown in Fig. 6. The red dashed line shows the penalty (cross-sectional area) value of the control profile. The solutions of all runs started to converge at the 17th generation (after 16 iterations). The optimal configuration of the design parameters of hollow box PFRP profile under bending was h/t = 43.2, h/b = 2.0, r/R = 1.84, fibre angle of the wound fibres = 36°, and axial fibre ratio = 83%, after rounding. The optimised profile obtained a buckling strength ratio of $\sigma/\sigma_o = 1.04$ and flexural stiffness ratio of 1.07 compared to the control profile with buckling strength and flexural stiffness of 338.4 MPa and 650.4 N/mm, respectively. The cross-sectional area of the optimised profile was 1406.34 mm^2 with a reduction in the weight (cost) per metre by 26.4%. The resulted layup properties do not represent the best configuration against local buckling of laminated walls as was noticed previously for the optimal configuration under compression. This deviation was due to the flexural stiffness constraint (inequality), which forced the layup properties to serve the flexural stiffness with high axial fibres ratio and low winding angle similar to the optimal profile under compression.

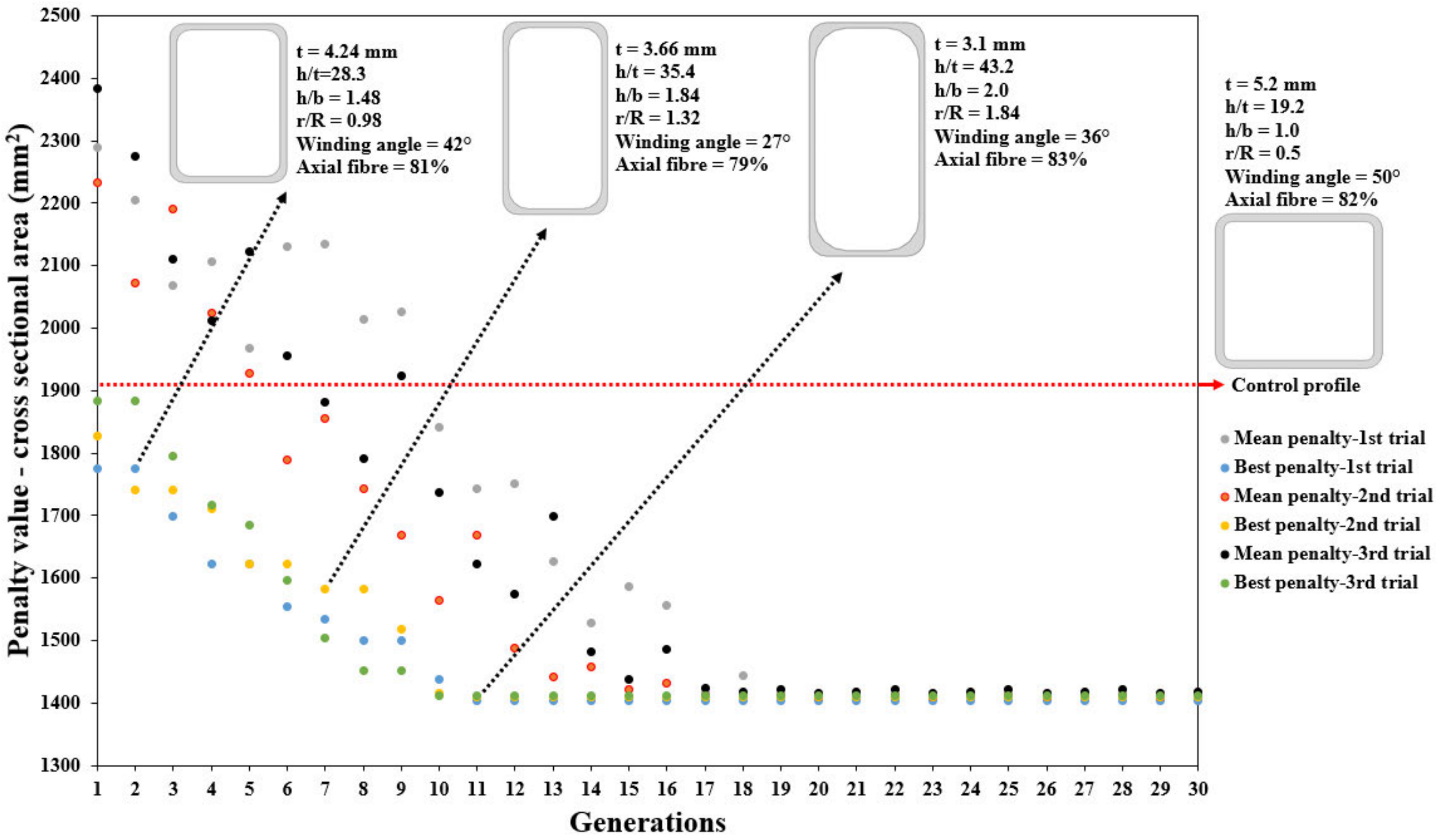

Fig. 6. Convergence of the objective function (cross-sectional area) and the change in the configurations of the design parameters versus the number of generations for the hollow box PFRP profile under four-point bending (wound fibre percentage = 100% - axial fibre percentage).

The larger h/b ratio enhanced the flexural stiffness by increasing the moment of inertia and increased the buckling strength by reducing the unsupported width of the top flange. The section area was shifted from the walls towards the corners as the r/R ratio increased and the wall thickness decreased when the solution converged. The larger r/R ratio redistributed the concentrated compressive stresses from the top flange in the control profile towards the larger corners in the optimal profile, as shown in Fig. 7. Because of the stresses redistribution, the optimal profile with the smaller cross-sectional area (by 26.39%) resisted the same buckling load as the control profile with the larger cross-sectional area. This observation on the significance of a larger r/R ratio in enhancing the buckling strength of hollow box PFRP profiles under bending agrees with the findings of the authors in previous research [27].

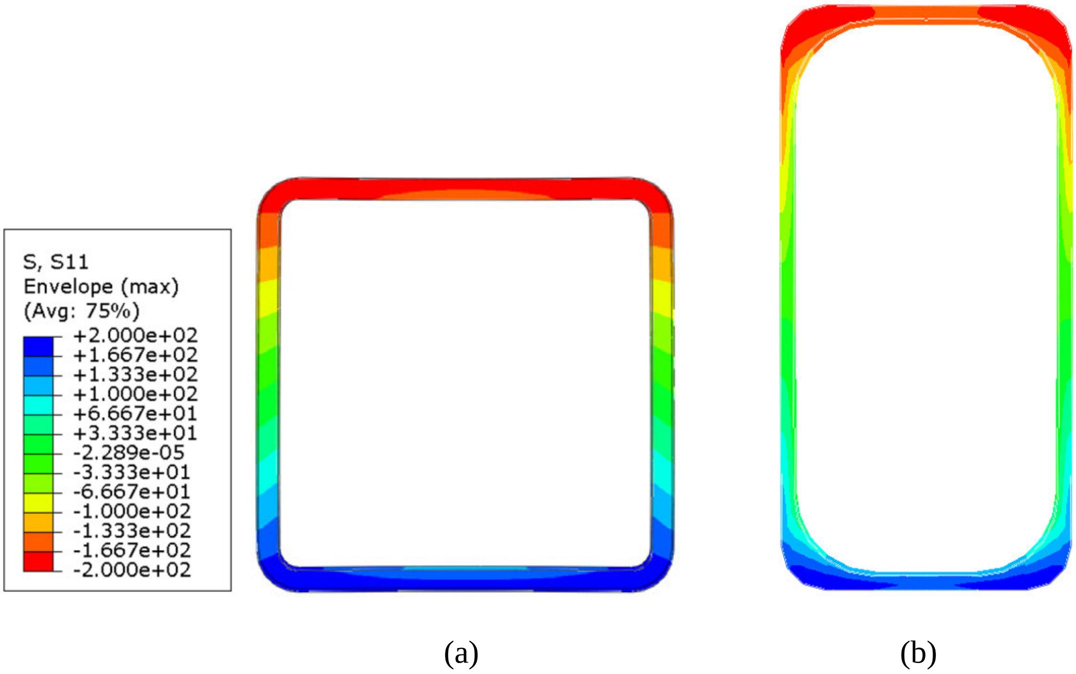

Fig. 7. The axial stresses distribution along cross-section of the (a) control versus the (b) optimal hollow box PFRP profiles under bending.

When comparing the optimal configurations of the profile under compression versus bending, it is noticed that the r/R ratio increases and the wall thickness decreases as the solution converges under both loading conditions. This observation emphasises the significance of a larger corner zone (flange-web junction) in providing more stable sections against local instabilities. However, the h/b ratio of the profile increases under bending (h/b=2.0) unlike its behaviour under compression (h/b=1.0). Moreover, the resulted r/R ratio was larger for the profile under compression (r/R=2.5) compared to its value for the profile under bending (r/R=1.84). The wall slenderness was larger for the profile under bending (h/t=43.2) compared to its counterpart for the profile under compression (h/t=31.2). These variations in geometry of the optimal configurations were referred to the different nature of local buckling under compression versus bending. Under compression, the four walls are affected and a square cross-section represents the optimal case allowing all the walls to buckle simultaneously under higher buckling strength compared to a rectangular section. Whereas only the top flange and upper parts of the webs (half the section area) are affected by the compressive stresses under bending. Consequently, local buckling is more severe under compression compared to bending, and smaller wall slenderness under compression is needed to provide thicker walls and shorter unsupported width. Moreover, a larger r/R ratio is needed under compression to redistribute the compressive stress along the four corners and walls and strengthen them. Thus, the reduction in the optimised cross-section area (lower cost per metre of pultrusion) under bending was 2.2 times its equivalent under compression. The optimisation range of the geometric parameters is wider under bending compared to compression as the cross-sectional aspect ratio serves both the flexural stiffness and strength constraints, while it weakens the buckling strength under compression and reduces the axial stiffness at the post-buckling zone. In addition, the values of the r/R ratio and the wall slenderness should be higher and lower, respectively, to strengthen the four walls and corners against buckling under compression, while only the top flange and its corners need to be strengthened against buckling under bending. Thus, the cross-sectional area is effectively reduced under bending compared to compression.

4.2 Design chart for interactive compressive and flexural buckling strengths

In this section, the relationship between the geometric parameters and the compressive and flexural buckling strengths of the hollow box PFRP profile is established to generate design curves, which collectively combine all these geometric parameters (the wall slenderness, the cross-sectional aspect ratio, and the corner radii ratio) along with their interactions. The results of the two GA codes (axial compression and four-point bending) were stored by saving the buckling strength resulting for each configuration of the design parameters at each iteration. This dataset of 1800 points (for each loading condition) was used to generate the design chart connecting the compressive and flexural buckling strengths with the geometric design parameters. The layup properties were excluded from this chart because the contribution of these parameters (the winding angle and the axial-to-wound fibre ratio) towards the buckling strength was found to be negligible (2.5% under compression and 7.8% under bending from two-way analysis of variance ANOVA) compared to the geometric parameters. This design chart was then used to design a rectangular girder of a bridge as a case study on the design of hollow box PFRP profiles. The full list of the design configurations and results of the numerical study on the hollow box pultruded FRP profile are presented in Appendix A.

4.2.1 Generating design chart using the Kriging Model

The compressive and flexural buckling strengths should be both prescribed for each data point (design configuration of the geometric parameters) resulted from the two GA codes in order to plot these strengths in one design chart. However, not all the resulted data points have the values of both compressive and flexural buckling strengths after combining the results of the two GA codes, as most of these points have one known strength value but miss the other one. The data combined from both GA codes can be divided into three groups of points having both compressive and flexural strengths (4.64%), points having only compressive strength (47.68%), and points having only flexural strength (47.68%). The known values of strengths will be labelled as “measured values” and the missing values in the design space will be predicted using the Kriging model. This geostatistical tool is widely utilised to interpolate the missing values in spatial and computer experiments with a linear unbiased predictor to minimise the variance (error) of the prediction. It is based on autocorrelation of the data governed by prior covariances as the statistical relationship (weights) among the measured points in the neighbourhood is considered when estimating the target points [57], which makes it an excellent choice for the current problem. Mathematically, the interpolated value equals the weighted measured values depending on their distance from the interpolated value [57]**:**

$$\hat{Z}(\mathbf{x_0}) = \sum_{i=1}^{N} \lambda_i z(\mathbf{x}_i) \tag{7}$$

Where $\hat{Z}(\mathbf{x_0})$ is the predicted (strength) value at the targeted point, $z(\mathbf{x}_i)$ is the design variable (strength) at the sampling data point $\mathbf{x}_i$, λ_i are the weights of the measured values $z(\mathbf{x}_i)$. The closer the measured values are to the interpolated value, the larger is the weight they have. The summation of λ_i is assumed to equal one to ensure unbiased estimations. The Kriging model does not only obtain a prediction for the required point, but it also estimates the prediction variance (error) [58]. The prediction error can be calculated based on the assumed expected difference of $E\left[\hat{Z}(\mathbf{x_0}) - z(\mathbf{x_0})\right] = 0$ [57]:

$$var\left[\hat{Z}(\boldsymbol{x_0})\right] = E\left[\{\hat{Z}(\boldsymbol{x_0}) - z(\boldsymbol{x_0})\}^2\right] = 2\sum_{i=1}^{N} \lambda_i \gamma(\boldsymbol{x_i} - \boldsymbol{x_0}) - \sum_{i=1}^{N}\sum_{j=1}^{N} \lambda_i \lambda_j \gamma(\boldsymbol{x_i} - \boldsymbol{x_j}) \tag{8}$$

Where E refers to "expectation", the quantity $\gamma(\boldsymbol{x_i} - \boldsymbol{x_0})$ is the semivariance of Z between the sampling point $\boldsymbol{x_i}$ and the target point $\boldsymbol{x_0}$, and $\gamma\left(\boldsymbol{x_i} - \boldsymbol{x_j}\right)$ is the semivariance between the ith and the jth sampling points. The weights of the measured values must be determined in order to obtain the prediction value and its error. These weights can be calculated using a geostatistical representation of the variance (γ) of the measured values with respect to the distance between their points. This graphical representation of spatial autocorrelation (continuity of data) is called the "variogram", which is an x-y plot of the data with the distance between the measured points presented on the x-axis and the variance of their values presented on the y-axis. This type of Kriging, which depends on generating the variogram of a dataset to predict values within it, is called the ordinary Kriging model. It is the most common type of Kriging, at which the mean is unknown and the variogram is a prerequisite [59]. The dataset should be stationarity (the data attributes such as the mean and standard deviation should be constant) and have a constant variogram in order to use this Kriging model on it [60]. The first condition is satisfied for this type of problem and the second condition was confirmed as shown next. The Matheron's method of moments (MoM) is usually used to compute the variance [57]:

$$\hat{\gamma}(h) = \frac{1}{2m(h)} \sum_{i=1}^{m(h)} \{z(x_i) - z(x_i + h)\}^2 \quad (9)$$

Where $z(x_i)$ and $z(x_i + h)$ are the values of z at the locations x_i and $x_i + h$, respectively. $m(h)$ is the number of paired comparisons at a lag distance h between these locations. The experimental variograms of the axial compression and four-point bending design data were plotted and fitted to obtain the best sill (the maximum variance in values for autocorrelation between sampling points) and range (the maximum lag distance for autocorrelation between sampling points) values ensuring spatial correlation for the estimation, as shown in Fig. 8. The sill and range values circle the zone that its measured values will be used to calculate the weights for the prediction. The sampling points outside the sill-range intersection do not spatially correlate to the prediction because they are far from it, and their measured values will not be used to calculate the weights.

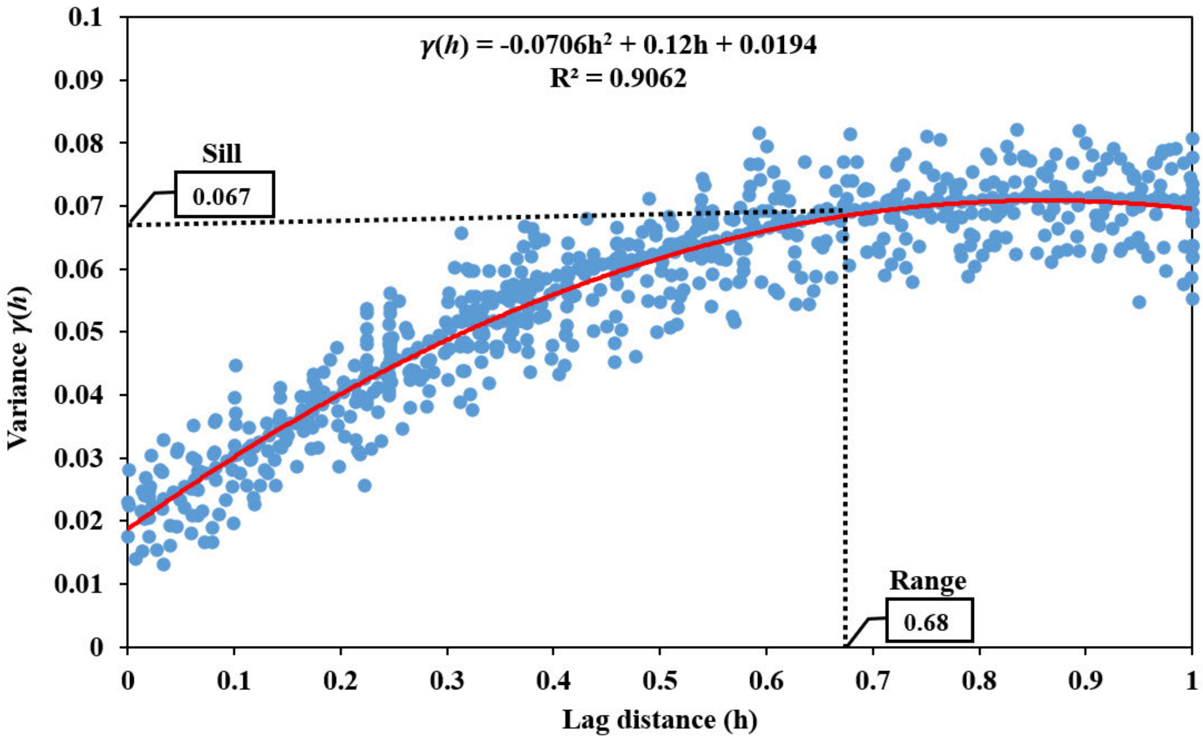

(a)

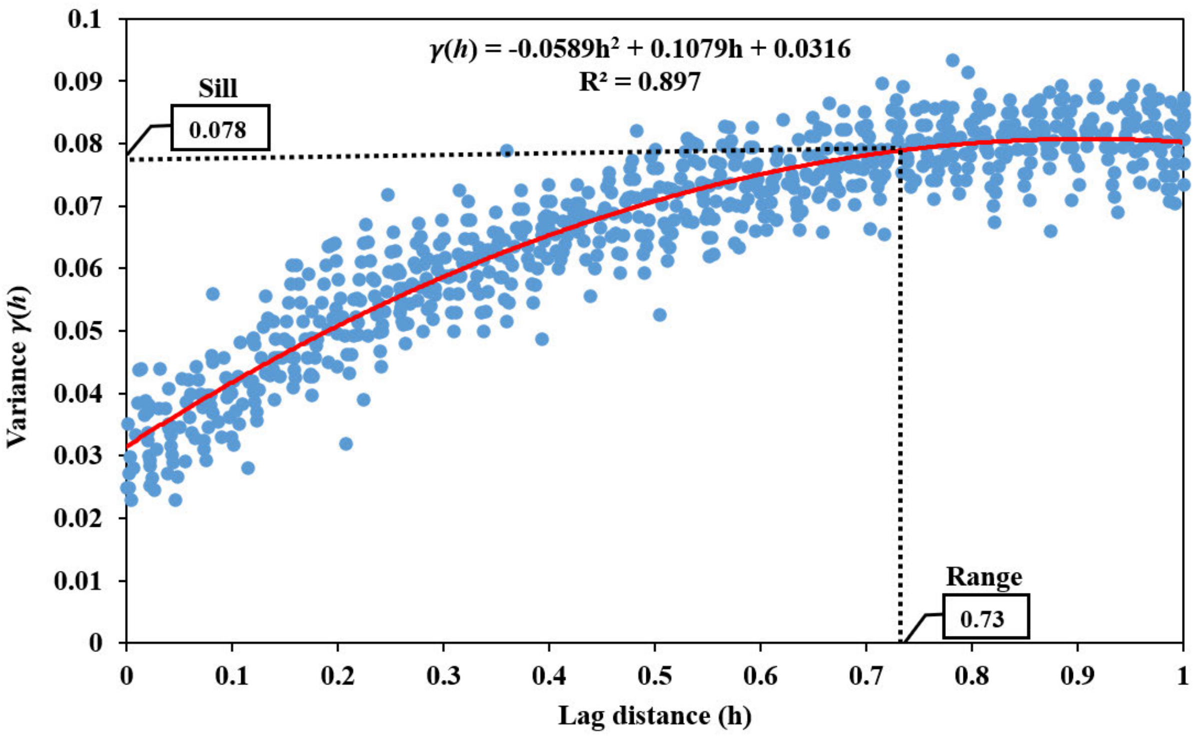

(b)

Fig. 8. Experimental variograms of the measured strength values resulted from the (a) compression and (b) bending GA codes along with their best curve fit.

The low variance values indicate that the relative difference between the strength values when their locations (values of geometric parameters) were slowly changing was small. The noise in the variance values was referred to the neglected layup parameters (winding angle and axial-to-wound fibre ratio), which slightly deviated the strength values for the same location (values of geometric parameters). The variance between the measured values was not zero when the distance between the sampling points was zero (the same configuration of the geometric parameters). This observation is called the "Nugget" effect, which refers to the noise in the data caused by the different winding angles and axial-to-wound fibre ratios for the same configuration of geometric parameters. This effect was found to be higher under bending compared to compression because the effect of the layup parameters on local buckling strength was found to be higher under bending with 5.25% and 2.55% for winding angle and axial-to-wound fibre ratio, respectively, compared to 1.22% and 1.25% for winding angle and axial-to-wound fibre ratio, respectively, under compression. Moreover, the autocorrelation zone bounded by the sill and range was larger under bending compared to compression. This was referred to the more severe buckling effect under compression compared to bending, which increased the variance in buckling strength values between the successive points and limited the spatial correlation zone.

The Kriging model was implemented in MATLAB 2020b to obtain the flexural buckling strength for the points having only the compressive strength, and the compressive buckling strength for the points having only the flexural strength. The MATLAB code used here was developed by Thomas Hansen [61]. The sill and range values obtained from the experimental variograms of axial compression and four-point bending data were implemented in the mGstat MATLAB code [61] to compute the semivariances, the target prediction value $\hat{Z}(\mathbf{x_0})$, and its error $var\left[\hat{Z}(\boldsymbol{x_0})\right]$. The complete design space with the measured values resulted from the GA codes and the prediced values resulted from the Kriging model is presented in Fig. 9. The maximum error in the Kriging model predictions was 24.1 MPa (8.44%) for the flexural strength value 285.5 MPa at the (285.5, 253.7) MPa point. The average error of all predictions was 6.52%. The right-angled triangle shape of the design space was referred to the larger flexural strength compared to the compressive strength at every point (design configuration of the geometric parameters) since the local buckling is more severe under compression and the flexural strength is increased when the h/b ratio is increased, unlike the compressive strength.

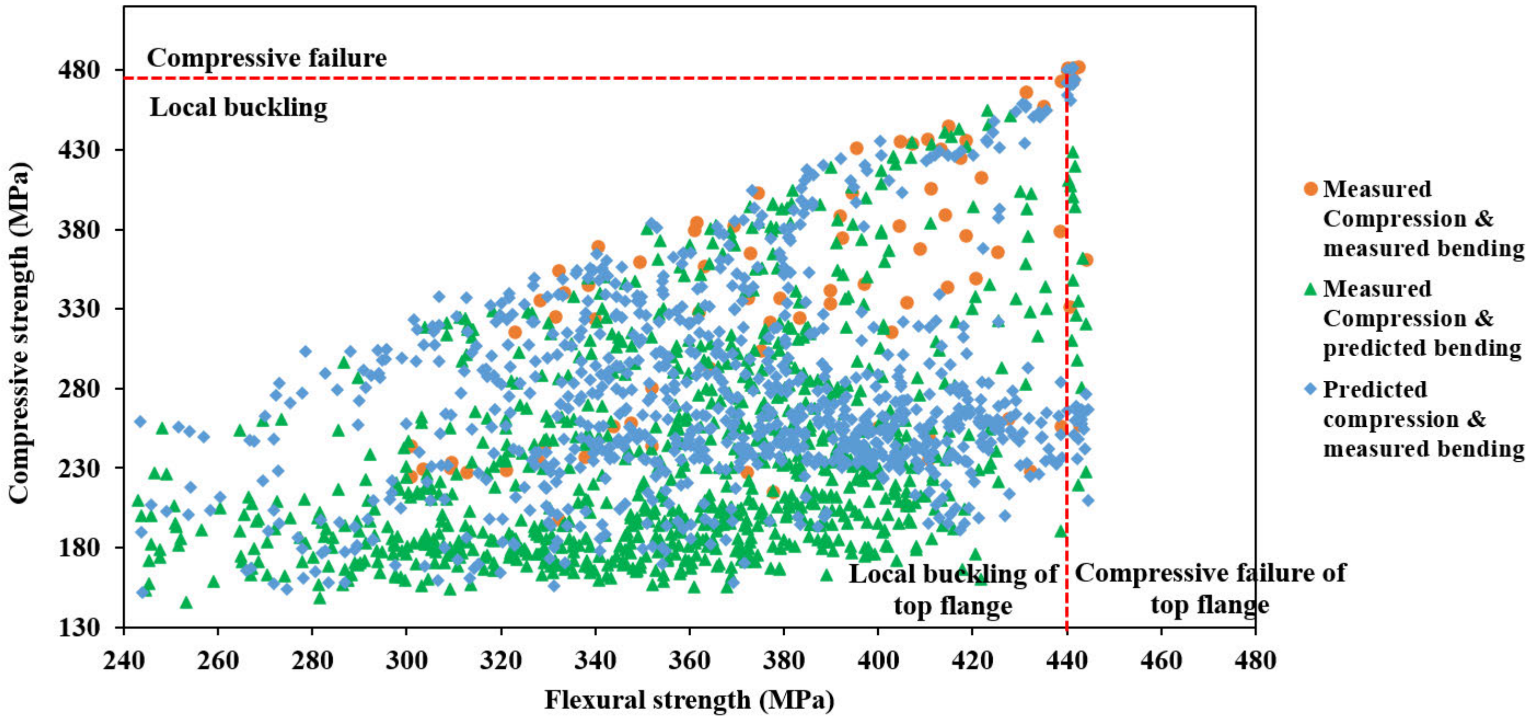

Fig. 9. The complete design space with the measured values resulted from the GA codes and the predicted values resulted from the Kriging model.

From the complete design space, the critical points of different wall slenderness and the same h/b and r/R ratios were connected to obtain design curves, as shown in Fig. 10. The font colour and type refer to specific h/b ratio and r/R ratio, respectively. The intermediate points of the geometric parameters, which are not presented by the design curves, can still be interpolated depending on their locations from the curves. In order to use the design chart universally, each local buckling strength (σ_{bl}) was normalised using the ultimate material strength (σ_{ult}), which was 473 MPa and 440 MPa under compression and bending, respectively, as obtained from the coupon tests [44]. The maximum wall slenderness (h/t) was presented in the design chart since it controls the profile local buckling under compression. The corresponding top flange slenderness (b/t), which controls the profile local buckling under bending, can be calculated using the formula presented in the figure. When the σ_{bl}/σ_{ult} ratio is lower than 1.0, then local buckling of the walls or local buckling of the top flange controls the failure mode of the profile under compression or bending, respectively. The failure mode shifts to compressive failure of fibre and matrix followed by transverse shear (local buckling is completely eliminated) when this ratio equals 1.0. The design chart also highlights the interactions between the geometric parameters. Considering these interactions during the design stage is very important and can facilitate optimised designs with economic attributes instead of costly designs when these interactions are disregarded. The buckling curves shift in a concave up shape towards the flexural strength while the compressive strength is decreased as the h/b ratio is increased for the reasons explained in the aforementioned paragraph. The enhancement in the compressive strength from decreasing the wall slenderness is higher when the h/b ratio is small (up to 9.1% for 1.0 increment in h/t ratio when h/b = 1.0). On the contrary, the flexural strength is significantly increased as the wall slenderness is decreased at a larger h/b ratio (up to 17.6% for 1.0 increment in h/b ratio at the same value of h/t ratio). Increasing the r/R ratio for slender walls (h/t > 15.6 under compression and > 16.4 under bending) exhibited a higher increase in the compressive and flexural strengths compared to thick walls since the failure mode of thick walls is closer to the ultimate compressive failure of the material than to local buckling. Moreover, the increase in the compressive and flexural strengths of the profile due to the increase in r/R ratio was higher when the h/b ratio was small (up to 13.2% and 19.4% for 1.0 increment in r/R ratio when h/b = 1.0 under compression and bending, respectively). The design of a hollow rectangular PFRP girder was undertaken in the next section using the design chart to eliminate local buckling and reach the ultimate material strength.

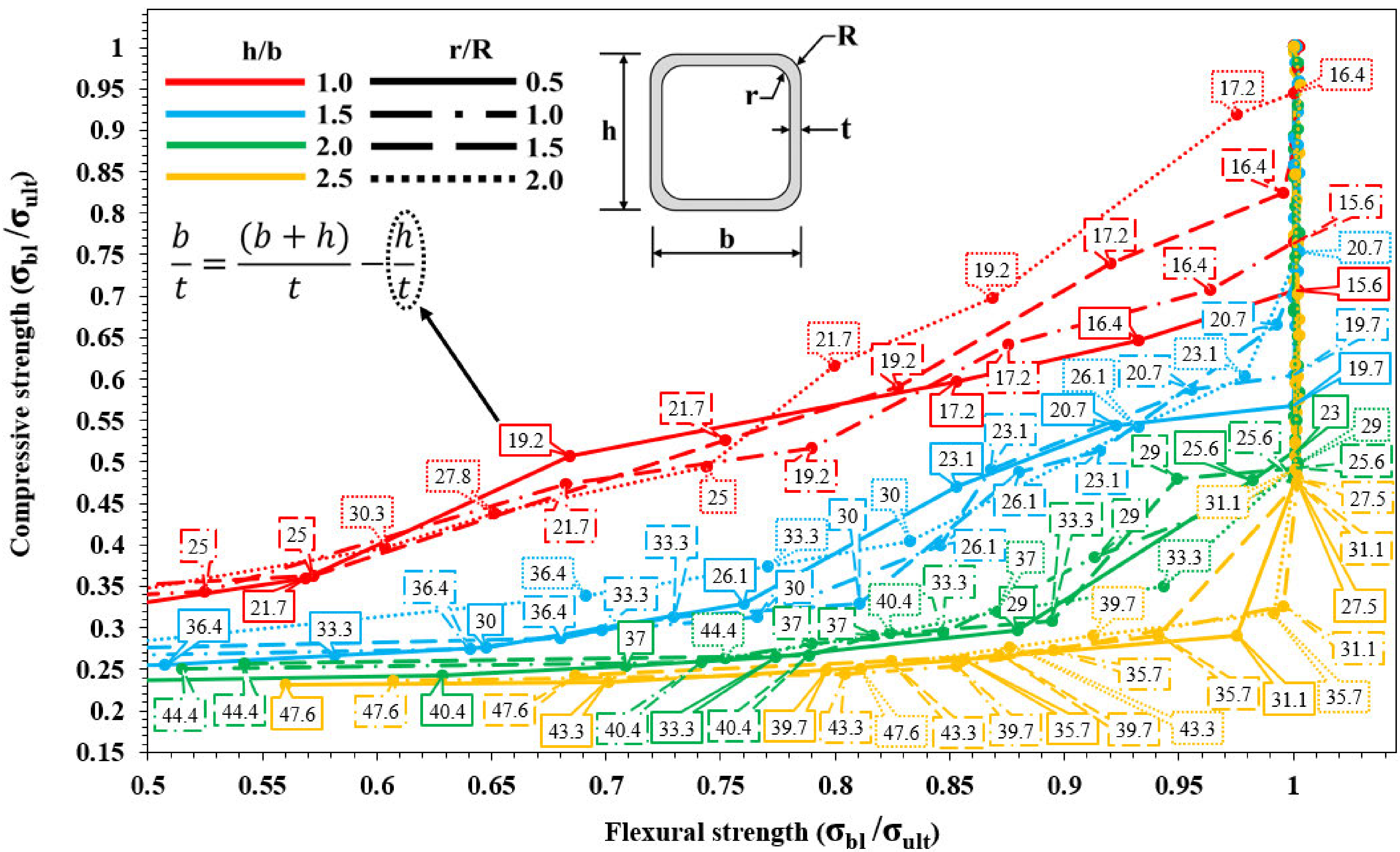

Fig. 10. Local buckling design chart of hollow box PFRP profiles in terms of the geometric parameters.

4.2.2 Case study on the design of hollow box PFRP girder

In this section, the design of a new rectangular beam by Wagners (CFT) to serve as a bridge girder is presented. The motivation of this case study was to produce a large rectangular profile to replace the in-service double-cell bonded girder shown in Fig. 11. Manufacturing such a profile is going to alleviate the need for bonding of smaller square profiles and reduce the post-processing cost.

Fig. 11. Double-cell bonded girder assembled by two 125×125×6.4 mm hollow square PFRP profiles [44].

The new profile must have the same or better mechanical properties as the double-cell bonded girder with an elastic modulus (E) of 39100 MPa and flexural strength of 296.4 MPa. The failure mode of the double-cell bonded girder was local buckling of the top flange (in the top cell) and the new profile will be designed to overcome this instability failure and reach the ultimate compressive strength of the material. The flexural stiffness requirement was met with simple calculations on the layup properties to obtain a value of 45400 MPa for the elastic modulus (E) of the profile with a stacking sequence of [0°/+θ/0°/-θ/0°/-θ/0°/+θ/0°]. The assigned values of the winding angle and axial-to-wound fibre ratio were 35° and (0°:80.9%, 35°:19.1%), respectively, and the fibre volume fraction (V_f) of the lamina was 0.62 as found experimentally. Regarding the design against local buckling, the current standards [12–15] do not provide comprehensive design charts or formulas of the geometric parameters (wall slenderness, cross-sectional aspect ratio, and corner radii ratio) and their interactions, but only conservative uneconomic formulas. Thus, the design chart (Fig. 10) generated in this study was used to choose the proper values of the geometric parameters to eliminate the local buckling of the girder under bending. First, the section height was assumed to equal the section height of the double-cell bonded girder with a value of 250 mm and the h/b ratio was assigned to a value of 2.5 (yellow lines) in order to achieve the required flexural stiffness with the minimum material used. The outer and inner corner radii were assigned as 5 mm and 7.5 mm, respectively, with an r/R ratio of 1.5 (dashed yellow line) to obtain a higher increase of the flexural strength and economic design of cost compared to reducing the wall slenderness, as discussed in section 4.1. Finally, the first point (of the dashed yellow line) that intersects the perpendicular line directed from the x-axis at σ_{bl}/σ_{ult} = 1.0 is selected, which has a wall slenderness value of 31.1 resulting in a wall thickness of 8 mm. From Fig. 10, the chosen design (h/t = 31.1, r/R = 1.5, and h/b = 2.5) is expected to provide σ_{bl}/σ_{ult} = 0.474 under compression and σ_{bl}/σ_{ult} = 1.0 under bending. The chosen design with 250×100×8 mm cross-sectional dimensions was expected to eliminate local buckling, shift the failure mode to compressive failure of the top flange, and exhibit a flexural strength equivalent to the ultimate material strength. The layup properties and cross-sectional geometry of the hollow square profile 125×125×6.4 mm and the new rectangular profile 250×100×8 mm are summarised in Table 4.

Table 4: Layup and geometric properties of hollow PFRP profiles.

	Profile label	S-125×125×6.4	R-250×100×8
Geometric properties	Wall width (mm)	125	100
	Wall depth (mm)	125	250
	Wall thickness (mm)	6.4	8.0
	Outer corner radius (mm)	10.0	5.0
	Inner corner radius (mm)	4.8	7.5
Layup properties	Stacking sequence	[0/+50/0/-50/0/-50/0/+50/0]	[0/+35/0/-35/0/-35/0/+35/0]
	Fibre percentage (%)	0°: 78.1, 50°: 21.9	0°:80.9, 35°:19.1

To verify the design approach, the new hollow rectangular girder was tested under four-point bending. Table 5 presents the experimental results of the bending test, which was undertaken with a span length of 4500 mm (Span-to-depth ratio L/D = 18) and a shear span of 1850 mm (shear span-to-depth ratio a/D = 7.4) in compliance with ASTM D7249/D7249M specifications [35–38]. The numerical results closely agree with the experimental results in terms of the flexural strength and the failure mode, as shown in Fig. 12. The failure sequence started with a compressive failure of the top flange followed by web shear failure and fibre delamination. No evidence of local buckling was monitored. The new rectangular girder (A = 5370 mm^2) fulfilled the design requirements with a 10.6% lower cost per metre of pultrusion, elastic modulus ratio (E/E_o) = 1.16, and flexural strength ratio (σ/σ_o) = 1.41 compared to the double-cell bonded girder (A = 5940 mm^2).

Table 5: The experimental versus numerical results of the new hollow rectangular girder subjected to four-point bending.

No. Specimen	Ultimate load (kN)	Moment (kN.m)	EXP Flexural strength (MPa)	FEA Flexural strength (MPa)	Error in $\boldsymbol{\sigma_{bl}/\sigma_{ult}}$ = 1.0 (%)
S-1	150.4	139.1	425.1		
S-2	145.8	134.9	412.3		
S-3	147.3	136.2	416.2	440.0	5.31
Avg	147.8	136.7	417.8		
SD	2.3	2.1	6.5		

(a)

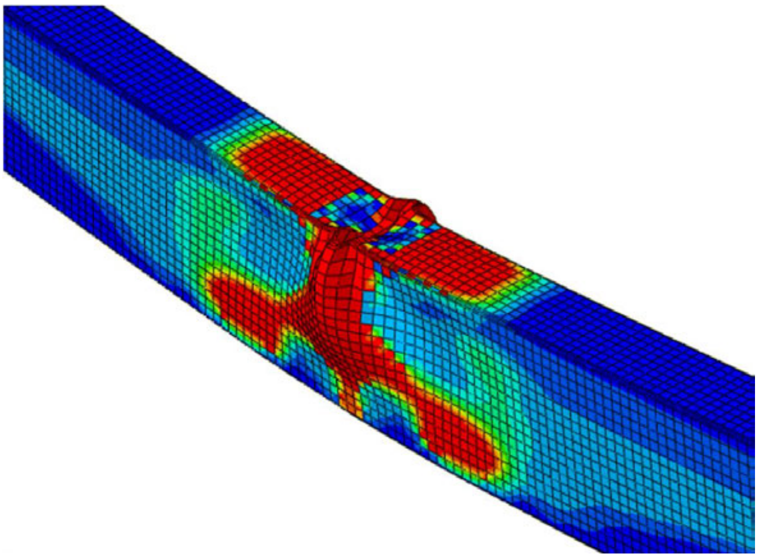

(b) (c)

Fig. 12. Manufacturing and testing the new hollow rectangular PFRP girder: (a) the new girder versus the double-cell bonded girder and (b) experimental failure mode versus (c) numerical failure mode under four-point bending.

5. CONCLUSIONS

In this research, a numerical investigation was undertaken to optimise the structural behaviour and reduce the manufacturing cost of hollow box pulwound FRP profiles. A significant drawback for these profiles is they are prone to local buckling failure, well below their ultimate load capacity, due to their anisotropic elasticity and application-driven slenderness. The layup (winding angle and axial-to-wound fibre ratio) and geometric (wall slenderness, cross-sectional aspect ratio, and corner radii ratio) parameters controlling the local buckling behaviour of these profiles were studied to obtain design guidelines and curves. The numerical approach combines the Finite Element Modelling (FEM) and the Genetic Algorithm (GA) to predict the optimal configuration of the design parameters against local buckling under two separate loading conditions of axial compression and four-point bending. The FEM code was parametrised using Python 3.9.1, and Abaqus 2019 was used to simulate the structural behaviour and progressive failure of the hollow box PFRP profile to evaluate the nonlinear buckling strength constraint. The "MI-LXPM" GA code [41] was used to solve the mixed-integer constrained optimisation problem using MATLAB 2020b. The optimisation objective was to minimise the manufacturing cost per metre of pultrusion while maintaining the same stiffness and strength properties of the control profile. The Kriging model was implemented on the generated datasets from the GA codes to map the design space and interpolate the missing strength values of the data points under axial compression and four-point bending to obtain the design curves. The interactions of the geometric design parameters were considered. Guidelines and recommendations on the design for manufacturing were reported for the optimal compressive and flexural behaviours of hollow PFRP profiles to withstand local buckling. An experimental case study on the design of a hollow rectangular PFRP girder was undertaken to assess the accuracy of the predictions. From this study, the following points were concluded:

- The controlled increment size approach introduced by the authors in previous research [26,27] was adjusted here to achieve faster analysis and lower computational cost. The adjusted FEM approach incorporating geometric imperfections and controlled increment size proved to be an efficient and fast-converging tool that reduces the computational cost up to three times compared to the models with controlled increment size only.

- The “MI-LXPM” GA code succeeded in optimising the manufacturing design parameters of hollow pulwound FRP profiles. The optimised designs were estimated to save 11.53% and 26.39% of the materials cost per metre of pultrusion for compression and bending applications, respectively, compared to the current (control) design. The cost was effectively reduced under bending compared to compression because of the severity of local buckling under compression.
- Considering a large corner radii ratio (r/R) in the design is an efficient and economic practice for manufacturing optimised hollow PFRP profiles. The larger area at the corners (flange-web junctions) of the profile can eliminate any concentration of stresses while maintaining the same stress distribution at the thinner walls under compression and bending. Thus, making the entire cross-section (walls and corners) works at the same level of stress instead of stressing the corners more than the walls as in the control profile. Moreover, thicker corners exhibit higher rotational restraint and reduce the effective unsupported wall width.
- The implementation of the Kriging model was proved to be a robust approach to maximise the data use from the GA codes and map the design space of hollow box PFRP profiles to generate design and interaction charts for designers to use.
- The generated design chart (Fig. 10) is a simple and reliable design tool against local buckling of hollow box PFRP profiles as it combines all the critical geometric parameters and considers their interactions, while the current standards [12–15] do not.

ACKNOWLEDGEMENTS

The work was funded through a Cooperative Research Centres Projects (CRC-P) Grant (CRCPSIX000117). The authors wish to thank all the supporters for their finance and for providing the required computational resources and testing specimens.

APPENDIX A.

Table A. 1 shows the design configurations of the numerical study on the geometric parameters (wall slenderness, cross-sectional aspect ratio h/b, and corner radii ratio r/R) of the hollow box pultruded FRP profile along with their numerical results. When the σ_{bl}/σ_{ult} ratio is lower than 1.0, then local buckling of the walls or local buckling of the top flange controls the failure mode of the profile under compression or bending, respectively. The failure mode shifts to compressive failure of fibre and matrix followed by transverse shear (local buckling is completely eliminated) when this ratio equals 1.0.

Table A. 1: Design configurations of the numerical study on the geometric parameters of the hollow box PFRP profile along with their numerical results.

Wall slenderness b/t	Wall slenderness h/t	h/b	r/R	Flexural strength (MPa)	σ_{bl} /σ_{ult}	Compressive strength (MPa)	σ_{bl} /σ_{ult}
10.0	10.0	1.0	0.5	480.3	1.0	480.1	1.0
11.4	11.4	1.0	0.5	480.9	1.0	480.9	1.0
13.2	13.2	1.0	0.5	480.5	1.0	480.4	1.0
15.6	15.6	1.0	0.5	480.8	1.0	339.4	0.71
16.4	16.4	1.0	0.5	447.6	0.93	310.2	0.64
17.2	17.2	1.0	0.5	409.4	0.85	286.4	0.59
19.2	19.2	1.0	0.5	328.3	0.68	243.8	0.51
21.7	21.7	1.0	0.5	273.0	0.56	172.8	0.36
25.0	25.0	1.0	0.5	210.0	0.43	146.2	0.30
27.8	27.8	1.0	0.5	176.0	0.36	139.7	0.29
30.3	30.3	1.0	0.5	147.0	0.30	132.9	0.27
33.3	33.3	1.0	0.5	138.0	0.28	125.4	0.26
8.9	11.1	1.25	0.5	480.6	1.0	480.6	1.0
10.1	12.6	1.25	0.5	480.2	1.0	480.2	1.0
11.7	14.6	1.25	0.5	481.4	1.0	414.9	0.86
13.9	17.4	1.25	0.5	480.5	1.0	327.8	0.68
14.6	18.2	1.25	0.5	461.9	0.96	296.5	0.61
15.3	19.2	1.25	0.5	427.7	0.89	272.3	0.56
17.1	21.4	1.25	0.5	391.1	0.81	237.2	0.49
19.3	24.2	1.25	0.5	335.3	0.69	165.9	0.34
22.2	27.8	1.25	0.5	273.0	0.56	136.8	0.28
24.7	30.9	1.25	0.5	241.7	0.50	131.7	0.27

26.9	33.7	1.25	0.5	214.2	0.44	126.2	0.26
29.6	37.0	1.25	0.5	149.2	0.31	121.7	0.25
8.0	12.0	1.5	0.5	480.5	1.0	480.6	1.0
9.1	13.6	1.5	0.5	480.9	1.0	442.7	0.92
10.5	15.8	1.5	0.5	481.2	1.0	407.1	0.84
12.5	18.8	1.5	0.5	480.4	1.0	318.5	0.66
13.1	19.7	1.5	0.5	480.2	1.0	272.6	0.56
13.8	20.7	1.5	0.5	442.9	0.92	260.8	0.54
15.4	23.1	1.5	0.5	409.4	0.85	225.7	0.47
17.4	26.1	1.5	0.5	364.9	0.76	158.3	0.32
20.0	30.0	1.5	0.5	310.8	0.64	132.4	0.27
22.2	33.3	1.5	0.5	279.2	0.58	127.8	0.26
24.2	36.4	1.5	0.5	243.6	0.51	122.4	0.25
26.7	40.0	1.5	0.5	162.1	0.33	118.9	0.24
7.3	12.7	1.75	0.5	480.5	1.0	480.5	1.0
8.3	14.5	1.75	0.5	480.1	1.0	431.2	0.89
9.6	16.7	1.75	0.5	480.4	1.0	397.8	0.82
11.4	19.9	1.75	0.5	480.6	1.0	309.7	0.64
11.9	20.9	1.75	0.5	480.7	1.0	260.8	0.54
12.5	21.9	1.75	0.5	468.5	0.97	252.4	0.52
14.0	24.5	1.75	0.5	440.4	0.92	217.3	0.45
15.8	27.7	1.75	0.5	392.4	0.81	148.7	0.31
18.2	31.8	1.75	0.5	345.1	0.72	129.3	0.26
20.2	35.4	1.75	0.5	306.2	0.63	124.7	0.25
22.0	38.6	1.75	0.5	272.8	0.56	119.8	0.24
24.2	42.4	1.75	0.5	178.3	0.37	115.4	0.24
6.7	13.3	2.0	0.5	480.6	1.0	480.1	1.0
7.6	15.2	2.0	0.5	480.2	1.0	420.9	0.87
8.8	17.5	2.0	0.5	480.1	1.0	352.3	0.73
10.4	20.8	2.0	0.5	481.1	1.0	280.5	0.58
10.9	21.9	2.0	0.5	480.4	1.0	253.4	0.52
11.5	23.0	2.0	0.5	480.5	1.0	246.2	0.51
12.8	25.6	2.0	0.5	471.6	0.98	229.4	0.47
14.5	29.0	2.0	0.5	422.1	0.88	142.5	0.29
16.7	33.3	2.0	0.5	371.6	0.77	127.4	0.26
18.5	37.0	2.0	0.5	340.2	0.71	122.1	0.25
20.2	40.4	2.0	0.5	301.8	0.62	116.2	0.24
22.2	44.4	2.0	0.5	232.3	0.48	113.8	0.23
5.7	14.3	2.5	0.5	480.5	1.0	466.2	0.97
6.5	16.2	2.5	0.5	480.0	1.0	371.0	0.77
7.5	18.8	2.5	0.5	481.3	1.0	322.4	0.67
8.9	22.3	2.5	0.5	480.7	1.0	269.1	0.56
9.4	23.4	2.5	0.5	480.5	1.0	243.8	0.51

9.9	24.6	2.5	0.5	480.9	1.0	238.4	0.49
11.0	27.5	2.5	0.5	480.3	1.0	229.3	0.47
12.4	31.1	2.5	0.5	468.1	0.97	139.5	0.29
14.3	35.7	2.5	0.5	411.0	0.85	125.9	0.26
15.9	39.7	2.5	0.5	382.1	0.79	119.4	0.24
17.3	43.3	2.5	0.5	336.4	0.70	113.0	0.23
19.0	47.6	2.5	0.5	268.9	0.56	110.8	0.23
10.0	10.0	1.0	1.0	480.2	1.0	480.7	1.0
11.4	11.4	1.0	1.0	480.6	1.0	480.6	1.0
13.2	13.2	1.0	1.0	480.5	1.0	480.2	1.0
15.6	15.6	1.0	1.0	480.1	1.0	367.2	0.76
16.4	16.4	1.0	1.0	462.5	0.96	339.3	0.70
17.2	17.2	1.0	1.0	420.2	0.87	307.9	0.64
19.2	19.2	1.0	1.0	379.0	0.78	248.3	0.51
21.7	21.7	1.0	1.0	327.7	0.68	227.4	0.47
25.0	25.0	1.0	1.0	252.0	0.52	165.2	0.34
27.8	27.8	1.0	1.0	199.3	0.41	158.9	0.33
30.3	30.3	1.0	1.0	180.6	0.37	146.4	0.31
33.3	33.3	1.0	1.0	151.2	0.31	139.3	0.29
8.9	11.1	1.25	1.0	480.2	1.0	480.6	1.0
10.1	12.6	1.25	1.0	480.4	1.0	480.2	1.0
11.7	14.6	1.25	1.0	480.9	1.0	441.5	0.91
13.9	17.4	1.25	1.0	480.2	1.0	355.6	0.74
14.6	18.2	1.25	1.0	472.4	0.98	311.8	0.64
15.3	19.2	1.25	1.0	441.4	0.91	294.8	0.61
17.1	21.4	1.25	1.0	403.2	0.84	241.2	0.50
19.3	24.2	1.25	1.0	369.1	0.76	216.5	0.45
22.2	27.8	1.25	1.0	336.0	0.70	156.4	0.32
24.7	30.9	1.25	1.0	274.5	0.57	149.1	0.31
26.9	33.7	1.25	1.0	227.2	0.47	138.2	0.28
29.6	37.0	1.25	1.0	159.9	0.33	129.7	0.27
8.0	12.0	1.5	1.0	480.6	1.0	480.6	1.0
9.1	13.6	1.5	1.0	480.9	1.0	459.2	0.95
10.5	15.8	1.5	1.0	480.5	1.0	416.3	0.86
12.5	18.8	1.5	1.0	480.0	1.0	334.8	0.69
13.1	19.7	1.5	1.0	480.2	1.0	290.3	0.60
13.8	20.7	1.5	1.0	458.6	0.95	281.8	0.58
15.4	23.1	1.5	1.0	416.6	0.86	236.1	0.49
17.4	26.1	1.5	1.0	406.2	0.84	191.7	0.39
20.0	30.0	1.5	1.0	367.7	0.76	150.2	0.31
22.2	33.3	1.5	1.0	335.2	0.69	142.6	0.29
24.2	36.4	1.5	1.0	307.6	0.64	131.7	0.27
26.7	40.0	1.5	1.0	171.3	0.35	124.9	0.26

7.3	12.7	1.75	1.0	480.5	1.0	480.7	1.0
8.3	14.5	1.75	1.0	480.1	1.0	442.2	0.92
9.6	16.7	1.75	1.0	480.6	1.0	405.8	0.84
11.4	19.9	1.75	1.0	480.9	1.0	319.2	0.66
11.9	20.9	1.75	1.0	481.1	1.0	283.8	0.59
12.5	21.9	1.75	1.0	480.2	1.0	274.1	0.57
14.0	24.5	1.75	1.0	462.0	0.96	232.9	0.48
15.8	27.7	1.75	1.0	414.5	0.86	188.7	0.39
18.2	31.8	1.75	1.0	388.2	0.81	145.8	0.30
20.2	35.4	1.75	1.0	350.4	0.73	138.2	0.28
22.0	38.6	1.75	1.0	331.5	0.69	127.7	0.26
24.2	42.4	1.75	1.0	189.2	0.39	121.0	0.25
6.7	13.3	2.0	1.0	480.6	1.0	480.5	1.0
7.6	15.2	2.0	1.0	480.2	1.0	428.7	0.89
8.8	17.5	2.0	1.0	480.5	1.0	388.3	0.81
10.4	20.8	2.0	1.0	480.9	1.0	296.1	0.61
10.9	21.9	2.0	1.0	480.4	1.0	272.3	0.56
11.5	23.0	2.0	1.0	480.2	1.0	266.2	0.55
12.8	25.6	2.0	1.0	480.0	1.0	230.1	0.47
14.5	29.0	2.0	1.0	438.4	0.91	184.9	0.38
16.7	33.3	2.0	1.0	406.5	0.84	141.2	0.29
18.5	37.0	2.0	1.0	379.2	0.79	134.7	0.28
20.2	40.4	2.0	1.0	355.9	0.74	123.9	0.25
22.2	44.4	2.0	1.0	247.2	0.51	120.1	0.25
5.7	14.3	2.5	1.0	480.2	1.0	477.6	0.99
6.5	16.2	2.5	1.0	480.6	1.0	391.7	0.81
7.5	18.8	2.5	1.0	480.0	1.0	345.1	0.71
8.9	22.3	2.5	1.0	481.1	1.0	276.6	0.57
9.4	23.4	2.5	1.0	480.7	1.0	259.2	0.54
9.9	24.6	2.5	1.0	480.5	1.0	251.4	0.52
11.0	27.5	2.5	1.0	480.9	1.0	230.1	0.47
12.4	31.1	2.5	1.0	478.0	0.99	156.4	0.32
14.3	35.7	2.5	1.0	429.7	0.89	130.8	0.27
15.9	39.7	2.5	1.0	409.5	0.85	122.1	0.25
17.3	43.3	2.5	1.0	386.0	0.80	117.3	0.24
19.0	47.6	2.5	1.0	291.4	0.61	113.2	0.23
10.0	10.0	1.0	1.5	480.2	1.0	480.7	1.0
11.4	11.4	1.0	1.5	480.6	1.0	480.6	1.0
13.2	13.2	1.0	1.5	480.5	1.0	480.2	1.0
15.6	15.6	1.0	1.5	480.4	1.0	424.2	0.88
16.4	16.4	1.0	1.5	477.8	0.99	395.6	0.82
17.2	17.2	1.0	1.5	441.6	0.92	355.1	0.74
19.2	19.2	1.0	1.5	397.1	0.82	283.2	0.59

21.7	21.7	1.0	1.5	361.0	0.75	252.4	0.52
25.0	25.0	1.0	1.5	274.6	0.57	174.2	0.36
27.8	27.8	1.0	1.5	220.1	0.45	166.5	0.34
30.3	30.3	1.0	1.5	194.6	0.41	157.6	0.32
33.3	33.3	1.0	1.5	162.4	0.33	141.9	0.29
8.9	11.1	1.25	1.5	480.1	1.0	480.1	1.0
10.1	12.6	1.25	1.5	480.5	1.0	480.7	1.0
11.7	14.6	1.25	1.5	480.8	1.0	452.5	0.94
13.9	17.4	1.25	1.5	480.1	1.0	412.6	0.85
14.6	18.2	1.25	1.5	480.4	1.0	372.0	0.77
15.3	19.2	1.25	1.5	465.2	0.96	347.3	0.72
17.1	21.4	1.25	1.5	421.0	0.87	270.1	0.56
19.3	24.2	1.25	1.5	384.9	0.80	246.7	0.51
22.2	27.8	1.25	1.5	361.5	0.75	163.1	0.33
24.7	30.9	1.25	1.5	298.9	0.62	158.3	0.32
26.9	33.7	1.25	1.5	244.9	0.51	149.7	0.31
29.6	37.0	1.25	1.5	178.5	0.37	134.2	0.27
8.0	12.0	1.5	1.5	480.2	1.0	480.6	1.0
9.1	13.6	1.5	1.5	480.4	1.0	471.3	0.98
10.5	15.8	1.5	1.5	480.1	1.0	427.2	0.89
12.5	18.8	1.5	1.5	480.0	1.0	381.5	0.79
13.1	19.7	1.5	1.5	481.0	1.0	350.2	0.72
13.8	20.7	1.5	1.5	476.4	0.99	319.4	0.66
15.4	23.1	1.5	1.5	439.5	0.91	246.6	0.51
17.4	26.1	1.5	1.5	422.6	0.88	234.3	0.48
20.0	30.0	1.5	1.5	389.0	0.81	157.8	0.32
22.2	33.3	1.5	1.5	350.1	0.72	150.1	0.31
24.2	36.4	1.5	1.5	326.4	0.68	137.9	0.28
26.7	40.0	1.5	1.5	190.2	0.39	129.4	0.26
7.3	12.7	1.75	1.5	480.6	1.0	480.2	1.0
8.3	14.5	1.75	1.5	480.4	1.0	460.7	0.95
9.6	16.7	1.75	1.5	480.2	1.0	418.2	0.87
11.4	19.9	1.75	1.5	481.0	1.0	363.0	0.75
11.9	20.9	1.75	1.5	480.5	1.0	335.4	0.69
12.5	21.9	1.75	1.5	480.9	1.0	302.2	0.62
14.0	24.5	1.75	1.5	475.1	0.98	240.5	0.50
15.8	27.7	1.75	1.5	436.7	0.91	231.7	0.48
18.2	31.8	1.75	1.5	405.4	0.84	151.1	0.31
20.2	35.4	1.75	1.5	369.8	0.77	144.9	0.30
22.0	38.6	1.75	1.5	350.2	0.73	132.8	0.27
24.2	42.4	1.75	1.5	207.0	0.43	125.3	0.26
6.7	13.3	2.0	1.5	480.2	1.0	480.2	1.0
7.6	15.2	2.0	1.5	480.9	1.0	446.2	0.92

8.8	17.5	2.0	1.5	480.0	1.0	405.3	0.84
10.4	20.8	2.0	1.5	480.1	1.0	328.6	0.68
10.9	21.9	2.0	1.5	481.0	1.0	312.4	0.65
11.5	23.0	2.0	1.5	480.7	1.0	290.7	0.61
12.8	25.6	2.0	1.5	480.6	1.0	236.8	0.49
14.5	29.0	2.0	1.5	455.7	0.94	230.3	0.47
16.7	33.3	2.0	1.5	429.4	0.89	148.3	0.30
18.5	37.0	2.0	1.5	392.0	0.81	139.6	0.29
20.2	40.4	2.0	1.5	378.4	0.78	128.4	0.26
22.2	44.4	2.0	1.5	260.1	0.54	123.1	0.25
5.7	14.3	2.5	1.5	480.6	1.0	480.5	1.0
6.5	16.2	2.5	1.5	481.2	1.0	419.0	0.87
7.5	18.8	2.5	1.5	480.9	1.0	366.2	0.76
8.9	22.3	2.5	1.5	480.5	1.0	296.4	0.61
9.4	23.4	2.5	1.5	480.3	1.0	286.1	0.59
9.9	24.6	2.5	1.5	480.5	1.0	263.4	0.54
11.0	27.5	2.5	1.5	480.7	1.0	232.5	0.48
12.4	31.1	2.5	1.5	480.6	1.0	227.3	0.47
14.3	35.7	2.5	1.5	451.7	0.94	139.4	0.29
15.9	39.7	2.5	1.5	418.4	0.87	128.1	0.26
17.3	43.3	2.5	1.5	395.7	0.82	124.8	0.26
19.0	47.6	2.5	1.5	329.6	0.68	116.6	0.24
10.0	10.0	1.0	2.0	480.3	1.0	480.2	1.0
11.4	11.4	1.0	2.0	480.0	1.0	481.3	1.0
13.2	13.2	1.0	2.0	481.1	1.0	480.4	1.0
15.6	15.6	1.0	2.0	480.8	1.0	468.2	0.97
16.4	16.4	1.0	2.0	480.1	1.0	453.3	0.94
17.2	17.2	1.0	2.0	468.2	0.97	440.8	0.91
19.2	19.2	1.0	2.0	416.8	0.86	335.1	0.69
21.7	21.7	1.0	2.0	383.7	0.79	295.6	0.61
25.0	25.0	1.0	2.0	357.0	0.74	237.1	0.49
27.8	27.8	1.0	2.0	312.6	0.65	210.4	0.43
30.3	30.3	1.0	2.0	289.8	0.60	190.7	0.39
33.3	33.3	1.0	2.0	204.4	0.42	150.7	0.31
8.9	11.1	1.25	2.0	480.4	1.0	480.7	1.0
10.1	12.6	1.25	2.0	480.5	1.0	481.0	1.0
11.7	14.6	1.25	2.0	480.9	1.0	470.4	0.98
13.9	17.4	1.25	2.0	480.0	1.0	442.1	0.92
14.6	18.2	1.25	2.0	480.2	1.0	430.8	0.89
15.3	19.2	1.25	2.0	480.1	1.0	385.2	0.80
17.1	21.4	1.25	2.0	438.8	0.91	309.2	0.64
19.3	24.2	1.25	2.0	413.7	0.86	271.6	0.56
22.2	27.8	1.25	2.0	382.2	0.79	204.7	0.42

24.7	30.9	1.25	2.0	341.1	0.71	201.8	0.42
26.9	33.7	1.25	2.0	319.2	0.66	174.2	0.36
29.6	37.0	1.25	2.0	219.4	0.45	142.6	0.29
8.0	12.0	1.5	2.0	480.3	1.0	480.8	1.0
9.1	13.6	1.5	2.0	480.6	1.0	480.6	1.0
10.5	15.8	1.5	2.0	481.1	1.0	460.7	0.95
12.5	18.8	1.5	2.0	480.8	1.0	423.8	0.88
13.1	19.7	1.5	2.0	480.0	1.0	411.7	0.85
13.8	20.7	1.5	2.0	481.2	1.0	361.7	0.75
15.4	23.1	1.5	2.0	469.8	0.97	289.4	0.60
17.4	26.1	1.5	2.0	447.4	0.93	260.7	0.54
20.0	30.0	1.5	2.0	399.8	0.83	194.5	0.40
22.2	33.3	1.5	2.0	369.9	0.77	179.3	0.37
24.2	36.4	1.5	2.0	331.8	0.69	162.5	0.39
26.7	40.0	1.5	2.0	231.1	0.48	134.0	0.27
7.3	12.7	1.75	2.0	480.1	1.0	480.6	1.0
8.3	14.5	1.75	2.0	480.5	1.0	480.3	1.0
9.6	16.7	1.75	2.0	480.7	1.0	448.6	0.93
11.4	19.9	1.75	2.0	480.1	1.0	406.0	0.84
11.9	20.9	1.75	2.0	480.5	1.0	368.4	0.76
12.5	21.9	1.75	2.0	481.3	1.0	342.7	0.71
14.0	24.5	1.75	2.0	480.6	1.0	272.1	0.56
15.8	27.7	1.75	2.0	465.3	0.96	248.4	0.51
18.2	31.8	1.75	2.0	416.9	0.86	179.6	0.37
20.2	35.4	1.75	2.0	390.2	0.81	164.5	0.34
22.0	38.6	1.75	2.0	368.5	0.76	150.2	0.31
24.2	42.4	1.75	2.0	348.4	0.72	129.7	0.27
6.7	13.3	2.0	2.0	480.1	1.0	480.6	1.0
7.6	15.2	2.0	2.0	480.8	1.0	471.3	0.98
8.8	17.5	2.0	2.0	480.9	1.0	432.5	0.90
10.4	20.8	2.0	2.0	481.1	1.0	372.4	0.77
10.9	21.9	2.0	2.0	480.5	1.0	359.1	0.74
11.5	23.0	2.0	2.0	480.2	1.0	327.6	0.68
12.8	25.6	2.0	2.0	480.6	1.0	264.2	0.55
14.5	29.0	2.0	2.0	480.9	1.0	239.9	0.49
16.7	33.3	2.0	2.0	452.8	0.94	167.9	0.34
18.5	37.0	2.0	2.0	418.1	0.87	153.8	0.32
20.2	40.4	2.0	2.0	395.4	0.82	141.2	0.29
22.2	44.4	2.0	2.0	361.0	0.75	126.7	0.26
5.7	14.3	2.5	2.0	480.1	1.0	480.1	1.0
6.5	16.2	2.5	2.0	481.4	1.0	457.8	0.95
7.5	18.8	2.5	2.0	480.3	1.0	406.8	0.84
8.9	22.3	2.5	2.0	480.8	1.0	337.1	0.70

9.4	23.4	2.5	2.0	481.1	1.0	313.6	0.65
9.9	24.6	2.5	2.0	480.9	1.0	289.9	0.60
11.0	27.5	2.5	2.0	480.3	1.0	251.0	0.52
12.4	31.1	2.5	2.0	480.5	1.0	235.5	0.49
14.3	35.7	2.5	2.0	475.9	0.99	152.4	0.31
15.9	39.7	2.5	2.0	438.1	0.91	139.8	0.29
17.3	43.3	2.5	2.0	420.6	0.87	132.7	0.27
19.0	47.6	2.5	2.0	389.4	0.81	120.1	0.25

REFERENCES

[1] Gand AK, Chan T-M, Mottram JT. Civil and structural engineering applications, recent trends, research and developments on pultruded fiber reinforced polymer closed sections: a review. Front Struct Civ Eng 2013;7:227–44. https://doi.org/10.1007/s11709-013-0216-8.

[2] Vedernikov A, Safonov A, Tucci F, Carlone P, Akhatov I. Pultruded materials and structures: A review. J Compos Mater 2020;54:4081–117. https://doi.org/10.1177/0021998320922894.

[3] Gemi L, Madenci E, Özkılıç YO. Experimental, analytical and numerical investigation of pultruded GFRP composite beams infilled with hybrid FRP reinforced concrete. Eng Struct 2021;244:112790. https://doi.org/10.1016/j.engstruct.2021.112790.

[4] Al-saadi AU, Aravinthan T, Lokuge W. Effects of fibre orientation and layup on the mechanical properties of the pultruded glass fibre reinforced polymer tubes. Eng Struct 2019;198:109448. https://doi.org/10.1016/j.engstruct.2019.109448.

[5] Hizam RM, Manalo AC, Karunasena W, Bai Y. Behaviour of pultruded GFRP truss system connected using through-bolt with mechanical insert. Compos Part B Eng 2019;168:44–57. https://doi.org/10.1016/j.compositesb.2018.12.052.

[6] Ali AM, Masmoudi R. Experimental and analytical investigation of new concrete filled FRP tube beam-column connections. Eng Struct 2019;191:311–22. https://doi.org/10.1016/j.engstruct.2019.04.065.

[7] Muttashar M, Karunasena W, Manalo A, Lokuge W. Behaviour of hollow pultruded GFRP square beams with different shear span-to-depth ratios. J Compos Mater 2016;50:2925–40. https://doi.org/10.1177/0021998315614993.

[8] Sayyad AS, Ghugal YM. Bending, buckling and free vibration of laminated composite and sandwich beams: A critical review of literature. Compos Struct 2017;171:486–504. https://doi.org/10.1016/j.compstruct.2017.03.053.

[9] Correia JR, Branco FA, Silva NMF, Camotim D, Silvestre N. First-order, buckling and post-buckling behaviour of GFRP pultruded beams. Part 1: Experimental study. Comput Struct 2011;89:2052–64. https://doi.org/10.1016/j.compstruc.2011.07.005.

[10] Xu J, Zhao Q, Qiao P. A critical review on buckling and post-buckling analysis of composite structures. Front Aerosp Eng 2013;2:157–68.

[11] Minghini F, Tullini N, Laudiero F. Elastic buckling analysis of pultruded FRP portal frames having semi-rigid connections. Eng Struct 2009;31:292–9. https://doi.org/10.1016/j.engstruct.2008.09.003.

[12] American Society of Civil Engineers. Pre-standard for load & resistance factor design (LRFD) of pultruded fiber reinforced polymer (FRP) structures. Arlingt VA ACMA 2012:215.

[13] Ascione L, Caron J-F, Godonou P, van Ijselmuijden K, Knippers J, Mottram T, et al. Prospect for new guidance in the design of FRP : Support to the implementation, harmonization and further development of the Eurocodes. Publications Office of the European Union; 2016.

[14] Clarke JL. Structural Design of Polymer Composites EUROCOMP Design Code and Handbook. CRC Press; 2005.

[15] National Research Council. Guide for the Design and Construction of Structures made of FRP Pultruded Elements. CNR-DT 2007;205:25–31.

[16] Mohite PM, Upadhyay CS. Adaptive finite element based shape optimization in laminated composite plates. Comput Struct 2015;153:19–35. https://doi.org/10.1016/j.compstruc.2015.02.020.

[17] Damghani M, Kennedy D, Featherston C. Critical buckling of delaminated composite plates using exact stiffness analysis. Comput Struct 2011;89:1286–94. https://doi.org/10.1016/j.compstruc.2011.04.003.

[18] Feng P, Wu Y, Ding Y, Liu T, Tian Y. Quasi-plastic flexural behavior of adhesive-bolt hybrid connection for large scale pultruded GFRP frame. Eng Struct 2021;238:112200. https://doi.org/10.1016/j.engstruct.2021.112200.

[19] Wang Z, Sobey A. A comparative review between Genetic Algorithm use in composite optimisation and the state-of-the-art in evolutionary computation. Compos Struct 2020;233:111739. https://doi.org/10.1016/j.compstruct.2019.111739.

[20] Nikbakt S, Kamarian S, Shakeri M. A review on optimization of composite structures Part I: Laminated composites. Compos Struct 2018;195:158–85. https://doi.org/10.1016/j.compstruct.2018.03.063.

[21] Lagaros ND, Papadrakakis M, Kokossalakis G. Structural optimization using evolutionary algorithms. Comput Struct 2002;80:571–89. https://doi.org/10.1016/S0045-7949(02)00027-5.

[22] Pelletier JL, Vel SS. Multi-objective optimization of fiber reinforced composite laminates for strength, stiffness and minimal mass. Comput Struct 2006;84:2065–80. https://doi.org/10.1016/j.compstruc.2006.06.001.

[23] Awad ZK, Aravinthan T, Zhuge Y, Gonzalez F. A review of optimization techniques used in the design of fibre composite structures for civil engineering applications. Mater Des 2012;33:534–44. https://doi.org/10.1016/j.matdes.2011.04.061.

[24] Ghiasi H, Pasini D, Lessard L. Optimum stacking sequence design of composite materials Part I: Constant stiffness design. Compos Struct 2009;90:1–11. https://doi.org/10.1016/j.compstruct.2009.01.006.

[25] Pathan MV, Patsias S, Tagarielli VL. A real-coded genetic algorithm for optimizing the damping response of composite laminates. Comput Struct 2018;198:51–60. https://doi.org/10.1016/j.compstruc.2018.01.005.

[26] Alhawamdeh M, Alajarmeh O, Aravinthan T, Shelley T, Schubel P, Kemp M, et al. Modelling hollow pultruded FRP profiles under axial compression: Local buckling and progressive failure. Compos Struct 2021;262:113650. https://doi.org/10.1016/j.compstruct.2021.113650.

[27] Alhawamdeh M, Alajarmeh O, Aravinthan T, Shelley T, Schubel P, Mohammad A, et al. Modelling flexural performance of hollow pultruded FRP profiles. Compos Struct 2021;276:114553. https://doi.org/10.1016/j.compstruct.2021.114553.

[28] Ragheb WF. Development of Closed-Form Equations for Estimating the Elastic Local Buckling Capacity of Pultruded FRP Structural Shapes. J Compos Constr 2017;21:04017015. https://doi.org/10.1061/(ASCE)CC.1943-5614.0000798.

[29] Alhawamdeh M, Alajarmeh O, Aravinthan T, Shelley T, Schubel P, Mohammed A, et al. Review on Local Buckling of Hollow Box FRP Profiles in Civil Structural Applications. Polymers 2021;13:4159. https://doi.org/10.3390/polym13234159.

[30] Ascione F, Feo L, Lamberti M, Minghini F, Tullini N. A closed-form equation for the local buckling moment of pultruded FRP I-beams in major-axis bending. Compos Part B Eng 2016;97:292–9. https://doi.org/10.1016/j.compositesb.2016.04.069.

[31] Attaf B. Advances in Composite Materials: Ecodesign and Analysis. BoD – Books on Demand; 2011.

[32] Kollár LP, Springer GS. Mechanics of Composite Structures. Cambridge University Press; 2003.

[33] Hagel KV, Joglekar S, Pankow M, Ferguson SM. Exploring Composite Panels Using Multi-Objective Optimization and Varying Load Conditions. 15th AIAAISSMO Multidiscip. Anal. Optim. Conf., Atlanta, GA: American Institute of Aeronautics and Astronautics; 2014. https://doi.org/10.2514/6.2014-3161.

[34] He Y, Aref AJ. An optimization design procedure for fiber reinforced polymer web-core sandwich bridge deck systems. Compos Struct 2003;60:183–95. https://doi.org/10.1016/S0263-8223(02)00311-2.

[35] Abouzied A, Masmoudi R. Flexural behavior of rectangular FRP-tubes filled with reinforced concrete: Experimental and theoretical studies. Eng Struct 2017;133:59–73. https://doi.org/10.1016/j.engstruct.2016.12.010.

[36] ASTM D7249/D7249M. Standard test method for facing properties of sandwich constructions by long beam flexure. Am Soc Test Mater 2012.

[37] Cole B, Fam A. Flexural Load Testing of Concrete-Filled FRP Tubes with Longitudinal Steel and FRP Rebar. J Compos Constr 2006;10:161–71. https://doi.org/10.1061/(ASCE)1090-0268(2006)10:2(161).

[38] Muttashar M, Manalo A, Karunasena W, Lokuge W. Influence of infill concrete strength on the flexural behaviour of pultruded GFRP square beams. Compos Struct 2016;145:58–67. https://doi.org/10.1016/j.compstruct.2016.02.071.

[39] Zeng X, Long AC, Ashcroft I, Potluri P. Fibre architecture design of 3D woven composite with genetic algorithms: a unit cell based optimisation framework and performance assessment. 20th Int. Conf. Compos. Mater., Denmark: 2015.

[40] Simulia DS. Abaqus 6.14 Scripting User`s Guide. Dassault Syst Provid RI 2014.

[41] Deep K, Singh KP, Kansal ML, Mohan C. A real coded genetic algorithm for solving integer and mixed integer optimization problems. Appl Math Comput 2009;212:505–18. https://doi.org/10.1016/j.amc.2009.02.044.

[42] Deb K. An efficient constraint handling method for genetic algorithms. Comput Methods Appl Mech Eng 2000;186:311–38. https://doi.org/10.1016/S0045-7825(99)00389-8.

[43] The MathWorks Inc. MATLAB R2020b Documentation. Natick Mass US 2020.

[44] Wagners CFT. Wagners-Composite Fibre Technologies (CFT). Wagner n.d. https://www.wagner.com.au/main/what-we-do/composite-fibre-technologies/cft-home/ (accessed March 8, 2020).

[45] Simulia DS. Abaqus 6.13 Analysis User's Guide. Dassault Syst Provid RI 2013.

[46] Barbero EJ. Introduction to Composite Materials Design. CRC Press; 2017. https://doi.org/10.1201/9781315296494.

[47] Kobayashi T, Mihara Y. Application of Abaqus for Practical Postbuckling Analyses of Cylindrical Shells under Axial Compression, Providence, Rhode Island: Dassault Systemes, 2010; 2010.

[48] Tafreshi A, Oswald T. Global buckling behaviour and local damage propagation in composite plates with embedded delaminations. Int J Press Vessels Pip 2003;80:9–20. https://doi.org/10.1016/S0308-0161(02)00152-7.

[49] Bank LC. Composites for Construction: Structural Design with FRP Materials. John Wiley & Sons; 2006.

[50] McCarthy MJ, Bank LC. Sensitivity studies on local flange buckling equations for pultruded beams and columns. Adv. FRP Compos. Civ. Eng., Beijing, China: Springer; 2010, p. 115–8.

[51] Ragheb WF. Local buckling analysis of pultruded FRP structural shapes subjected to eccentric compression. Thin-Walled Struct 2010;48:709–17. https://doi.org/10.1016/j.tws.2010.04.011.

[52] Buragohain MK. Composite Structures: Design, Mechanics, Analysis, Manufacturing, and Testing. CRC Press; 2017.

[53] Mustafa A. An introduction to polymer-matrix composites. bookboom. com; 2015.

[54] Ravi Kumar P, Gupta G, Shamili GK, Anitha D. Linear Buckling Analysis and Comparative Study of Un-stiffened and Stiffened Composite Plate. Mater Today Proc 2018;5:6059–71. https://doi.org/10.1016/j.matpr.2017.12.211.

[55] Silva NMF, Silvestre N, Camotim D. GBT formulation to analyse the buckling behaviour of FRP composite open-section thin-walled columns. Compos Struct 2010;93:79–92. https://doi.org/10.1016/j.compstruct.2010.06.013.

[56] Asadi A, Sheikh AH, Thomsen OT. Buckling behaviour of thin-walled laminated composite beams having open and closed sections subjected to axial and end moment loading. Thin-Walled Struct 2019;141:85–96. https://doi.org/10.1016/j.tws.2019.04.005.

[57] Oliver MA, Webster R. Basic steps in geostatistics: the variogram and kriging. Springer; 2015.

[58] Samui P, Bui DT, Chakraborty S, Deo R. Handbook of probabilistic models. Butterworth-Heinemann; 2020.

[59] Chiles J-P, Delfiner P. Geostatistics: modeling spatial uncertainty. vol. 497. Second Edition. John Wiley & Sons; 2012.

[60] Hengl T. A practical guide to geostatistical mapping. BPR Publishers; 2009.

[61] Hansen T. mGstat: A Geostatistical Matlab toolbox. GitHub, https://au.mathworks.com/matlabcentral/fileexchange/87237-mgstat; 2021.

CHAPTER 7: CONCLUSIONS AND RECOMMENDATIONS

Hollow box Pultruded Fibre-reinforced Polymers (PFRP) profiles are increasingly used as structural elements in many civil infrastructure applications due to their cost-effective manufacturing process, excellent mechanical properties-to-weight ratios, and superior corrosion resistance. However, the anisotropic elasticity and the application-driven slenderness make these profiles prone to local buckling failure, well below their ultimate load capacity. In addition, there is still a lack of knowledge and guidelines in the design for manufacturing against local buckling, which deprives this novel construction material of a large market share compared to the conventional construction materials. Therefore, this research focused on investigating the local buckling behaviour of hollow box PFRP profiles subjected to compressive and flexural loadings and facilitating practical design guidelines for the manufacturing parameters of hollow pulwound FRP profiles to optimise their structural performance against local buckling.

To fulfil the objectives of this study, the conclusions were categorised to address the following aspects:

1- Developing a reliable Finite Element Method (FEM) modelling approach to simulate the local buckling, post-buckling, and progressive failure behaviours of hollow box PFRP profiles under compression and bending loadings.
2- Characterising the local buckling failure of hollow box pulwound FRP profiles under compression and bending loadings.
3- Investigating the effect of the layup and geometric parameters on the local buckling of hollow box PFRP profiles subjected to compression and bending loadings and studying their interactions.
4- Optimising the design configurations of the manufacturing parameters of hollow box PFRP profiles subjected to compression and bending loadings against local buckling.

7.1 Numerical simulation of hollow box PFRP profiles

In this study, a numerical approach based on the FEM was developed using Abaqus 2019 to simulate the structural performance of hollow box PFRP profiles and their failure modes, especially local buckling. The modelling approach was validated against experimental data in terms of the load-displacement curves and failure modes for hollow box PFRP profiles subjected to compression and bending loadings. The following conclusions can be drawn out of this study:

- The proposed FEM modelling approach proved its accuracy and validity against theoretical, experimental, and published data under compression. The incremental approach using the Newton method along with the adaptive automatic stabilisation scheme, controlled increment size, and Hashin damage model represents a simple and robust tool to undertake nonlinear geometric analysis, investigate the mechanical behaviour, and overcome the numerical difficulties in simulating local buckling of hollow box PFRP profiles in time-incremental analysis.
- The controlled maximum increment size of 0.35% of the total step time was suitable to achieve convergence for the local buckling load capacity of the hollow box PFRP profiles with a 5% tolerance. This simplified approach alleviated the model's dependency on the increment size as a numerical parameter and allowed to inspect the experimental failure modes using the sensitivity of the increment size. The approach was extended and validated under flexural loading with reduced computational cost. The solution converged faster against the number of increments under bending compared to compression due to the severity of local buckling under compression compared to bending. The numerical ultimate buckling stress converged at 1.33% of the total step time under bending with the same tolerance on the load capacity provided for compression.
- The proposed energy parameters and constituent failure modes of the FEM model helped greatly in explaining the effect of the dimensions, layups, and slenderness ratios on the post-buckling of the hollow box PFRP profiles and were used to compare the failure modes of the hollow box and circular PFRP

profiles. Moreover, the relationship between the strain energy restoration and the post-buckling behaviour was established.

- The adjusted FEM approach incorporating geometric imperfections and controlled increment size achieved faster analysis and reduced the computational cost up to 3.1 and 1.4 times under compression and bending, respectively, compared to the models with controlled increment size only.

7.2 Local buckling behaviour of hollow box PFRP profiles

The local buckling behaviour of hollow box pulwound FRP profiles subjected to compression and bending loadings was investigated and characterised using both experimental and numerical approaches. Moreover, the structural behaviour and failure mode of the profiles under compression versus bending were compared. The conclusions of this study are summarised below:

- Under compression, the profiles failed by local buckling of the walls. The profiles showed a post-buckling behaviour after the buckling point and before the final collapse. During the post-buckling zone, the axial stiffness was degraded under either a stable path (positive slope) in the rectangular sections or an unstable path (zero slope) in the square section. The failure in the buckled profiles was initiated by shear, tensile, and compressive damage in the matrix at the waviness regions due to the out-of-plane deformation. Afterwards, the localised waviness subsided when the full profile collapse occurred due to compressive failure of fibres at the mid-height of the profile.
- Increasing the profile slenderness ratio (length-to-width ratio L/D) from 2.0 to 5.0 decreases the local buckling load capacity and the axial stiffness, and increases the number of localised waves (delamination zones). Also, the post-buckling zone (in the load-displacement curve) increases when the L/D ratio is increased because of the lower normalised strain energy at the buckling point and the distributed matrix failure by compression, tension, and shear on larger zones.
- Under bending, the failure sequence started by local buckling of the top flange at 95.5% of the ultimate load. The localised waviness occurred at the mid-span

of the beams and propagated until the ultimate load was reached. As the top corners were resisting the load, they exhibited tensile damage of matrix accompanying the buckling of the top flange. The local buckling then extended to the webs causing more damage. Nevertheless, the flange-web junction maintained its rotational stiffness (due to the continuous wound fibres around the corners) to resist the buckling transfer from the top flange to the webs until the beam collapses. Finally, the buckling waviness subsided when the collapse occurred at the top flange due to compressive failure of fibres, spalling, and delamination at the top flange and webs.

- The local buckling behaviour of hollow box PFRP profiles differs depending on the loading condition and test setup. Under compression, the low buckling strength exhibited a post-buckling behaviour with degraded stiffness while the higher buckling strength under bending diminished the post-buckling before failure. The wall slenderness threshold to eliminate local buckling and shift the failure mode to material compressive failure under compression (b/t = 13.2) is lower than bending (b/t = 16.4) referring to the thicker walls needed under compression. This is because the four walls are buckled under compression compared to the top flange only under bending, which provides higher support to the top flange from the adjacent webs and corners. This finding emphasises the severity of local buckling under compression compared to bending due to the lower restraint provided by adjacent walls in compression members. Moreover, in profiles subjected to compression, all the walls buckle with a smaller buckle half-wavelength. However, only the walls under compressive stresses will buckle with a larger buckle half-wavelength in bending. Consequently, investigating and optimising the local buckling behaviour should be undertaken under both loading conditions in which compression provides the upper limit case and bending provides the lower limit case.

7.3 Effect of manufacturing parameters on the behaviour of hollow box PFRP profiles

The effect of the layup and geometric parameters on the structural performance of hollow box PFRP profiles was investigated and the contribution of each parameter on the local buckling strength was analysed. In addition, the interactions between the design parameters were explored and considered to facilitate practical and economic designs. Based on the results of this study, the following conclusions can be drawn:

- The geometric parameters control the structural behaviour of hollow box PFRP profiles dominated by local buckling (stability limit), while the layup parameters govern the behaviour of these profiles dominated by material ultimate failure (strength limit).
- The most significant design parameter affecting the local buckling strength of hollow box PFRP profiles under compressive and flexural loadings is the corner radii ratio (r/R), which contributed up to 49% of the buckling strength as it reduces the effective buckling width of the wall, enhances the corners restraint, and increase the rigidity transferred between the walls. The wall slenderness and cross-sectional aspect ratio (h/b) are the second and third influencing parameters contributing up to 28% and 18%, respectively. The layup parameters contribution towards the buckling strength is negligible (2.5% under compression and 7.8% under bending) compared to the geometric parameters.
- The geometric parameters shape the failure mode of hollow box PFRP profiles. Hollow box PFRP profile with h/b = 1.0 and either $(b/t)_{max} \leq 13.2$ or $(r/R) \geq 2.5$ presents a recommended configuration of the geometric parameters to shift the failure mode from local buckling to material compressive failure and fully utilise the profile strength under compression. Local buckling can be eliminated and the ultimate strength of the profile under bending can be attained using either a wall slenderness ratio of $b/t \leq 16.4$, a cross-sectional aspect ratio of $3 > h/b \geq 1.5$, or corner radii ratio of $r/R \geq 2.5$.
- For compression applications, a cross-sectional aspect ratio h/b = 1.0 (square section) presents the optimal design for hollow box PFRP profiles to ensure a simultaneous buckling of all walls and a minimum value of $(b/t)_{max}$. Moreover, the optimal enhancement in strength from the increase in the wall thickness or the r/R ratio occurs when h/b = 1.0.
- Increasing the outer corner radius enhances the buckling strength of hollow box PFRP profiles subjected to axial compression by 3.77% while slightly reducing the axial stiffness by 5.52%. An impractically large corner radius

(Corner-to-width ratio (b/R) ≤ 2.8) is needed to exhibit a significant effect and transfer the local buckling to material compressive failure. For hollow box PFRP profiles subjected to flexural loading, the moment capacity deteriorates when the outer corner radius is increased even though the failure mode is shifted from local buckling towards material compressive failure of the top flange. This is because of the reduction in the cross-sectional area of the top flange.

- As long as symmetric and balanced layups are used, the effect of the stacking sequence on the compressive and flexural behaviours of hollow box PFRP profiles is negligible. Thus, the manufacturing process limitations can control any preferable stacking configuration of the axial and wound fibres provided that an axial ply will form the profile core.
- The wound fibre angle affects the compressive strength of the hollow PFRP profile depending on the failure mode. A medium angle is recommended to resist local buckling, while small or large angles should be used against material compressive failure. Similarly, the optimal axial-to-wound fibres ratio depends on the failure mode. A higher axial fibre percentage is recommended to endure material compressive failure, whereas a higher wound fibre percentage is preferred to sustain local buckling. As the axial fibre percentage increases, the effect of the wound fibre angle on the stiffness and strength of the profile decreases.
- Because of local buckling, the maximum axial (EA/L) and flexural stiffness (EI/L^3) and strength cannot be achieved by using one design configuration of the layup parameters as each one of these design targets requires a different configuration. The maximum axial and flexural stiffness requires a small winding angle and a low percentage of wound fibres, while the maximum compressive and flexural strength requires a large winding angle and a high percentage of wound fibres. Using the recommended configurations of the geometric parameters presented previously will eliminate local buckling and shift the failure mode to material compressive failure of walls or the top flange under compression or bending, respectively. Thus, allowing for both maximum stiffness and strength to be attained by the smallest winding angle and the highest axial fibre percentage.

- For hollow box PFRP profiles subjected to flexural loading, the flange-web junction plays a major role in resisting buckling of top flange and webs. The top corners geometry is the main parameter controlling the rigidity, strength, and failure mode of the flange-web junction. Taking the interaction between the r/R ratio and the walls slenderness ratio into account can provide an enhanced design configuration to shift the failure to material compressive failure. This configuration consists of wall slenderness ratios of $b/t_f \leq 15.6$ and $19.2 \geq h/t_w \geq 16.4$ along with a corner radii ratio of $r/R \geq 2$. Economically, it is better to invest in a thicker flange with thin webs to eliminate local buckling in the profile and the optimal design for stiff corners and stable flange would have the highest investment in the r/R ratio.
- Considering the interactions of the geometric parameters during the design for manufacturing stage obtains more economical and enhanced design configurations with a higher buckling strength up to 2.25 times and half material cost. The enhancement in the compressive strength from decreasing the wall slenderness is higher when the h/b ratio is small. On the contrary, the flexural strength is significantly increased as the wall slenderness is decreased at a larger h/b ratio. Increasing the r/R ratio for thin walls exhibits a higher increase in the compressive and flexural strengths compared to thick walls. Moreover, the increase in the compressive and flexural strengths of the profile due to the increase in the r/R ratio is higher when the h/b ratio is small.

7.4 Numerical optimisation of hollow box PFRP profiles

A new fast-converging optimisation approach combining the FEM and the Genetic Algorithm (GA) was proposed to design the optimal configuration of the geometry and layup design parameters against local buckling under compression and bending loadings. The mixed-integer constrained optimisation GA code (MI-LXPM) was used to minimise the manufacturing cost per metre of pultrusion and enhance the structural stiffness and strength properties. The Kriging model was used to interpolate the design space and produce a practical design chart linking the profile geometry to the local buckling capacity. An experimental case study on the design of a hollow rectangular

PFRP girder demonstrated the proposed optimisation approach. Based on the results, the following conclusions were drawn:

- The MI-LXPM GA code represents a robust tool to optimise the manufacturing design parameters of hollow box PFRP profiles. In the current study, the optimised designs were estimated to save 11.5% and 26.4% of the materials cost per metre of pultrusion for compression and bending applications, respectively, compared to the control design. The cost was effectively reduced under bending compared to compression because of the severity of local buckling under compression.
- The geometry of the optimal configurations varies depending on the different nature of local buckling under compression versus bending. Under compression, the four walls are affected and a square cross-section represents the optimal case allowing all the walls to buckle simultaneously under higher buckling strength compared to a rectangular section, whereas only the top flange and upper parts of the webs (half the section area) are affected by the compressive stresses under bending. Consequently, smaller wall slenderness and a larger r/R ratio are needed to strengthen the four walls and corners against buckling under compression. Thus, the reduction in the material cost under bending was 2.2 times its equivalent under compression as the cross-sectional area is effectively reduced under bending compared to compression.
- The experimental case study on the design of a hollow rectangular PFRP girder demonstrated the proposed optimisation approach. The new design saved 10.6% of the material cost and enhanced the flexural strength by 41% and the flexural stiffness by 16% compared to the double-cell bonded girder.
- Considering a large corner radii ratio (r/R) in the design is an efficient and economic practice for manufacturing optimised hollow PFRP profiles. The larger area at the corners (flange-web junctions) of the profile can eliminate any concentration of stresses while maintaining the same stress distribution at the thinner walls. Thus, making the entire cross-section (walls and corners) works at the same level of stress instead of stressing the corners more than the walls as in the control profile.
- The implementation of the Kriging model, which is a geostatistical prediction tool capable of handling such design problems, was proved to be a robust

approach to maximise the data use from the GA codes and map the design space of hollow box PFRP profiles to generate design and interaction charts for designers to use. The generated design charts represent a simple and reliable design tool against local buckling of hollow box PFRP profiles combining all the critical geometric parameters and considering their interactions to facilitate optimised designs with economic attributes instead of costly designs when these interactions are disregarded.

7.5 Contributions of the study

This study has contributed to the growing area of research of the hollow box PFRP profiles by investigating the modelling approaches of hollow box PFRP profiles and their local buckling behaviour, characterising the compressive and flexural behaviours of these profiles, reporting the effects and interactions of the design parameters of these profiles, and developing a numerical optimisation approach to optimise the design configurations of the manufacturing parameters against local buckling. The results obtained from this research discovered the optimisation opportunities for these profiles. This study also generated numerous experimental data and numerical design tools useful for design engineers to expand the use of these profiles in different civil engineering applications. These significant contributions can be summarised as follows:

1- Understanding the structural behaviour of hollow box PFRP profiles subjected to compression and bending loadings and reporting the failure sequence of these profiles triggered by local buckling.
2- Addressing the knowledge gap on the effect and interactions of the critical design parameters controlling the structural behaviour of hollow box PFRP profiles and providing design guidelines and recommendations to manufacture optimised profiles with economic designs and enhanced structural performance.
3- Developing a numerical simulation and optimisation tool to accurately predict the structural performance of hollow box PFRP profiles and obtain optimised design configurations of the manufacturing parameters of hollow box pulwound FRP profiles against local buckling.

7.6 Recommendations and future research

The research work accomplished in this study on investigating the local buckling behaviour of hollow box PFRP profiles subjected to compressive and flexural loadings and facilitating practical design guidelines for their manufacturing parameters to optimise their structural performance against local buckling is comprehensive and achieved a deep understanding of the design for manufacturing parameters.

Further research in related areas still needs to be conducted to broaden the use of hollow box PFRP profiles in civil structural applications, these research points are listed as follows:

1- Since the local buckling behaviour of hollow box PFRP profiles depends on the loading conditions, it is worth studying the effect of the test setup and configuration under bending (4-point versus 3-point bending) on the local buckling behaviour and moment capacity of these profiles. Generating failure maps to connect the effect of the span-to-depth ratio and shear span to the failure modes and moment capacity is necessary to develop standards and design provisions for testing hollow box PFRP profiles on the structural level.
2- Besides local buckling, there are other failure modes worth investigating such as flexural global buckling, lateral-torsional buckling, and shear failure. Studying the design parameters under these failure modes will help to understand the structural performance of slender profiles and their recommended supporting and bracing guidelines.
3- While studying the design parameters under a single loading condition is essential, investigating the local buckling behaviour and the design parameters under combined compressive load and bending moment is vital to understand the load-moment interactions for future design provisions.
4- Since the structural performance of hollow PFRP profiles depends on the fibres type, it is worth studying the potentials of using hybrid fibres and their effect on the other design parameters and local buckling of hollow box PFRP profiles.
5- As PFRP profiles possess low transverse mechanical properties, it is worth investigating other manufacturing processes incorporating pultrusion of

different fibre architectures through the thickness, such as braidtrusion, and studying their local buckling behaviour and the associated design parameters.

6- The developed modelling approach can be further enhanced in the future by incorporating the delamination failure and the lamina progressive failure in a more comprehensive approach to address a wider range of loading conditions and micro-structure problems. Several recommendations and guidelines can be proposed based on this research to help reduce the computational cost of such an approach. For instance, cohesive contact surfaces are more preferred for hollow PFRP profiles compared to cohesive elements to simulate the very thin interlaminar layers of resin and increase the computational efficiency. Moreover, the delamination between laminas can be defined at the zone of interest (e.g. mid-span of the profile) to reduce the computational cost.

7- Investigating the optimised designs reported in this research experimentally to verify their structural behaviour will provide feedback to enhance and calibrate the modelling approach presented in this study.

REFERENCES

Abramovich, H 2017, *Stability and Vibrations of Thin-Walled Composite Structures*, Woodhead Publishing.

Advani, SG & Hsiao, K-T 2012, *Manufacturing Techniques for Polymer Matrix Composites (PMCs)*, Elsevier.

Ahn, N, Lee, J, Lee, K & Jang, HS 2014, 'An experimental study on flexural behavior for a FRP composite girder', *Construction and Building Materials*, vol. 50, pp. 13–21.

Alajarmeh, O, Zeng, X, Aravinthan, T, Shelley, T, Alhawamdeh, M, Mohammed, A, … Schubel, P 2021, 'Compressive behaviour of hollow box pultruded FRP columns with continuous-wound fibres', Thin-Walled Structures, vol. 168, p. 108300.

Almeida, JHS, Tonatto, MLP, Ribeiro, ML, Tita, V & Amico, SC 2018, 'Buckling and post-buckling of filament wound composite tubes under axial compression: Linear, nonlinear, damage and experimental analyses', *Composites Part B: Engineering*, vol. 149, pp. 227–239.

Al-saadi, AU, Aravinthan, T & Lokuge, W 2019, 'Effects of fibre orientation and layup on the mechanical properties of the pultruded glass fibre reinforced polymer tubes', *Engineering Structures*, vol. 198, p. 109448.

American Society of Civil Engineers 2012, 'Pre-standard for load & resistance factor design (LRFD) of pultruded fiber reinforced polymer (FRP) structures', *Arlington, VA: ACMA*, p. 215.

Ascione, L, Caron, J-F, Godonou, P, van Ijselmuijden, K, Knippers, J, Mottram, T, … Tromp, L 2016, *Prospect for new guidance in the design of FRP : Support to the implementation, harmonization and further development of the Eurocodes*, Publications Office of the European Union.

Attaf, B 2011, *Advances in Composite Materials: Ecodesign and Analysis*, BoD – Books on Demand.

Bakis, CE, Bank, LC, Brown, Vl, Cosenza, E, Davalos, JF, Lesko, JJ, … Triantafillou, TC 2002, ‘Fiber-reinforced polymer composites for construction—State-of-the-art review’, *Journal of Composites for Construction*, vol. 6, no. 2, pp. 73–87.

Balasubramanian, M 2013, *Composite Materials and Processing*, CRC Press.

Bank, LC 2006, *Composites for Construction: Structural Design with FRP Materials*, John Wiley & Sons.

Barbero, EJ 2017, *Introduction to Composite Materials Design*, CRC Press.

Boisse, P 2015, *Advances in Composites Manufacturing and Process Design*, Woodhead Publishing.

Bunsell, AR & Renard, J 2005, *Fundamentals of Fibre Reinforced Composite Materials*, CRC Press.

Buragohain, MK 2017, *Composite Structures: Design, Mechanics, Analysis, Manufacturing, and Testing*, CRC Press.

Butler, R, Rhead, A & Dodwell, T 2018, ‘8.7 Optimum Design and Damage Tolerance of Compressively Loaded Laminates’, in PWR Beaumont & CH Zweben (eds), *Comprehensive Composite Materials II*, Elsevier, Oxford, pp. 118–135.

Cardoso, DCT, Harries, KA & Batista, E de M 2014, ‘Compressive strength equation for GFRP square tube columns’, *Composites Part B: Engineering*, vol. 59, pp. 1–11.

Clarke, JL 2005, *Structural Design of Polymer Composites EUROCOMP Design Code and Handbook*, CRC Press.

Correia, JR, Branco, FA, Silva, NMF, Camotim, D & Silvestre, N 2011, ‘First-order, buckling and post-buckling behaviour of GFRP pultruded beams. Part 1: Experimental study’, *Computers & Structures*, vol. 89, Civil-Comp, no. 21, pp. 2052–2064.

Daniel, IM & Ishai, O 2006, *Engineering Mechanics of Composite Materials*, Oxford University Press.

Eslami, MR 2017, *Buckling and Postbuckling of Beams, Plates, and Shells*, Springer.

Fangueiro, R 2011, *Fibrous and Composite Materials for Civil Engineering Applications*, Elsevier.

Friberg, E & Olsson, J 2014, 'Application of fibre reinforced polymer materials in road bridges – General requirements and design considerations', Master's Thesis, CHALMERS UNIVERSITY OF TECHNOLOGY, Göteborg, Sweden.

GAJJAR, D 2020, 'Development of applications and innovation of FRP Pultruded Profiles in India & Asia', Fifteenth World Pultrusion Conference.

Garrido, M, Madeira, JFA, Proença, M & Correia, JR 2019, 'Multi-objective optimization of pultruded composite sandwich panels for building floor rehabilitation', *Construction and Building Materials*, vol. 198, pp. 465–478.

Godat, A, Légeron, F, Gagné, V & Marmion, B 2013, 'Use of FRP pultruded members for electricity transmission towers', *Composite Structures*, vol. 105, pp. 408–421.

Guades, E, Aravinthan, T, Islam, M & Manalo, A 2012, 'A review on the driving performance of FRP composite piles', *Composite Structures*, vol. 94, no. 6, pp. 1932–1942.

Hizam, RM, Manalo, AC, Karunasena, W & Bai, Y 2019, 'Behaviour of pultruded GFRP truss system connected using through-bolt with mechanical insert', *Composites Part B: Engineering*, vol. 168, pp. 44–57.

Hoa, SV 2009, *Principles of the Manufacturing of Composite Materials*, DEStech Publications, Inc.

Johnston, J, Mirza, O, Kemp, M & Gates, T 2018, 'Flexural behaviour of alternate transom using composite fibre pultruded sections', *Engineering Failure Analysis*, vol. 94, pp. 47–68.

Jones, RM 1998, *Mechanics Of Composite Materials*, CRC Press.

Kaw, AK 2005, *Mechanics of Composite Materials*, CRC Press.

Li, Y-F, Hsu, T-H & Hsieh, F-C 2019, ‘A Study on Improving the Mechanical Behaviors of the Pultruded GFRP Composite Material Members’, *Sustainability*, vol. 11, no. 3, p. 577.

Meyer, R 2012, *Handbook of Pultrusion Technology*, Springer Science & Business Media.

Minchenkov, K, Vedernikov, A, Safonov, A & Akhatov, I 2021, ‘Thermoplastic Pultrusion: A Review’, Polymers, 2, vol. 13, no. 2, p. 180.

Mottram, JT & Henderson, J 2018, *Fibre-reinforced polymer bridges - guidance for designers*, C779, C779, CIRIA, London, p. 156.

Muttashar, M, Karunasena, W, Manalo, A & Lokuge, W 2016, ‘Behaviour of hollow pultruded GFRP square beams with different shear span-to-depth ratios’, *Journal of Composite Materials*, vol. 50, no. 21, pp. 2925–2940.

Muttashar, M, Karunasena, W, Manalo, A & Lokuge, W 2019, ‘Behavior of pultruded multi-celled GFRP hollow beams with low-strength concrete infill’, in *Mechanics of Structures and Materials XXIV: Proceedings of the 24th Australian Conference on the Mechanics of Structures and Materials (ACMSM24, Perth, Australia, 6-9 December 2016)*, CRC Press, p. 243.

Muttashar, MD 2017, ‘Behaviour of multi-celled GFRP beam assembly with concrete infill: experimental and theoretical evaluations’, PhD Thesis, University of Southern Queensland, Toowoomba, Queensland.

National Research Council 2007, ‘Guide for the Design and Construction of Structures made of FRP Pultruded Elements’, *CNR-DT*, vol. 205, pp. 25–31.

Nguyen, N-D, Nguyen, T-K, Vo, TP, Nguyen, T-N & Lee, S 2019, ‘Vibration and buckling behaviours of thin-walled composite and functionally graded sandwich I-beams’, *Composites Part B: Engineering*, vol. 166, pp. 414–427.

Rangappa, SM, Parameswaranpillai, J, Siengchin, S & Kroll, L 2020, *Lightweight Polymer Composite Structures: Design and Manufacturing Techniques*, CRC Press, Boca Raton.

Sapuan, SM 2017, *Composite Materials: Concurrent Engineering Approach*, Butterworth-Heinemann.

Satasivam, S & Bai, Y 2014, 'Mechanical performance of bolted modular GFRP composite sandwich structures using standard and blind bolts', *Composite Structures*, vol. 117, pp. 59–70.

Sayyad, AS & Ghugal, YM 2017, 'Bending, buckling and free vibration of laminated composite and sandwich beams: A critical review of literature', *Composite Structures*, vol. 171, pp. 486–504.

Sellier, J 2019, 'Identifying the barriers and opportunities to the adoption of advanced materials in construction', paper presented at Amconf 2019-Advanced Materials for Construction, University of Manchester, UK.

Serhat, G & Basdogan, I 2019, 'Multi-objective optimization of composite plates using lamination parameters', *Materials & Design*, vol. 180, p. 107904.

Singer, J, Arbocz, J & Weller, T 2002, *Buckling Experiments: Experimental Methods in Buckling of Thin-Walled Structures Shells, Built-up Structures, Composites and Additional Topics*, vol. 2, John Wiley & Sons, New York.

Starr, T 2000, *Pultrusion for Engineers*, Elsevier.

Turvey, GJ & Marshall, IH 1995, *Buckling and Postbuckling of Composite Plates*, Springer Science & Business Media.

Uddin, N 2013, *Developments in Fiber-Reinforced Polymer (FRP) Composites for Civil Engineering*, Elsevier.

Unity Fibers n.d., *Pultruded Section*, indiamart.com, viewed 2 December 2021, <https://www.indiamart.com/proddetail/pultruded-section-15875392355.html>.

Van Den Einde, L, Zhao, L & Seible, F 2003, 'Use of FRP composites in civil structural applications', *Construction and Building Materials*, vol. 17, Fibre-reinforced polymer composites in construction, no. 6, pp. 389–403.

Vedernikov, A, Safonov, A, Tucci, F, Carlone, P & Akhatov, I 2020, ‘Pultruded materials and structures: A review’, *Journal of Composite Materials*, vol. 54, no. 26, pp. 4081–4117.

Vinson, JR & Sierakowski, RL 2006, *The Behavior of Structures Composed of Composite Materials*, Springer.

Wagners CFT n.d., *Wagners-Composite Fibre Technologies (CFT)*, Wagner, viewed 8 March 2020, <https://www.wagner.com.au/main/what-we-do/composite-fibre-technologies/cft-home/>.

Xu, J, Zhao, Q & Qiao, P 2013, ‘A critical review on buckling and post-buckling analysis of composite structures’, *Frontiers in Aerospace Engineering*, vol. 2, no. 3, pp. 157–168.

Zhang, S, Caprani, CC & Heidarpour, A 2018, ‘Strain rate studies of pultruded glass fibre reinforced polymer material properties: A literature review’, *Construction and Building Materials*, vol. 171, pp. 984–1004.

APPENDIX A: SUPPLEMENTARY DATA OF CHAPTER 3: MODELLING HOLLOW PULTRUDED FRP PROFILES UNDER AXIAL COMPRESSION: LOCAL BUCKLING AND PROGRESSIVE FAILURE

Fig. A. 1 shows the results of the mesh sensitivity study on the hollow pultruded FRP profiles. The study was performed on the full model, including local buckling and progressive failure behaviours to select the suitable mesh which is able to capture the experimental behaviour entirely. The selected mesh for each profile was the one that convergence starts at so that it will provide accurate results with the least computational cost.

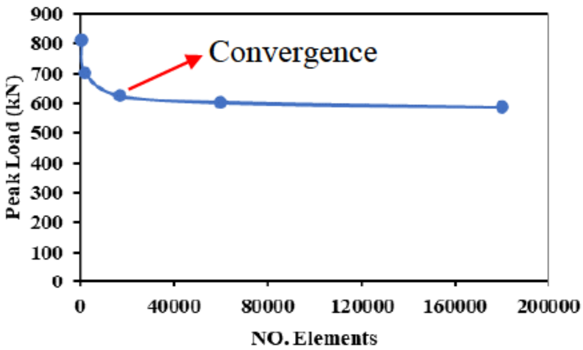

(a)

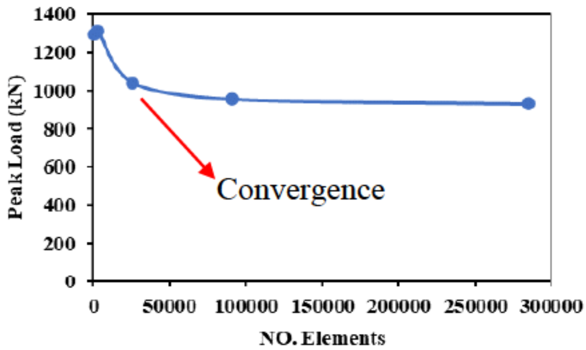

(b)

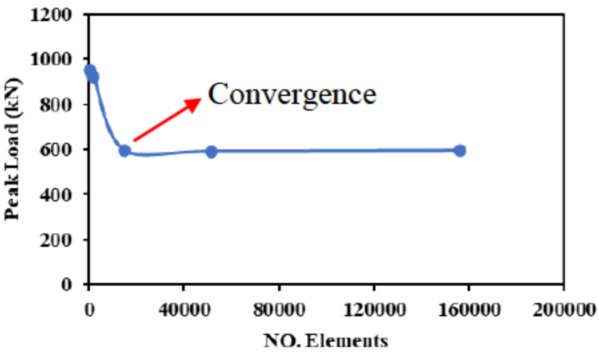

(c)

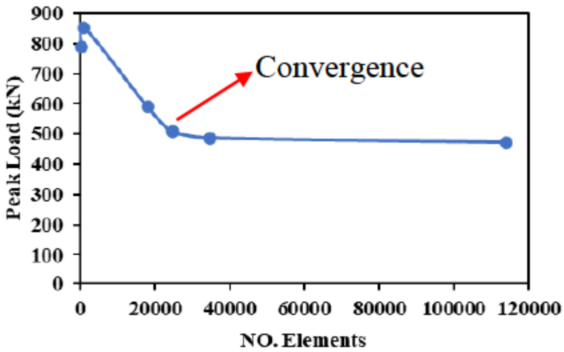

(d)

Fig. A. 1. mesh sensitivity study for pultruded FRP profiles with L/D equals 2 (a) S100×100×5.2(b) S125×125×6.4 (c) R100×75×5.2 and (d) C-89×6.

Fig. A. 2 shows the meshed hollow box pultruded FRP profiles. The element size is 5 and 3 mm for the box and circular profiles, respectively. The profiles meshed through the thickness with five elements to capture the through-thickness behaviour accurately and to reduce the hourglass modes. The corners of the box profiles meshed with five elements to allow for better simulation along the walls junctions.

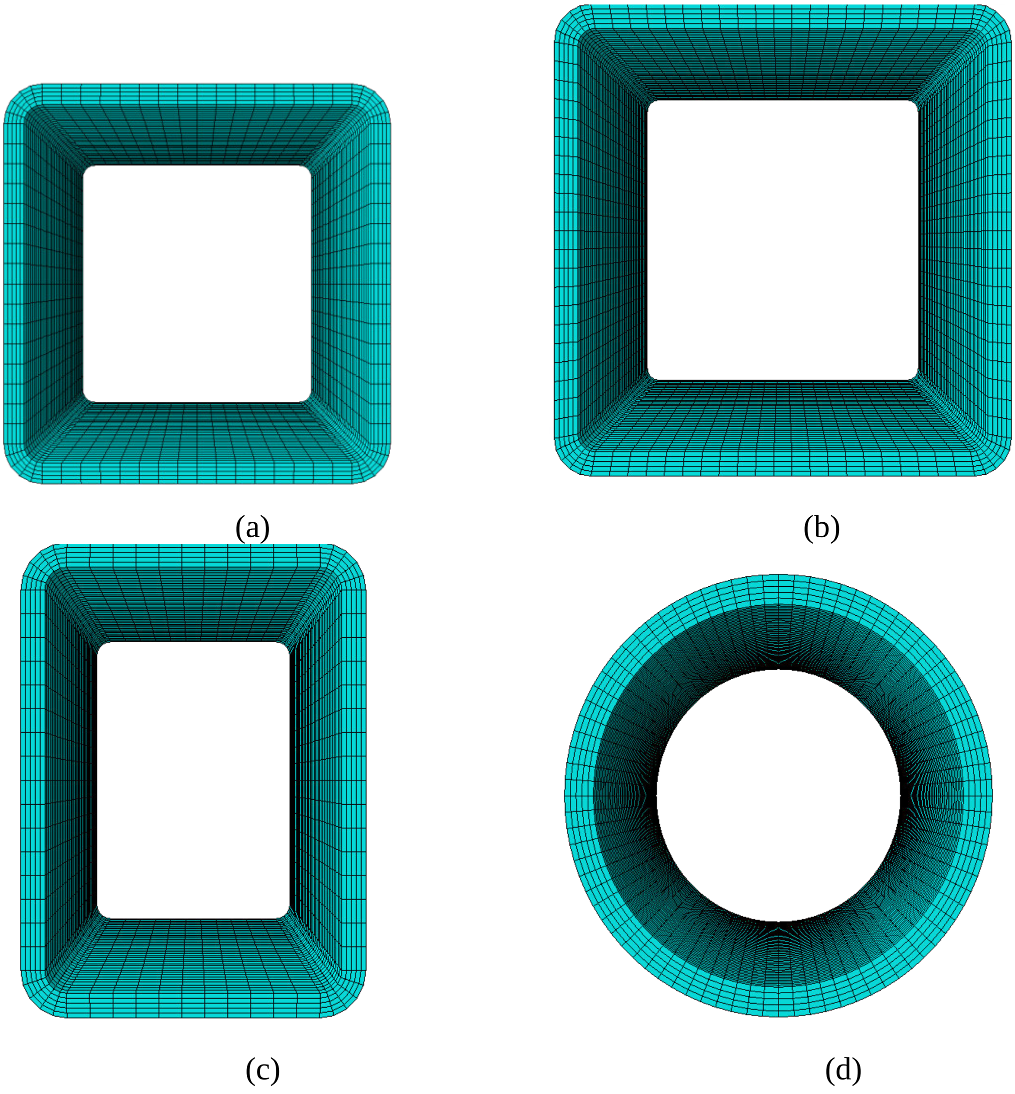

Fig. A. 2. Cross-sectional mesh distribution of the hollow pultruded FRP profiles (a) S-100×100×5.2(b) S-125×125×6.4 (c) R-100×75×5.2 and (d) C-89×6.

Fig. A. 3 presents the FEM vs experimental load-displacement curves of the hollow profiles from phase one. The shown FEM results were obtained by modelling only the local buckling behaviour without any failure criteria. That is why the load-displacement path keeps increasing after the local buckling point (the point at which the line slope degraded). The FEM and experimental results agreed in terms of the axial stiffness and buckling load. The circular profiles did not experience local buckling.

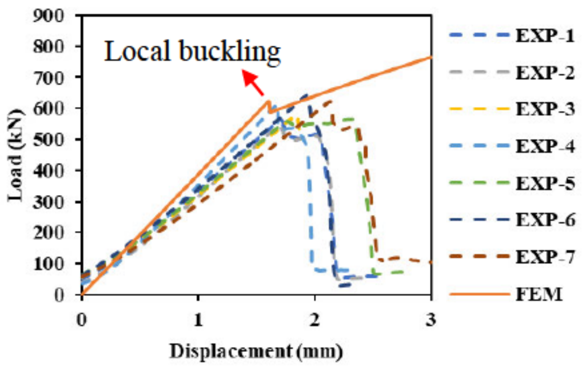

(a)

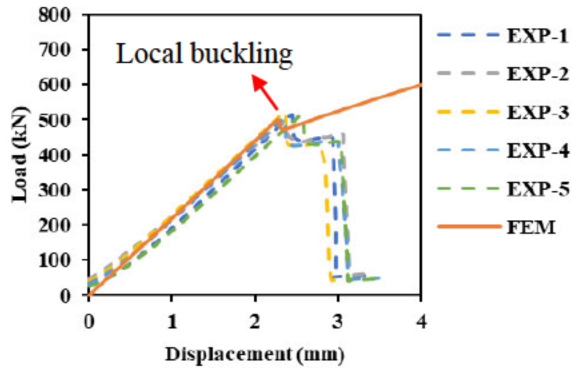

(b)

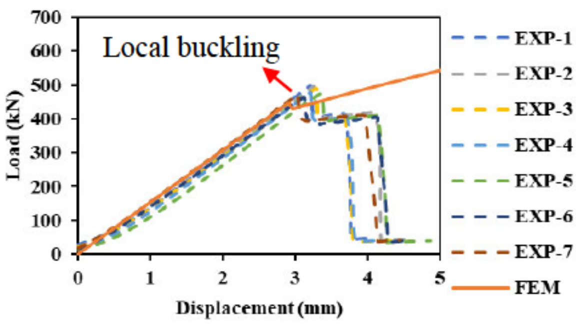

(c)

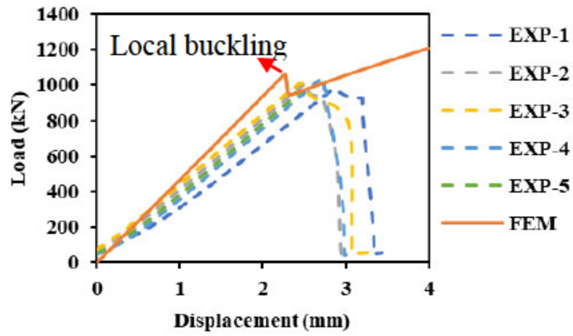

(d)

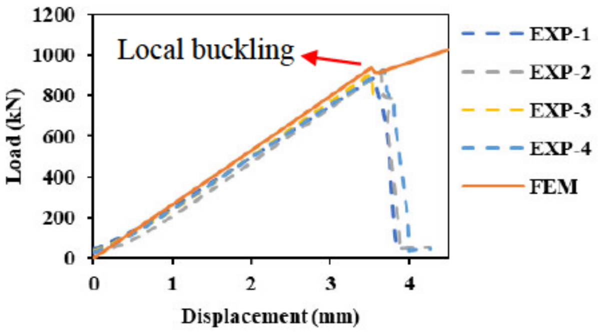

(e)

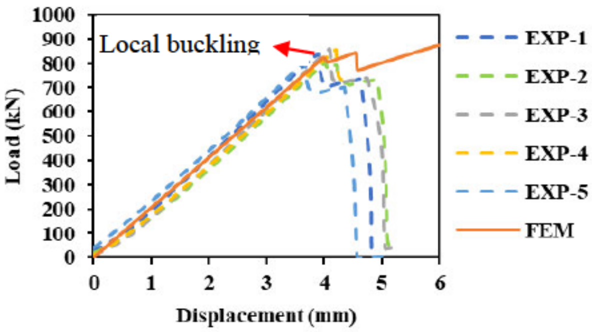

(f)

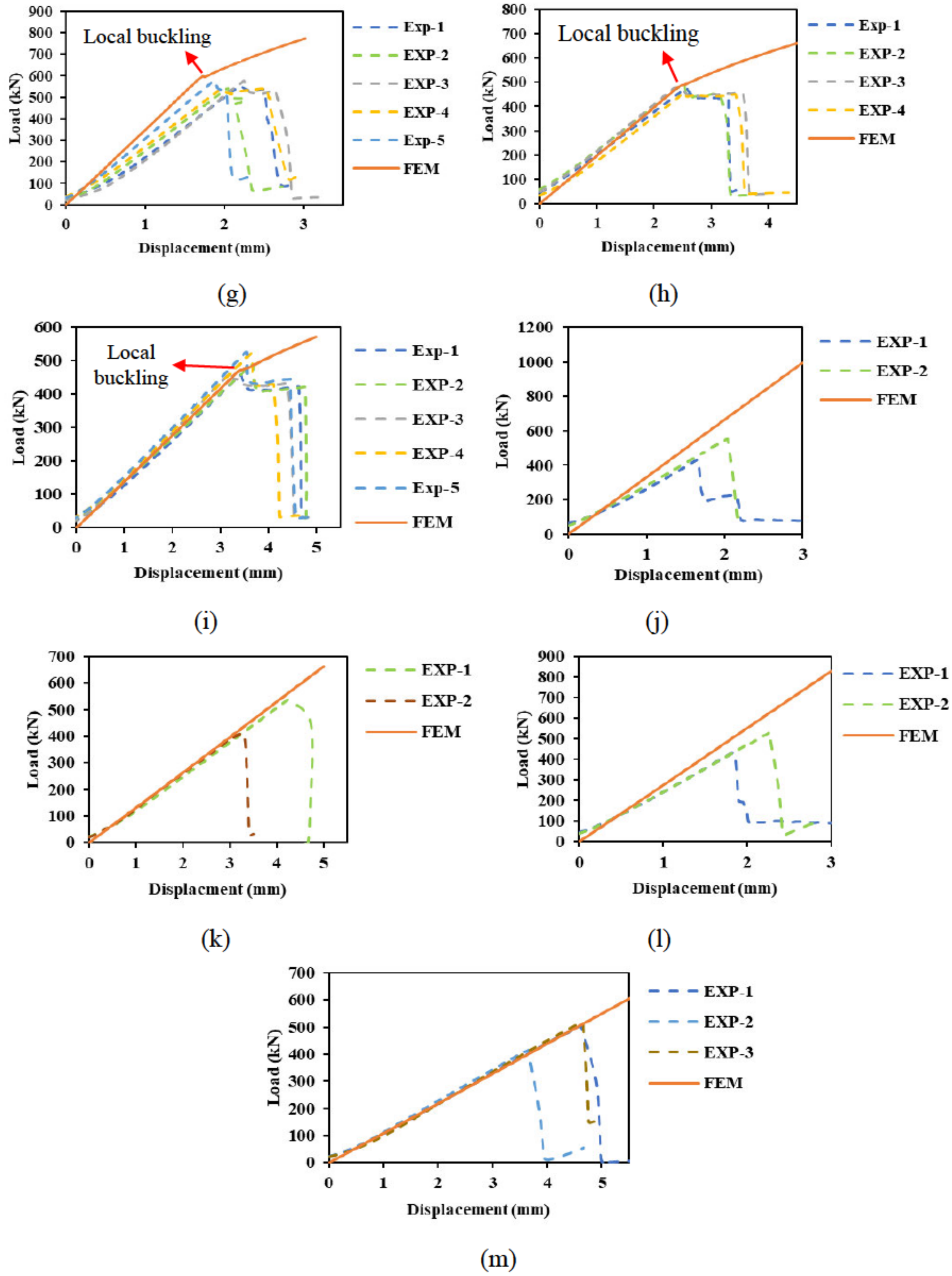

Fig. A. 3. Phase one FEM vs Experimental load-displacement curves for (a) S-100×100×5.2 with L/D equals 2 (b) S-100×100×5.2 with L/D equals 3.5 (c) S-100×100×5.2 with L/D equals 5 (d) S-125×125×6.4 with L/D equals 2 (e) S-125×125×6.4 with L/D equals 3.5 (f) S-125×125×6.4 with L/D equals 5 (g) R-75×100×5.2 with L/D equals 2 (h) R-75×100×5.2 with L/D equals 3.5 (i) R-75×100×5.2 with L/D equals 5 (j) C1-89×6 with L/D equals 2 (k) C1-89×6 with L/D equals 5 (l) C2-89×6 with L/D equals 2 and (m) C2-89×6 with L/D equals 5.

Fig. A. 4 presents the FEM vs experimental load-displacement curves of the hollow profiles from phase two. The shown FEM results were obtained by modelling both the local buckling and progressive failure behaviours. The FEM and experimental results agreed in terms of the axial stiffness, buckling load, and post-peak trend for the hollow box profiles. The circular profiles did not experience local buckling.

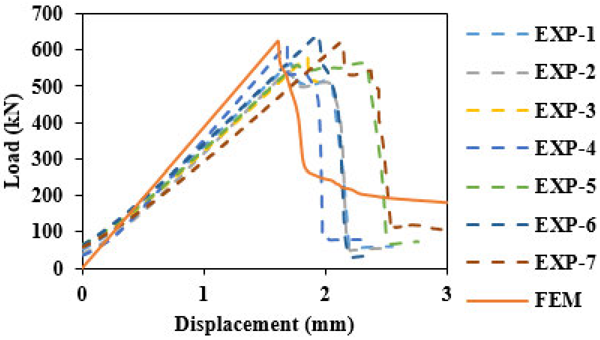

(a)

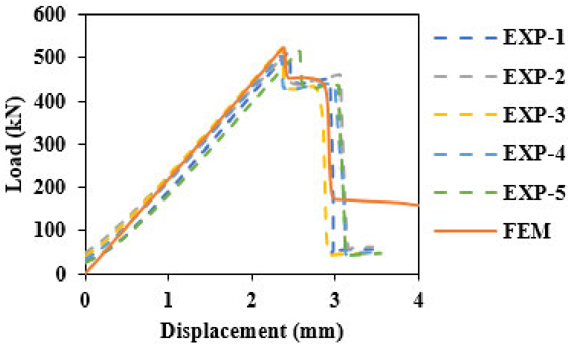

(b)

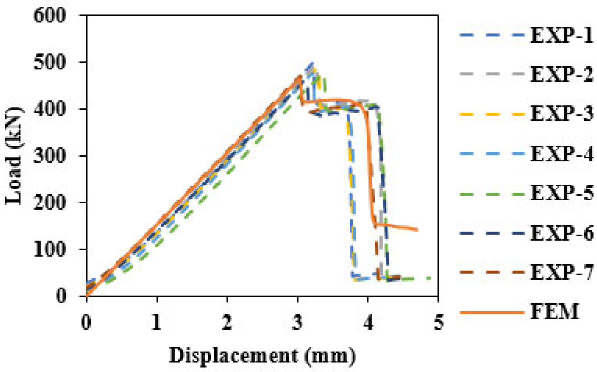

(c)

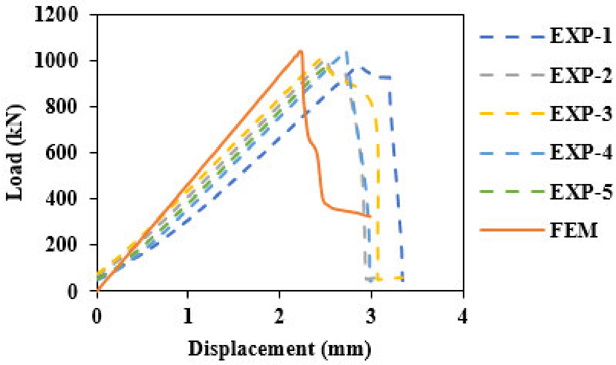

(d)

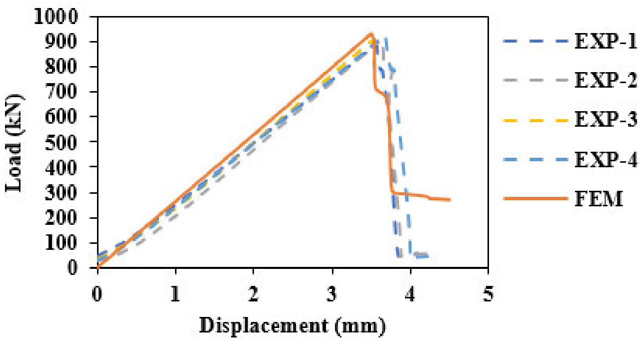

(e)

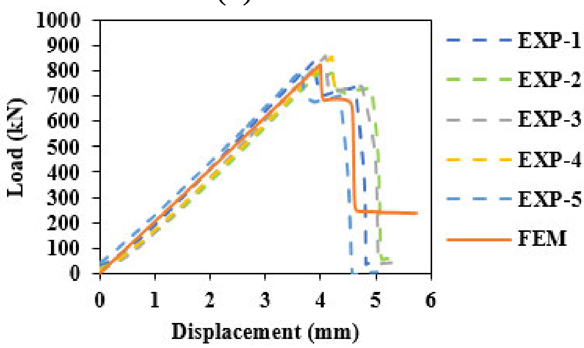

(f)

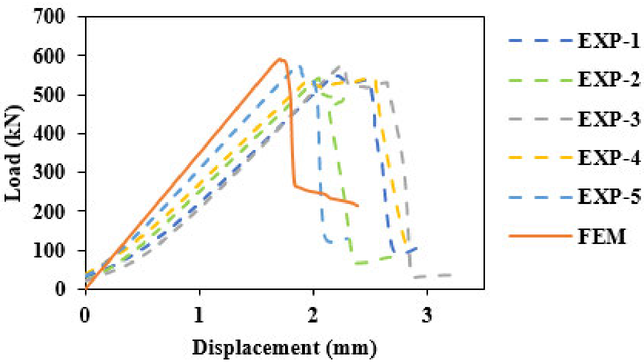

(g)

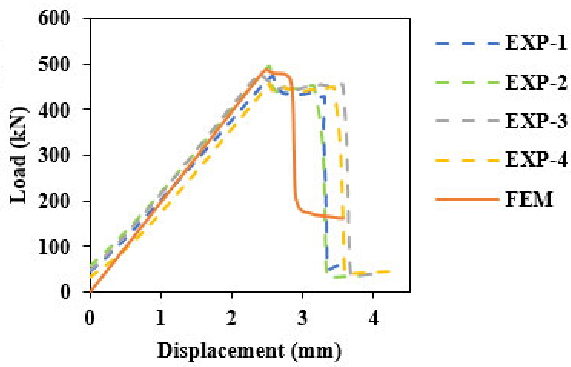

(h)

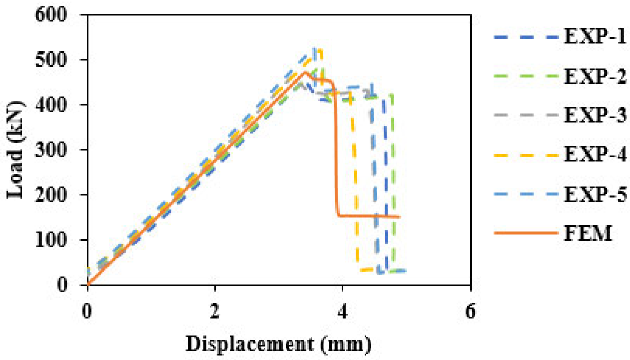

(i)

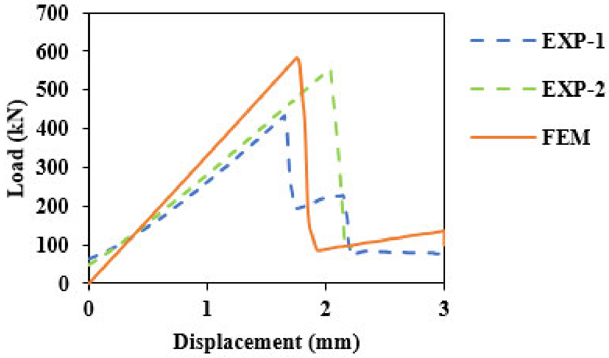

(j)

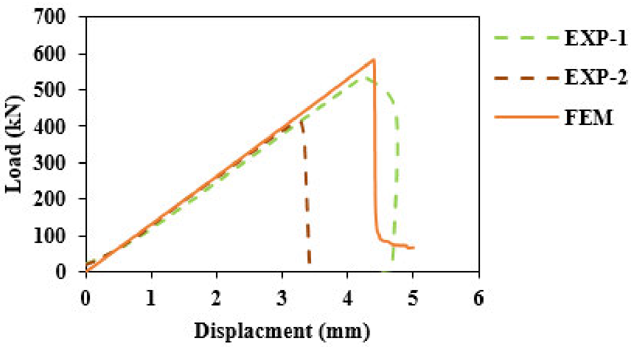

(k)

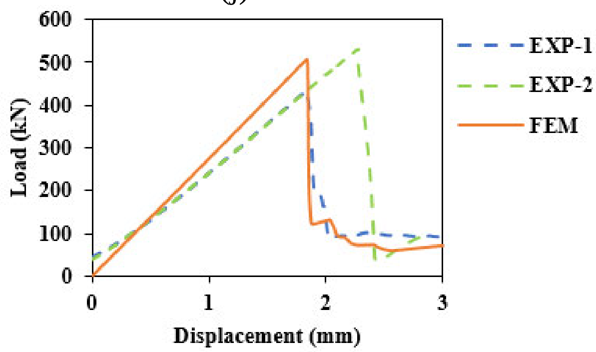

(l)

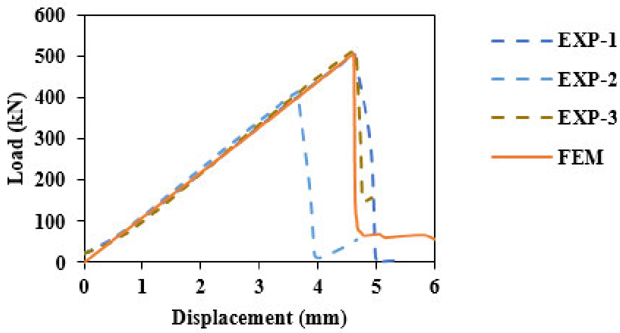

(m)

Fig. A. 4. Phase two FEM vs Experimental load-displacement curves for (a) S-100×100×5.2 with L/D equals 2 (b) S-100×100×5.2 with L/D equals 3.5 (c) S-100×100×5.2 with L/D equals 5 (d) S-125×125×6.4 with L/D equals 2 (e) S-125×125×6.4 with L/D equals 3.5 (f) S-125×125×6.4 with L/D equals 5 (g) R-75×100×5.2 with L/D equals 2 (h) R-75×100×5.2 with L/D equals 3.5 (i) R-75×100×5.2 with L/D equals 5 (j) C1-89×6 with L/D equals 2 (k) C1-89×6 with L/D equals 5 (l) C2-89×6 with L/D equals 2 and (m) C2-89×6 with L/D equals 5.

Fig. A. 5 depicts the failure sequence in the hollow box pultruded FRP profiles, which was triggered by local buckling. The presented matrix tensile failure counters highlight the localised waves propagation, which is compared to the experimental buckled shape at the same time increment.

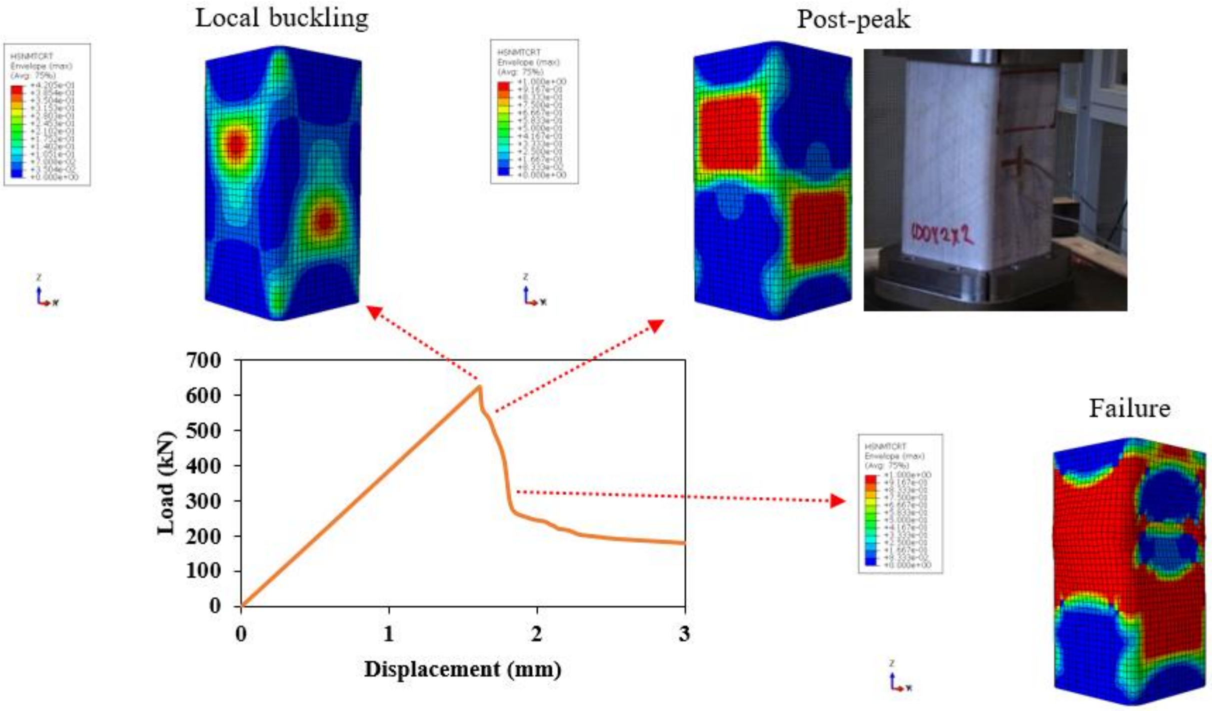

(a)

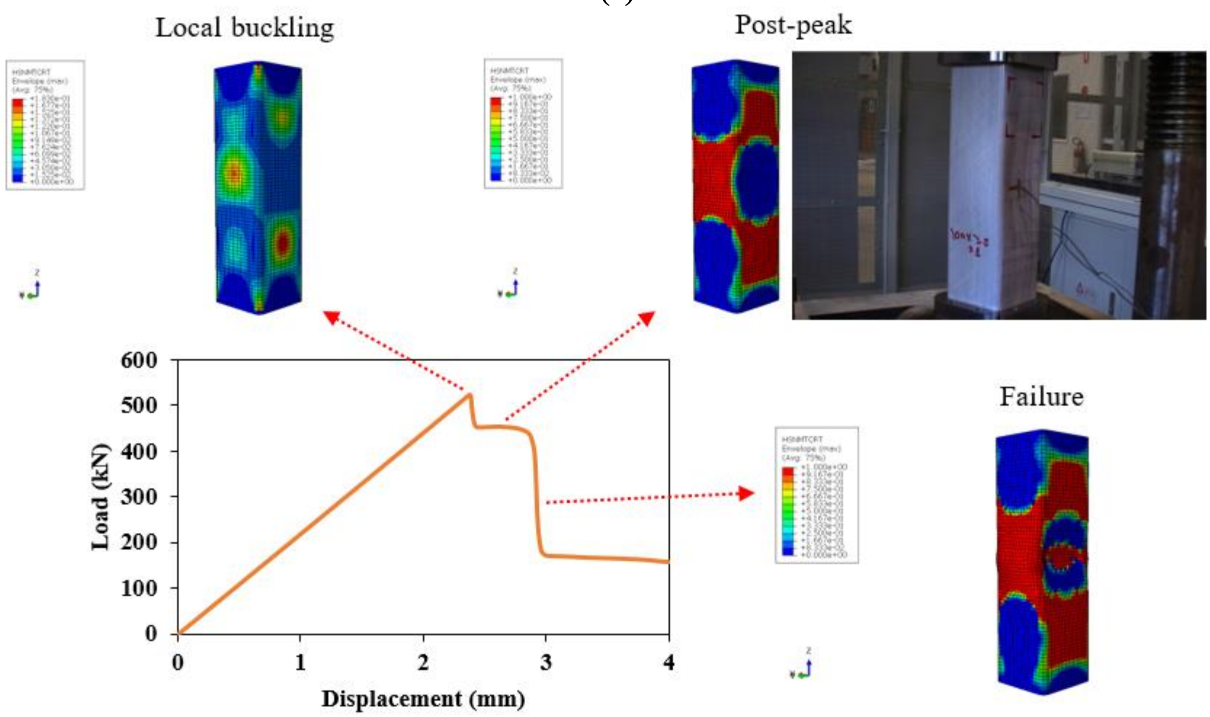

(b)

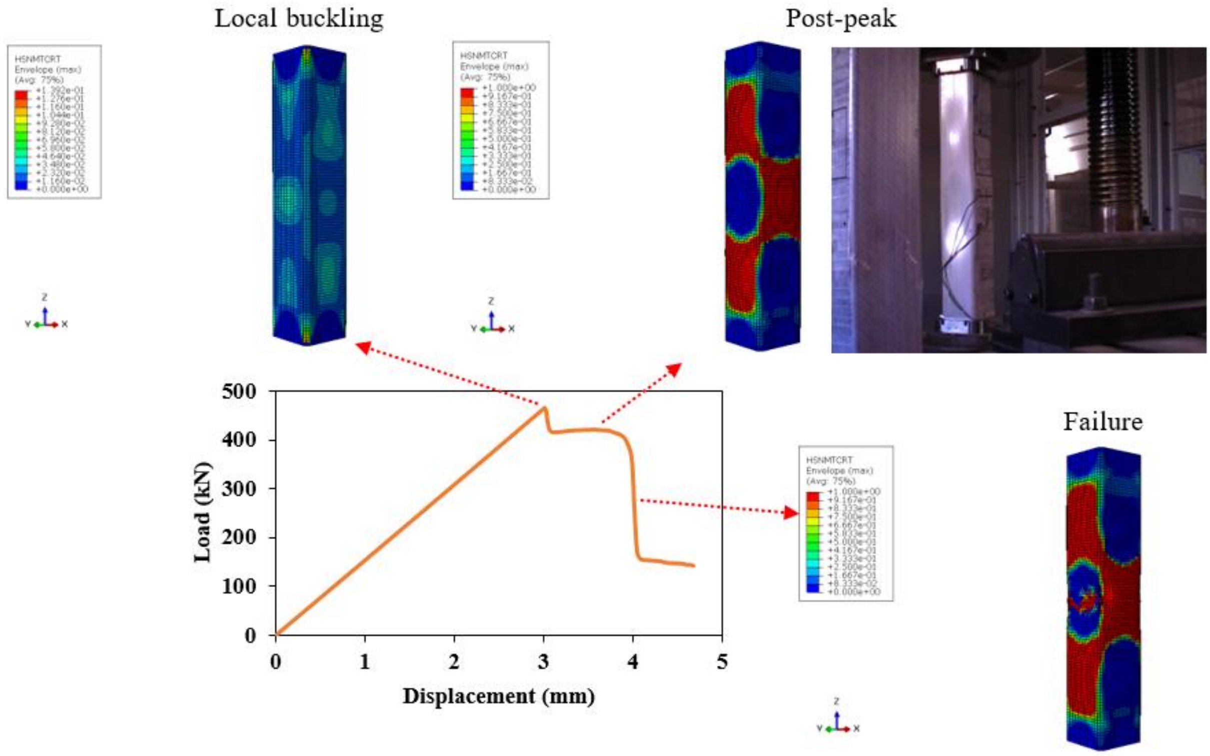
Local buckling
Post-peak
Failure
Load (kN)
Displacement (mm)
0
100
200
300
400
500
1
2
3
4
5

(c)

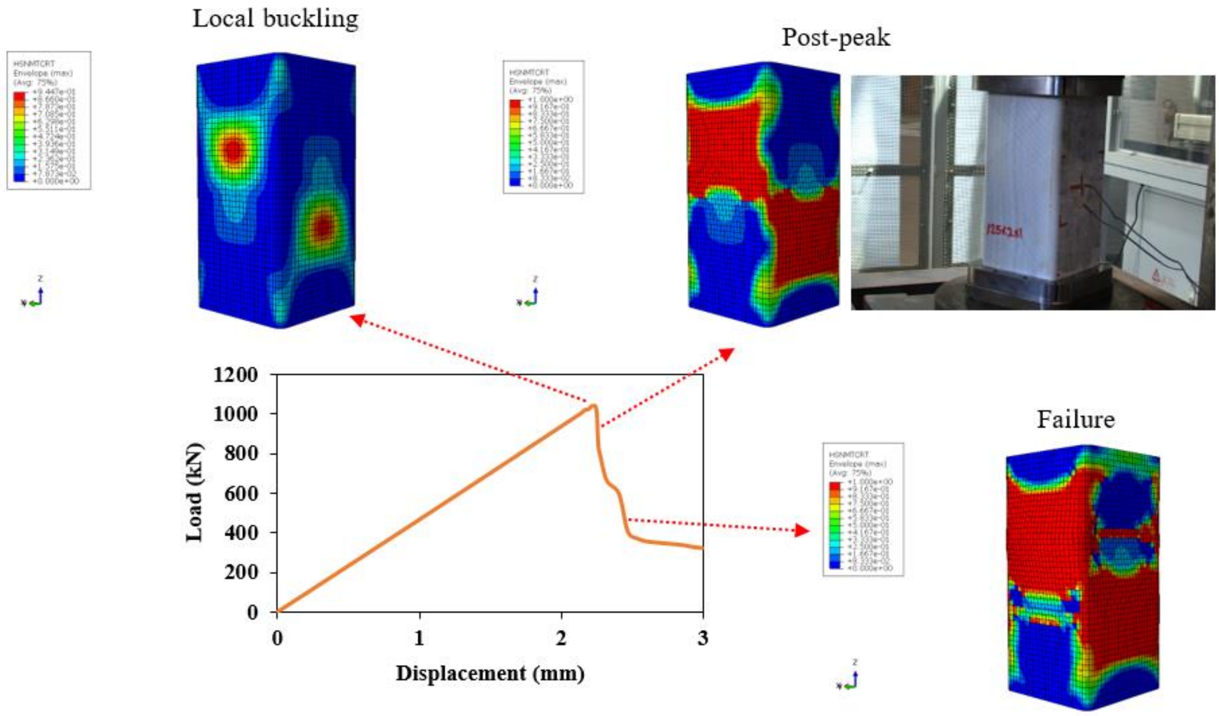
Local buckling
Post-peak
Failure
Load (kN)
Displacement (mm)
0
200
400
600
800
1000
1200
1
2
3

(d)

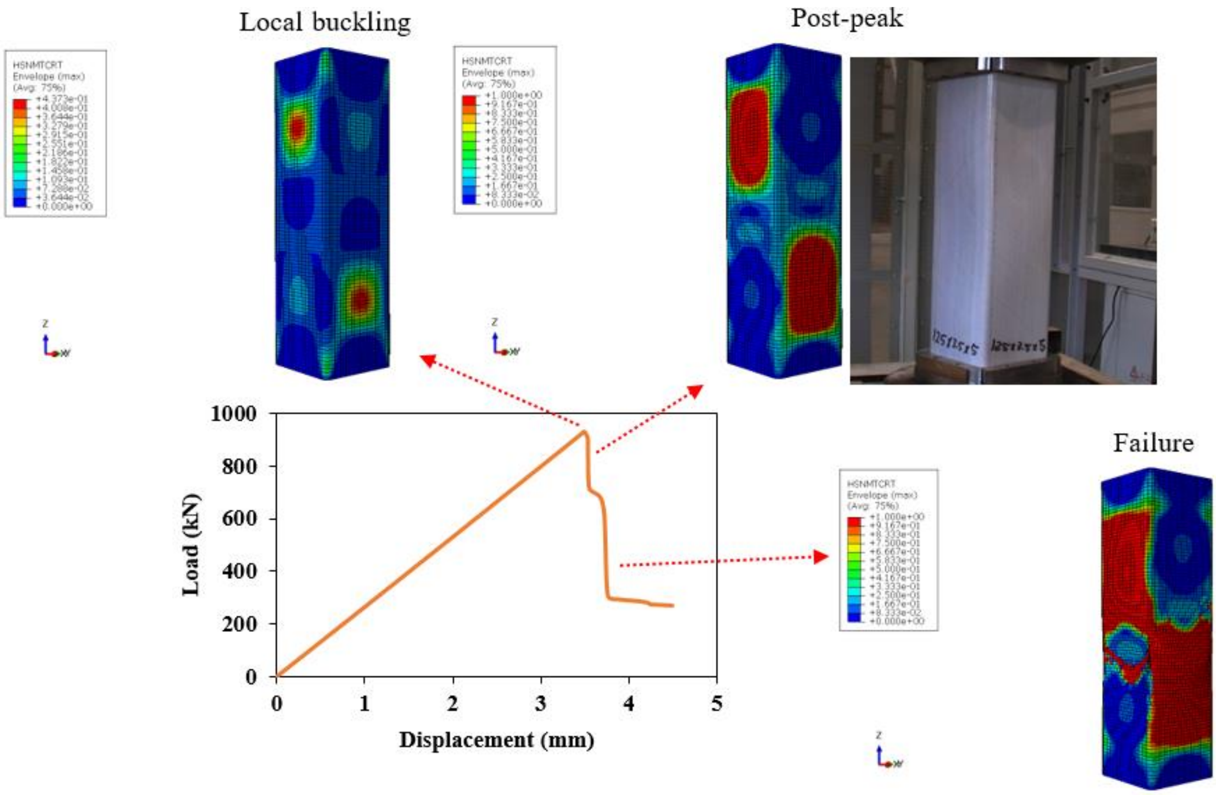

Local buckling
Post-peak
Failure
Load (kN)
Displacement (mm)

(e)

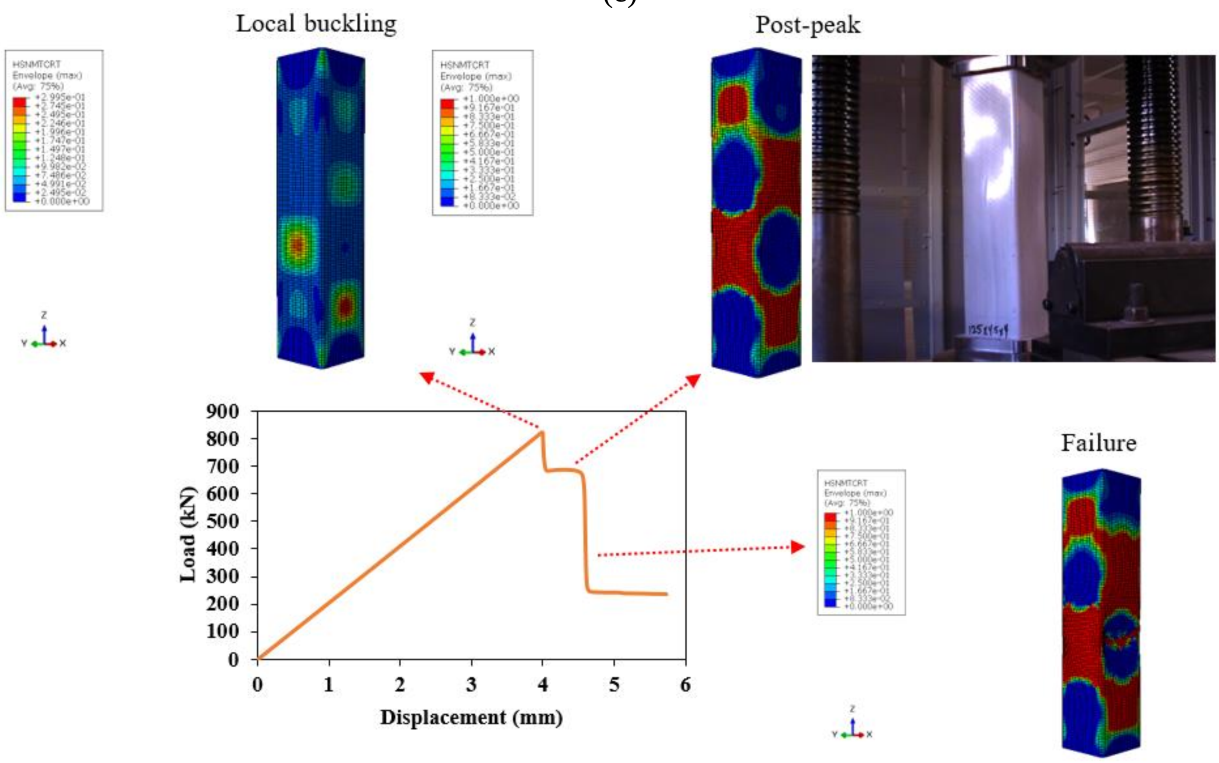

Local buckling
Post-peak
Failure
Load (kN)
Displacement (mm)

(f)

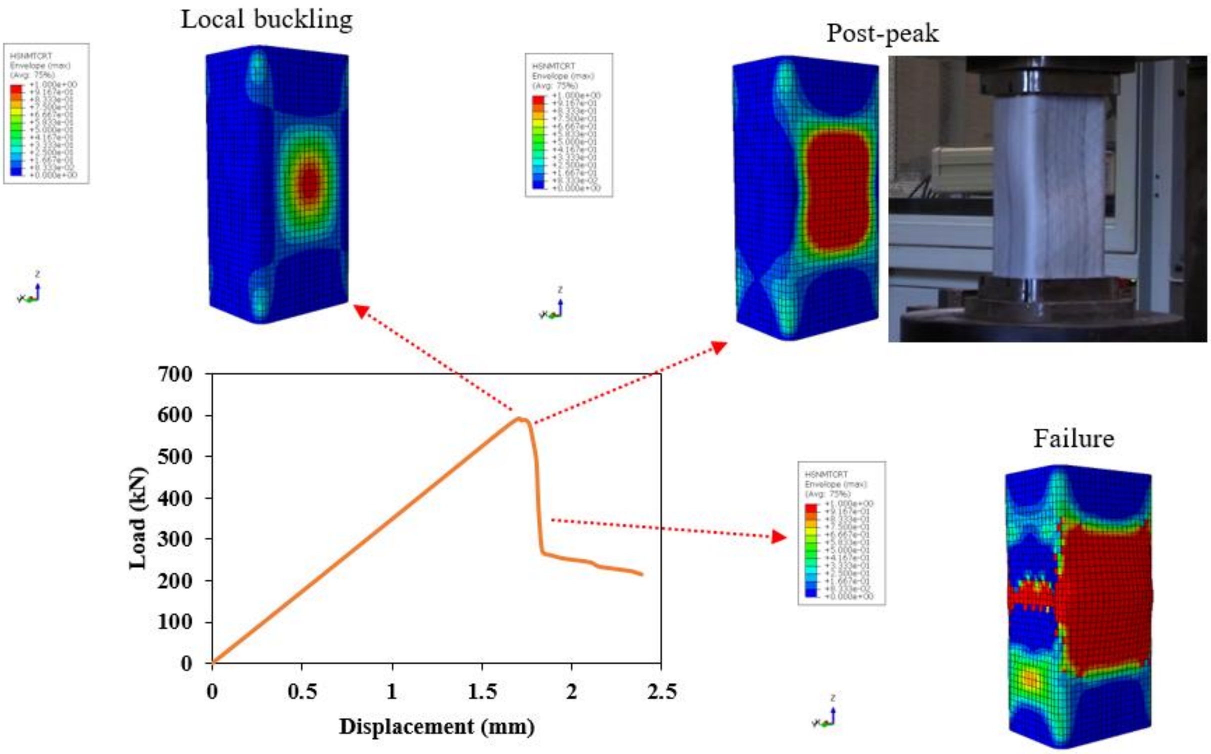

Local buckling
Post-peak
Failure
Load (kN)
Displacement (mm)

(g)

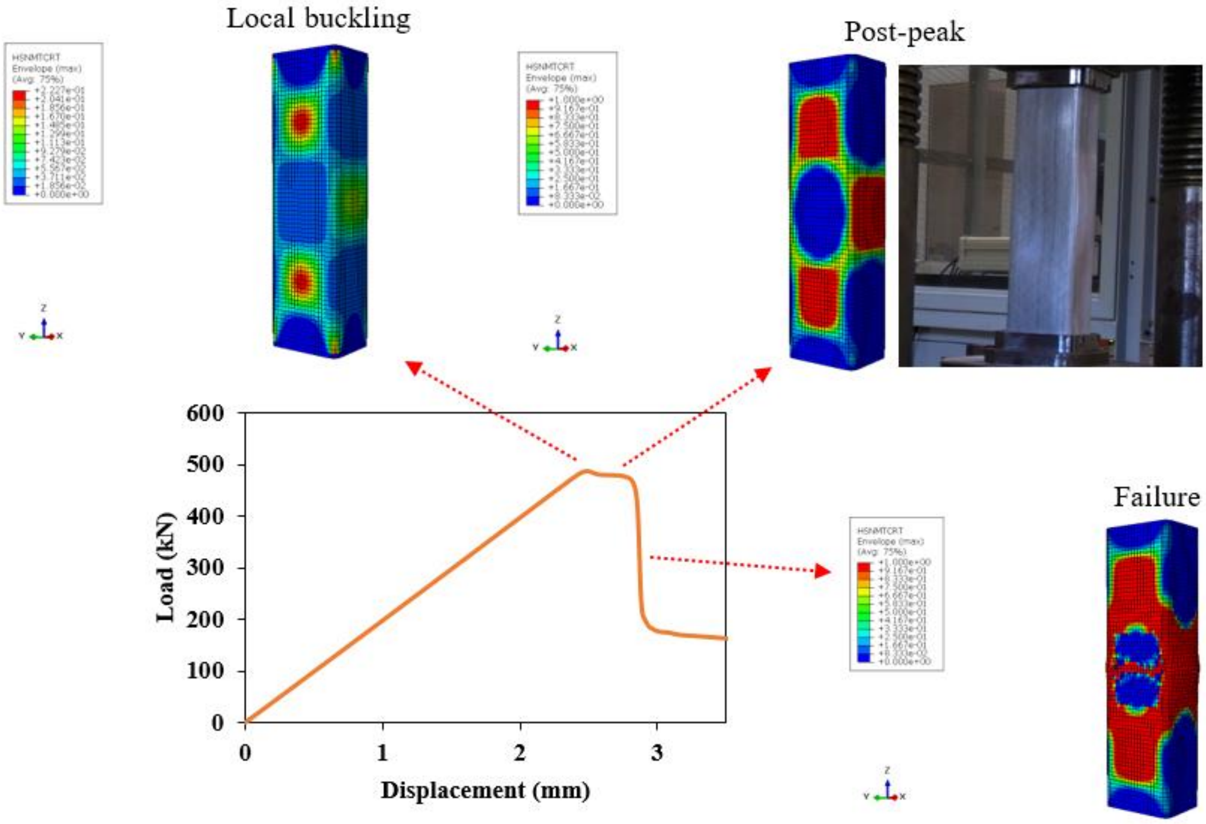

Local buckling
Post-peak
Failure
Load (kN)
Displacement (mm)

(h)

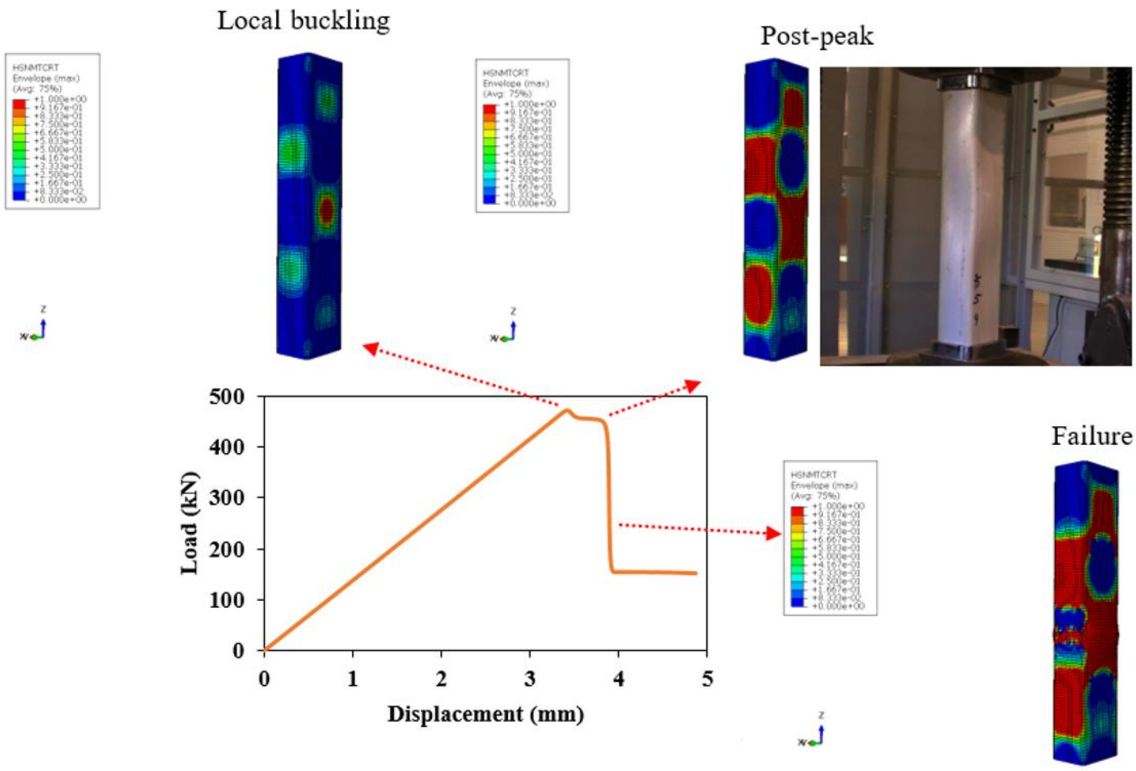

(i)

Fig. A. 5. Failure sequence in the hollow box pultruded FRP profiles (a) S-100×100×5.2 with L/D equals 2 (b) S-100×100×5.2 with L/D equals 3.5 (c) S-100×100×5.2 with L/D equals 5 (d) S-125×125×6.4 with L/D equals 2 (e) S-125×125×6.4 with L/D equals 3.5 (f) S-125×125×6.4 with L/D equals 5 (g) R-75×100×5.2 with L/D equals 2 (h) R-75×100×5.2 with L/D equals 3.5 and (i) R-75×100×5.2 with L/D equals 5.

Fig. A. 6 shows the experimental vs FEM failed hollow box pultruded FRP profiles. The shear output variable was used to reflect the experimentally observed delamination numerically.

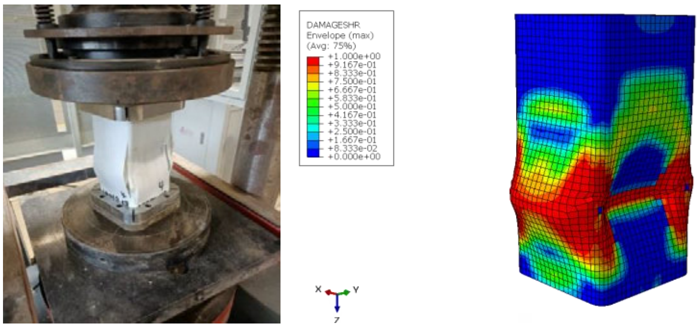

(a)

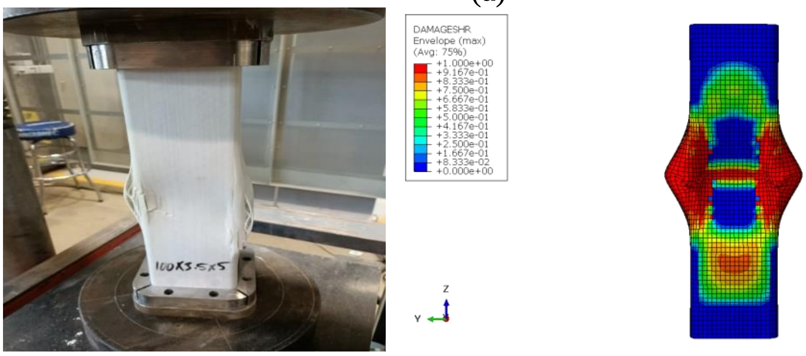

(b)

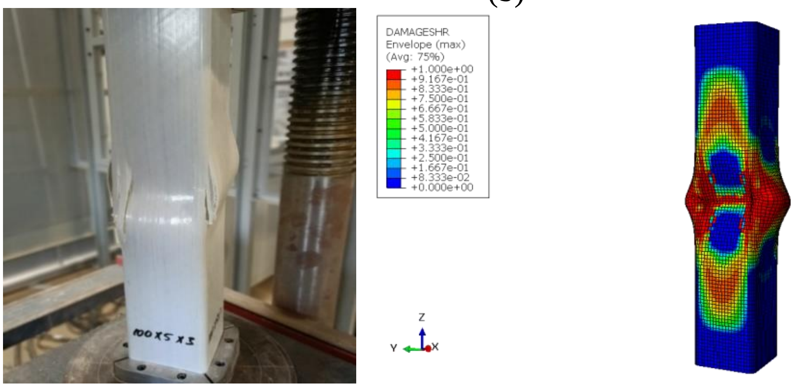

(c)

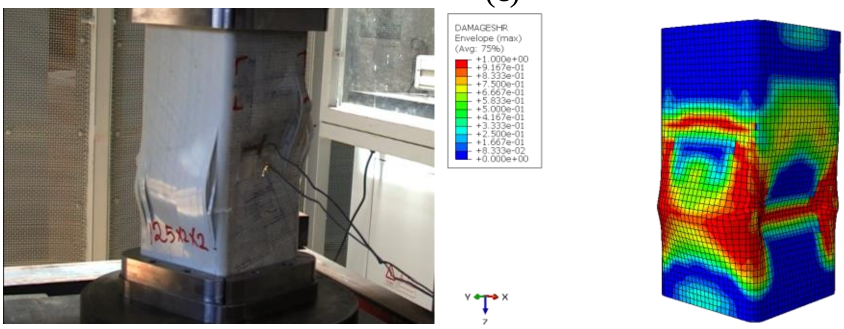

(d)

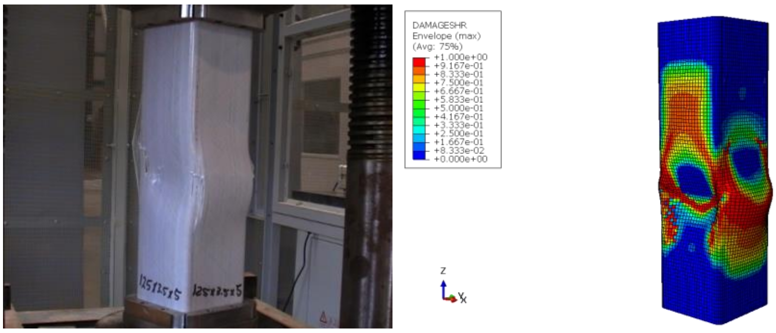
DAMAGESHR
Envelope (max)
(Avg: 75%)
+1.000e+00
+9.167e-01
+8.333e-01
+7.500e-01
+6.667e-01
+5.833e-01
+5.000e-01
+4.167e-01
+3.333e-01
+2.500e-01
+1.667e-01
+8.333e-02
+0.000e+00

(e)

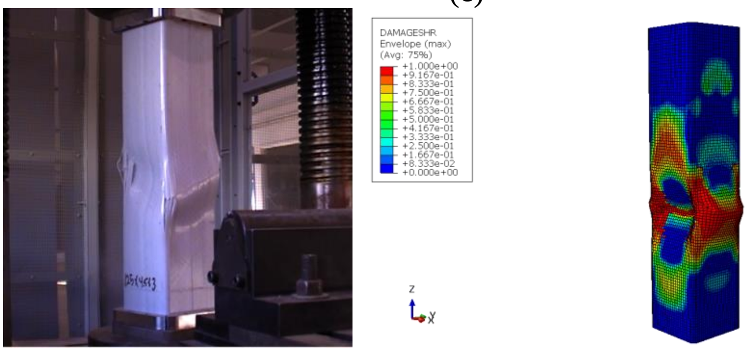
DAMAGESHR
Envelope (max)
(Avg: 75%)
+1.000e+00
+9.167e-01
+8.333e-01
+7.500e-01
+6.667e-01
+5.833e-01
+5.000e-01
+4.167e-01
+3.333e-01
+2.500e-01
+1.667e-01
+8.333e-02
+0.000e+00

(f)

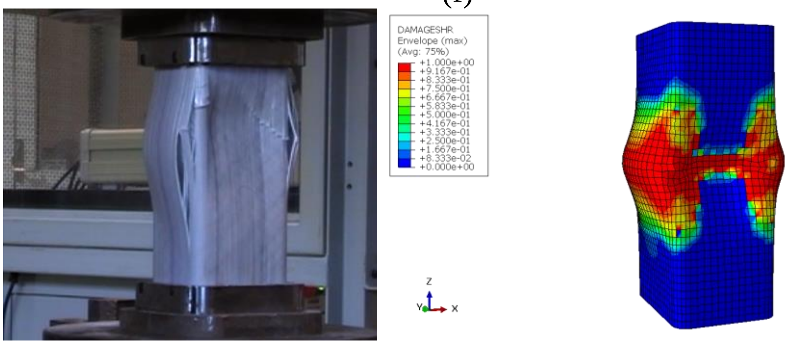
DAMAGESHR
Envelope (max)
(Avg: 75%)
+1.000e+00
+9.167e-01
+8.333e-01
+7.500e-01
+6.667e-01
+5.833e-01
+5.000e-01
+4.167e-01
+3.333e-01
+2.500e-01
+1.667e-01
+8.333e-02
+0.000e+00

(g)

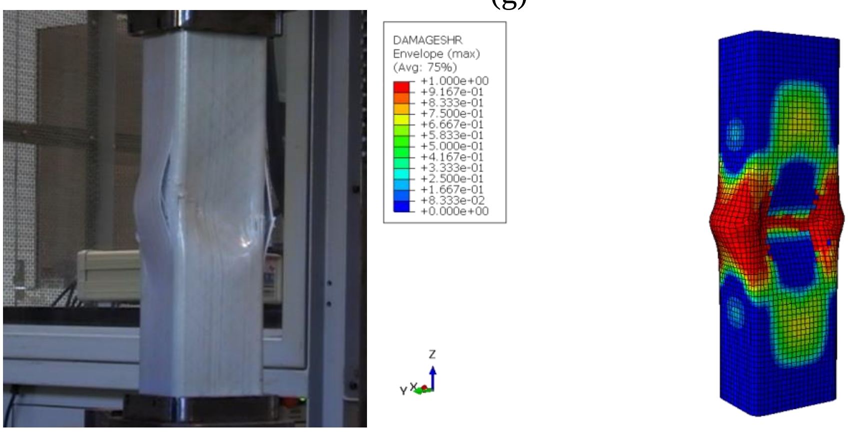
DAMAGESHR
Envelope (max)
(Avg: 75%)
+1.000e+00
+9.167e-01
+8.333e-01
+7.500e-01
+6.667e-01
+5.833e-01
+5.000e-01
+4.167e-01
+3.333e-01
+2.500e-01
+1.667e-01
+8.333e-02
+0.000e+00

(h)

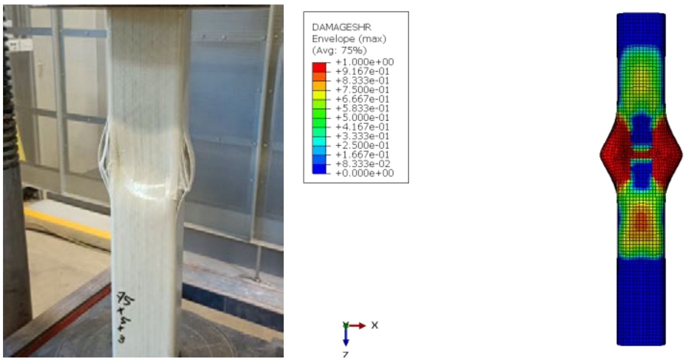

(i)

Fig. A. 6. FEM vs Experimental failed profiles (a) S-100×100×5.2 with L/D equals 2 (b) S-100×100×5.2 with L/D equals 3.5 (c) S-100×100×5.2 with L/D equals 5 (d) S-125×125×6.4 with L/D equals 2 (e) S-125×125×6.4 with L/D equals 3.5 (f) S-125×125×6.4 with L/D equals 5 (g) R-75×100×5.2 with L/D equals 2 (h) R-75×100×5.2 with L/D equals 3.5 and (i) R-75×100×5.2 with L/D equals 5.

Fig. A. 7 shows the strain energy and load values vs the axial shortening of the specimens. The local buckling and the localised release in the strain energy occur simultaneously in the hollow box profiles. Neither local buckling nor release in the strain energy occurred in the hollow circular profiles.

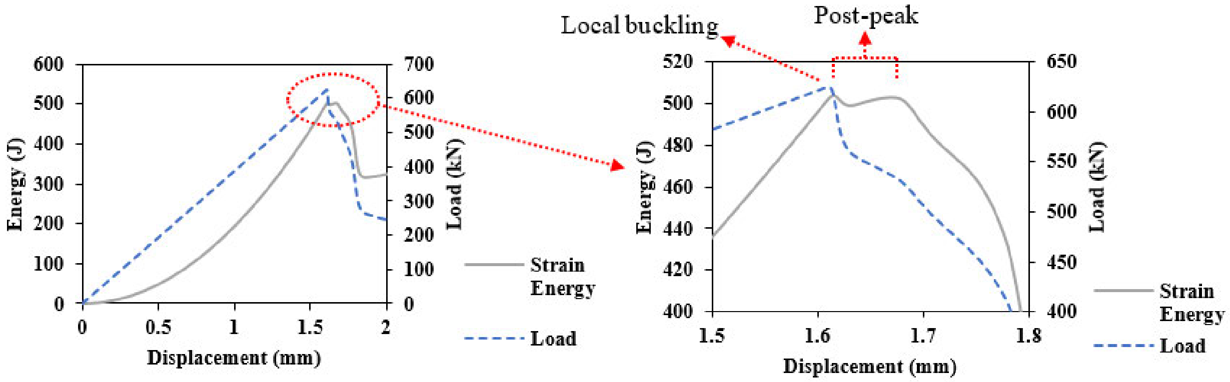

(a)

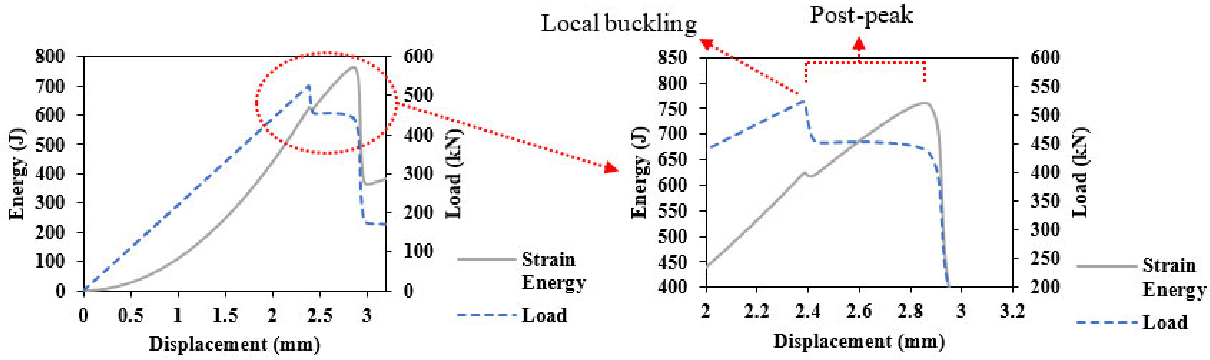

(b)

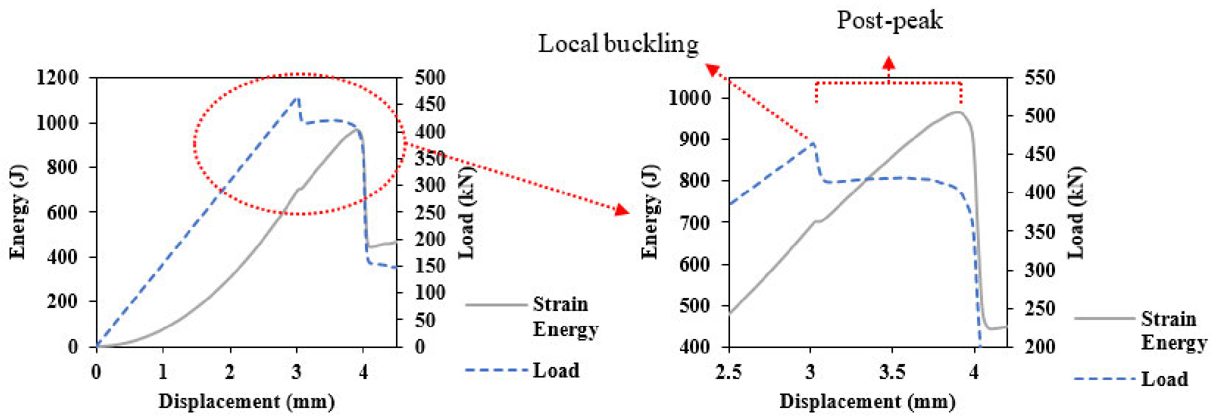

(c)

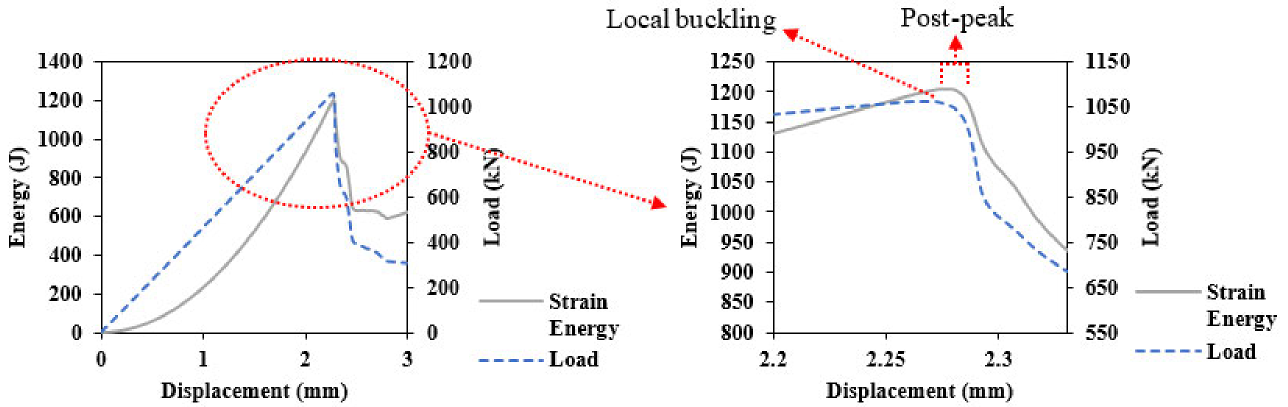
Local buckling
Post-peak
Energy (J)
Load (kN)
Displacement (mm)
Strain Energy
Load

(d)

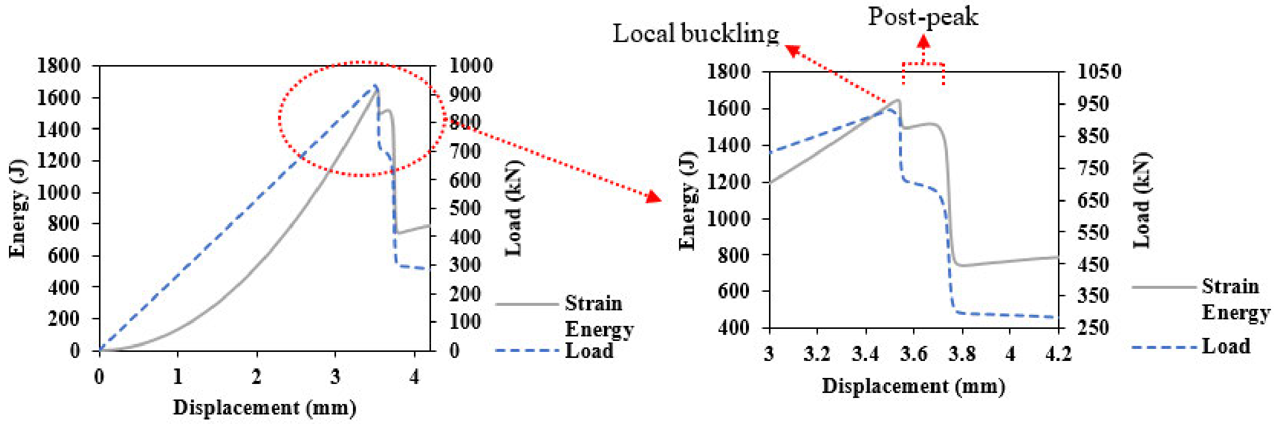
Local buckling
Post-peak
Energy (J)
Load (kN)
Displacement (mm)
Strain Energy
Load

(e)

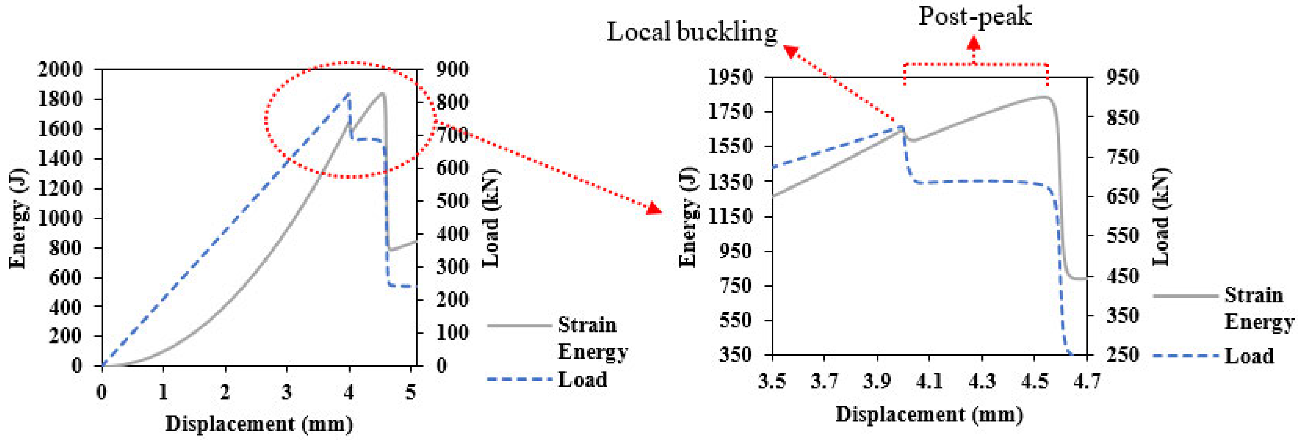
Local buckling
Post-peak
Energy (J)
Load (kN)
Displacement (mm)
Strain Energy
Load

(f)

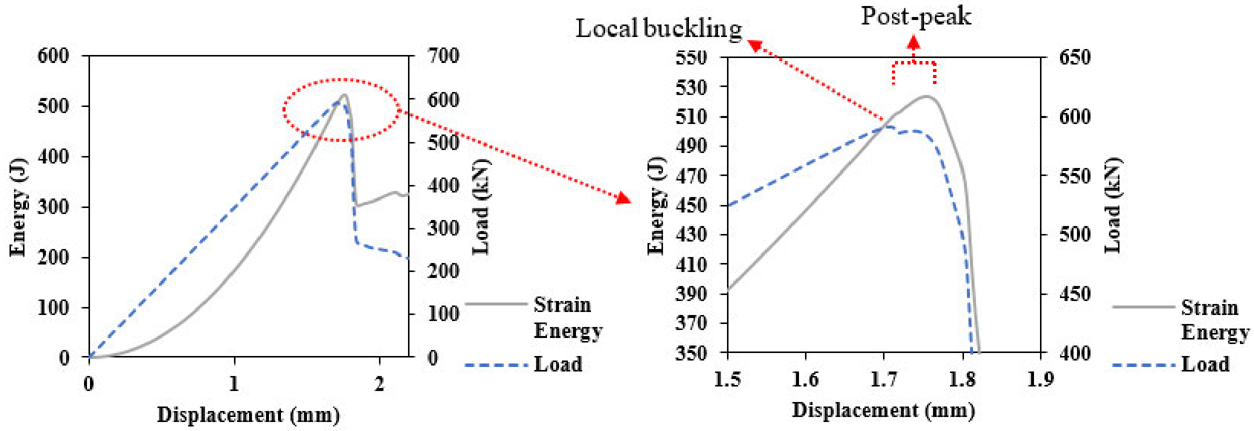
Local buckling
Post-peak
Energy (J)
Load (kN)
Displacement (mm)
Strain Energy
Load

(g)

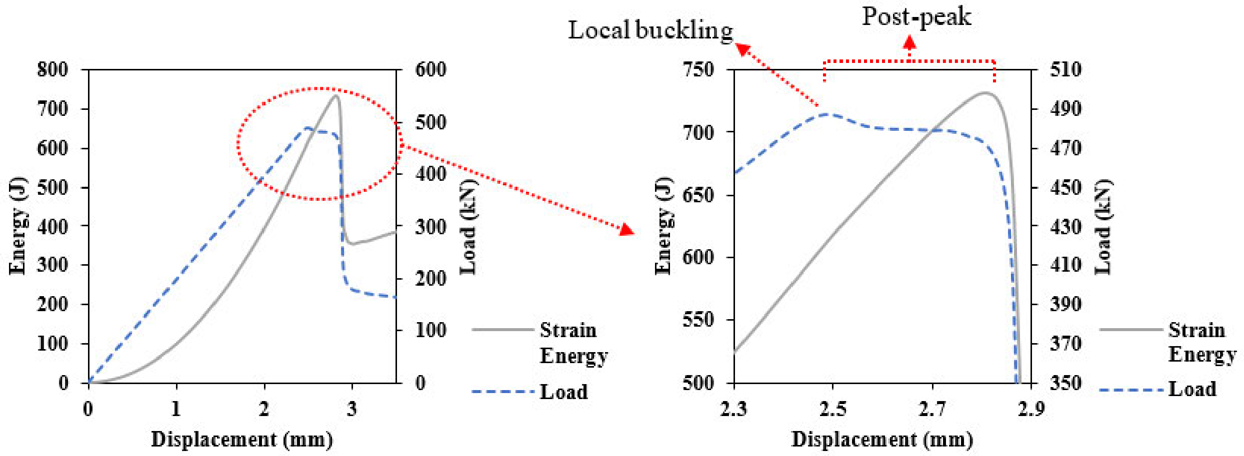
Local buckling
Post-peak
Energy (J)
Load (kN)
Displacement (mm)
Strain Energy
Load

(h)

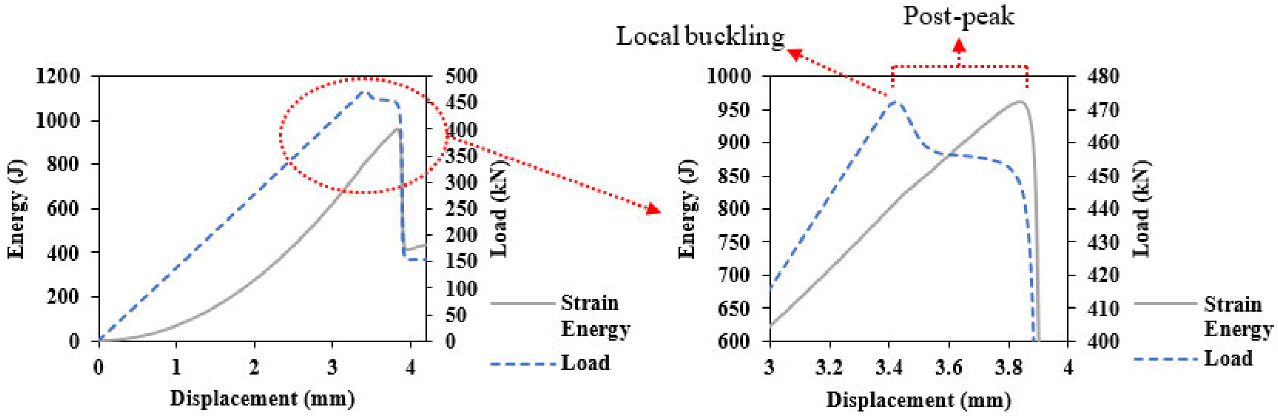
Local buckling
Post-peak
Energy (J)
Load (kN)
Displacement (mm)
Strain Energy
Load

(i)

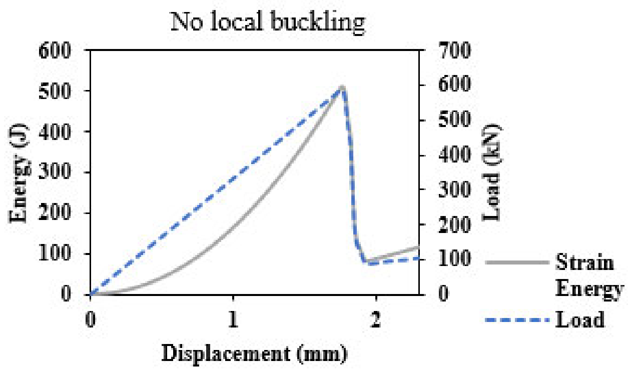

(j)

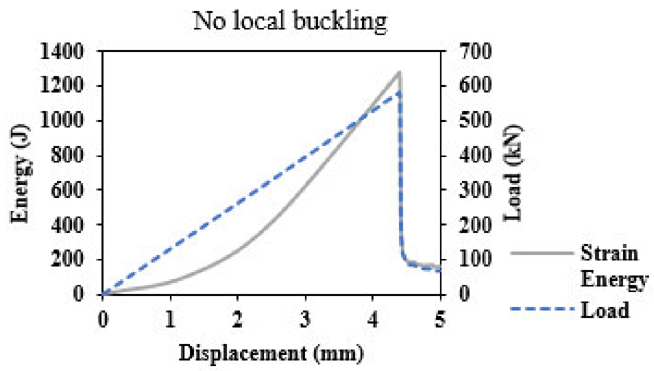

(k)

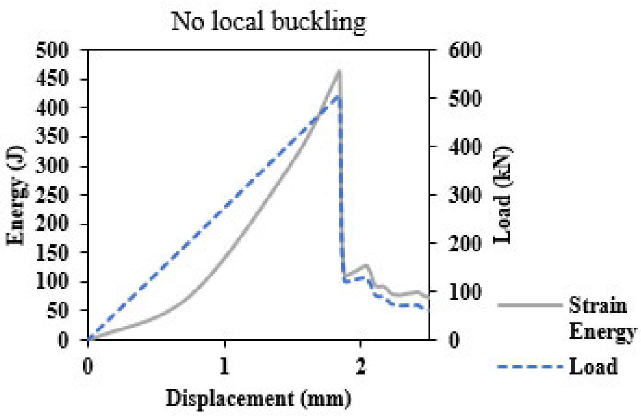

(l)

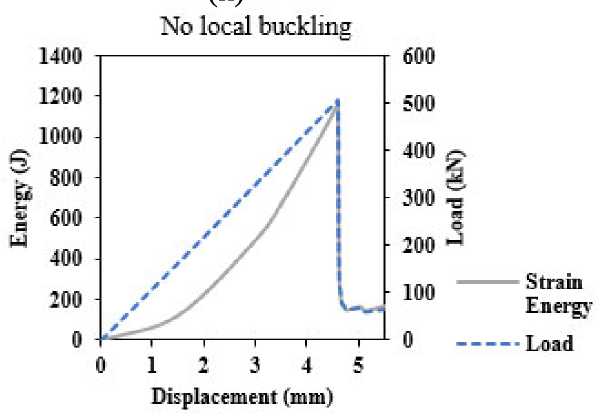

(m)

Fig. A. 7. Strain energy and load values vs the axial displacement of the hollow pultruded FRP profiles. (a) S-100×100×5.2 with L/D equals 2 (b) S-100×100×5.2 with L/D equals 3.5 (c) S-100×100×5.2 with L/D equals 5 (d) S-125×125×6.4 with L/D equals 2 (e) S-125×125×6.4 with L/D equals 3.5 (f) S-125×125×6.4 with L/D equals 5 (g) R-75×100×5.2 with L/D equals 2 (h) R-75×100×5.2 with L/D equals 3.5 (i) R-75×100×5.2 with L/D equals 5 (j) C1-89×6 with L/D equals 2 (k) C1-89×6 with L/D equals 5 (l) C2-89×6 with L/D equals 2 and (m) C2-89×6 with L/D equals 5.

Fig. A. 8 shows the damage index and load vs axial shortening in the specimens. The load-bearing capacity is a function of the damage index of the specimen.

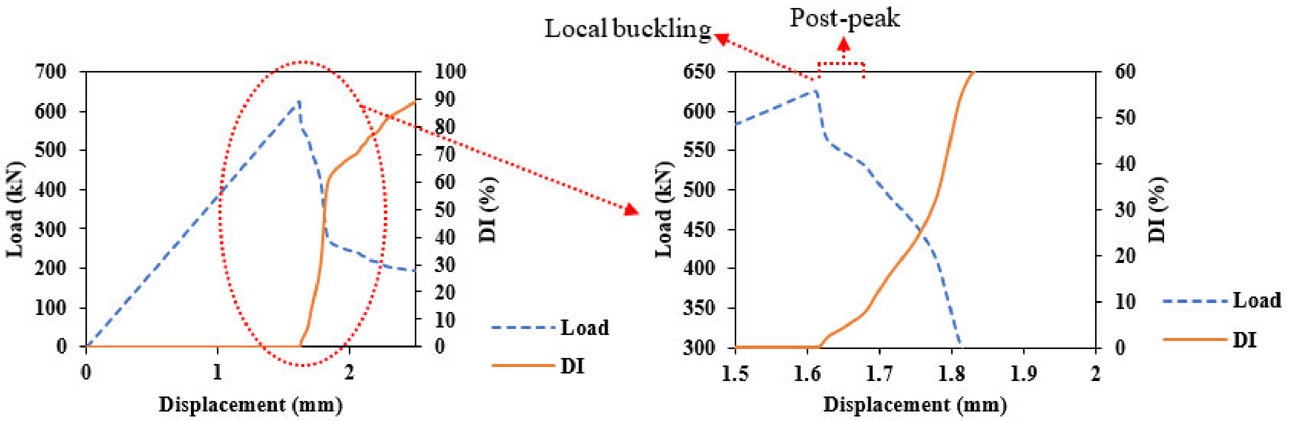

(a)

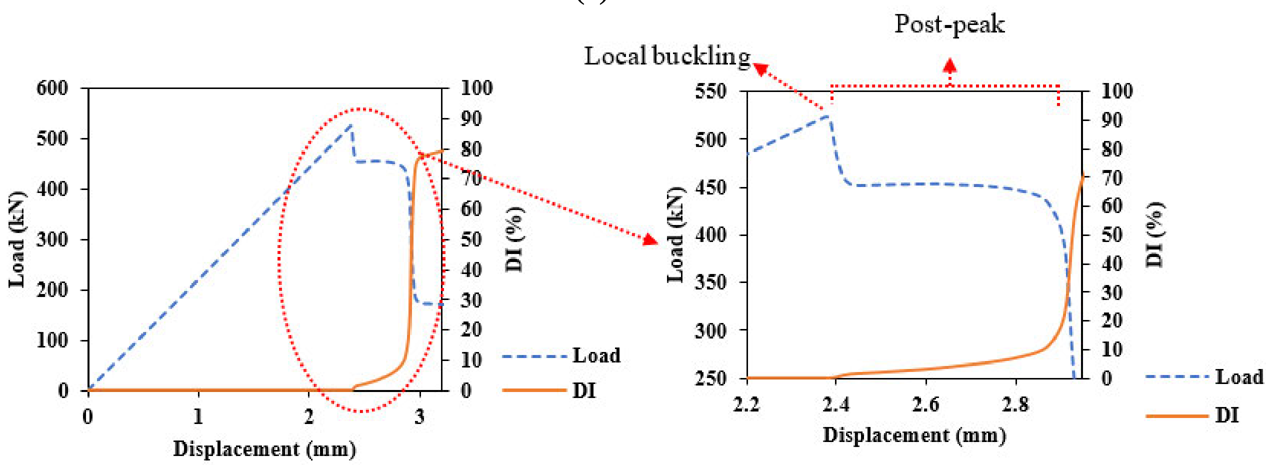

(b)

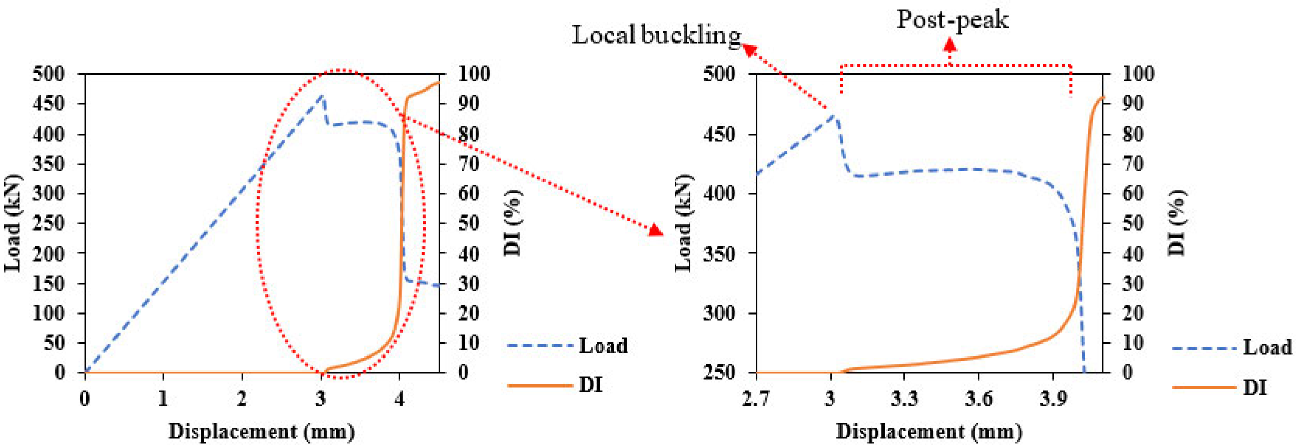

(c)

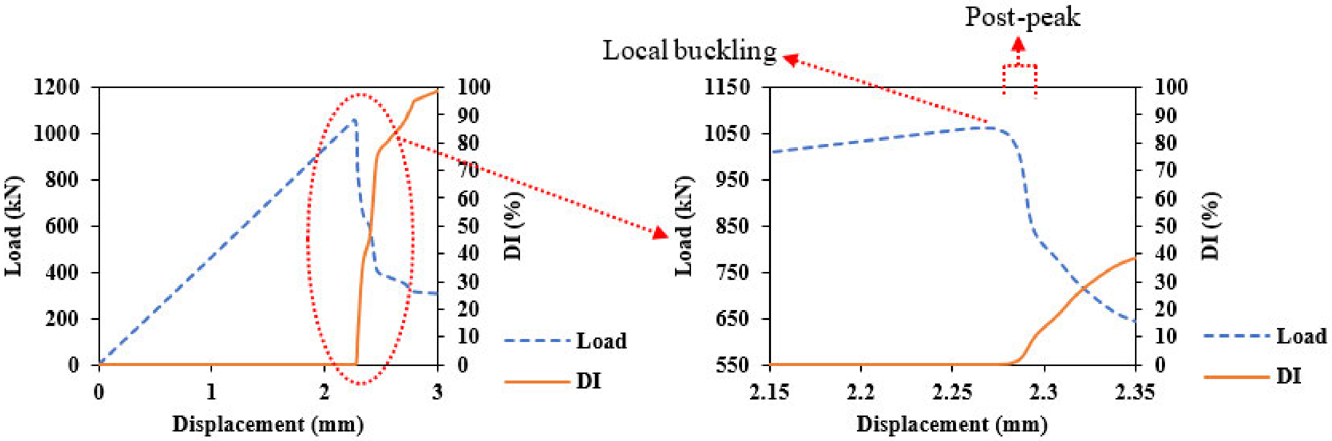
Local buckling
Post-peak
Load (kN)
DI (%)
Displacement (mm)
Load
DI
1200
1000
800
600
400
200
0
100
90
80
70
60
50
40
30
20
10
0
1
2
3
1150
1050
950
850
750
650
550
2.15
2.2
2.25
2.3
2.35

(d)

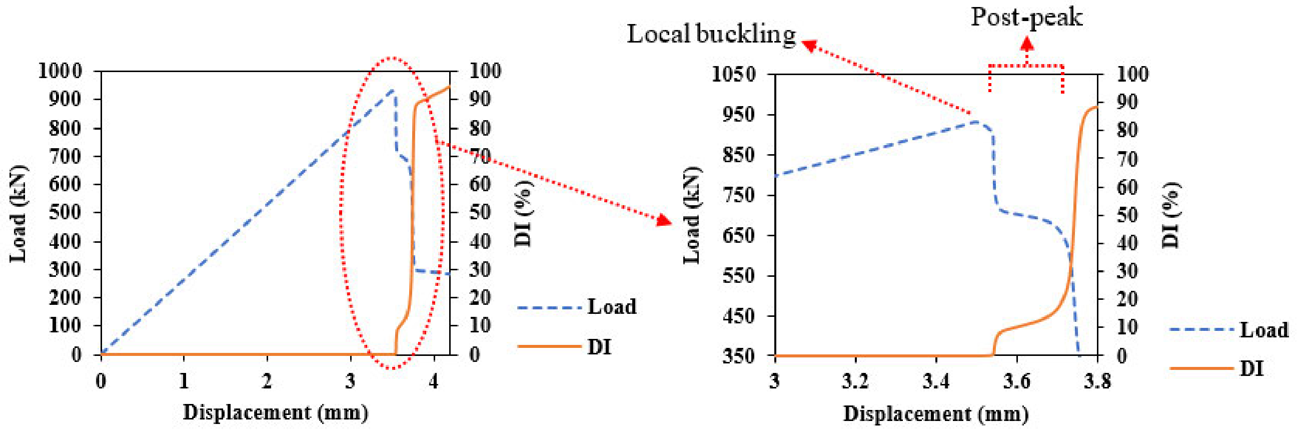
Local buckling
Post-peak
Load (kN)
DI (%)
Displacement (mm)
Load
DI
1000
900
800
700
600
500
400
300
200
100
0
1
2
3
4
1050
950
850
750
650
550
450
350
3
3.2
3.4
3.6
3.8

(e)

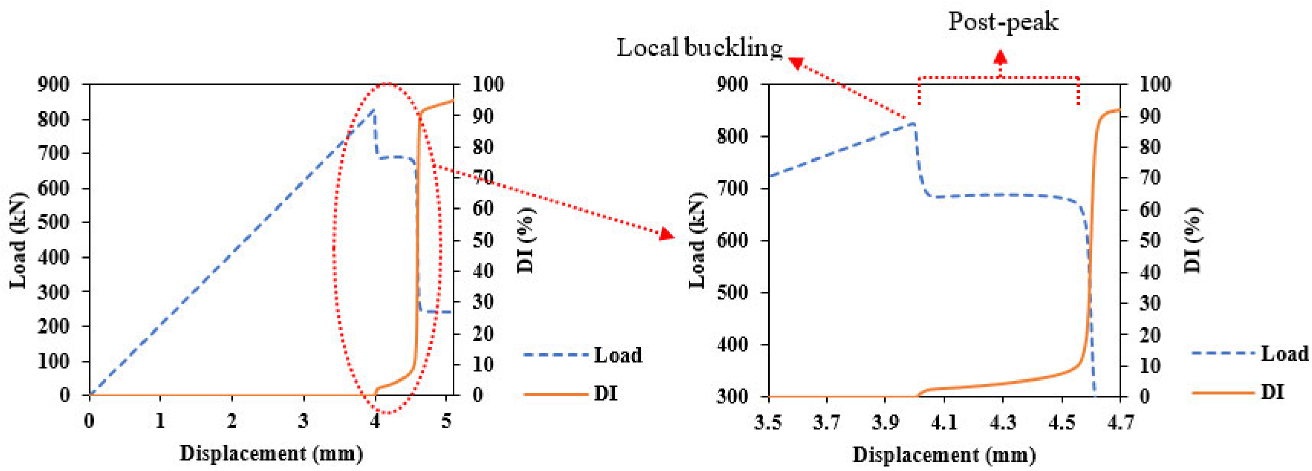
Local buckling
Post-peak
Load (kN)
DI (%)
Displacement (mm)
Load
DI
900
800
700
600
500
400
300
200
100
0
1
2
3
4
5
3.5
3.7
3.9
4.1
4.3
4.5
4.7

(f)

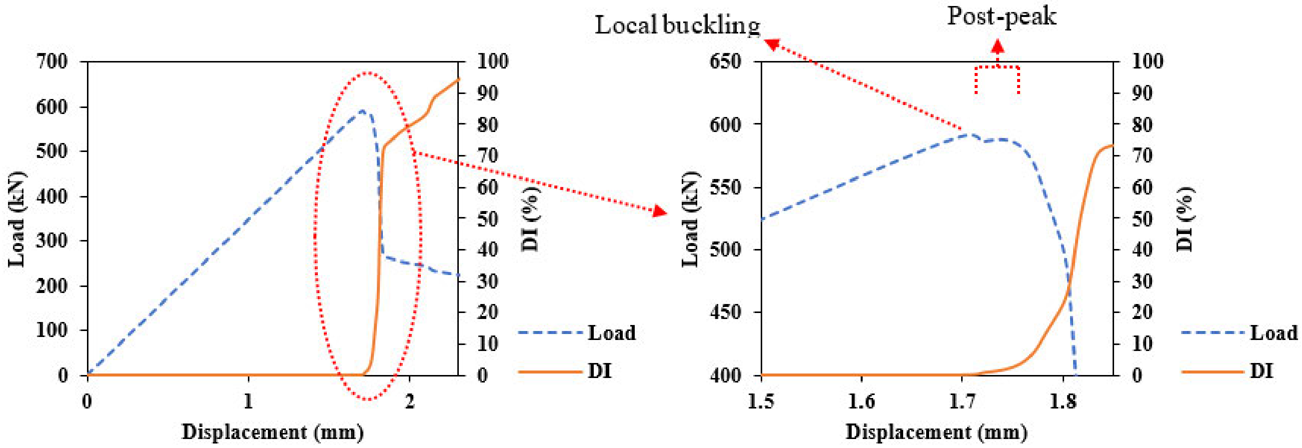
Local buckling
Post-peak
Load (kN)
DI (%)
Displacement (mm)
Load
DI

(g)

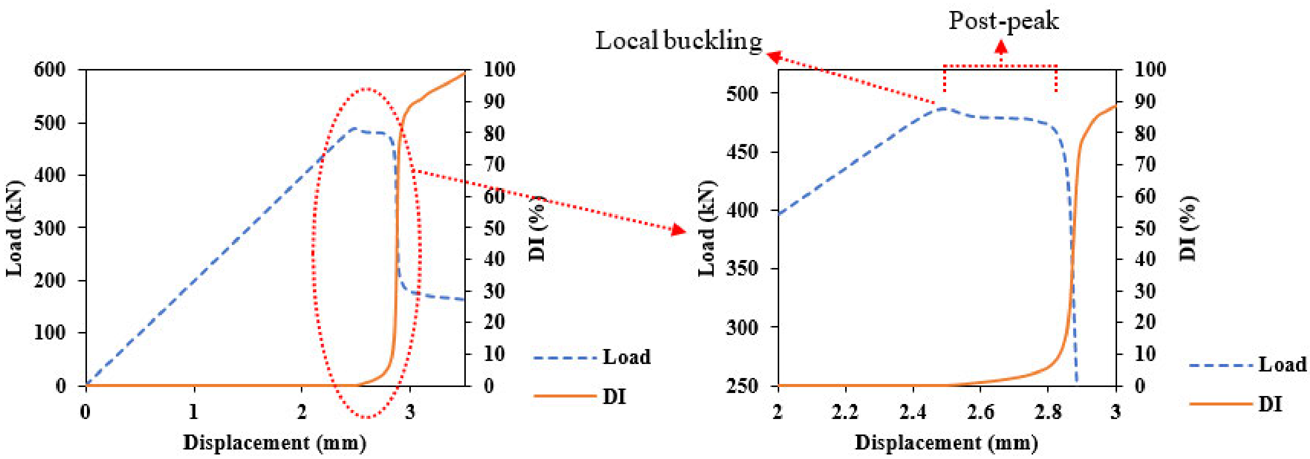
Local buckling
Post-peak
Load (kN)
DI (%)
Displacement (mm)
Load
DI

(h)

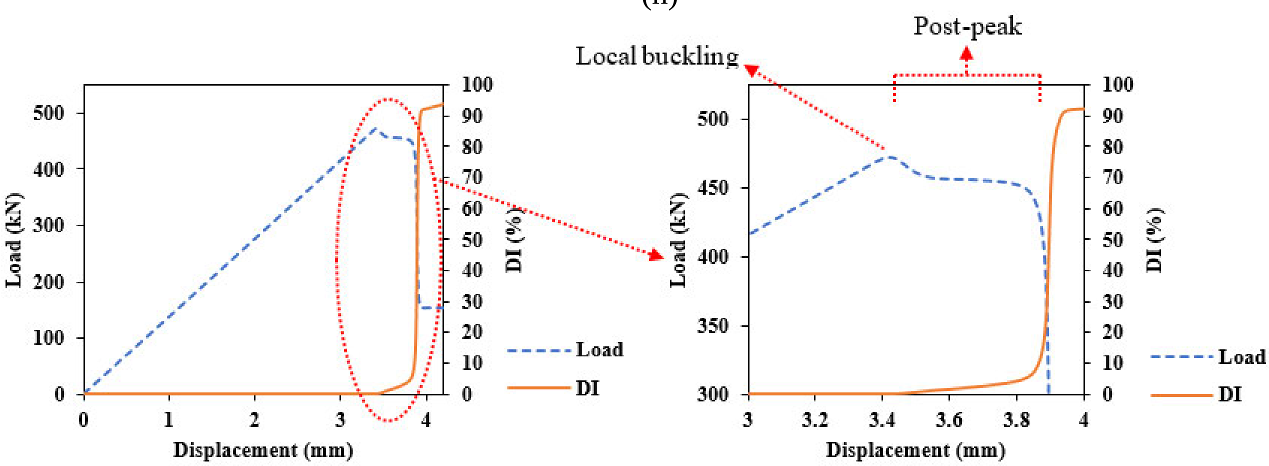
Local buckling
Post-peak
Load (kN)
DI (%)
Displacement (mm)
Load
DI

(i)

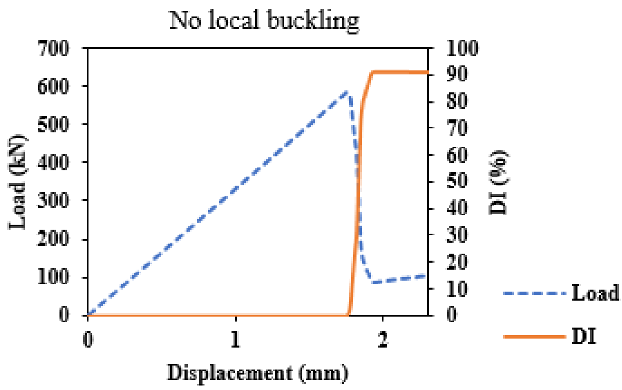

(j)

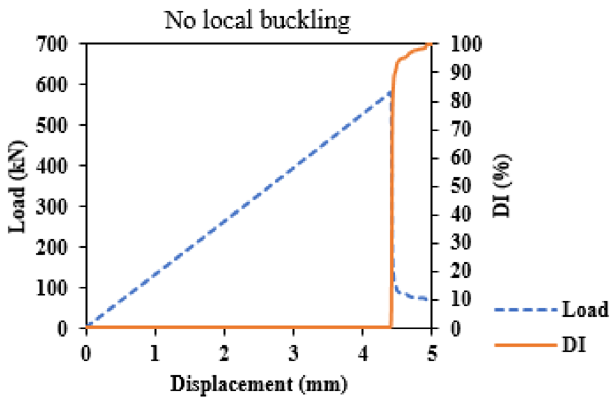

(k)

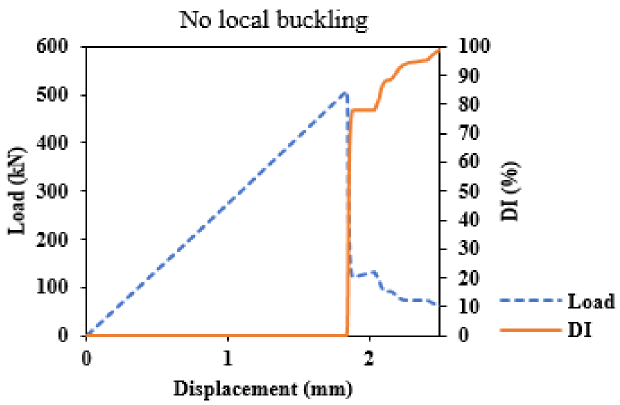

(l)

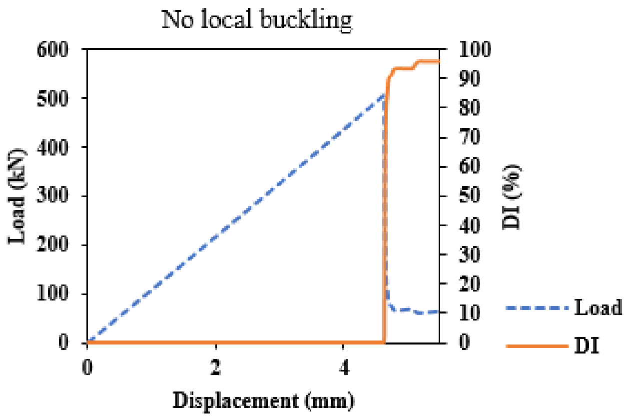

(m)

Fig. A. 8. DI and load vs the axial displacement of the hollow pultruded FRP profiles (a) S-100×100×5.2 with L/D equals 2 (b) S-100×100×5.2 with L/D equals 3.5 (c) S-100×100×5.2 with L/D equals 5 (d) S-125×125×6.4 with L/D equals 2 (e) S-125×125×6.4 with L/D equals 3.5 (f) S-125×125×6.4 with L/D equals 5 (g) R-75×100×5.2 with L/D equals 2 (h) R-75×100×5.2 with L/D equals 3.5 (i) R-75×100×5.2 with L/D equals 5 (j) C1-89×6 with L/D equals 2 (k) C1-89×6 with L/D equals 5 (l) C2-89×6 with L/D equals 2 and (m) C2-89×6 with L/D equals 5.

Fig. A. 9 shows the load-displacement curves of the hollow box pultruded FRP profiles with various L/D ratios. As the profile length is increasing, the axial stiffness is decreased. The profiles capability to withstand loads at the post-peak zone is increasing when the L/D ratio is increased.

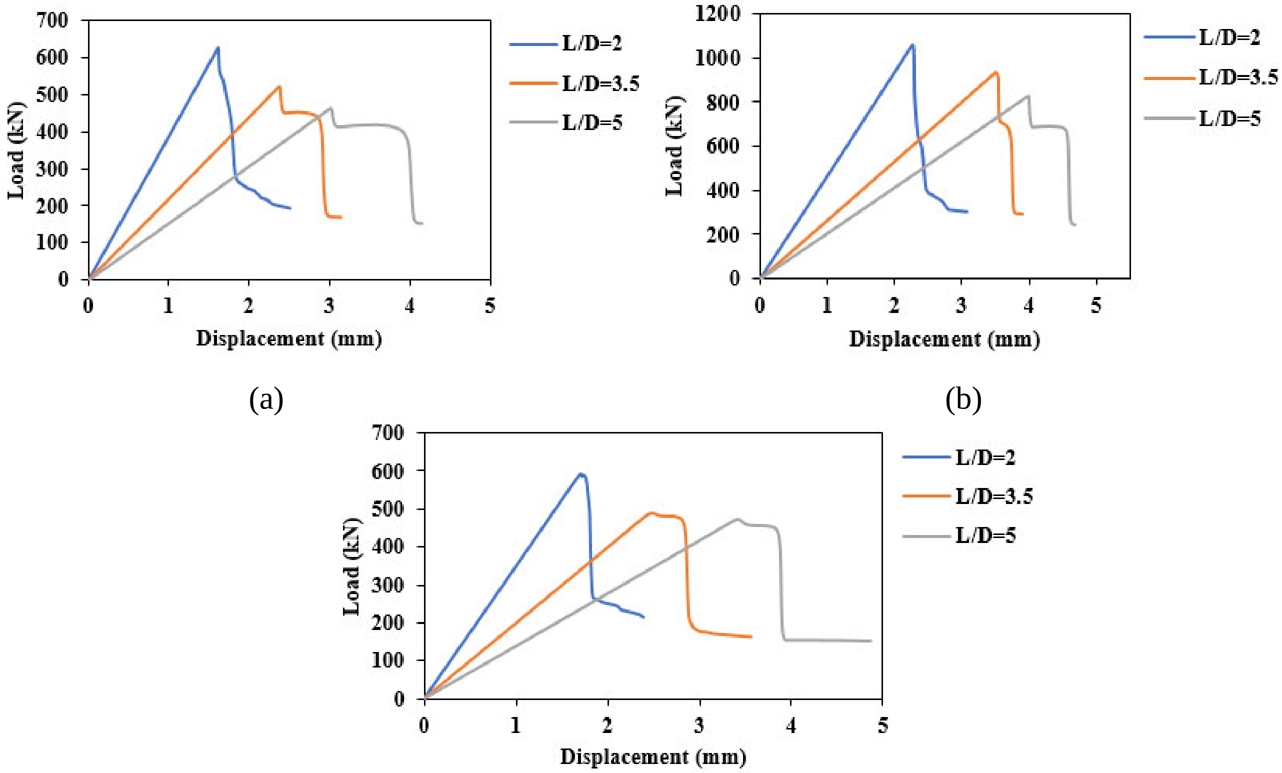

(a) (b)

(c)

Fig. A. 9. Load-displacement curves for various L/D ratios (a) S-100×100×5.2 (b) S-125×125×6.4 and (c) R-75×100×5.2.

Fig. A. 10 shows the normalised strain energy-time curves of the hollow box pultruded FRP profiles with various L/D ratios. As the profile length is increasing, the normalised strain energy at the buckling point is decreased since it is being stored in a higher number of localised waves. Thus, the post-peak zone will be visible because the damage evolution criteria just after the local buckling point need more strain energy to be met.

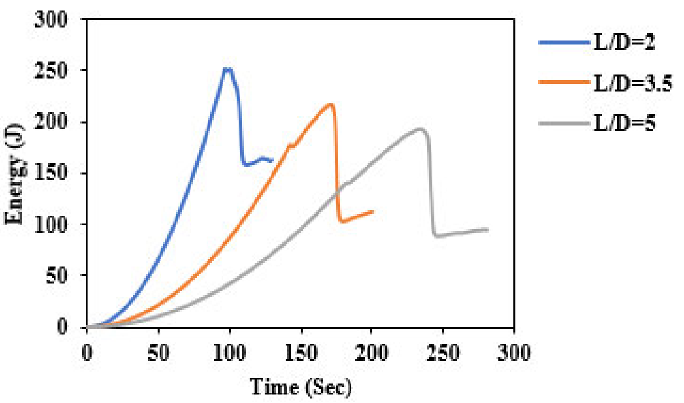

(a)

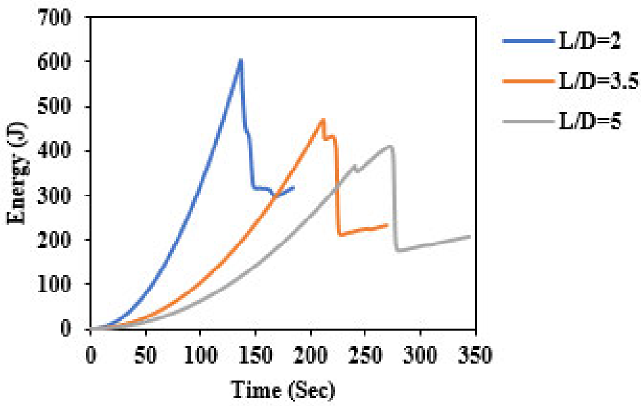

(b)

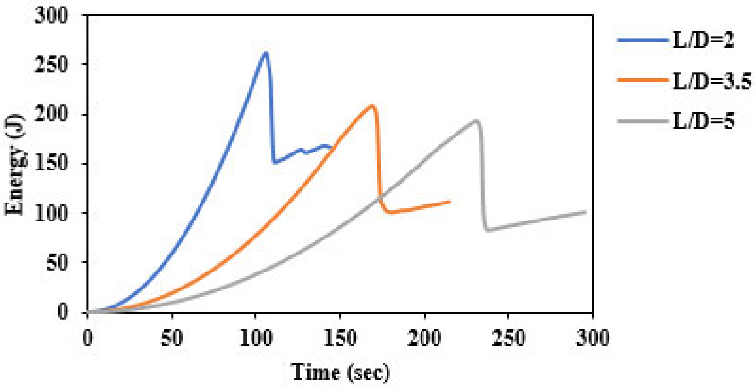

(c)

Fig. A. 10. Normalised strain energy vs time for each L/D ratio for hollow box pultruded FRP profiles (a) S-100×100×5.2 (b) S-125×125×6.4 and (c) R-75×100×5.2.

Fig. A. 11 shows the density of each failure mode of the constituents in the hollow box pultruded FRP profiles with various L/D ratios. The number of the fibres-related failed elements remains constant when L/D ratio is increased. However, the number of matrix-related failed elements is increasing when L/D ratio is increased, which refers to the increase in the delamination zones.

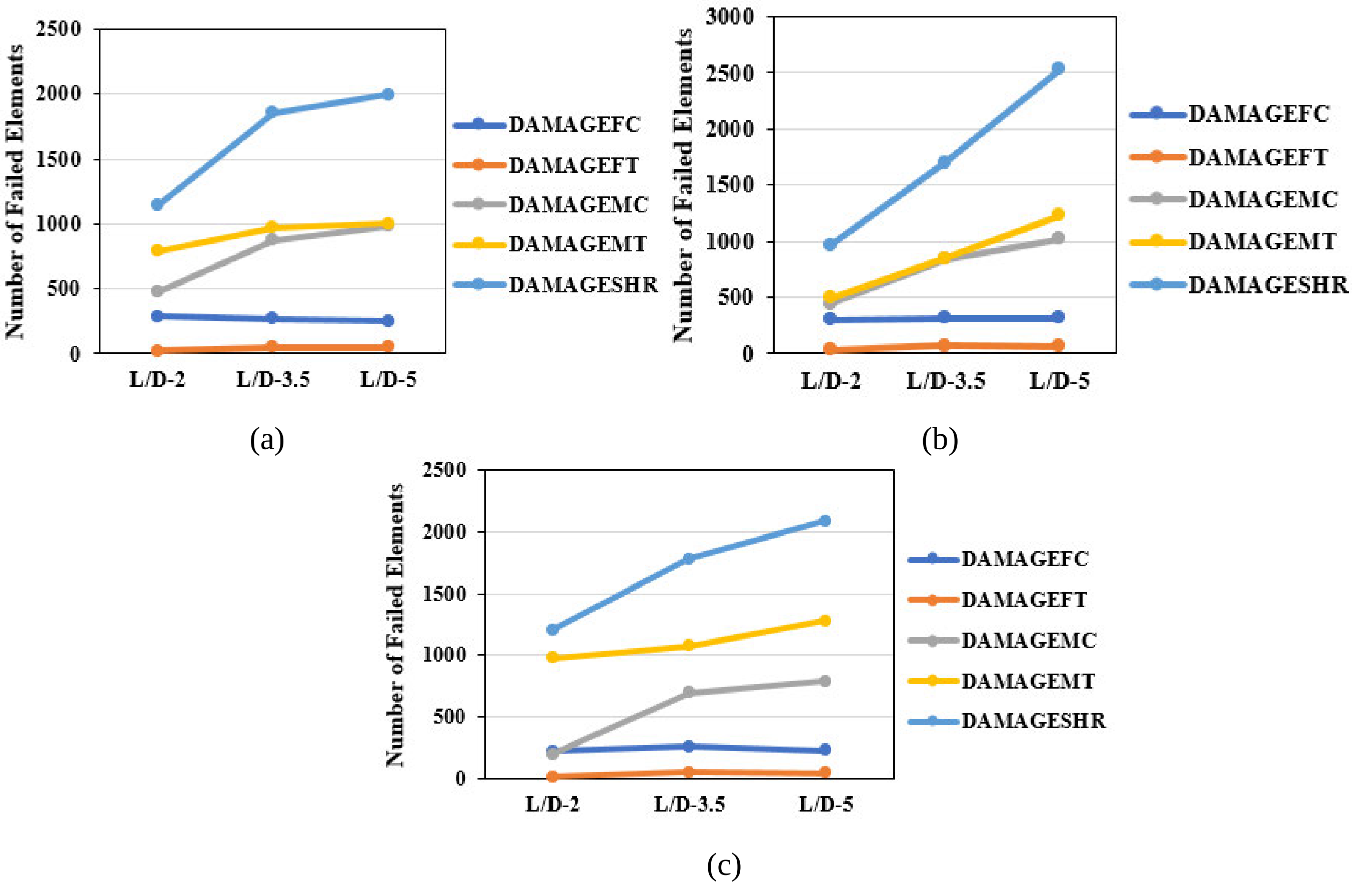

Fig. A. 11. Density of failure modes vs L/D ratio for hollow box pultruded FRP profiles (a) S-100×100×5.2 (b) S-125×125×6.4 and (c) R-75×100×5.2.

Fig. A. 12 shows the load-displacement curves of the hollow circular pultruded FRP profiles with various L/D ratios. As the profile length is increasing, the axial stiffness is decreased; however, the strength remains constant.

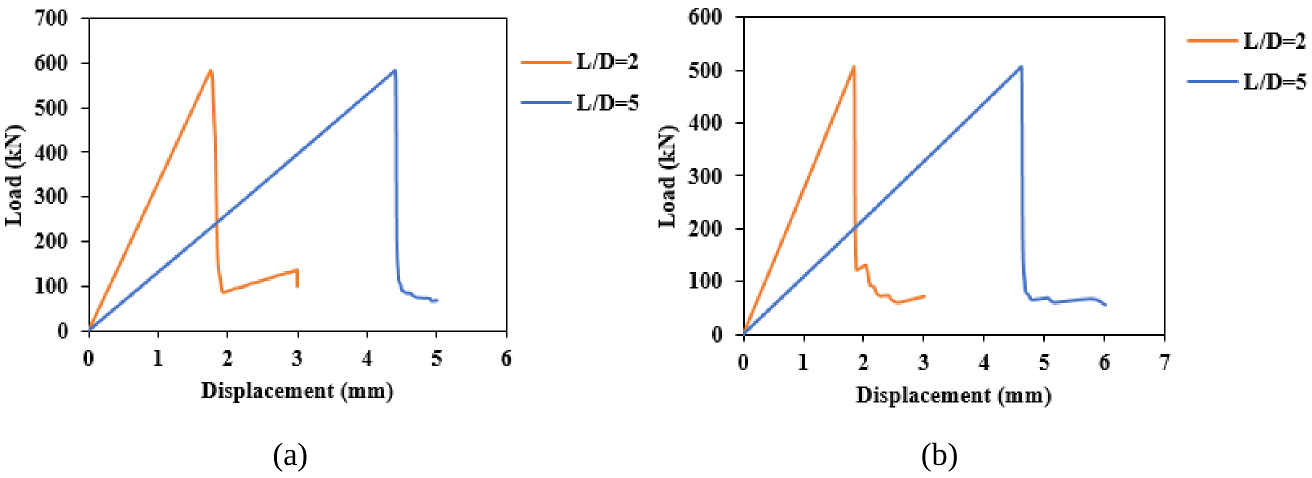

Fig. A. 12. Load-displacement curves for various L/D ratios (a) C1-89×6 and (b) C2-89×6.

Fig. A. 13 shows the normalised strain energy-time curves of the hollow circular pultruded FRP profiles with various L/D ratios. The normalised strain energy remains constant when changing the profile length, which indicates that the failure zone is constant (profile ends) across all L/D ratios.

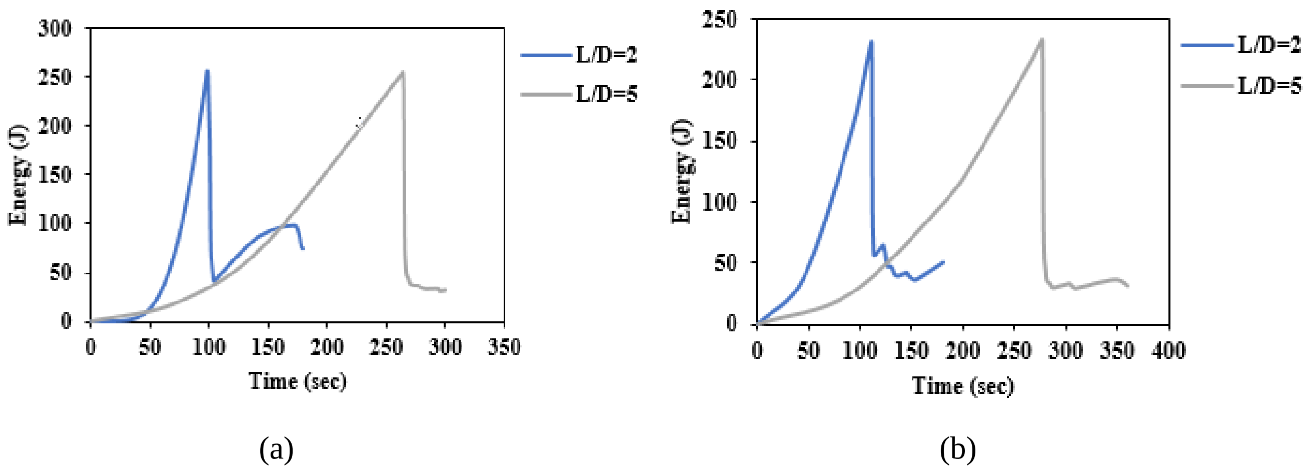

Fig. A. 13. Normalised strain energy vs time for each L/D ratio for hollow circular pultruded FRP profiles (a) C1-89×6 and (b) C2-89×6.

Fig. A. 14 shows the density of each failure mode of the constituents in the hollow circular pultruded FRP profiles with various L/D ratios. The number of the fibres-related and matrix-related failed elements remains nearly constant when L/D ratio is increased, which indicates that the failure zone is constant (profile ends) across all L/D ratios.

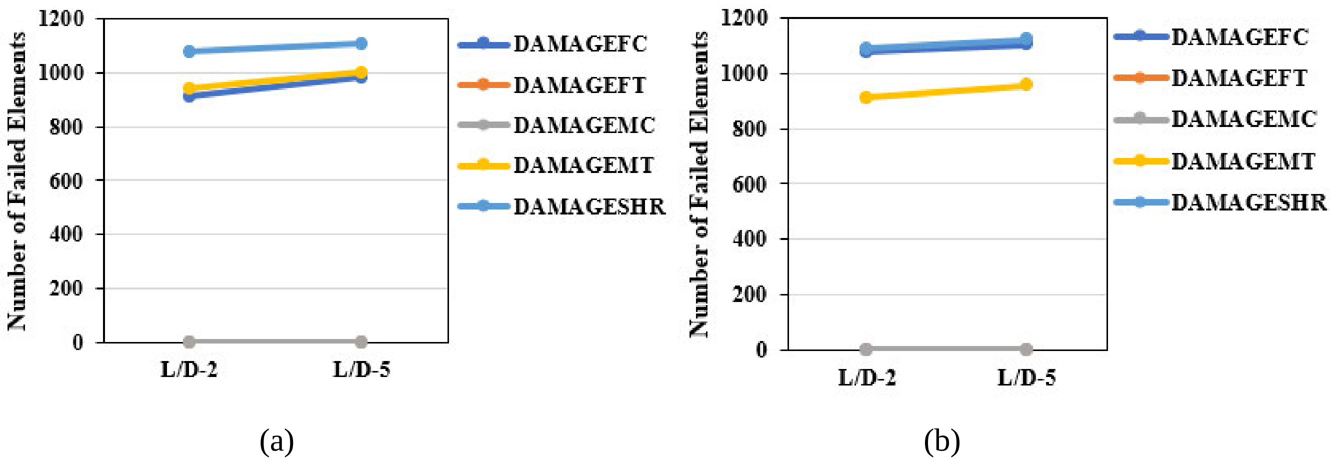

Fig. A. 14. Density of failure modes vs L/D ratio for circular pultruded FRP profiles (a) C1-89×6 and (b) C2-89×6.

APPENDIX B: RESULTS OF THE PARAMETRIC STUDIES ON THE LAYUP PARAMETERS OF CHAPTER 5: EFFECTS OF LAYUP AND GEOMETRY ON FLEXURAL PERFORMANCE OF HOLLOW PULTRUDED FRP PROFILES

Table B. 1 shows the design of experiment of the full factorial study on the layup parameters of the hollow box pultruded FRP beam along with its numerical results. The observed failure mode was local buckling of the top flange at all the series.

Table B. 1: Design matrix and results of the full factorial study on the layup parameters of the hollow box beam (Wall thickness=5.2 mm, h/b=1, R=10 mm, r=4.8 mm).

Series	Wound fibre angle (Deg)	Axial-to-wound fibre ratio (%)	Stacking sequence	Flexural Stiffness (N/mm)	Flexural Strength (MPa)
S-1	20	[60/40]	[0/+θ/-θ/0/-θ/+θ/0]	628.4	337.5
S-2	20	[60/40]	[+θ/0/-θ/0/-θ/0/+θ]	628.4	347.8
S-3	20	[60/40]	[+θ/-θ/0/-θ/+θ]	628.4	350.8
S-4	20	[75/25]	[0/+θ/-θ/0/-θ/+θ/0]	638.0	330.8
S-5	20	[75/25]	[+θ/0/-θ/0/-θ/0/+θ]	638.4	335.1
S-6	20	[75/25]	[+θ/-θ/0/-θ/+θ]	638.0	337.2
S-7	20	[90/10]	[0/+θ/-θ/0/-θ/+θ/0]	645.5	328.2
S-8	20	[90/10]	[+θ/0/-θ/0/-θ/0/+θ]	645.5	331.2
S-9	20	[90/10]	[+θ/-θ/0/-θ/+θ]	645.5	332.2
S-10	50	[60/40]	[0/+θ/-θ/0/-θ/+θ/0]	533.1	374.9
S-11	50	[60/40]	[+θ/0/-θ/0/-θ/0/+θ]	533.3	389.8
S-12	50	[60/40]	[+θ/-θ/0/-θ/+θ]	533.3	394.9
S-13	50	[75/25]	[0/+θ/-θ/0/-θ/+θ/0]	584.5	358.9
S-14	50	[75/25]	[+θ/0/-θ/0/-θ/0/+θ]	584.6	368.1
S-15	50	[75/25]	[+θ/-θ/0/-θ/+θ]	584.6	371.8
S-16	50	[90/10]	[0/+θ/-θ/0/-θ/+θ/0]	627.1	337.1
S-17	50	[90/10]	[+θ/0/-θ/0/-θ/0/+θ]	627.1	342.9
S-18	50	[90/10]	[+θ/-θ/0/-θ/+θ]	627.2	344.1
S-19	80	[60/40]	[0/+θ/-θ/0/-θ/+θ/0]	493.0	368.3
S-20	80	[60/40]	[+θ/0/-θ/0/-θ/0/+θ]	493.8	398.6
S-21	80	[60/40]	[+θ/-θ/0/-θ/+θ]	493.7	410.5
S-22	80	[75/25]	[0/+θ/-θ/0/-θ/+θ/0]	554.1	357.6
S-23	80	[75/25]	[+θ/0/-θ/0/-θ/0/+θ]	554.3	377.8
S-24	80	[75/25]	[+θ/-θ/0/-θ/+θ]	554.3	384.9
S-25	80	[90/10]	[0/+θ/-θ/0/-θ/+θ/0]	612.3	341.0
S-26	80	[90/10]	[+θ/0/-θ/0/-θ/0/+θ]	612.5	351.1
S-27	80	[90/10]	[+θ/-θ/0/-θ/+θ]	612.5	354.2

Table B. 2 shows the design of experiment of the full factorial study on the chosen parameters (wall thickness, wound fibre angle, and axial-to-wound fibre ratio) of the hollow box pultruded FRP beam along with its numerical results.

Table B. 2: Design matrix and results of the full factorial study on the chosen parameters of the hollow box beam ((h/b)=1, R=10 mm, r=4.8 mm, Stacking sequence=[0/+θ/-θ/0/-θ/+θ/0]).

Series	Wall thickness (mm)	Wound fibre angle (Deg)	Axial-to-wound fibre ratio (%)	Flexural Stiffness (N/mm)	Flexural Strength (MPa)	Failure mode
S-1	5.2	20	[60/40]	628.4	337.5	Local buckling of top flange
S-2	5.2	20	[75/25]	638.0	330.8	Local buckling of top flange
S-3	5.2	20	[90/10]	645.5	328.2	Local buckling of top flange
S-4	5.2	50	[60/40]	533.1	374.9	Local buckling of top flange
S-5	5.2	50	[75/25]	584.5	358.9	Local buckling of top flange
S-6	5.2	50	[90/10]	627.0	337.1	Local buckling of top flange
S-7	5.2	80	[60/40]	493.0	368.3	Local buckling of top flange
S-8	5.2	80	[75/25]	554.1	357.6	Local buckling of top flange
S-9	5.2	80	[90/10]	612.3	341.0	Local buckling of top flange
S-10	5.8	20	[60/40]	690.8	420.6	Local buckling of top flange
S-11	5.8	20	[75/25]	701.3	414.7	Local buckling of top flange
S-12	5.8	20	[90/10]	709.7	401.8	Local buckling of top flange
S-13	5.8	50	[60/40]	585.8	389.7	Compressive failure of top flange
S-14	5.8	50	[75/25]	642.3	380.0	Compressive failure of top flange
S-15	5.8	50	[90/10]	689.3	364.5	Local buckling of top flange
S-16	5.8	80	[60/40]	542.0	377.8	Compressive failure of top flange
S-17	5.8	80	[75/25]	609.1	362.2	Compressive failure of top flange
S-18	5.8	80	[90/10]	673.2	351.3	Local buckling of top flange
S-19	6.4	20	[60/40]	750.9	432.1	Compressive failure of top flange
S-20	6.4	20	[75/25]	762.5	443.9	Compressive failure of top flange
S-21	6.4	20	[90/10]	771.7	454.2	Compressive failure of top flange
S-22	6.4	50	[60/40]	636.6	360.9	Compressive failure of top flange
S-23	6.4	50	[75/25]	698.2	393.7	Compressive failure of top flange
S-24	6.4	50	[90/10]	749.4	425.9	Compressive failure of top flange
S-25	6.4	80	[60/40]	589.4	326.2	Compressive failure of top flange
S-26	6.4	80	[75/25]	662.4	369.7	Compressive failure of top flange
S-27	6.4	80	[90/10]	732.1	422.9	Compressive failure of top flange

APPENDIX C: OPTIMISATION CODES OF CHAPTER 6: DESIGN OPTIMISATION OF HOLLOW BOX PULTRUDED FRP PROFILES USING MIXED INTEGER CONSTRAINED GENETIC ALGORITHM

C.1 Introduction

The MATLAB and Python codes generated from this study will be compiled to develop a design App for the analysis and design optimisation of hollow box PFRP profiles manufactured by any pultrusion technology and subjected to a wider range of loading applications and failure modes. Meanwhile, these codes can be used by design engineers to analyse or design hollow box PFRP profiles with different dimensions and layups subjected to axial compression or four-point bending loadings. Fig. C.1 presents the flowchart of the codes to perform analysis or design of hollow box PFRP profiles subjected to compression or bending.

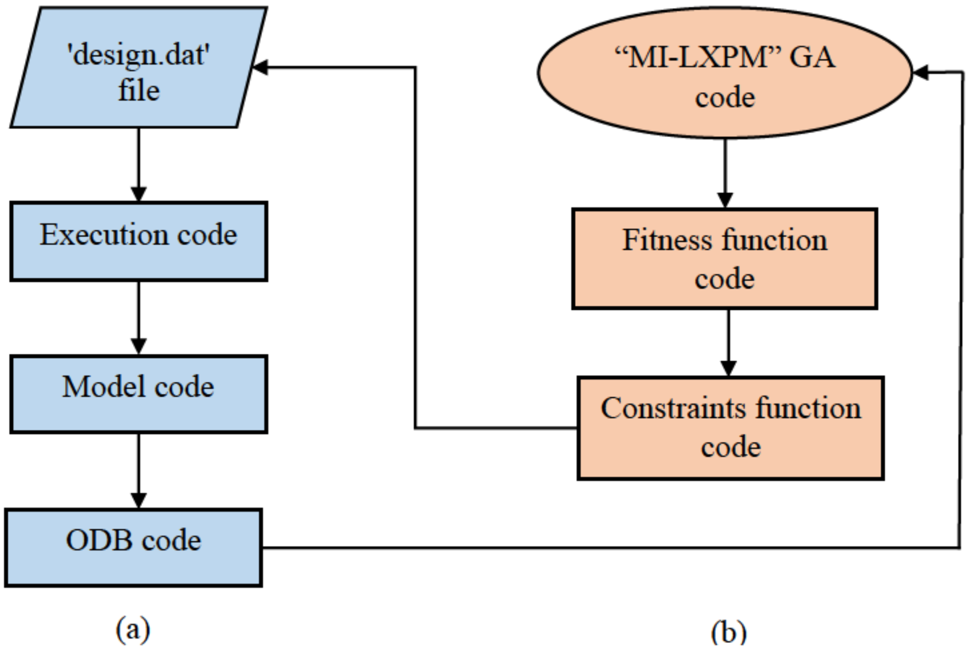

Fig. C.1. Flowchart of the codes sequence to perform (a) analysis or (b) design optimisation of hollow box PFRP profiles subjected to compression or bending.

The "model.py" parameterised code can be used to analyse the structural behaviour of a hollow box PFRP profile subjected to compression or bending by inserting the required values of the design parameters in their locations in the code. The fibre angle and percentage can be changed in the composite layup section. The cross-sectional dimensions and material properties can also be changed in the part and materials sections, respectively. Alternatively, the design parameters can be inserted via a “design.dat” file type starting from the wall thickness, cross-sectional aspect ratio, corner radii ratio, fibre angle (integer), then axial fibre percentage. The “MI-LXPM” GA and constraints function codes can be used to design hollow box PFRP profiles with optimised design parameters and cost by inserting the structural design requirements (strength and stiffness) and design limitations (boundaries of geometry and layup) in their locations in the codes. The targeted strength and stiffness can be inserted in the inequality matrix “c” in the constraints function code while the design limitations can be changed in the lower and upper bounds matrices in the “MI-LXPM” GA code. The analysis and design codes are presented in the following section based on the loading condition.

C.2 Hollow box pultruded FRP profile subjected to axial compression

C.2.1 MATLAB scripts

1. Constraints function:

```
% constraints function of axial stiffness and strength
% the design variables are:
 % x(1): wall thickness (t)
 % x(2): cross-sectional aspect ratio (h/b)
 % x(3): corner radii ratio (r/R)
 % x(4): winding angle
 % x(5): axial fibre percentage
 function [c, ceq] = Constraints(x) % constraints function of axial stiffness and
strength
 ceq = []; % no equality constraints
 R = [x(1) x(2) x(3) x(4) x(5)]; % design variables vector
 Log1 = xlsread('Log_Compression.xlsx','Sheet1'); % reading from library
 Log2 = Log1(:,1:5); % matrix of design variables inserted from the library
```

[C,ia,ib] = intersect(Log2,R,'rows'); % comparing the current configuration with the data from the library

if ib == 1 % the current configuration exists in the library

c = [-Log1(ia,6)+ $(\frac{EA}{L})_{control}$; -Log1(ia,7)+ $\sigma_{control}$]; % assigning the inequality constraints

else % the current configuration does not exist in the library

fid = fopen('design.dat', 'w'); % open a file to write the current configuration

fprintf(fid, '%f %f %d %d %f\n', R); % print the design parameters

fclose(fid); % close the file

[status,cmdout] = system(['starter.py']); % run the python script

% script for importing the FEM results from the following text file:

filename = 'C:\Simulations\GA\Compression\abaqus.txt'; % FEM results text file

startRow = 2;

formatSpec = '%29f%16f%[^\n\r]';

% open the text file

fileID = fopen(filename,'r');

% read columns of data according to the format.

textscan(fileID, '%[^\n\r]', startRow-1, 'WhiteSpace', '', 'ReturnOnError', false, 'EndOfLine', '\r\n');

dataArray = textscan(fileID, formatSpec, 'Delimiter', '', 'WhiteSpace', '', 'TextType', 'string', 'EmptyValue', NaN, 'ReturnOnError', false);

% close the text file.

fclose(fileID);

% create output variable

abaqus = [dataArray{1:end-1}];

% clear temporary variables

clearvars filename startRow formatSpec fileID dataArray ans;

T = 2*(200-(200/(x(2)+1)))*x(1)+2*(200/(x(2)+1))*x(1)-4*(x(1))^2-(4-3.14159265359)*((10)^2-(x(3))^2); % cross-sectional area of the profile

Stiff = -(abaqus(5,2)/abaqus(5,1))+ $(\frac{EA}{L})_{control}$; % calculating the axial stiffness constraint

Str = -(max(abaqus(:,2))/T)+ $\sigma_{control}$; % calculating the compressive strength constraint

```
    c = [Stiff; Str]; % assigning the inequality constraints
    i = xlsread('Timer.xlsx','Sheet1','A1'); % import external timer
    Log1(1779+i,1) = x(1); % assigning the new value of x(1) variable
    Log1(1779+i,2) = x(2); % assigning the new value of x(2) variable
    Log1(1779+i,3) = x(3); % assigning the new value of x(3) variable
    Log1(1779+i,4) = x(4); % assigning the new value of x(4) variable
    Log1(1779+i,5) = x(5); % assigning the new value of x(5) variable
    Log1(1779+i,6) = (abaqus(5,2)/abaqus(5,1)); % assigning the new axial stiffness
    Log1(1779+i,7) = (max(abaqus(:,2))/T); % assigning the new strength
    Log1(1779+i,8) = T; % assigning the new cross-sectional area
    filename = 'Log_Compression.xlsx'; % assigning the library for writing
    writematrix(Log1,filename,'sheet',1); % writing the new data in the library
    i = i + 1; % timer to move down one row in the library
    Timername = 'Timer.xlsx'; % assigning the new timer value
    writematrix(i,Timername,'sheet',1); % writing the new timer value
 end
 end
```

2. Fitness function:

```
% fitness function of the cross-sectional area (A)
% the design variables are:
 % x(1): wall thickness (t)
 % x(2): cross-sectional aspect ratio (h/b)
 % x(3): corner radii ratio (r/R)
 % x(4): winding angle
 % x(5): axial fibre percentage
 function A = Fitnessfunction(x) % fitness function of the cross-sectional area
 A = 2*(200-(200/(x(2)+1)))*x(1)+2*(200/(x(2)+1))*x(1)-4*(x(1))^2-(4-
3.14159265359)*((10)^2-(x(3))^2); % the cross-sectional area function
 End
```

3. “MI-LXPM” genetic algorithm function:

```
% “MI-LXPM” GA script
```

```
% the design variables are:
 % x(1): wall thickness (t)
 % x(2): cross-sectional aspect ratio (h/b)
 % x(3): corner radii ratio (r/R)
 % x(4): winding angle
 % x(5): axial fibre percentage
ObjFcn=@Fitnessfunction; % assigning the fitness function
nvars = 5; % assigning the number of variables
LB = [2 1 0.5 20 0.6]; % assigning the lower bounds of the variables
UB = [12 3 2.5 80 0.9]; % assigning the upper bounds of the variables

ConsFcn=@Constraints; % assigning the constraints function
IntCon = [4]; % assigning the location of the integer variable
% “MI-LXPM” GA options:
options =
optimoptions('ga','PlotFcn','gaplotbestf','Display','iter','PopulationSize',20,...
'EliteCount', 1,'CrossoverFraction', 1.0,'Generations', 30,'StallGenLimit',15);
% GA solver:
[x, fval, exitflag, output, population, scores] = ga(ObjFcn, nvars, [], [], [], [], LB,
UB,...
   ConsFcn, IntCon, options);
```

C.2.2 Python scripts

1. Model script:

```
# -*- coding: mbcs -*-

# importing the required modules:

from part import *

from material import *

from section import *

from assembly import *

from step import *
```

```
from interaction import *
from load import *
from mesh import *
from optimization import *
from job import *
from sketch import *
from visualization import *
from connectorBehavior import *
# importing the design variables from MATLAB:
f = open("design.dat", "r")
[t, h_b, r, deg, Axial_fibre_ratio] = [float(x) for x in f.readline().split()]
f.close()
# adjusting the variables to the code:
b = (200/((h_b)+1))
h = 200 - b
ta = Axial_fibre_ratio / 3 # Ply thickness of axial fibres.
Wound_fibre_ratio = 1.0 - Axial_fibre_ratio
tw = Wound_fibre_ratio / 4 # Ply thickness of wound fibres.
# generating the “Part” geometry:
mdb.models['Model-1'].ConstrainedSketch(name='__profile__', sheetSize=200.0)
mdb.models['Model-1'].sketches['__profile__'].rectangle(point1=(-(b/2), -(h/2)),
    point2=((b/2), (h/2)))
mdb.models['Model-1'].sketches['__profile__'].geometry.findAt((-(b/2), 0.0))
mdb.models['Model-1'].sketches['__profile__'].geometry.findAt((0.0, (h/2)))
```

```
mdb.models['Model-1'].sketches['__profile__'].geometry.findAt(((b/2), 0.0))
mdb.models['Model-1'].sketches['__profile__'].geometry.findAt((0.0, -(h/2)))
mdb.models['Model-1'].sketches['__profile__'].offset(distance=t, objectList=(
    mdb.models['Model-1'].sketches['__profile__'].geometry.findAt((-(b/2), 0.0),
    ), mdb.models['Model-1'].sketches['__profile__'].geometry.findAt((0.0,
    (h/2)), ), mdb.models['Model-1'].sketches['__profile__'].geometry.findAt((
    (b/2), 0.0), ),
    mdb.models['Model-1'].sketches['__profile__'].geometry.findAt((0.0, -(h/2)),
    )), side=LEFT)
mdb.models['Model-1'].sketches['__profile__'].geometry.findAt((-(b/2), 0.0))
mdb.models['Model-1'].sketches['__profile__'].geometry.findAt((0.0, (h/2)))
mdb.models['Model-1'].sketches['__profile__'].FilletByRadius(curve1=
    mdb.models['Model-1'].sketches['__profile__'].geometry.findAt((-(b/2), 0.0),
    ), curve2=mdb.models['Model-1'].sketches['__profile__'].geometry.findAt((
    0.0, (h/2)), ), nearPoint1=(-((b/2)-0.3), ((h/2)-3)), nearPoint2=
    (-((b/2)-6.5), ((h/2)+1.2)), radius=10.0)
mdb.models['Model-1'].sketches['__profile__'].geometry.findAt((0.0, (h/2)))
mdb.models['Model-1'].sketches['__profile__'].geometry.findAt(((b/2), 0.0))
mdb.models['Model-1'].sketches['__profile__'].FilletByRadius(curve1=
    mdb.models['Model-1'].sketches['__profile__'].geometry.findAt((0.0, (h/2)),
    ), curve2=mdb.models['Model-1'].sketches['__profile__'].geometry.findAt((
    (b/2), 0.0), ), nearPoint1=(-((b/2)-27.1), ((h/2)+1)),
    nearPoint2=(((b/2)-1.2), ((h/2)-6.5)), radius=10.0)
mdb.models['Model-1'].sketches['__profile__'].geometry.findAt(((b/2), 0.0))
```

```
mdb.models['Model-1'].sketches['__profile__'].geometry.findAt((0.0, -(h/2)))
mdb.models['Model-1'].sketches['__profile__'].FilletByRadius(curve1=
    mdb.models['Model-1'].sketches['__profile__'].geometry.findAt(((b/2), 0.0),
    ), curve2=mdb.models['Model-1'].sketches['__profile__'].geometry.findAt((
    0.0, -(h/2)), ), nearPoint1=((b/2), -((h/2)-12.5)),
    nearPoint2=(((b/2)-8.2), -((h/2)+0.8)), radius=10.0)
mdb.models['Model-1'].sketches['__profile__'].geometry.findAt((0.0, -(h/2)))
mdb.models['Model-1'].sketches['__profile__'].geometry.findAt((-(b/2), 0.0))
mdb.models['Model-1'].sketches['__profile__'].FilletByRadius(curve1=
    mdb.models['Model-1'].sketches['__profile__'].geometry.findAt((0.0,
    -(h/2)), ), curve2=
    mdb.models['Model-1'].sketches['__profile__'].geometry.findAt((-(b/2),
    0.0), ), nearPoint1=(-((b/2)-5.5), -((h/2)+0.5)), nearPoint2=(
    -((b/2)-1.3), -((h/2)-6)), radius=10.0)
mdb.models['Model-1'].sketches['__profile__'].geometry.findAt((-((b/2)-t), 0.0))
mdb.models['Model-1'].sketches['__profile__'].geometry.findAt((0.0, ((h/2)-t)))
mdb.models['Model-1'].sketches['__profile__'].FilletByRadius(curve1=
    mdb.models['Model-1'].sketches['__profile__'].geometry.findAt((-((b/2)-t), 0.0),
    ), curve2=mdb.models['Model-1'].sketches['__profile__'].geometry.findAt((
    0.0, ((h/2)-t)), ), nearPoint1=(-((b/2)-5.6), ((h/2)-11.2)), nearPoint2=(
    -((b/2)-11.6), ((h/2)-5.4)), radius=r)
mdb.models['Model-1'].sketches['__profile__'].geometry.findAt((0.0, ((h/2)-t)))
mdb.models['Model-1'].sketches['__profile__'].geometry.findAt((((b/2)-t), 0.0))
mdb.models['Model-1'].sketches['__profile__'].FilletByRadius(curve1=
```

```
    mdb.models['Model-1'].sketches['__profile__'].geometry.findAt((0.0, ((h/2)-t)),
    ), curve2=mdb.models['Model-1'].sketches['__profile__'].geometry.findAt((
    ((b/2)-t), 0.0), ), nearPoint1=(-((b/2)-39.5), ((h/2)-5.2)),
    nearPoint2=(((b/2)-6), ((h/2)-15)), radius=r)
mdb.models['Model-1'].sketches['__profile__'].geometry.findAt((((b/2)-t), 0.0))
mdb.models['Model-1'].sketches['__profile__'].geometry.findAt((0.0, -((h/2)-t)))
mdb.models['Model-1'].sketches['__profile__'].FilletByRadius(curve1=
    mdb.models['Model-1'].sketches['__profile__'].geometry.findAt((((b/2)-t), 0.0),
    ), curve2=mdb.models['Model-1'].sketches['__profile__'].geometry.findAt((
    0.0, -((h/2)-t)), ), nearPoint1=(((b/2)-5), -((h/2)-45.4)),
    nearPoint2=(((b/2)-14.2), -((h/2)-4.5)), radius=r)
mdb.models['Model-1'].sketches['__profile__'].geometry.findAt((0.0, -((h/2)-t)))
mdb.models['Model-1'].sketches['__profile__'].geometry.findAt((-((b/2)-t), 0.0))
mdb.models['Model-1'].sketches['__profile__'].FilletByRadius(curve1=
    mdb.models['Model-1'].sketches['__profile__'].geometry.findAt((0.0,
    -((h/2)-t)), ), curve2=
    mdb.models['Model-1'].sketches['__profile__'].geometry.findAt((-((b/2)-t),
    0.0), ), nearPoint1=(-((b/2)-35), ((h/2)-6)), nearPoint2=(
    -((b/2)-6.3), -((h/2)-14.2)), radius=r)
mdb.models['Model-1'].Part(dimensionality=THREE_D, name='Part-1', type=
    DEFORMABLE_BODY)
mdb.models['Model-1'].parts['Part-1'].BaseSolidExtrude(depth=500.0, sketch=
    mdb.models['Model-1'].sketches['__profile__'])
del mdb.models['Model-1'].sketches['__profile__']
```

```
mdb.models['Model-1'].parts['Part-1'].DatumPlaneByPrincipalPlane(offset=0.0,
    principalPlane=YZPLANE)
mdb.models['Model-1'].parts['Part-1'].DatumPlaneByPrincipalPlane(offset=0.0,
    principalPlane=XZPLANE)
mdb.models['Model-1'].parts['Part-1'].PartitionCellByDatumPlane(cells=
    mdb.models['Model-1'].parts['Part-1'].cells.findAt(((-((b/2)-0.1), ((h/2)-15),
    333.333333), )), datumPlane=
    mdb.models['Model-1'].parts['Part-1'].datums[2])
mdb.models['Model-1'].parts['Part-1'].PartitionCellByDatumPlane(cells=
    mdb.models['Model-1'].parts['Part-1'].cells.findAt(((-((b/2)-t), ((h/2)-36.7),
    333.333333), ), ((((b/2)-t), ((h/2)-36.7), 333.333333), ), ), datumPlane=
    mdb.models['Model-1'].parts['Part-1'].datums[3])
# generating the “Mesh”:
mdb.models['Model-1'].parts['Part-1'].seedPart(deviationFactor=0.1,
    minSizeFactor=0.1, size=5.0)
mdb.models['Model-1'].parts['Part-1'].seedEdgeByNumber(constraint=FINER,
edges=
    mdb.models['Model-1'].parts['Part-1'].edges.findAt(((-(b/2),
    -((h/2)-9.99999), 500.0), ), (((b/2), -((h/2)-9.99999), 500.0), ), (((b/2),
    ((h/2)-9.99999), 500.0), ), ((-(b/2), ((h/2)-9.99999), 500.0), ), ), number=3)
mdb.models['Model-1'].parts['Part-1'].seedEdgeByNumber(constraint=FINER,
edges=
    mdb.models['Model-1'].parts['Part-1'].edges.findAt(((-((b/2)-1.3), 0.0, 500.0), ),
    ((((b/2)-1.3), 0.0, 500.0), ), ((0.0, -((h/2)-1.3), 500.0), ), ((0.0, ((h/2)-1.3), 500.0), ),
),
```

```
    number=5)
mdb.models['Model-1'].parts['Part-1'].assignStackDirection(cells=
    mdb.models['Model-1'].parts['Part-1'].cells.findAt(((-(b/2), ((h/2)-36.7),
    333.333333), ), ((((b/2)-12), -((h/2)-t), 333.333333), ), ((((b/2)-12), ((h/2)-t),
    166.666667), ), ((-(b/2), -((h/2)-36.7), 166.666667), ), ), referenceRegion=
    mdb.models['Model-1'].parts['Part-1'].faces.findAt((-((b/2)-15), (h/2),
    166.666667), ))
mdb.models['Model-1'].parts['Part-1'].setMeshControls(algorithm=MEDIAL_AXIS,
    regions=mdb.models['Model-1'].parts['Part-1'].cells.findAt(((-(b/2),
    ((h/2)-36.7), 333.333333), ), ((((b/2)-15), -((h/2)-t), 333.333333), ), ((((b/2)-15),
    ((h/2)-t), 166.666667), ), ((-(b/2), -((h/2)-36.7), 166.666667), ), ))
mdb.models['Model-1'].parts['Part-1'].generateMesh()
mdb.models['Model-1'].parts['Part-1'].setElementType(elemTypes=(ElemType(
    elemCode=SC8R, elemLibrary=STANDARD, secondOrderAccuracy=OFF,
    hourglassControl=DEFAULT), ElemType(elemCode=SC6R,
elemLibrary=STANDARD),
    ElemType(elemCode=UNKNOWN_TET, elemLibrary=STANDARD)),
regions=(
    mdb.models['Model-1'].parts['Part-1'].cells.findAt(((-(b/2), ((h/2)-36.7),
    333.333333), ), ((((b/2)-12), -((h/2)-t), 333.333333), ), ((((b/2)-12), ((h/2)-t),
    166.666667), ), ((-(b/2), -((h/2)-36.7), 166.666667), ), ), ))
# generating the “Materials” properties:
mdb.models['Model-1'].Material(name='Material-1')
mdb.models['Model-1'].materials['Material-1'].Density(table=((2.03e-09, ), ))
mdb.models['Model-1'].materials['Material-1'].Elastic(table=((45700.0, 12100.0,
```

```
    0.28, 4600.0, 4600.0, 4000.0), ), type=LAMINA)
mdb.models['Model-1'].materials['Material-1'].HashinDamageInitiation(alpha=1.0,
    table=((803.0, 548.0, 43.0, 187.0, 64.0, 50.0), ))
mdb.models['Model-1'].materials['Material-
1'].hashinDamageInitiation.DamageEvolution(
    table=((92.0, 79.0, 5.0, 5.0), ), type=ENERGY)
mdb.models['Model-1'].materials['Material-
1'].hashinDamageInitiation.DamageStabilization(
    fiberCompressiveCoeff=0.1, fiberTensileCoeff=0.1, matrixCompressiveCoeff=
    0.1, matrixTensileCoeff=0.1)
mdb.models['Model-1'].parts['Part-1'].Surface(name='Surf-1', side1Faces=
    mdb.models['Model-1'].parts['Part-1'].faces.findAt(((-(b/2), -((h/2)-36.7),
    166.666667), ), (((b/2), -((h/2)-36.7), 333.333333), ), ((((b/2)-15), (h/2),
    333.333333), ), ((((b/2)-15), -(h/2), 166.666667), ), ((-(b/2), ((h/2)-36.7),
    333.333333), ), ((-(b/2), ((h/2)-9.99999), 333.333333), ), ((-((b/2)-15),
    (h/2), 166.666667), ), (((b/2), ((h/2)-9.99999), 333.333333), ), (((b/2),
   ((h/2)-36.7), 166.666667), ), (((b/2), -((h/2)-9.99999), 333.333333), ), ((
    -((b/2)-15), -(h/2), 333.333333), ), ((-(b/2), -((h/2)-9.99999), 333.333333),
    ), ))
mdb.models['Model-1'].parts['Part-1'].Set(edges=
    mdb.models['Model-1'].parts['Part-1'].edges.findAt((((((b/2)-10), (h/2), 125.0), ))
    , name='Set-1')
# generating the "Composite layup":
mdb.models['Model-1'].parts['Part-1'].CompositeLayup(description='',
```

```
    elementType=CONTINUUM_SHELL, name='CompositeLayup-1',
symmetric=False)
mdb.models['Model-1'].parts['Part-1'].compositeLayups['CompositeLayup-
1'].Section(
    integrationRule=SIMPSON, poissonDefinition=DEFAULT, preIntegrate=OFF,
    temperature=GRADIENT, thicknessModulus=None, useDensity=OFF)
mdb.models['Model-1'].parts['Part-1'].compositeLayups['CompositeLayup-
1'].CompositePly(
    additionalRotationField='', additionalRotationType=ROTATION_NONE,
angle=0.0
    , axis=AXIS_3, material='Material-1', numIntPoints=3, orientationType=
    SPECIFY_ORIENT, orientationValue=0.0, plyName='Ply-1', region=Region(
    cells=mdb.models['Model-1'].parts['Part-1'].cells.findAt(((-(b/2),
    ((h/2)-36.7), 333.333333), ), ((((b/2)-12), -((h/2)-t), 333.333333), ), ((((b/2)-12),
    ((h/2)-t), 166.666667), ), ((-(b/2), -((h/2)-36.7), 166.666667), ), )), suppressed=
    False, thickness=ta, thicknessType=SPECIFY_THICKNESS)
mdb.models['Model-1'].parts['Part-1'].compositeLayups['CompositeLayup-
1'].CompositePly(
    additionalRotationField='', additionalRotationType=ROTATION_NONE,
angle=0.0
    , axis=AXIS_3, material='Material-1', numIntPoints=3, orientationType=
    SPECIFY_ORIENT, orientationValue=deg, plyName='Ply-2', region=Region(
    cells=mdb.models['Model-1'].parts['Part-1'].cells.findAt(((-(b/2),
    ((h/2)-36.7), 333.333333), ), ((((b/2)-12), -((h/2)-t), 333.333333), ), ((((b/2)-12),
    ((h/2)-t), 166.666667), ), ((-(b/2), -((h/2)-36.7), 166.666667), ), )), suppressed=
    False, thickness=tw, thicknessType=SPECIFY_THICKNESS)
```

```
mdb.models['Model-1'].parts['Part-1'].compositeLayups['CompositeLayup-
1'].CompositePly(
    additionalRotationField='', additionalRotationType=ROTATION_NONE,
angle=0.0
    , axis=AXIS_3, material='Material-1', numIntPoints=3, orientationType=
    SPECIFY_ORIENT, orientationValue=-deg, plyName='Ply-3', region=Region(
    cells=mdb.models['Model-1'].parts['Part-1'].cells.findAt(((-(b/2),
    ((h/2)-36.7), 333.333333), ), ((((b/2)-12), -((h/2)-t), 333.333333), ), ((((b/2)-12),
    ((h/2)-t), 166.666667), ), ((-(b/2), -((h/2)-36.7), 166.666667), ), )), suppressed=
    False, thickness=tw, thicknessType=SPECIFY_THICKNESS)
mdb.models['Model-1'].parts['Part-1'].compositeLayups['CompositeLayup-
1'].CompositePly(
    additionalRotationField='', additionalRotationType=ROTATION_NONE,
angle=0.0
    , axis=AXIS_3, material='Material-1', numIntPoints=3, orientationType=
    SPECIFY_ORIENT, orientationValue=0.0, plyName='Ply-4', region=Region(
    cells=mdb.models['Model-1'].parts['Part-1'].cells.findAt(((-(b/2),
    ((h/2)-36.7), 333.333333), ), ((((b/2)-12), -((h/2)-t), 333.333333), ), ((((b/2)-12),
    ((h/2)-t), 166.666667), ), ((-(b/2), -((h/2)-36.7), 166.666667), ), )), suppressed=
    False, thickness=ta, thicknessType=SPECIFY_THICKNESS)
mdb.models['Model-1'].parts['Part-1'].compositeLayups['CompositeLayup-
1'].CompositePly(
    additionalRotationField='', additionalRotationType=ROTATION_NONE,
angle=0.0
    , axis=AXIS_3, material='Material-1', numIntPoints=3, orientationType=
    SPECIFY_ORIENT, orientationValue=-deg, plyName='Ply-5', region=Region(
```

```
    cells=mdb.models['Model-1'].parts['Part-1'].cells.findAt(((-(b/2),
    ((h/2)-36.7), 333.333333), ), ((((b/2)-12), -((h/2)-t), 333.333333), ), ((((b/2)-12),
    ((h/2)-t), 166.666667), ), ((-(b/2), -((h/2)-36.7), 166.666667), ), )), suppressed=
    False, thickness=tw, thicknessType=SPECIFY_THICKNESS)
mdb.models['Model-1'].parts['Part-1'].compositeLayups['CompositeLayup-
1'].CompositePly(
    additionalRotationField='', additionalRotationType=ROTATION_NONE,
angle=0.0
    , axis=AXIS_3, material='Material-1', numIntPoints=3, orientationType=
    SPECIFY_ORIENT, orientationValue=deg, plyName='Ply-6', region=Region(
    cells=mdb.models['Model-1'].parts['Part-1'].cells.findAt(((-(b/2),
    ((h/2)-36.7), 333.333333), ), ((((b/2)-12), -((h/2)-t), 333.333333), ), ((((b/2)-12),
    ((h/2)-t), 166.666667), ), ((-(b/2), -((h/2)-36.7), 166.666667), ), )), suppressed=
    False, thickness=tw, thicknessType=SPECIFY_THICKNESS)
mdb.models['Model-1'].parts['Part-1'].compositeLayups['CompositeLayup-
1'].CompositePly(
    additionalRotationField='', additionalRotationType=ROTATION_NONE,
angle=0.0
    , axis=AXIS_3, material='Material-1', numIntPoints=3, orientationType=
    SPECIFY_ORIENT, orientationValue=0.0, plyName='Ply-7', region=Region(
    cells=mdb.models['Model-1'].parts['Part-1'].cells.findAt(((-(b/2),
    ((h/2)-36.7), 333.333333), ), ((((b/2)-12), -((h/2)-t), 333.333333), ), ((((b/2)-12),
    ((h/2)-t), 166.666667), ), ((-(b/2), -((h/2)-36.7), 166.666667), ), )), suppressed=
    False, thickness=ta, thicknessType=SPECIFY_THICKNESS)
mdb.models['Model-1'].parts['Part-1'].compositeLayups['CompositeLayup-
1'].ReferenceOrientation(
```

```
    additionalRotationField='', additionalRotationType=ROTATION_NONE, 
angle=0.0
    , axis=AXIS_3, flipNormalDirection=False, flipPrimaryDirection=False,
    localCsys=None, normalAxisDefinition=SURFACE, 
normalAxisDirection=AXIS_3,
    normalAxisRegion=mdb.models['Model-1'].parts['Part-1'].surfaces['Surf-1'],
    orientationType=DISCRETE, primaryAxisDefinition=EDGE, 
primaryAxisDirection=
    AXIS_1, primaryAxisRegion=
    mdb.models['Model-1'].parts['Part-1'].sets['Set-1'], stackDirection=
    STACK_3)
# generating the "Assembly" geometry:
mdb.models['Model-1'].rootAssembly.DatumCsysByDefault(CARTESIAN)
mdb.models['Model-1'].rootAssembly.Instance(dependent=ON, name='Part-1-1',
    part=mdb.models['Model-1'].parts['Part-1'])
mdb.models['Model-1'].rootAssembly.Set(name='Top_point', vertices=
    mdb.models['Model-1'].rootAssembly.instances['Part-1-1'].vertices.findAt(((
    ((b/2)-10), (h/2), 500.0), )))
# generating the "Boundary conditions" geometry:
mdb.models['Model-1'].rootAssembly.Set(faces=
    mdb.models['Model-1'].rootAssembly.instances['Part-1-1'].faces.findAt(((
    -((b/2)-1.3), ((h/2)-36.7), 0.0), ), ((((b/2)-1.7), ((h/2)-36.7), 0.0), ), ((
    -((b/2)-1.7), -((h/2)-36.7), 0.0), ), ((((b/2)-1.3), -((h/2)-36.7), 0.0), ), ), name=
    'Set-2')
mdb.models['Model-1'].EncastreBC(createStepName='Initial', localCsys=None,
```

```
    name='Bot_Fixed', region=mdb.models['Model-1'].rootAssembly.sets['Set-2'])
mdb.models['Model-1'].rootAssembly.Set(faces=
    mdb.models['Model-1'].rootAssembly.instances['Part-1-1'].faces.findAt(((
    -((b/2)-1.3), -((h/2)-36.7), 500.0), ), ((((b/2)-1.8), -((h/2)-36.7), 500.0), ), ((
    ((b/2)-1.3), ((h/2)-36.7), 500.0), ), ((-((b/2)-1.8), ((h/2)-36.7), 500.0), ), ),
    name='Set-3')
mdb.models['Model-1'].DisplacementBC(amplitude=UNSET,
createStepName='Initial',
    distributionType=UNIFORM, fieldName='', localCsys=None, name='Top_Disp',
    region=mdb.models['Model-1'].rootAssembly.sets['Set-3'], u1=SET, u2=SET,
    u3=UNSET, ur1=SET, ur2=SET, ur3=SET)
# generating the “first step/linear buckling”:
mdb.models['Model-1'].BuckleStep(maxIterations=300, name='Step-1',
numEigen=3,
    previous='Initial', vectors=6)
mdb.models['Model-1'].rootAssembly.Surface(name='Surf-1', side1Faces=
    mdb.models['Model-1'].rootAssembly.instances['Part-1-1'].faces.findAt(((
    -((b/2)-1.3), -((h/2)-36.7), 500.0), ), ((((b/2)-1.8), -((h/2)-36.7), 500.0), ), ((
    ((b/2)-1.3), ((h/2)-36.7), 500.0), ), ((-((b/2)-1.8), ((h/2)-36.7), 500.0), ), ))
mdb.models['Model-1'].Pressure(createStepName='Step-1', distributionType=
    UNIFORM, field='', magnitude=1.0, name='Unit_load', region=
    mdb.models['Model-1'].rootAssembly.surfaces['Surf-1'])
# printing nodal outputs:
mdb.models['Model-
1'].keywordBlock.synchVersions(storeNodesAndElements=False)
```

```
mdb.models['Model-1'].keywordBlock.replace(55,
    '\n*Output, field, variable=PRESELECT\n*NODE FILE \nU,')
# executing the "Linear buckling" analysis:
mdb.Job(atTime=None, contactPrint=OFF, description='', echoPrint=OFF,
    explicitPrecision=SINGLE, getMemoryFromAnalysis=True, historyPrint=OFF,
    memory=90, memoryUnits=PERCENTAGE, model='Model-1', modelPrint=OFF,
    multiprocessingMode=DEFAULT, name='LinearBL',
nodalOutputPrecision=SINGLE,
    numCpus=1, numGPUs=0, queue=None, resultsFormat=ODB, scratch='', type=
    ANALYSIS, userSubroutine='', waitHours=0, waitMinutes=0)
# submitting the "Linear buckling" job:
mdb.jobs['LinearBL'].submit(consistencyChecking=OFF)
# generating the "second step/nonlinear buckling":
mdb.models['Model-1'].StaticStep(adaptiveDampingRatio=0.05,
    continueDampingFactors=False, initialInc=4.0, maxInc=4.0,
maxNumInc=1000000
    , minInc=1e-40, name='Step-2', nlgeom=ON, previous='Step-1',
    stabilizationMagnitude=0.0002, stabilizationMethod=
    DISSIPATED_ENERGY_FRACTION, timePeriod=360.0)
mdb.models['Model-
1'].boundaryConditions['Top_Disp'].setValuesInStep(stepName=
    'Step-2', u3=-6.0)
mdb.models['Model-1'].steps['Step-2'].control.setValues(allowPropagation=OFF,
    resetDefaultValues=OFF, timeIncrementation=(4.0, 8.0, 9.0, 16.0, 10.0, 4.0,
    12.0, 10.0, 6.0, 3.0, 50.0))
```

```
# defining the "Integrated output section" geometry:
mdb.models['Model-1'].rootAssembly.Surface(name='Surf-2', side1Faces=
    mdb.models['Model-1'].rootAssembly.instances['Part-1-1'].faces.findAt(((
    -((b/2)-1.3), ((h/2)-36.7), 0.0), ), ((((b/2)-1.8), ((h/2)-36.7), 0.0), ), ((
    -((b/2)-1.8), -((h/2)-36.7), 0.0), ), ((((b/2)-1.3), -((h/2)-36.7), 0.0), ), ))
mdb.models['Model-1'].IntegratedOutputSection(name='Bot_Reaction', surface=
    mdb.models['Model-1'].rootAssembly.surfaces['Surf-2'])
# requesting the "Field output":
mdb.models['Model-1'].fieldOutputRequests['F-Output-2'].setValues(variables=(
    'S', 'PE', 'PEEQ', 'PEMAG', 'LE', 'U', 'RF', 'CF', 'CSTRESS', 'CDISP',
    'DAMAGEFT', 'DAMAGEFC', 'DAMAGEMT', 'DAMAGEMC',
'DAMAGESHR', 'DMICRT'))
# requesting the "History output":
mdb.models['Model-1'].HistoryOutputRequest(createStepName='Step-2', name=
    'Top_Disp', rebar=EXCLUDE, region=
    mdb.models['Model-1'].rootAssembly.sets['Top_point'], sectionPoints=DEFAULT
    , variables=('U1', 'U2', 'U3', 'UR1', 'UR2', 'UR3'))
mdb.models['Model-1'].HistoryOutputRequest(createStepName='Step-2',
    integratedOutputSection='Bot_Reaction', name='Bot_R', rebar=EXCLUDE,
    sectionPoints=DEFAULT, variables=('SOF', 'SOM'))
# requesting the "Geometric imperfiction":
mdb.models['Model-
1'].keywordBlock.synchVersions(storeNodesAndElements=False)
mdb.models['Model-1'].keywordBlock.replace(45,
```

```
    '\n** ---------------------------------------------------------------\n**
\n*IMPERFECTION, FILE=LinearBL, STEP=1\n1, 5e-4\n2, 5e-4\n3, 5e-4\n**')
# executing the “second step/nonlinear buckling”:
mdb.Job(atTime=None, contactPrint=OFF, description='', echoPrint=OFF,
    explicitPrecision=SINGLE, getMemoryFromAnalysis=True, historyPrint=OFF,
    memory=90, memoryUnits=PERCENTAGE, model='Model-1', modelPrint=OFF,
    multiprocessingMode=DEFAULT, name='NonlinearBL', nodalOutputPrecision=
    SINGLE, numCpus=1, numDomains=1, numGPUs=0, queue=None,
resultsFormat=ODB,
    scratch='', type=ANALYSIS, userSubroutine='', waitHours=0, waitMinutes=0)
# writing the “input file”:
mdb.jobs['NonlinearBL'].writeInput(consistencyChecking=OFF)
# closing the “model database”:
mdb.close()
```

2. ODB (output database) script:

```
# -*- coding: mbcs -*-
# Abaqus/Viewer Release 2019 replay file
# Internal Version: 2016_09_28-07.54.59 126836
# Run by U1122090 on Mon Apr 05 11:57:31 2021
# from driverUtils import executeOnCaeGraphicsStartup
# executeOnCaeGraphicsStartup()
#: Executing "onCaeGraphicsStartup()" in the site directory ...
# importing the required modules:
from abaqus import *
```

```
from abaqusConstants import *

# assigning the "session veiwport":

session.Viewport(name='Viewport: 1', origin=(0.0, 0.0), width=125.046257019043,
    height=146.844451904297)

session.viewports['Viewport: 1'].makeCurrent()

session.viewports['Viewport: 1'].maximize()

from viewerModules import *

from driverUtils import executeOnCaeStartup

executeOnCaeStartup()

o2 = session.openOdb(name='NonlinearBL.odb')

#: Model: C:/Simulations/Compression/11/NonlinearBL.odb

#: Number of Assemblies:         1

#: Number of Assembly instances: 0

#: Number of Part instances:     1

#: Number of Meshes:             1

#: Number of Element Sets:       6

#: Number of Node Sets:          5

#: Number of Steps:              2

session.viewports['Viewport: 1'].setValues(displayedObject=o2)

# locating the "ODB file directory":

odb = session.odbs['C:/Simulations/GA/Compression/NonlinearBL.odb']

# requesting the "axial displacement":

xy_result = session.XYDataFromHistory(name='Disp', odb=odb,

    outputVariableName='Spatial displacement: U3 at Node 38 in NSET
TOP_POINT',
```

```
    steps=('Step-2', ), __linkedVpName__='Viewport: 1')
c1 = session.Curve(xyData=xy_result)
xyp = session.XYPlot('XYPlot-1')
chartName = xyp.charts.keys()[0]
chart = xyp.charts[chartName]
chart.setValues(curvesToPlot=(c1, ), )
session.viewports['Viewport: 1'].setValues(displayedObject=xyp)
odb = session.odbs['C:/Simulations/GA/Compression/NonlinearBL.odb']
# requesting the “axial load”:
xy_result = session.XYDataFromHistory(name='Ld', odb=odb,
    outputVariableName='Total force on the surface: SOF3  on section
BOT_REACTION in SSET SURF-2',
    steps=('Step-2', ), __linkedVpName__='Viewport: 1')
c1 = session.Curve(xyData=xy_result)
# generating the “load-displacement” curve:
xyp = session.xyPlots['XYPlot-1']
chartName = xyp.charts.keys()[0]
chart = xyp.charts[chartName]
chart.setValues(curvesToPlot=(c1, ), )
xy1 = session.xyDataObjects['Disp']
xy2 = session.xyDataObjects['Ld']
xy3 = combine(-1*xy1, -1*xy2)
xy3.setValues(sourceDescription='combine (  - 1 * "Disp", - 1 * "Ld" )')
tmpName = xy3.name
session.xyDataObjects.changeKey(tmpName, 'Load')
```

```
x0 = session.xyDataObjects['Load']

# writing the “load-displacement” curve in text file:

session.writeXYReport(fileName='abaqus.txt', appendMode=OFF, xyData=(x0, ))

# close the “output database”:

odb.close()
```

3. Execution script:

```
# importing the required module:

import os

# command prompt commands to run the scripts:

os.system('cmd /c "abaqus cae noGUI=model.py"')

os.system('cmd /c "abaqus j=NonlinearBL int"')

os.system('cmd /c "abaqus cae noGUI=ODB.py"')
```

C.3 Hollow box pultruded FRP profile subjected to four-point bending

C.3.1 MATLAB scripts

1. Constraints function:

```
% constraints function of axial stiffness and strength
% the design variables are:
 % x(1): wall thickness (t)
 % x(2): cross-sectional aspect ratio (h/b)
 % x(3): corner radii ratio (r/R)
 % x(4): winding angle
 % x(5): axial fibre percentage
 function [c, ceq] = Constraints(x) % constraints function of axial stiffness and
strength
```

ceq = []; % no equality constraints

R = [x(1) x(2) x(3) x(4) x(5)]; % design variables vector

Log1 = xlsread('Log_Bending.xlsx','Sheet1'); % reading from library

Log2 = Log1(:,1:5); % matrix of design variables inserted from the library

[C,ia,ib] = intersect(Log2,R,'rows'); % comparing the current configuration with the data from the library

if ib == 1 % the current configuration exists in the library

c = [-Log1(ia,6)+ $\frac{EI}{L^3}(X,Y)$; -Log1(ia,7)+ $\sigma_{control}$]; % assigning the inequality constraints

else % the current configuration does not exist in the library

fid = fopen('design.dat', 'w'); % open a file to write the current configuration

fprintf(fid, '%f %f %d %d %f\n', R); % print the design parameters

fclose(fid); % close the file

[status,cmdout] = system(['starter.py']); % run the python script

% script for importing the FEM results from the following text file:

filename = 'C:\Simulations\GA\Bending\abaqus.txt'; % FEM results text file

startRow = 2;

formatSpec = '%29f%16f%[^\n\r]';

% open the text file

fileID = fopen(filename,'r');

% read columns of data according to the format.

textscan(fileID, '%[^\n\r]', startRow-1, 'WhiteSpace', '', 'ReturnOnError', false, 'EndOfLine', '\r\n');

dataArray = textscan(fileID, formatSpec, 'Delimiter', '', 'WhiteSpace', '', 'TextType', 'string', 'EmptyValue', NaN, 'ReturnOnError', false);

% close the text file.

fclose(fileID);

% create output variable

abaqus = [dataArray{1:end-1}];

% clear temporary variables

clearvars filename startRow formatSpec fileID dataArray ans;

% moment of inertia of the profile

MoI = ((((200/(x(2)+1)))*((200-(200/(x(2)+1))))^3)/(12))-((10)^4/(3))-((10)^2*(((200-(200/(x(2)+1))))-(10))^2)...

+(((3.14159265359)*(10)^4)/(4))-(((16)*(10)^4)/(9*3.14159265359))...

+((3.14159265359)*(10)^2*((((200-(200/(x(2)+1))))/(2))-(10)+((4*10)/(3*3.14159265359)))^2)...

-(((((200/(x(2)+1)))-(2*x(1)))*(((200-(200/(x(2)+1))))-(2*x(1)))^3)/(12))+((x(3))^4/(3))...

+((x(3))^2*((((200-(200/(x(2)+1))))-(2*x(1)))-(x(3)))^2)-(((3.14159265359)*(x(3))^4)/(4))...

+(((16)*(x(3))^4)/(9*3.14159265359))...

-((3.14159265359)*(x(3))^2*(((((200-(200/(x(2)+1))))-(2*x(1)))/(2))-(x(3))+(((4)*(x(3)))/(3*3.14159265359)))^2);

Centroid = ((200-(200/(x(2)+1))))/2; % the profile centroid

a = 838; % the shear span length

Half_P = max(abaqus(:,2))/2; % P/2

Moment = Half_P*a; % bending moment

Stiff = -(abaqus(5,2)/abaqus(5,1))+ $\frac{EI}{L^3}(X,Y)$; % calculating the axial stiffness constraint

Str = -(Moment*Centroid/MoI)+ $\sigma_{control}$; % calculating the flexural strength constraint

c = [Stiff; Str]; % assigning the inequality constraints

T = 2*(200-(200/(x(2)+1)))*x(1)+2*(200/(x(2)+1))*x(1)-4*(x(1))^2-(4-3.14159265359)*((10)^2-(x(3))^2); % cross-sectional area of the profile

i = xlsread('Timer.xlsx','Sheet1','A1'); % import external timer

Log1(1697+i,1) = x(1); % assigning the new value of x(1) variable

Log1(1697+i,2) = x(2); % assigning the new value of x(2) variable

Log1(1697+i,3) = x(3); % assigning the new value of x(3) variable

Log1(1697+i,4) = x(4); % assigning the new value of x(4) variable

Log1(1697+i,5) = x(5); % assigning the new value of x(5) variable

Log1(1697+i,6) = (abaqus(5,2)/abaqus(5,1)); % assigning the new axial stiffness

Log1(1697+i,7) = (Moment*Centroid/MoI); % assigning the new strength

Log1(1697+i,8) = T; % assigning the new cross-sectional area

```
    filename = 'Log_Bending.xlsx'; % assigning the library for writing
    writematrix(Log1,filename,'sheet',1); % writing the new data in the library
    i = i + 1; % timer to move down one row in the library
    Timername = 'Timer.xlsx'; % assigning the new timer value
    writematrix(i,Timername,'sheet',1); % writing the new timer value
 end
 end
```

2. Fitness function:

```
% fitness function of the cross-sectional area (A)
% the design variables are:
 % x(1): wall thickness (t)
 % x(2): cross-sectional aspect ratio (h/b)
 % x(3): corner radii ratio (r/R)
 % x(4): winding angle
 % x(5): axial fibre percentage
 function A = Fitnessfunction(x) % fitness function of the cross-sectional area
 A = 2*(200-(200/(x(2)+1)))*x(1)+2*(200/(x(2)+1))*x(1)-4*(x(1))^2-(4-
3.14159265359)*((10)^2-(x(3))^2); % the cross-sectional area function
 end
```

3. “MI-LXPM” genetic algorithm function:

```
% “MI-LXPM” GA script
% the design variables are:
 % x(1): wall thickness (t)
 % x(2): cross-sectional aspect ratio (h/b)
 % x(3): corner radii ratio (r/R)
 % x(4): winding angle
 % x(5): axial fibre percentage
ObjFcn=@Fitnessfunction; % assigning the fitness function
nvars = 5; % assigning the number of variables
LB = [2 1 0.5 20 0.6]; % assigning the lower bounds of the variables
```

UB = [12 3 2.5 80 0.9]; % assigning the upper bounds of the variables

ConsFcn=@Constraints; % assigning the constraints function

IntCon = [4]; % assigning the location of the integer variable

% “MI-LXPM” GA options:

options =

optimoptions('ga','PlotFcn','gaplotbestf','Display','iter','PopulationSize',20,...

'EliteCount', 1,'CrossoverFraction', 1.0,'Generations', 30,'StallGenLimit',15);

% GA solver:

[x, fval, exitflag, output, population, scores] = ga(ObjFcn, nvars, [], [], [], [], LB, UB,...

ConsFcn, IntCon, options);

C.3.2 Python scripts

1. Model script:

-*- coding: mbcs -*-

importing the required modules:

from part import *

from material import *

from section import *

from assembly import *

from step import *

from interaction import *

from load import *

from mesh import *

from optimization import *

from job import *

from sketch import *

```
from visualization import *
from connectorBehavior import *
# importing the design variables from MATLAB:
f = open("design.dat", "r")
[t, h_b, r, deg, Axial_fibre_ratio] = [float(x) for x in f.readline().split()]
f.close()
# adjusting the variables to the code:
b = (200/((h_b)+1))
h = 200 - b
ta = Axial_fibre_ratio / 3 # Ply thickness of axial fibres.
Wound_fibre_ratio = 1.0 - Axial_fibre_ratio
tw = Wound_fibre_ratio / 4 # Ply thickness of wound fibres.
# generating the "Part" geometry:
mdb.models['Model-1'].ConstrainedSketch(name='__profile__', sheetSize=200.0)
mdb.models['Model-1'].sketches['__profile__'].rectangle(point1=(-(b/2), -(h/2)),
    point2=((b/2), (h/2)))
mdb.models['Model-1'].sketches['__profile__'].geometry.findAt((-(b/2), 0.0))
mdb.models['Model-1'].sketches['__profile__'].geometry.findAt((0.0, (h/2)))
mdb.models['Model-1'].sketches['__profile__'].geometry.findAt(((b/2), 0.0))
mdb.models['Model-1'].sketches['__profile__'].geometry.findAt((0.0, -(h/2)))
mdb.models['Model-1'].sketches['__profile__'].offset(distance=t, objectList=(
    mdb.models['Model-1'].sketches['__profile__'].geometry.findAt((-(b/2), 0.0),
    ), mdb.models['Model-1'].sketches['__profile__'].geometry.findAt((0.0,
    (h/2)), ), mdb.models['Model-1'].sketches['__profile__'].geometry.findAt((
```

```
    (b/2), 0.0), ),
    mdb.models['Model-1'].sketches['__profile__'].geometry.findAt((0.0, -(h/2)),
    )), side=LEFT)
mdb.models['Model-1'].sketches['__profile__'].geometry.findAt((-(b/2), 0.0))
mdb.models['Model-1'].sketches['__profile__'].geometry.findAt((0.0, (h/2)))
mdb.models['Model-1'].sketches['__profile__'].FilletByRadius(curve1=
    mdb.models['Model-1'].sketches['__profile__'].geometry.findAt((-(b/2), 0.0),
    ), curve2=mdb.models['Model-1'].sketches['__profile__'].geometry.findAt((
    0.0, (h/2)), ), nearPoint1=(-((b/2)-0.3), ((h/2)-3)), nearPoint2=
    (-((b/2)-6.5), ((h/2)+1.2)), radius=10.0)
mdb.models['Model-1'].sketches['__profile__'].geometry.findAt((0.0, (h/2)))
mdb.models['Model-1'].sketches['__profile__'].geometry.findAt(((b/2), 0.0))
mdb.models['Model-1'].sketches['__profile__'].FilletByRadius(curve1=
    mdb.models['Model-1'].sketches['__profile__'].geometry.findAt((0.0, (h/2)),
    ), curve2=mdb.models['Model-1'].sketches['__profile__'].geometry.findAt((
    (b/2), 0.0), ), nearPoint1=(-((b/2)-27.1), ((h/2)+1)),
    nearPoint2=(((b/2)-1.2), ((h/2)-6.5)), radius=10.0)
mdb.models['Model-1'].sketches['__profile__'].geometry.findAt(((b/2), 0.0))
mdb.models['Model-1'].sketches['__profile__'].geometry.findAt((0.0, -(h/2)))
mdb.models['Model-1'].sketches['__profile__'].FilletByRadius(curve1=
    mdb.models['Model-1'].sketches['__profile__'].geometry.findAt(((b/2), 0.0),
    ), curve2=mdb.models['Model-1'].sketches['__profile__'].geometry.findAt((
    0.0, -(h/2)), ), nearPoint1=((b/2), -((h/2)-12.5)),
    nearPoint2=(((b/2)-8.2), -((h/2)+0.8)), radius=10.0)
```

```
mdb.models['Model-1'].sketches['__profile__'].geometry.findAt((0.0, -(h/2)))
mdb.models['Model-1'].sketches['__profile__'].geometry.findAt((-(b/2), 0.0))
mdb.models['Model-1'].sketches['__profile__'].FilletByRadius(curve1=
    mdb.models['Model-1'].sketches['__profile__'].geometry.findAt((0.0,
    -(h/2)), ), curve2=
    mdb.models['Model-1'].sketches['__profile__'].geometry.findAt((-(b/2),
    0.0), ), nearPoint1=(-((b/2)-5.5), -((h/2)+0.5)), nearPoint2=(
    -((b/2)-1.3), -((h/2)-6)), radius=10.0)
mdb.models['Model-1'].sketches['__profile__'].geometry.findAt((-((b/2)-t), 0.0))
mdb.models['Model-1'].sketches['__profile__'].geometry.findAt((0.0, ((h/2)-t)))
mdb.models['Model-1'].sketches['__profile__'].FilletByRadius(curve1=
    mdb.models['Model-1'].sketches['__profile__'].geometry.findAt((-((b/2)-t), 0.0),
    ), curve2=mdb.models['Model-1'].sketches['__profile__'].geometry.findAt((
    0.0, ((h/2)-t)), ), nearPoint1=(-((b/2)-5.6), ((h/2)-11.2)), nearPoint2=(
    -((b/2)-11.6), ((h/2)-5.4)), radius=r)
mdb.models['Model-1'].sketches['__profile__'].geometry.findAt((0.0, ((h/2)-t)))
mdb.models['Model-1'].sketches['__profile__'].geometry.findAt((((b/2)-t), 0.0))
mdb.models['Model-1'].sketches['__profile__'].FilletByRadius(curve1=
    mdb.models['Model-1'].sketches['__profile__'].geometry.findAt((0.0, ((h/2)-t)),
    ), curve2=mdb.models['Model-1'].sketches['__profile__'].geometry.findAt((
    ((b/2)-t), 0.0), ), nearPoint1=(-((b/2)-39.5), ((h/2)-5.2)),
    nearPoint2=(((b/2)-6), ((h/2)-15)), radius=r)
mdb.models['Model-1'].sketches['__profile__'].geometry.findAt((((b/2)-t), 0.0))
mdb.models['Model-1'].sketches['__profile__'].geometry.findAt((0.0, -((h/2)-t)))
```

```
mdb.models['Model-1'].sketches['__profile__'].FilletByRadius(curve1=
    mdb.models['Model-1'].sketches['__profile__'].geometry.findAt((((b/2)-t), 0.0),
    ), curve2=mdb.models['Model-1'].sketches['__profile__'].geometry.findAt((
    0.0, -((h/2)-t)), ), nearPoint1=(((b/2)-5), -((h/2)-45.4)),
    nearPoint2=(((b/2)-14.2), -((h/2)-4.5)), radius=r)
mdb.models['Model-1'].sketches['__profile__'].geometry.findAt((0.0, -((h/2)-t)))
mdb.models['Model-1'].sketches['__profile__'].geometry.findAt((-((b/2)-t), 0.0))
mdb.models['Model-1'].sketches['__profile__'].FilletByRadius(curve1=
    mdb.models['Model-1'].sketches['__profile__'].geometry.findAt((0.0,
    -((h/2)-t)), ), curve2=
    mdb.models['Model-1'].sketches['__profile__'].geometry.findAt((-((b/2)-t),
    0.0), ), nearPoint1=(-((b/2)-35), ((h/2)-6)), nearPoint2=(
    -((b/2)-6.3), -((h/2)-14.2)), radius=r)
mdb.models['Model-1'].Part(dimensionality=THREE_D, name='Part-1', type=
    DEFORMABLE_BODY)
mdb.models['Model-1'].parts['Part-1'].BaseSolidExtrude(depth=2235.0, sketch=
    mdb.models['Model-1'].sketches['__profile__'])
del mdb.models['Model-1'].sketches['__profile__']
mdb.models['Model-1'].parts['Part-1'].DatumPlaneByPrincipalPlane(offset=0.0,
    principalPlane=YZPLANE)
mdb.models['Model-1'].parts['Part-1'].DatumPlaneByPrincipalPlane(offset=0.0,
    principalPlane=XZPLANE)
mdb.models['Model-1'].parts['Part-1'].PartitionCellByDatumPlane(cells=
    mdb.models['Model-1'].parts['Part-1'].cells.findAt(((-((b/2)-0.1), ((h/2)-15),
```

```
    333.333333), )), datumPlane=
    mdb.models['Model-1'].parts['Part-1'].datums[2])
mdb.models['Model-1'].parts['Part-1'].PartitionCellByDatumPlane(cells=
    mdb.models['Model-1'].parts['Part-1'].cells.findAt(((-((b/2)-t), ((h/2)-36.7),
    333.333333), ), ((((b/2)-t), ((h/2)-36.7), 333.333333), ), ), datumPlane=
    mdb.models['Model-1'].parts['Part-1'].datums[3])
mdb.models['Model-1'].parts['Part-1'].DatumPlaneByPrincipalPlane(offset=888.0,
    principalPlane=XYPLANE)
mdb.models['Model-1'].parts['Part-1'].DatumPlaneByPrincipalPlane(offset=988.0,
    principalPlane=XYPLANE)
mdb.models['Model-1'].parts['Part-1'].DatumPlaneByPrincipalPlane(offset=1247.0,
    principalPlane=XYPLANE)
mdb.models['Model-1'].parts['Part-1'].DatumPlaneByPrincipalPlane(offset=1347.0,
    principalPlane=XYPLANE)
mdb.models['Model-1'].parts['Part-1'].DatumPlaneByPrincipalPlane(offset=-((b/2)-
10),
    principalPlane=YZPLANE)
mdb.models['Model-1'].parts['Part-1'].DatumPlaneByPrincipalPlane(offset=((b/2)-
10),
    principalPlane=YZPLANE)
mdb.models['Model-1'].parts['Part-1'].PartitionCellByDatumPlane(cells=
    mdb.models['Model-1'].parts['Part-1'].cells.findAt(((-(b/2), ((h/2)-15),
    1490.0), ), ((((b/2)-10), -((h/2)-t), 1490.0), ), ((((b/2)-10), ((h/2)-t), 745.0), ), (
    (-(b/2), -((h/2)-15), 745.0), ), ), datumPlane=
    mdb.models['Model-1'].parts['Part-1'].datums[6])
```

```
mdb.models['Model-1'].parts['Part-1'].PartitionCellByDatumPlane(cells=
    mdb.models['Model-1'].parts['Part-1'].cells.findAt(((-((b/2)-t), -((h/2)-15),
    1337.0), ), (((b/2), -((h/2)-15), 1337.0), ), ((((b/2)-t), ((h/2)-15), 1337.0), ),
    ((-(b/2), ((h/2)-15), 1337.0), ), ), datumPlane=
    mdb.models['Model-1'].parts['Part-1'].datums[7])
mdb.models['Model-1'].parts['Part-1'].PartitionCellByDatumPlane(cells=
    mdb.models['Model-1'].parts['Part-1'].cells.findAt(((((b/2)-t), ((h/2)-15),
    1403.666667), ), ((-(b/2), ((h/2)-15), 1403.666667), ), (((b/2), -((h/2)-15),
    1403.666667), ), ((-(b/2), -((h/2)-15), 1403.666667), ), ), datumPlane=
    mdb.models['Model-1'].parts['Part-1'].datums[8])
mdb.models['Model-1'].parts['Part-1'].PartitionCellByDatumPlane(cells=
    mdb.models['Model-1'].parts['Part-1'].cells.findAt(((-((b/2)-t), -((h/2)-15),
    1576.333333), ), (((b/2), -((h/2)-15), 1576.333333), ), ((-(b/2), ((h/2)-15),
    1576.333333), ), (((b/2), ((h/2)-15), 1576.333333), ), ), datumPlane=
    mdb.models['Model-1'].parts['Part-1'].datums[9])
mdb.models['Model-1'].parts['Part-1'].PartitionCellByDatumPlane(cells=
    mdb.models['Model-1'].parts['Part-1'].cells.findAt(((-((b/2)-10), ((h/2)-t),
    1313.666667), ), ((-(b/2), ((h/2)-15), 1643.0), ), ((-(b/2), -((h/2)-15),
    1643.0), ), ((-((b/2)-10), -(h/2), 1160.666667), ), ((-(b/2), ((h/2)-15),
    1160.666667), ), ((-((b/2)-10), -(h/2), 1313.666667), ), ((-(b/2), ((h/2)-15),
    954.666667), ), ((-(b/2), -((h/2)-15), 592.0), ), ((-((b/2)-10), -(h/2),
    954.666667), ), ((-(b/2), ((h/2)-15), 592.0), ), ), datumPlane=
    mdb.models['Model-1'].parts['Part-1'].datums[10])
mdb.models['Model-1'].parts['Part-1'].PartitionCellByDatumPlane(cells=
```

```
    mdb.models['Model-1'].parts['Part-1'].cells.findAt(((((b/2)-15), (h/2),
    1313.666667), ), (((b/2), -((h/2)-15), 1313.666667), ), ((((b/2)-t), ((h/2)-15),
    1643.0), ), (((b/2), -((h/2)-15), 1643.0), ), ((((b/2)-15), -((h/2)-t),
    1160.666667), ), ((((b/2)-15), (h/2), 954.666667), ), ((((b/2)-15), -((h/2)-t),
    954.666667), ), ((((b/2)-15), (h/2), 1160.666667), ), ((((b/2)-t), -((h/2)-15),
    592.0), ), (((b/2), ((h/2)-15), 592.0), ), ), datumPlane=
    mdb.models['Model-1'].parts['Part-1'].datums[11])
# generating the “Mesh”:
mdb.models['Model-1'].parts['Part-1'].seedPart(deviationFactor=0.1,
    minSizeFactor=0.1, size=7.0)
mdb.models['Model-1'].parts['Part-1'].seedEdgeByNumber(constraint=FINER,
edges=
    mdb.models['Model-1'].parts['Part-1'].edges.findAt(((-(b/2),
    -((h/2)-9.99999), 2235.0), ), (((b/2), -((h/2)-9.99999), 2235.0), ), (((b/2),
    ((h/2)-9.99999), 2235.0), ), ((-(b/2), ((h/2)-9.99999), 2235.0), ), ), number=3)
mdb.models['Model-1'].parts['Part-1'].seedEdgeByNumber(constraint=FINER,
edges=
    mdb.models['Model-1'].parts['Part-1'].edges.findAt(((-((b/2)-1.3), 0.0, 2235.0), ),
    ((((b/2)-1.3), 0.0, 2235.0), ), ((0.0, -((h/2)-1.3), 2235.0), ), ((0.0, ((h/2)-1.3),
2235.0), ), ),
    number=5)
mdb.models['Model-1'].parts['Part-1'].assignStackDirection(cells=
    mdb.models['Model-1'].parts['Part-1'].cells.findAt((((b/2), -((h/2)-15),
    1643.0), ), (((b/2), -((h/2)-15), 1160.666667), ), (((b/2), -((h/2)-15),
    954.666667), ), (((b/2), -((h/2)-15), 592.0), ), ((((b/2)-15), -(h/2), 1643.0),
```

```
), ((((b/2)-15), -((h/2)-t), 1160.666667), ), ((((b/2)-15), -((h/2)-t), 954.666667), ),
((((b/2)-15), -((h/2)-t), 592.0), ), ((((b/2)-15), -(h/2), 1313.666667), ), ((
((b/2)-15), (h/2), 592.0), ), ((((b/2)-15), (h/2), 954.666667), ), ((((b/2)-15),
(h/2), 1160.666667), ), ((((b/2)-15), ((h/2)-t), 1643.0), ), ((((b/2)-t), ((h/2)-15),
592.0), ), ((((b/2)-t), ((h/2)-15), 954.666667), ), ((((b/2)-t), ((h/2)-15),
1160.666667), ), ((((b/2)-t), ((h/2)-15), 1643.0), ), ((((b/2)-15), ((h/2)-t),
1313.666667), ), ((-((b/2)-15), -((h/2)-t), 1313.666667), ), ((-((b/2)-15), -((h/2)-t),
1160.666667), ), ((-((b/2)-15), -((h/2)-t), 954.666667), ), ((-((b/2)-15), -((h/2)-t),
592.0), ), ((-((b/2)-9.99999), -(h/2), 1313.666667), ), ((-((b/2)-t), -((h/2)-15),
1160.666667), ), ((-((b/2)-9.99999), -(h/2), 954.666667), ), ((-((b/2)-9.99999),
-(h/2), 592.0), ), ((-((b/2)-15), -((h/2)-t), 1643.0), ), ((-((b/2)-9.99999),
(h/2), 592.0), ), ((-((b/2)-9.99999), (h/2), 954.666667), ), ((-(b/2),
((h/2)-15), 1160.666667), ), ((-((b/2)-9.99999), (h/2), 1643.0), ), ((
-((b/2)-15), (h/2), 592.0), ), ((-((b/2)-15), (h/2), 954.666667), ), ((
-((b/2)-15), (h/2), 1160.666667), ), ((-((b/2)-15), ((h/2)-t), 1643.0), ), ((
-((b/2)-9.99999), (h/2), 1313.666667), ), ((((b/2)-9.99999), (h/2),
1313.666667), ), ((-((b/2)-15), (h/2), 1313.666667), ), ((((b/2)-9.99999),
-(h/2), 1313.666667), ), ((-((b/2)-t), -((h/2)-15), 1643.0), ), ),
referenceRegion=mdb.models['Model-1'].parts['Part-1'].faces.findAt((
-((b/2)-15), (h/2), 1643.0), ))
mdb.models['Model-1'].parts['Part-1'].setMeshControls(algorithm=MEDIAL_AXIS,
regions=mdb.models['Model-1'].parts['Part-1'].cells.findAt((((b/2), -((h/2)-15),
1643.0), ), (((b/2), -((h/2)-15), 1160.666667), ), (((b/2), -((h/2)-15),
954.666667), ), (((b/2), -((h/2)-15), 592.0), ), ((((b/2)-15), -(h/2), 1643.0),
```

```
    ), ((((b/2)-15), -((h/2)-t), 1160.666667), ), ((((b/2)-15), -((h/2)-t), 954.666667), ),
    ((((b/2)-15), -((h/2)-t), 592.0), ), ((((b/2)-15), -(h/2), 1313.666667), ), ((
    ((b/2)-15), (h/2), 592.0), ), ((((b/2)-15), (h/2), 954.666667), ), ((((b/2)-15),
    (h/2), 1160.666667), ), ((((b/2)-15), ((h/2)-t), 1643.0), ), ((((b/2)-t), ((h/2)-15),
    592.0), ), ((((b/2)-t), ((h/2)-15), 954.666667), ), ((((b/2)-t), ((h/2)-15),
    1160.666667), ), ((((b/2)-t), ((h/2)-15), 1643.0), ), ((((b/2)-15), ((h/2)-t),
    1313.666667), ), ((-((b/2)-15), -((h/2)-t), 1313.666667), ), ((-((b/2)-15), -((h/2)-t),
    1160.666667), ), ((-((b/2)-15), -((h/2)-t), 954.666667), ), ((-((b/2)-15), -((h/2)-t),
    592.0), ), ((-((b/2)-9.99999), -(h/2), 1313.666667), ), ((-((b/2)-t), -((h/2)-15),
    1160.666667), ), ((-((b/2)-9.99999), -(h/2), 954.666667), ), ((-((b/2)-9.99999),
    -(h/2), 592.0), ), ((-((b/2)-15), -((h/2)-t), 1643.0), ), ((-((b/2)-9.99999),
    (h/2), 592.0), ), ((-((b/2)-9.99999), (h/2), 954.666667), ), ((-(b/2),
    ((h/2)-15), 1160.666667), ), ((-((b/2)-9.99999), (h/2), 1643.0), ), ((
    -((b/2)-15), (h/2), 592.0), ), ((-((b/2)-15), (h/2), 954.666667), ), ((
    -((b/2)-15), (h/2), 1160.666667), ), ((-((b/2)-15), ((h/2)-t), 1643.0), ), ((
    -((b/2)-9.99999), (h/2), 1313.666667), ), ((((b/2)-9.99999), (h/2),
    1313.666667), ), ((-((b/2)-15), (h/2), 1313.666667), ), ((((b/2)-9.99999),
    -(h/2), 1313.666667), ), ((-((b/2)-t), -((h/2)-15), 1643.0), ), ), technique=
    SWEEP)
mdb.models['Model-1'].parts['Part-1'].generateMesh()
mdb.models['Model-1'].parts['Part-1'].setElementType(elemTypes=(ElemType(
    elemCode=SC8R, elemLibrary=STANDARD, secondOrderAccuracy=OFF,
    hourglassControl=DEFAULT), ElemType(elemCode=SC6R,
elemLibrary=STANDARD),
```

```
    ElemType(elemCode=UNKNOWN_TET, elemLibrary=STANDARD)),
regions=(
    mdb.models['Model-1'].parts['Part-1'].cells.findAt((((b/2), -((h/2)-15),
    1643.0), ), (((b/2), -((h/2)-15), 1160.666667), ), (((b/2), -((h/2)-15),
    954.666667), ), (((b/2), -((h/2)-15), 592.0), ), ((((b/2)-15), -(h/2), 1643.0),
    ), ((((b/2)-15), -((h/2)-t), 1160.666667), ), ((((b/2)-15), -((h/2)-t), 954.666667), ),
    ((((b/2)-15), -((h/2)-t), 592.0), ), ((((b/2)-15), -(h/2), 1313.666667), ), ((
    ((b/2)-15), (h/2), 592.0), ), ((((b/2)-15), (h/2), 954.666667), ), ((((b/2)-15),
    (h/2), 1160.666667), ), ((((b/2)-15), ((h/2)-t), 1643.0), ), ((((b/2)-t), ((h/2)-15),
    592.0), ), ((((b/2)-t), ((h/2)-15), 954.666667), ), ((((b/2)-t), ((h/2)-15),
    1160.666667), ), ((((b/2)-t), ((h/2)-15), 1643.0), ), ((((b/2)-15), ((h/2)-t),
    1313.666667), ), ((-((b/2)-15), -((h/2)-t), 1313.666667), ), ((-((b/2)-15), -((h/2)-t),
    1160.666667), ), ((-((b/2)-15), -((h/2)-t), 954.666667), ), ((-((b/2)-15), -((h/2)-t),
    592.0), ), ((-((b/2)-9.99999), -(h/2), 1313.666667), ), ((-((b/2)-t), -((h/2)-15),
    1160.666667), ), ((-((b/2)-9.99999), -(h/2), 954.666667), ), ((-((b/2)-9.99999),
    -(h/2), 592.0), ), ((-((b/2)-15), -((h/2)-t), 1643.0), ), ((-((b/2)-9.99999),
    (h/2), 592.0), ), ((-((b/2)-9.99999), (h/2), 954.666667), ), ((-(b/2),
    ((h/2)-15), 1160.666667), ), ((-((b/2)-9.99999), (h/2), 1643.0), ), ((
    -((b/2)-15), (h/2), 592.0), ), ((-((b/2)-15), (h/2), 954.666667), ), ((
    -((b/2)-15), (h/2), 1160.666667), ), ((-((b/2)-15), ((h/2)-t), 1643.0), ), ((
    -((b/2)-9.99999), (h/2), 1313.666667), ), ((((b/2)-9.99999), (h/2),
    1313.666667), ), ((-((b/2)-15), (h/2), 1313.666667), ), ((((b/2)-9.99999),
    -(h/2), 1313.666667), ), ((-((b/2)-t), -((h/2)-15), 1643.0), ), ), ))
# generating the “Materials” properties:
mdb.models['Model-1'].Material(name='Material-1')
```

```
mdb.models['Model-1'].materials['Material-1'].Density(table=((2.03e-09, ), ))
mdb.models['Model-1'].materials['Material-1'].Elastic(table=((45700.0, 12100.0,
    0.28, 4600.0, 4600.0, 4000.0), ), type=LAMINA)
mdb.models['Model-1'].materials['Material-1'].HashinDamageInitiation(alpha=1.0,
    table=((803.0, 548.0, 43.0, 187.0, 64.0, 50.0), ))
mdb.models['Model-1'].Material(name='Material-1-Fail')
mdb.models['Model-1'].materials['Material-1-Fail'].Density(table=((2.03e-09, ), ))
mdb.models['Model-1'].materials['Material-1-Fail'].Elastic(table=((45700.0,
12100.0,
    0.28, 4600.0, 4600.0, 4000.0), ), type=LAMINA)
mdb.models['Model-1'].materials['Material-1-
Fail'].HashinDamageInitiation(alpha=1.0,
    table=((803.0, 548.0, 43.0, 187.0, 64.0, 50.0), ))
mdb.models['Model-1'].materials['Material-1-
Fail'].hashinDamageInitiation.DamageEvolution(
    table=((92.0, 79.0, 5.0, 5.0), ), type=ENERGY)
mdb.models['Model-1'].materials['Material-1-
Fail'].hashinDamageInitiation.DamageStabilization(
    fiberCompressiveCoeff=0.1, fiberTensileCoeff=0.1, matrixCompressiveCoeff=
    0.1, matrixTensileCoeff=0.1)
# generating the “Composite layup”:
mdb.models['Model-1'].parts['Part-1'].Surface(name='Surf-1', side1Faces=
    mdb.models['Model-1'].parts['Part-1'].faces.findAt((((b/2), ((h/2)-9.99999),
    1643.0), ), ((((b/2)-15), (h/2), 1643.0), ), ((-((b/2)-15), (h/2), 1643.0), ),
    ((-((b/2)-9.99999), (h/2), 1643.0), ), ((-((b/2)-15), -(h/2), 1643.0), ), ((
```

```
    -(b/2), ((h/2)-15), 1643.0), ), ((-(b/2), -((h/2)-9.99999), 1643.0), ), ((
    ((b/2)-15), -(h/2), 1643.0), ), ((((b/2)-9.99999), -(h/2), 1643.0), ), (((b/2),
    -((h/2)-15), 1643.0), ), (((b/2), ((h/2)-15), 1643.0), ), ((-(b/2), -((h/2)-15),
    1643.0), ), ))
mdb.models['Model-1'].parts['Part-1'].Set(edges=
    mdb.models['Model-1'].parts['Part-1'].edges.findAt(((((b/2)-10), (h/2), 1569.0),
    )), name='Set-6')
mdb.models['Model-1'].parts['Part-1'].CompositeLayup(description='',
    elementType=CONTINUUM_SHELL, name='CompositeLayup-1',
symmetric=False)
mdb.models['Model-1'].parts['Part-1'].compositeLayups['CompositeLayup-
1'].Section(
    integrationRule=SIMPSON, poissonDefinition=DEFAULT, preIntegrate=OFF,
    temperature=GRADIENT, thicknessModulus=None, useDensity=OFF)
mdb.models['Model-1'].parts['Part-1'].compositeLayups['CompositeLayup-
1'].CompositePly(
    additionalRotationField='', additionalRotationType=ROTATION_NONE,
angle=0.0
    , axis=AXIS_3, material='Material-1', numIntPoints=3, orientationType=
    SPECIFY_ORIENT, orientationValue=0.0, plyName='Ply-1', region=Region(
    cells=mdb.models['Model-1'].parts['Part-1'].cells.findAt((((b/2),
    -((h/2)-15), 1643.0), ), (((b/2), -((h/2)-15), 1160.666667), ), (((b/2),
    -((h/2)-15), 954.666667), ), (((b/2), -((h/2)-15), 592.0), ), ((((b/2)-15),
    -(h/2), 1643.0), ), ((((b/2)-15), -((h/2)-t), 1160.666667), ), ((((b/2)-15), -((h/2)-t),
    954.666667), ), ((((b/2)-15), -((h/2)-t), 592.0), ), ((((b/2)-15), -(h/2),
```

```
    1313.666667), ), ((((b/2)-t), ((h/2)-15), 592.0), ), ((((b/2)-t), ((h/2)-15),
    954.666667), ), ((((b/2)-t), ((h/2)-15), 1160.666667), ), ((((b/2)-t), ((h/2)-15),
    1643.0), ), ((-((b/2)-15), -((h/2)-t), 1313.666667), ), ((-((b/2)-15), -((h/2)-t),
    1160.666667), ), ((-((b/2)-15), -((h/2)-t), 954.666667), ), ((-((b/2)-15), -((h/2)-t),
    592.0), ), ((-((b/2)-9.99999), -(h/2), 1313.666667), ), ((-((b/2)-t), -((h/2)-15),
    1160.666667), ), ((-((b/2)-9.99999), -(h/2), 954.666667), ), ((-((b/2)-9.99999),
    -(h/2), 592.0), ), ((-((b/2)-15), -((h/2)-t), 1643.0), ), ((-((b/2)-9.99999),
    (h/2), 592.0), ), ((-((b/2)-9.99999), (h/2), 954.666667), ), ((-(b/2),
    ((h/2)-15), 1160.666667), ), ((-(b/2), ((h/2)-9.99999), 1643.0), ), ((
    -((b/2)-9.99999), (h/2), 1313.666667), ), ((((b/2)-9.99999), (h/2),
    1313.666667), ), ((((b/2)-9.99999), -(h/2), 1313.666667), ), ((-((b/2)-t),
    -((h/2)-15), 1643.0), ), )), suppressed=False, thickness=ta, thicknessType=
    SPECIFY_THICKNESS)
mdb.models['Model-1'].parts['Part-1'].compositeLayups['CompositeLayup-
1'].CompositePly(
    additionalRotationField='', additionalRotationType=ROTATION_NONE,
angle=0.0
    , axis=AXIS_3, material='Material-1', numIntPoints=3, orientationType=
    SPECIFY_ORIENT, orientationValue=deg, plyName='Ply-2', region=Region(
    cells=mdb.models['Model-1'].parts['Part-1'].cells.findAt((((b/2),
    -((h/2)-15), 1643.0), ), (((b/2), -((h/2)-15), 1160.666667), ), (((b/2),
    -((h/2)-15), 954.666667), ), (((b/2), -((h/2)-15), 592.0), ), ((((b/2)-15),
    -(h/2), 1643.0), ), ((((b/2)-15), -((h/2)-t), 1160.666667), ), ((((b/2)-15), -((h/2)-t),
    954.666667), ), ((((b/2)-15), -((h/2)-t), 592.0), ), ((((b/2)-15), -(h/2),
    1313.666667), ), ((((b/2)-t), ((h/2)-15), 592.0), ), ((((b/2)-t), ((h/2)-15),
```

```
    954.666667), ), ((((b/2)-t), ((h/2)-15), 1160.666667), ), ((((b/2)-t), ((h/2)-15),
    1643.0), ), ((-((b/2)-15), -((h/2)-t), 1313.666667), ), ((-((b/2)-15), -((h/2)-t),
    1160.666667), ), ((-((b/2)-15), -((h/2)-t), 954.666667), ), ((-((b/2)-15), -((h/2)-t),
    592.0), ), ((-((b/2)-9.99999), -(h/2), 1313.666667), ), ((-((b/2)-t), -((h/2)-15),
    1160.666667), ), ((-((b/2)-9.99999), -(h/2), 954.666667), ), ((-((b/2)-9.99999),
    -(h/2), 592.0), ), ((-((b/2)-15), -((h/2)-t), 1643.0), ), ((-((b/2)-9.99999),
    (h/2), 592.0), ), ((-((b/2)-9.99999), (h/2), 954.666667), ), ((-(b/2),
    ((h/2)-15), 1160.666667), ), ((-(b/2), ((h/2)-9.99999), 1643.0), ), ((
    -((b/2)-9.99999), (h/2), 1313.666667), ), ((((b/2)-9.99999), (h/2),
    1313.666667), ), ((((b/2)-9.99999), -(h/2), 1313.666667), ), ((-((b/2)-t),
    -((h/2)-15), 1643.0), ), )), suppressed=False, thickness=tw, thicknessType=
    SPECIFY_THICKNESS)
mdb.models['Model-1'].parts['Part-1'].compositeLayups['CompositeLayup-
1'].CompositePly(
    additionalRotationField='', additionalRotationType=ROTATION_NONE,
angle=0.0
    , axis=AXIS_3, material='Material-1', numIntPoints=3, orientationType=
    SPECIFY_ORIENT, orientationValue=-deg, plyName='Ply-3', region=Region(
    cells=mdb.models['Model-1'].parts['Part-1'].cells.findAt((((b/2),
    -((h/2)-15), 1643.0), ), (((b/2), -((h/2)-15), 1160.666667), ), (((b/2),
    -((h/2)-15), 954.666667), ), (((b/2), -((h/2)-15), 592.0), ), ((((b/2)-15),
    -(h/2), 1643.0), ), ((((b/2)-15), -((h/2)-t), 1160.666667), ), ((((b/2)-15), -((h/2)-t),
    954.666667), ), ((((b/2)-15), -((h/2)-t), 592.0), ), ((((b/2)-15), -(h/2),
    1313.666667), ), ((((b/2)-t), ((h/2)-15), 592.0), ), ((((b/2)-t), ((h/2)-15),
    954.666667), ), ((((b/2)-t), ((h/2)-15), 1160.666667), ), ((((b/2)-t), ((h/2)-15),
```

```
    1643.0), ), ((-((b/2)-15), -((h/2)-t), 1313.666667), ), ((-((b/2)-15), -((h/2)-t),
    1160.666667), ), ((-((b/2)-15), -((h/2)-t), 954.666667), ), ((-((b/2)-15), -((h/2)-t),
    592.0), ), ((-((b/2)-9.99999), -(h/2), 1313.666667), ), ((-((b/2)-t), -((h/2)-15),
    1160.666667), ), ((-((b/2)-9.99999), -(h/2), 954.666667), ), ((-((b/2)-9.99999),
    -(h/2), 592.0), ), ((-((b/2)-15), -((h/2)-t), 1643.0), ), ((-((b/2)-9.99999),
    (h/2), 592.0), ), ((-((b/2)-9.99999), (h/2), 954.666667), ), ((-(b/2),
    ((h/2)-15), 1160.666667), ), ((-(b/2), ((h/2)-9.99999), 1643.0), ), ((
    -((b/2)-9.99999), (h/2), 1313.666667), ), ((((b/2)-9.99999), (h/2),
    1313.666667), ), ((((b/2)-9.99999), -(h/2), 1313.666667), ), ((-((b/2)-t),
    -((h/2)-15), 1643.0), ), )), suppressed=False, thickness=tw, thicknessType=
    SPECIFY_THICKNESS)
mdb.models['Model-1'].parts['Part-1'].compositeLayups['CompositeLayup-
1'].CompositePly(
    additionalRotationField='', additionalRotationType=ROTATION_NONE,
angle=0.0
    , axis=AXIS_3, material='Material-1', numIntPoints=3, orientationType=
    SPECIFY_ORIENT, orientationValue=0.0, plyName='Ply-4', region=Region(
    cells=mdb.models['Model-1'].parts['Part-1'].cells.findAt((((b/2),
    -((h/2)-15), 1643.0), ), (((b/2), -((h/2)-15), 1160.666667), ), (((b/2),
    -((h/2)-15), 954.666667), ), (((b/2), -((h/2)-15), 592.0), ), ((((b/2)-15),
    -(h/2), 1643.0), ), ((((b/2)-15), -((h/2)-t), 1160.666667), ), ((((b/2)-15), -((h/2)-t),
    954.666667), ), ((((b/2)-15), -((h/2)-t), 592.0), ), ((((b/2)-15), -(h/2),
    1313.666667), ), ((((b/2)-t), ((h/2)-15), 592.0), ), ((((b/2)-t), ((h/2)-15),
    954.666667), ), ((((b/2)-t), ((h/2)-15), 1160.666667), ), ((((b/2)-t), ((h/2)-15),
    1643.0), ), ((-((b/2)-15), -((h/2)-t), 1313.666667), ), ((-((b/2)-15), -((h/2)-t),
```

```
    1160.666667), ), ((-((b/2)-15), -((h/2)-t), 954.666667), ), ((-((b/2)-15), -((h/2)-t),
    592.0), ), ((-((b/2)-9.99999), -(h/2), 1313.666667), ), ((-((b/2)-t), -((h/2)-15),
    1160.666667), ), ((-((b/2)-9.99999), -(h/2), 954.666667), ), ((-((b/2)-9.99999),
    -(h/2), 592.0), ), ((-((b/2)-15), -((h/2)-t), 1643.0), ), ((-((b/2)-9.99999),
    (h/2), 592.0), ), ((-((b/2)-9.99999), (h/2), 954.666667), ), ((-(b/2),
    ((h/2)-15), 1160.666667), ), ((-(b/2), ((h/2)-9.99999), 1643.0), ), ((
    -((b/2)-9.99999), (h/2), 1313.666667), ), ((((b/2)-9.99999), (h/2),
    1313.666667), ), ((((b/2)-9.99999), -(h/2), 1313.666667), ), ((-((b/2)-t),
    -((h/2)-15), 1643.0), ), )), suppressed=False, thickness=ta, thicknessType=
    SPECIFY_THICKNESS)
mdb.models['Model-1'].parts['Part-1'].compositeLayups['CompositeLayup-
1'].CompositePly(
    additionalRotationField='', additionalRotationType=ROTATION_NONE,
angle=0.0
    , axis=AXIS_3, material='Material-1', numIntPoints=3, orientationType=
    SPECIFY_ORIENT, orientationValue=-deg, plyName='Ply-5', region=Region(
    cells=mdb.models['Model-1'].parts['Part-1'].cells.findAt((((b/2),
    -((h/2)-15), 1643.0), ), (((b/2), -((h/2)-15), 1160.666667), ), (((b/2),
    -((h/2)-15), 954.666667), ), (((b/2), -((h/2)-15), 592.0), ), ((((b/2)-15),
    -(h/2), 1643.0), ), ((((b/2)-15), -((h/2)-t), 1160.666667), ), ((((b/2)-15), -((h/2)-t),
    954.666667), ), ((((b/2)-15), -((h/2)-t), 592.0), ), ((((b/2)-15), -(h/2),
    1313.666667), ), ((((b/2)-t), ((h/2)-15), 592.0), ), ((((b/2)-t), ((h/2)-15),
    954.666667), ), ((((b/2)-t), ((h/2)-15), 1160.666667), ), ((((b/2)-t), ((h/2)-15),
    1643.0), ), ((-((b/2)-15), -((h/2)-t), 1313.666667), ), ((-((b/2)-15), -((h/2)-t),
    1160.666667), ), ((-((b/2)-15), -((h/2)-t), 954.666667), ), ((-((b/2)-15), -((h/2)-t),
```

```
    592.0), ), ((-((b/2)-9.99999), -(h/2), 1313.666667), ), ((-((b/2)-t), -((h/2)-15),
    1160.666667), ), ((-((b/2)-9.99999), -(h/2), 954.666667), ), ((-((b/2)-9.99999),
    -(h/2), 592.0), ), ((-((b/2)-15), -((h/2)-t), 1643.0), ), ((-((b/2)-9.99999),
    (h/2), 592.0), ), ((-((b/2)-9.99999), (h/2), 954.666667), ), ((-(b/2),
    ((h/2)-15), 1160.666667), ), ((-(b/2), ((h/2)-9.99999), 1643.0), ), ((
    -((b/2)-9.99999), (h/2), 1313.666667), ), ((((b/2)-9.99999), (h/2),
    1313.666667), ), ((((b/2)-9.99999), -(h/2), 1313.666667), ), ((-((b/2)-t),
    -((h/2)-15), 1643.0), ), )), suppressed=False, thickness=tw, thicknessType=
    SPECIFY_THICKNESS)
mdb.models['Model-1'].parts['Part-1'].compositeLayups['CompositeLayup-
1'].CompositePly(
    additionalRotationField='', additionalRotationType=ROTATION_NONE,
angle=0.0
    , axis=AXIS_3, material='Material-1', numIntPoints=3, orientationType=
    SPECIFY_ORIENT, orientationValue=deg, plyName='Ply-6', region=Region(
    cells=mdb.models['Model-1'].parts['Part-1'].cells.findAt((((b/2),
    -((h/2)-15), 1643.0), ), (((b/2), -((h/2)-15), 1160.666667), ), (((b/2),
    -((h/2)-15), 954.666667), ), (((b/2), -((h/2)-15), 592.0), ), ((((b/2)-15),
    -(h/2), 1643.0), ), ((((b/2)-15), -((h/2)-t), 1160.666667), ), ((((b/2)-15), -((h/2)-t),
    954.666667), ), ((((b/2)-15), -((h/2)-t), 592.0), ), ((((b/2)-15), -(h/2),
    1313.666667), ), ((((b/2)-t), ((h/2)-15), 592.0), ), ((((b/2)-t), ((h/2)-15),
    954.666667), ), ((((b/2)-t), ((h/2)-15), 1160.666667), ), ((((b/2)-t), ((h/2)-15),
    1643.0), ), ((-((b/2)-15), -((h/2)-t), 1313.666667), ), ((-((b/2)-15), -((h/2)-t),
    1160.666667), ), ((-((b/2)-15), -((h/2)-t), 954.666667), ), ((-((b/2)-15), -((h/2)-t),
    592.0), ), ((-((b/2)-9.99999), -(h/2), 1313.666667), ), ((-((b/2)-t), -((h/2)-15),
```

```
    1160.666667), ), ((-((b/2)-9.99999), -(h/2), 954.666667), ), ((-((b/2)-9.99999),
    -(h/2), 592.0), ), ((-((b/2)-15), -((h/2)-t), 1643.0), ), ((-((b/2)-9.99999),
    (h/2), 592.0), ), ((-((b/2)-9.99999), (h/2), 954.666667), ), ((-(b/2),
    ((h/2)-15), 1160.666667), ), ((-(b/2), ((h/2)-9.99999), 1643.0), ), ((
    -((b/2)-9.99999), (h/2), 1313.666667), ), ((((b/2)-9.99999), (h/2),
    1313.666667), ), ((((b/2)-9.99999), -(h/2), 1313.666667), ), ((-((b/2)-t),
    -((h/2)-15), 1643.0), ), )), suppressed=False, thickness=tw, thicknessType=
    SPECIFY_THICKNESS)
mdb.models['Model-1'].parts['Part-1'].compositeLayups['CompositeLayup-
1'].CompositePly(
    additionalRotationField='', additionalRotationType=ROTATION_NONE,
angle=0.0
    , axis=AXIS_3, material='Material-1', numIntPoints=3, orientationType=
    SPECIFY_ORIENT, orientationValue=0.0, plyName='Ply-7', region=Region(
    cells=mdb.models['Model-1'].parts['Part-1'].cells.findAt((((b/2),
    -((h/2)-15), 1643.0), ), (((b/2), -((h/2)-15), 1160.666667), ), (((b/2),
    -((h/2)-15), 954.666667), ), (((b/2), -((h/2)-15), 592.0), ), ((((b/2)-15),
    -(h/2), 1643.0), ), ((((b/2)-15), -((h/2)-t), 1160.666667), ), ((((b/2)-15), -((h/2)-t),
    954.666667), ), ((((b/2)-15), -((h/2)-t), 592.0), ), ((((b/2)-15), -(h/2),
    1313.666667), ), ((((b/2)-t), ((h/2)-15), 592.0), ), ((((b/2)-t), ((h/2)-15),
    954.666667), ), ((((b/2)-t), ((h/2)-15), 1160.666667), ), ((((b/2)-t), ((h/2)-15),
    1643.0), ), ((-((b/2)-15), -((h/2)-t), 1313.666667), ), ((-((b/2)-15), -((h/2)-t),
    1160.666667), ), ((-((b/2)-15), -((h/2)-t), 954.666667), ), ((-((b/2)-15), -((h/2)-t),
    592.0), ), ((-((b/2)-9.99999), -(h/2), 1313.666667), ), ((-((b/2)-t), -((h/2)-15),
    1160.666667), ), ((-((b/2)-9.99999), -(h/2), 954.666667), ), ((-((b/2)-9.99999),
```

```
    -(h/2), 592.0), ), ((-((b/2)-15), -((h/2)-t), 1643.0), ), ((-((b/2)-9.99999),
    (h/2), 592.0), ), ((-((b/2)-9.99999), (h/2), 954.666667), ), ((-(b/2),
    ((h/2)-15), 1160.666667), ), ((-(b/2), ((h/2)-9.99999), 1643.0), ), ((
    -((b/2)-9.99999), (h/2), 1313.666667), ), ((((b/2)-9.99999), (h/2),
    1313.666667), ), ((((b/2)-9.99999), -(h/2), 1313.666667), ), ((-((b/2)-t),
    -((h/2)-15), 1643.0), ), )), suppressed=False, thickness=ta, thicknessType=
    SPECIFY_THICKNESS)
mdb.models['Model-1'].parts['Part-1'].compositeLayups['CompositeLayup-
1'].ReferenceOrientation(
    additionalRotationField='', additionalRotationType=ROTATION_NONE,
angle=0.0
    , axis=AXIS_3, flipNormalDirection=False, flipPrimaryDirection=False,
    localCsys=None, normalAxisDefinition=SURFACE,
normalAxisDirection=AXIS_3,
    normalAxisRegion=mdb.models['Model-1'].parts['Part-1'].surfaces['Surf-1'],
    orientationType=DISCRETE, primaryAxisDefinition=EDGE,
primaryAxisDirection=
    AXIS_1, primaryAxisRegion=
    mdb.models['Model-1'].parts['Part-1'].sets['Set-6'], stackDirection=
    STACK_3)
mdb.models['Model-1'].parts['Part-1'].Surface(name='Surf-2', side1Faces=
    mdb.models['Model-1'].parts['Part-1'].faces.findAt((((b/2), ((h/2)-9.99999),
    1643.0), ), ((((b/2)-15), (h/2), 1643.0), ), ((-((b/2)-15), (h/2), 1643.0), ),
    ((-((b/2)-9.99999), (h/2), 1643.0), ), ((-((b/2)-15), -(h/2), 1643.0), ), ((
    -(b/2), ((h/2)-15), 1643.0), ), ((-(b/2), -((h/2)-9.99999), 1643.0), ), ((
```

```
    ((b/2)-15), -(h/2), 1643.0), ), ((((b/2)-9.99999), -(h/2), 1643.0), ), (((b/2),
    -((h/2)-15), 1643.0), ), (((b/2), ((h/2)-15), 1643.0), ), ((-(b/2), -((h/2)-15),
    1643.0), ), ))
mdb.models['Model-1'].parts['Part-1'].Set(edges=
    mdb.models['Model-1'].parts['Part-1'].edges.findAt(((((b/2)-10), (h/2), 1569.0),
    )), name='Set-14')
mdb.models['Model-1'].parts['Part-1'].CompositeLayup(description='',
    elementType=CONTINUUM_SHELL, name='CompositeLayup-Fail',
symmetric=False)
mdb.models['Model-1'].parts['Part-1'].compositeLayups['CompositeLayup-
Fail'].Section(
    integrationRule=SIMPSON, poissonDefinition=DEFAULT, preIntegrate=OFF,
    temperature=GRADIENT, thicknessModulus=None, useDensity=OFF)
mdb.models['Model-1'].parts['Part-1'].compositeLayups['CompositeLayup-
Fail'].CompositePly(
    additionalRotationField='', additionalRotationType=ROTATION_NONE,
angle=0.0
    , axis=AXIS_3, material='Material-1-Fail', numIntPoints=3, orientationType=
    SPECIFY_ORIENT, orientationValue=0.0, plyName='Ply-1', region=Region(
    cells=mdb.models['Model-1'].parts['Part-1'].cells.findAt(((((b/2)-15), (h/2),
    592.0), ), ((((b/2)-15), (h/2), 954.666667), ), ((((b/2)-15), (h/2),
    1160.666667), ), ((((b/2)-15), ((h/2)-t), 1643.0), ), ((((b/2)-15), ((h/2)-t),
    1313.666667), ), ((-((b/2)-15), (h/2), 592.0), ), ((-((b/2)-15), (h/2),
    954.666667), ), ((-((b/2)-15), (h/2), 1160.666667), ), ((-((b/2)-15), ((h/2)-t),
    1643.0), ), ((-((b/2)-15), (h/2), 1313.666667), ), )), suppressed=False,
```

```
    thickness=ta, thicknessType=SPECIFY_THICKNESS)
mdb.models['Model-1'].parts['Part-1'].compositeLayups['CompositeLayup-
Fail'].CompositePly(
    additionalRotationField='', additionalRotationType=ROTATION_NONE,
angle=0.0
    , axis=AXIS_3, material='Material-1-Fail', numIntPoints=3, orientationType=
    SPECIFY_ORIENT, orientationValue=deg, plyName='Ply-2', region=Region(
    cells=mdb.models['Model-1'].parts['Part-1'].cells.findAt(((((b/2)-15), (h/2),
    592.0), ), ((((b/2)-15), (h/2), 954.666667), ), ((((b/2)-15), (h/2),
    1160.666667), ), ((((b/2)-15), ((h/2)-t), 1643.0), ), ((((b/2)-15), ((h/2)-t),
    1313.666667), ), ((-((b/2)-15), (h/2), 592.0), ), ((-((b/2)-15), (h/2),
    954.666667), ), ((-((b/2)-15), (h/2), 1160.666667), ), ((-((b/2)-15), ((h/2)-t),
    1643.0), ), ((-((b/2)-15), (h/2), 1313.666667), ), )), suppressed=False,
    thickness=tw, thicknessType=SPECIFY_THICKNESS)
mdb.models['Model-1'].parts['Part-1'].compositeLayups['CompositeLayup-
Fail'].CompositePly(
    additionalRotationField='', additionalRotationType=ROTATION_NONE,
angle=0.0
    , axis=AXIS_3, material='Material-1-Fail', numIntPoints=3, orientationType=
    SPECIFY_ORIENT, orientationValue=-deg, plyName='Ply-3', region=Region(
    cells=mdb.models['Model-1'].parts['Part-1'].cells.findAt(((((b/2)-15), (h/2),
    592.0), ), ((((b/2)-15), (h/2), 954.666667), ), ((((b/2)-15), (h/2),
    1160.666667), ), ((((b/2)-15), ((h/2)-t), 1643.0), ), ((((b/2)-15), ((h/2)-t),
    1313.666667), ), ((-((b/2)-15), (h/2), 592.0), ), ((-((b/2)-15), (h/2),
    954.666667), ), ((-((b/2)-15), (h/2), 1160.666667), ), ((-((b/2)-15), ((h/2)-t),
```

1643.0),), ((-((b/2)-15), (h/2), 1313.666667),),)), suppressed=False,

thickness=tw, thicknessType=SPECIFY_THICKNESS)

mdb.models['Model-1'].parts['Part-1'].compositeLayups['CompositeLayup-Fail'].CompositePly(

additionalRotationField='', additionalRotationType=ROTATION_NONE, angle=0.0

, axis=AXIS_3, material='Material-1-Fail', numIntPoints=3, orientationType=

SPECIFY_ORIENT, orientationValue=0.0, plyName='Ply-4', region=Region(

cells=mdb.models['Model-1'].parts['Part-1'].cells.findAt(((((b/2)-15), (h/2),

592.0),), ((((b/2)-15), (h/2), 954.666667),), ((((b/2)-15), (h/2),

1160.666667),), ((((b/2)-15), ((h/2)-t), 1643.0),), ((((b/2)-15), ((h/2)-t),

1313.666667),), ((-((b/2)-15), (h/2), 592.0),), ((-((b/2)-15), (h/2),

954.666667),), ((-((b/2)-15), (h/2), 1160.666667),), ((-((b/2)-15), ((h/2)-t),

1643.0),), ((-((b/2)-15), (h/2), 1313.666667),),)), suppressed=False,

thickness=ta, thicknessType=SPECIFY_THICKNESS)

mdb.models['Model-1'].parts['Part-1'].compositeLayups['CompositeLayup-Fail'].CompositePly(

additionalRotationField='', additionalRotationType=ROTATION_NONE, angle=0.0

, axis=AXIS_3, material='Material-1-Fail', numIntPoints=3, orientationType=

SPECIFY_ORIENT, orientationValue=-deg, plyName='Ply-5', region=Region(

cells=mdb.models['Model-1'].parts['Part-1'].cells.findAt(((((b/2)-15), (h/2),

592.0),), ((((b/2)-15), (h/2), 954.666667),), ((((b/2)-15), (h/2),

1160.666667),), ((((b/2)-15), ((h/2)-t), 1643.0),), ((((b/2)-15), ((h/2)-t),

1313.666667),), ((-((b/2)-15), (h/2), 592.0),), ((-((b/2)-15), (h/2), 954.666667),), ((-((b/2)-15), (h/2), 1160.666667),), ((-((b/2)-15), ((h/2)-t),

1643.0),), ((-((b/2)-15), (h/2), 1313.666667),),)), suppressed=False,

thickness=tw, thicknessType=SPECIFY_THICKNESS)

mdb.models['Model-1'].parts['Part-1'].compositeLayups['CompositeLayup-Fail'].CompositePly(

additionalRotationField='', additionalRotationType=ROTATION_NONE, angle=0.0

, axis=AXIS_3, material='Material-1-Fail', numIntPoints=3, orientationType=

SPECIFY_ORIENT, orientationValue=deg, plyName='Ply-6', region=Region(

cells=mdb.models['Model-1'].parts['Part-1'].cells.findAt(((((b/2)-15), (h/2),

592.0),), ((((b/2)-15), (h/2), 954.666667),), ((((b/2)-15), (h/2),

1160.666667),), ((((b/2)-15), ((h/2)-t), 1643.0),), ((((b/2)-15), ((h/2)-t),

1313.666667),), ((-((b/2)-15), (h/2), 592.0),), ((-((b/2)-15), (h/2),

954.666667),), ((-((b/2)-15), (h/2), 1160.666667),), ((-((b/2)-15), ((h/2)-t),

1643.0),), ((-((b/2)-15), (h/2), 1313.666667),),)), suppressed=False,

thickness=tw, thicknessType=SPECIFY_THICKNESS)

mdb.models['Model-1'].parts['Part-1'].compositeLayups['CompositeLayup-Fail'].CompositePly(

additionalRotationField='', additionalRotationType=ROTATION_NONE, angle=0.0

, axis=AXIS_3, material='Material-1-Fail', numIntPoints=3, orientationType=

SPECIFY_ORIENT, orientationValue=0.0, plyName='Ply-7', region=Region(

cells=mdb.models['Model-1'].parts['Part-1'].cells.findAt(((((b/2)-15), (h/2),

592.0),), ((((b/2)-15), (h/2), 954.666667),), ((((b/2)-15), (h/2),

1160.666667),), ((((b/2)-15), ((h/2)-t), 1643.0),), ((((b/2)-15), ((h/2)-t),

```
    1313.666667), ), ((-((b/2)-15), (h/2), 592.0), ), ((-((b/2)-15), (h/2),
    954.666667), ), ((-((b/2)-15), (h/2), 1160.666667), ), ((-((b/2)-15), ((h/2)-t),
    1643.0), ), ((-((b/2)-15), (h/2), 1313.666667), ), )), suppressed=False,
    thickness=ta, thicknessType=SPECIFY_THICKNESS)
mdb.models['Model-1'].parts['Part-1'].compositeLayups['CompositeLayup-
Fail'].ReferenceOrientation(
    additionalRotationField='', additionalRotationType=ROTATION_NONE,
angle=0.0
    , axis=AXIS_3, flipNormalDirection=False, flipPrimaryDirection=False,
    localCsys=None, normalAxisDefinition=SURFACE,
normalAxisDirection=AXIS_3,
    normalAxisRegion=mdb.models['Model-1'].parts['Part-1'].surfaces['Surf-2'],
    orientationType=DISCRETE, primaryAxisDefinition=EDGE,
primaryAxisDirection=
    AXIS_1, primaryAxisRegion=
    mdb.models['Model-1'].parts['Part-1'].sets['Set-14'], stackDirection=
    STACK_3)
# generating the "Assembly" geometry:
mdb.models['Model-1'].rootAssembly.DatumCsysByDefault(CARTESIAN)
mdb.models['Model-1'].rootAssembly.Instance(dependent=ON, name='Part-1-1',
    part=mdb.models['Model-1'].parts['Part-1'])
mdb.models['Model-1'].rootAssembly.Set(name='Bot_Mid_Def', vertices=
    mdb.models['Model-1'].rootAssembly.instances['Part-1-1'].vertices.findAt(((
    ((b/2)-10), -(h/2), 1247.0), )))
# generating the "Boundary conditions" geometry:
```

```
mdb.models['Model-1'].rootAssembly.Set(faces=
    mdb.models['Model-1'].rootAssembly.instances['Part-1-1'].faces.findAt(((
    ((b/2)-15), -((h/2)-1.5), 2235.0), ), ((((b/2)-15), ((h/2)-1.5), 2235.0), ), ((
    -((b/2)-15), -((h/2)-1.5), 2235.0), ), ((-((b/2)-1.5), ((h/2)-15), 2235.0), ), ((
    ((b/2)-1.5), -((h/2)-15), 2235.0), ), ((-((b/2)-15), ((h/2)-1.5), 2235.0), ), ((
    ((b/2)-1.5), ((h/2)-15), 2235.0), ), ((-((b/2)-1.5), -((h/2)-15), 2235.0), ), ),
    name='Set-2')
mdb.models['Model-1'].DisplacementBC(amplitude=UNSET,
createStepName='Initial',
    distributionType=UNIFORM, fieldName='', localCsys=None, name='R_Left',
    region=mdb.models['Model-1'].rootAssembly.sets['Set-2'], u1=SET, u2=SET,
    u3=UNSET, ur1=UNSET, ur2=UNSET, ur3=UNSET)
mdb.models['Model-1'].rootAssembly.Set(faces=
    mdb.models['Model-1'].rootAssembly.instances['Part-1-1'].faces.findAt(((
    ((b/2)-15), -((h/2)-1.5), 0.0), ), ((((b/2)-15), ((h/2)-1.5), 0.0), ), ((
    -((b/2)-1.5), -((h/2)-15), 0.0), ), ((-((b/2)-1.5), ((h/2)-15), 0.0), ), ((
    ((b/2)-1.5), ((h/2)-15), 0.0), ), ((-((b/2)-15), -((h/2)-1.5), 0.0), ), ((
    -((b/2)-15), ((h/2)-1.5), 0.0), ), ((((b/2)-1.5), -((h/2)-15), 0.0), ), ), name=
    'Set-3')
mdb.models['Model-1'].DisplacementBC(amplitude=UNSET,
createStepName='Initial',
    distributionType=UNIFORM, fieldName='', localCsys=None, name='R_Right',
    region=mdb.models['Model-1'].rootAssembly.sets['Set-3'], u1=SET, u2=SET,
    u3=UNSET, ur1=UNSET, ur2=UNSET, ur3=UNSET)
# generating the “first step/linear buckling”:
```

```
mdb.models['Model-1'].BuckleStep(maxIterations=300, name='Step-1',
numEigen=3,
    previous='Initial', vectors=6)
mdb.models['Model-1'].rootAssembly.Surface(name='Surf-1', side1Faces=
    mdb.models['Model-1'].rootAssembly.instances['Part-1-1'].faces.findAt(((
    -((b/2)-1.3), -((h/2)-36.7), 500.0), ), ((((b/2)-1.8), -((h/2)-36.7), 500.0), ), ((
    ((b/2)-1.3), ((h/2)-36.7), 500.0), ), ((-((b/2)-1.8), ((h/2)-36.7), 500.0), ), ))
mdb.models['Model-1'].Pressure(createStepName='Step-1', distributionType=
    UNIFORM, field='', magnitude=1.0, name='Unit_load', region=
    mdb.models['Model-1'].rootAssembly.surfaces['Surf-1'])
# printing nodal outputs:
mdb.models['Model-
1'].keywordBlock.synchVersions(storeNodesAndElements=False)
mdb.models['Model-1'].keywordBlock.replace(55,
    '\n*Output, field, variable=PRESELECT\n*NODE FILE \nU,')
# executing the “Linear buckling” analysis:
mdb.Job(atTime=None, contactPrint=OFF, description='', echoPrint=OFF,
    explicitPrecision=SINGLE, getMemoryFromAnalysis=True, historyPrint=OFF,
    memory=90, memoryUnits=PERCENTAGE, model='Model-1', modelPrint=OFF,
    multiprocessingMode=DEFAULT, name='LinearBL',
nodalOutputPrecision=SINGLE,
    numCpus=1, numGPUs=0, queue=None, resultsFormat=ODB, scratch='', type=
    ANALYSIS, userSubroutine='', waitHours=0, waitMinutes=0)
# submitting the “Linear buckling” job:
mdb.jobs['LinearBL'].submit(consistencyChecking=OFF)
```

generating the “second step/nonlinear buckling”:

```
mdb.models['Model-1'].StaticStep(adaptiveDampingRatio=0.05,
    continueDampingFactors=False, initialInc=450.0, maxInc=450.0, maxNumInc=
    10000000, minInc=1e-40, name='Step-1', nlgeom=ON, previous='Initial',
    stabilizationMagnitude=0.0002, stabilizationMethod=
    DISSIPATED_ENERGY_FRACTION, timePeriod=6000.0)
mdb.models['Model-1'].steps['Step-1'].control.setValues(allowPropagation=OFF,
    resetDefaultValues=OFF, timeIncrementation=(4.0, 8.0, 9.0, 16.0, 10.0, 4.0,
    12.0, 10.0, 6.0, 3.0, 50.0))
```

Assigning the “loading conditions”:

```
mdb.models['Model-1'].rootAssembly.Set(faces=
    mdb.models['Model-1'].rootAssembly.instances['Part-1-1'].faces.findAt(((
    (b/2), ((h/2)-15), 1313.666667), ), (((b/2), -((h/2)-15), 1313.666667), ), ((
    -(b/2), -((h/2)-15), 1313.666667), ), ((((b/2)-15), (h/2), 1313.666667), ), ((
    ((b/2)-9.99999), (h/2), 1313.666667), ), ((-((b/2)-15), (h/2), 1313.666667), ),
    ((-(b/2), ((h/2)-9.99999), 1313.666667), ), ((-(b/2), ((h/2)-15), 1313.666667),
    ), ), name='Set-4')
mdb.models['Model-1'].DisplacementBC(amplitude=UNSET,
createStepName='Step-1',
    distributionType=UNIFORM, fieldName='', fixed=OFF, localCsys=None, name=
    'Disp_Left', region=mdb.models['Model-1'].rootAssembly.sets['Set-4'], u1=
    UNSET, u2=-100.0, u3=UNSET, ur1=UNSET, ur2=UNSET, ur3=UNSET)
mdb.models['Model-1'].rootAssembly.Set(faces=
    mdb.models['Model-1'].rootAssembly.instances['Part-1-1'].faces.findAt(((
    -(b/2), -((h/2)-15), 954.666667), ), ((-(b/2), ((h/2)-15), 954.666667), ), ((
```

```
    -(b/2), ((h/2)-9.99999), 954.666667), ), ((-((b/2)-15), (h/2), 954.666667), ),
    (((b/2), ((h/2)-15), 954.666667), ), ((((b/2)-9.99999), (h/2), 954.666667), ),
    ((((b/2)-15), (h/2), 954.666667), ), (((b/2), -((h/2)-15), 954.666667), ), ),
    name='Set-5')
mdb.models['Model-1'].DisplacementBC(amplitude=UNSET,
createStepName='Step-1',
    distributionType=UNIFORM, fieldName='', fixed=OFF, localCsys=None, name=
    'Disp_Right', region=mdb.models['Model-1'].rootAssembly.sets['Set-5'], u1=
    UNSET, u2=-100.0, u3=UNSET, ur1=UNSET, ur2=UNSET, ur3=UNSET)
# defining the "Integrated output section" geometry:
mdb.models['Model-1'].rootAssembly.Surface(name='Surf-1', side1Faces=
    mdb.models['Model-1'].rootAssembly.instances['Part-1-1'].faces.findAt(((
    (b/2), ((h/2)-15), 1313.666667), ), (((b/2), -((h/2)-15), 1313.666667), ), ((
    -(b/2), -((h/2)-15), 1313.666667), ), ((((b/2)-15), (h/2), 1313.666667), ), ((
    ((b/2)-9.99999), (h/2), 1313.666667), ), ((-((b/2)-15), (h/2), 1313.666667), ),
    ((-(b/2), ((h/2)-9.99999), 1313.666667), ), ((-(b/2), ((h/2)-15), 1313.666667),
    ), ))
mdb.models['Model-1'].IntegratedOutputSection(name='Load_Left', surface=
    mdb.models['Model-1'].rootAssembly.surfaces['Surf-1'])
mdb.models['Model-1'].rootAssembly.Surface(name='Surf-2', side1Faces=
    mdb.models['Model-1'].rootAssembly.instances['Part-1-1'].faces.findAt(((
    -(b/2), -((h/2)-15), 954.666667), ), ((-(b/2), ((h/2)-15), 954.666667), ), ((
    -(b/2), ((h/2)-9.99999), 954.666667), ), ((-((b/2)-15), (h/2), 954.666667), ),
    (((b/2), ((h/2)-15), 954.666667), ), ((((b/2)-9.99999), (h/2), 954.666667), ),
    ((((b/2)-15), (h/2), 954.666667), ), (((b/2), -((h/2)-15), 954.666667), ), ))
```

```
mdb.models['Model-1'].IntegratedOutputSection(name='Load_Right', surface=
    mdb.models['Model-1'].rootAssembly.surfaces['Surf-2'])
# requesting the “Field output”:
mdb.models['Model-1'].fieldOutputRequests['F-Output-1'].setValues(variables=(
    'S', 'PE', 'PEEQ', 'PEMAG', 'LE', 'U', 'RF', 'CF', 'CSTRESS', 'CDISP',
    'DAMAGEFT', 'DAMAGEFC', 'DAMAGEMT', 'DAMAGEMC',
'DAMAGESHR', 'DMICRT'))
# requesting the “History output”:
mdb.models['Model-1'].HistoryOutputRequest(createStepName='Step-1', name=
    'Mid_Def', rebar=EXCLUDE, region=
    mdb.models['Model-1'].rootAssembly.sets['Bot_Mid_Def'], sectionPoints=
    DEFAULT, variables=('U1', 'U2', 'U3', 'UR1', 'UR2', 'UR3'))
mdb.models['Model-1'].HistoryOutputRequest(createStepName='Step-1',
    integratedOutputSection='Load_Left', name='Reaction_Left', rebar=EXCLUDE,
    sectionPoints=DEFAULT, variables=('SOF', 'SOM'))
mdb.models['Model-1'].HistoryOutputRequest(createStepName='Step-1',
    integratedOutputSection='Load_Right', name='Reaction_Right',
rebar=EXCLUDE,
    sectionPoints=DEFAULT, variables=('SOF', 'SOM'))
# requesting the “Geometric imperfiction”:
mdb.models['Model-
1'].keywordBlock.synchVersions(storeNodesAndElements=False)
mdb.models['Model-1'].keywordBlock.replace(45,
    '\n** ----------------------------------------------------------------\n**
\n*IMPERFECTION, FILE=LinearBL, STEP=1\n1, 5e-4\n2, 5e-4\n3, 5e-4\n**')
```

executing the “second step/nonlinear buckling”:

mdb.Job(atTime=None, contactPrint=OFF, description='', echoPrint=OFF,

explicitPrecision=SINGLE, getMemoryFromAnalysis=True, historyPrint=OFF,

memory=90, memoryUnits=PERCENTAGE, model='Model-1', modelPrint=OFF,

multiprocessingMode=DEFAULT, name='NonlinearBL', nodalOutputPrecision=

SINGLE, numCpus=1, numGPUs=0, queue=None, resultsFormat=ODB,
scratch='',

type=ANALYSIS, userSubroutine='', waitHours=0, waitMinutes=0)

writing the “input file”:

mdb.jobs['NonlinearBL'].writeInput(consistencyChecking=OFF)

closing the “model database”:

mdb.close()

2. ODB (output database) script:

-*- coding: mbcs -*-

Abaqus/Viewer Release 2019 replay file

Internal Version: 2016_09_28-07.54.59 126836

Run by U1122090 on Mon Apr 05 17:41:17 2021

from driverUtils import executeOnCaeGraphicsStartup

executeOnCaeGraphicsStartup()

#: Executing "onCaeGraphicsStartup()" in the site directory ...

importing the required modules:

from abaqus import *

from abaqusConstants import *

assigning the “session veiwport”:

```
session.Viewport(name='Viewport: 1', origin=(0.0, 0.0), width=125.046257019043,
    height=146.844451904297)
session.viewports['Viewport: 1'].makeCurrent()
session.viewports['Viewport: 1'].maximize()
from viewerModules import *
from driverUtils import executeOnCaeStartup
executeOnCaeStartup()
o2 = session.openOdb(name='NonlinearBL.odb')
#: Model: C:/Simulations/Bending/11/NonlinearBL.odb
#: Number of Assemblies:         1
#: Number of Assembly instances: 0
#: Number of Part instances:     1
#: Number of Meshes:             1
#: Number of Element Sets:       10
#: Number of Node Sets:          8
#: Number of Steps:              1
session.viewports['Viewport: 1'].setValues(displayedObject=o2)
# locating the “ODB file directory”:
odb = session.odbs['C:/Simulations/GA/Bending/NonlinearBL.odb']
# requesting the “axial displacement”:
xy_result = session.XYDataFromHistory(name='Disp', odb=odb,
    outputVariableName='Spatial displacement: U2 at Node 14 in NSET
BOT_MID_DEF',
    steps=('Step-1', ), __linkedVpName__='Viewport: 1')
c1 = session.Curve(xyData=xy_result)
```

```
xyp = session.XYPlot('XYPlot-1')
chartName = xyp.charts.keys()[0]
chart = xyp.charts[chartName]
chart.setValues(curvesToPlot=(c1, ), )
session.viewports['Viewport: 1'].setValues(displayedObject=xyp)
odb = session.odbs['C:/Simulations/GA/Bending/NonlinearBL.odb']
# requesting the “load”:
xy_result = session.XYDataFromHistory(name='Ld', odb=odb,
    outputVariableName='Total force on the surface: SOF2  on section LOAD_RIGHT in SSET SURF-2',
    steps=('Step-1', ), __linkedVpName__='Viewport: 1')
c1 = session.Curve(xyData=xy_result)
# generating the “load-displacement” curve:
xyp = session.xyPlots['XYPlot-1']
chartName = xyp.charts.keys()[0]
chart = xyp.charts[chartName]
chart.setValues(curvesToPlot=(c1, ), )
xy1 = session.xyDataObjects['Disp']
xy2 = session.xyDataObjects['Ld']
xy3 = combine(-1*xy1, 2*xy2)
xy3.setValues(sourceDescription='combine (  - 1 * "Disp",2  * "Ld" )')
tmpName = xy3.name
session.xyDataObjects.changeKey(tmpName, 'Load')
x0 = session.xyDataObjects['Load']
# writing the “load-displacement” curve in text file:
```

```
session.writeXYReport(fileName='abaqus.txt', appendMode=OFF, xyData=(x0, ))

# close the "output database":

odb.close()
```

3. Execution script:

```
# importing the required module:

import os

# command prompt commands to run the scripts:

os.system('cmd /c "abaqus cae noGUI=model.py"')

os.system('cmd /c "abaqus j=NonlinearBL int"')

os.system('cmd /c "abaqus cae noGUI=ODB.py"')
```